Advances in Printing and Media Technology

Vol. XLIX(IX)

Edited by Cathy Ridgway

Darmstadt
MMXXIII

Advances in Printing and Media Technology

Proceedings of the 49th International Research Conference of iarigai
Wuppertal, Germany, 18–20 September 2023

Published by the International Association of
Research Organizations for the Information,
Media and Graphic Arts Industries
Darmstadt, Germany, 2024

Edited by Cathy Ridgway, Oftringen, Switzerland

Online edition
ISBN 978-3-948039-04-2
ISSN 2409-4021
DOI 10.14622/Advances_49_2023

Contents

SESSION 4B Print Technologies & Systems III

SESSION 5B Print Technologies & Systems IV

SESSION 6B Print Technologies & Systems V

Preface

We live in challenging times – so does our industry.

Nevertheless, the printing industry continues to play a crucial role in various sectors such as packaging printing, advertising, printed electronics, and publishing. Despite the increasing digitalization, the demand for printed materials persists, especially for high-quality or specialized applications. The challenges faced by the printing industry are diverse, encompassing both technological and environmental aspects.

Key challenges include adapting to digitalization, developing more environmentally friendly printing processes, and finding more efficient and cost-effective production methods. In this context, science plays a pivotal role by researching and developing innovative solutions and technologies to help the industry overcome these challenges.

Against this backdrop, the 49th iarigai Conference, held from September 18–20, 2023, in Wuppertal, Germany, served as a confluence of international experts in printing and media technology. This gathering at the University of Wuppertal fostered dialogue and collaboration among academics, researchers, and industry professionals.

The conference's agenda included sessions on advancements in print technologies, applications in emerging media formats, and material science innovations, among others. These topics reflect the conference's commitment to addressing current challenges and exploring future possibilities in the industry.

To enhance the impact of the conference, the iarigai board decided to hold (again) a joint conference with the International Circle (IC). A notable addition to this year's event was the ESMA Networking Day, held in conjunction with the iarigai conference. This partnership with European Specialist Printing Manufacturers Association (ESMA) on September 20 provided a unique platform for bridging the gap between academic research and industry practice. The Networking Day featured keynote presentations, technical demonstrations, and valuable networking opportunities, emphasizing the synergy between industry and academia.

This proceedings volume contains research contributions presented at the 49th iarigai International Research Conference. The editors and publisher hope that you will find the contents of these proceedings informative and interesting.

Dr.-Ing. Daniel Bohn

Iarigai & IC Communication & Conference Organization
School of Electrical, Information and Media Engineering
Chair for Digital and Offset Printing
dbohn@uni-wuppertal.de

September 2023, Wuppertal, Germany

Link:
www.dmt.uni-wuppertal.de
www.dod.uni-wuppertal.de
www.iarigai.com
www.internationalcircle.net

DOI 10.14622/Advances_49_2023_02

A static compression study on the lateral pressure variations of flexo post-print on corrugated board

Li Yang, Hans Christiansson, Anni Hagberg and Cecilia Rydefalk

RISE – Research Institutes of Sweden, pulp, papermaking and packaging, Drottning Kristinas väg 61, 11428 Stockholm, Sweden
E-mails: (li.yang, hans.christiansson, anni.hagberg, cecilia.rydfalk)@ri.se

Short abstract

A method for evaluation of lateral pressure variation of flexo post-print on corrugated board has been developed. Material sandwiches of print plates and corrugated boards were prepared with Tekscan sensor matrix being embedded in between the print plate and the corrugated board. The material sandwich was compressed by a Universal Testing Machine (UTM). With help of calibration, the pressure signals (0–255) of the sensor matrix were converted to the SI units, i.e. N/m^2 (Pa) or kPa. Lateral pressure variations inherent to the fluting structure of the corrugated board could thus be analysed. Seven commercial corrugated boards and two print plates (one hard and one soft) were involved in the study. It was found that the tensile stiffness of the top liners, especially in short-span, exhibited very strong and negative correlation with the pressure variations.

Keywords: stripiness, banding, tensile stiffness, bending stiffness.

1. Introduction and background

Print stripiness or banding is often a quality concern of flexo post-printing on corrugated boards. It appears as periodic density and/or gloss variations parallel to the flutes. The underlying causes were studied by several researchers with experimental and numerical means. Holmvall and co-workers (Holmwall and Uesaka, 2007; 2008; Holmwall, 2010) reported their studies of nip mechanics in flexo post-printing. In these studies, non-linear finite element models were constructed in both corrugated board and halftone dot scales to study the nip mechanics. Variations in nip pressure inherent to the fluting structure of the corrugated boards were found to be responsible for the stripiness. Hallberg Hofstrand (2006) measured the pressure variation with the Tekscan pressure sensing device and studied the influence of print forms on stripiness in flexo post-print using an IGT F1 Printability Tester. They concluded that a higher local contact pressure on the fluting tips than in the fluting valleys is the major cause of print banding as it leads to a higher ink transfer to the fluting tips than to the valleys. Thorman and Sandin (2020) introduced a calibration method for the Tekscan pressure sensing system. After the calibration, the Tekscan pressure signals (0–255) can be converted to international system of units (SI) in Pa or kPa (kilo pascal).

Our hypothesis is that the lateral nip pressure variation depends on the resistance of the top liner towards tensile & bending deformations. The goal of the work is to verify or falsify the hypothesis and to get in-depth understanding of the relationship between the topliner properties and the stripiness.

The study for the hypothesis verification consists of three steps:

1. Static compression – the material sandwich consisting of the corrugated boards together with the print plate and the pressure sensor matrix were compressed by a metal plate of a universal testing machine (UTM).
2. Dynamic compression – the material sandwich was compressed by the pressing cylinder of an IGT-F1 lab press without ink.
3. Print verification – the corrugated boards were printed with the IGT-F1 lab press.

This work presents the major findings obtained in the first step, namely the static compression situation. The other parts will be published elsewhere.

2. Materials and methods

2.1 Corrugated boards and polymer plates

Seven commercial corrugated boards of type B and two print plates were involved in this study (Table 1). The corrugated boards were made of topliners of different grades and different grammages and two different fluting media denoted as FM1 and FM2, respectively. The print plates have the same thickness but different Shore A values and colours.

Table 1: Parameters of the corrugated boards and print plates

Corrugated boards			**Polymer plate**		
Sample	Topliner (g/m^2)	Fluting media	Name (color)	Thickness (mm)	Hardness (Shore A)
WT1	Double coated (145)	FM1	Asahi DSE (red)	4.7	34
WT2	Double coated (175)	FM1	Flint FAC (blue)	4.7	32
WT3	White top (175)	FM1			
WT4	White top (145)	FM1			
WT5	Pure white (110)	FM2			
WT6	White top (135)	FM2			
WT7	White top (175)	FM2			

2.2 Measurements of the tensile stiffness

Tensile stiffness of the seven topliners were measured with the UTM system equipped with pneumatic grips. Short-span tensile stiffness (span 5 mm) was measured as it may be more relevant for the study because the top liner is "fixed" in position by gluing onto the fluting tips of the corrugated boards. Ten measurements were made for the short-span tensile stiffness of each topliner. Table 2 lists the tensile stiffness values of the topliners used in the respective corrugated board samples WT1 through WT7. Columns 3 and 4 are the means of the tensile stiffness values and their standard deviations. Column 2 is the strain corresponding to the tensile stiffness values.

Table 2: The tensile stiffness values (means and standard deviations) of the topliners and the corresponding strains where the measurements were made

Sample	**Strain (%)**	**Stiffness (KN/m)**	
		Mean	Std
WT1	2.87	989.14	21.59
WT2	2.96	1 181.12	53.70
WT3	3.58	1 233.10	54.87
WT4	3.34	958.58	35.63
WT5	3.45	797.99	32.30
WT6	2.78	1 212.82	51.93
WT7	3.38	1 374.00	57.47

2.3 Measurement of the pressure profile

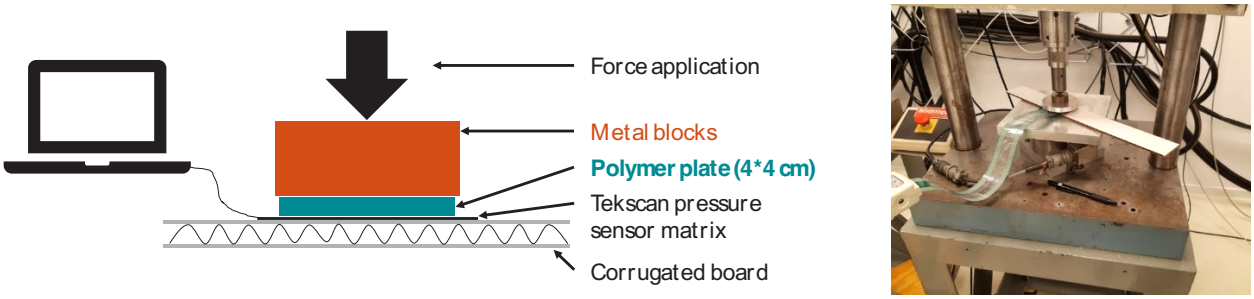

a) *b)*

Figure 1: Illustration (a) and the measurement setup (b) of compression test using a UTM

Figure 1 illustrates the setup of the pressure measurement of a material sandwich. The material sandwich consists of a piece of corrugated board at the bottom, a polymer plate on top, and the pressure sensing matrix (from Tekscan Inc., USA) in the middle. The sensor matrix possesses 44 × 44 = 1 936 sensor cells, equal number in MD and CD of the corrugated board. The center-to-center distance of two adjacent sensor cells is about 1 mm. The signals from the pressure sensor cells are transferred to the computer. With help of calibration, the pressure signals (0–255) from the sensor matrix are converted into Pa or kPa.

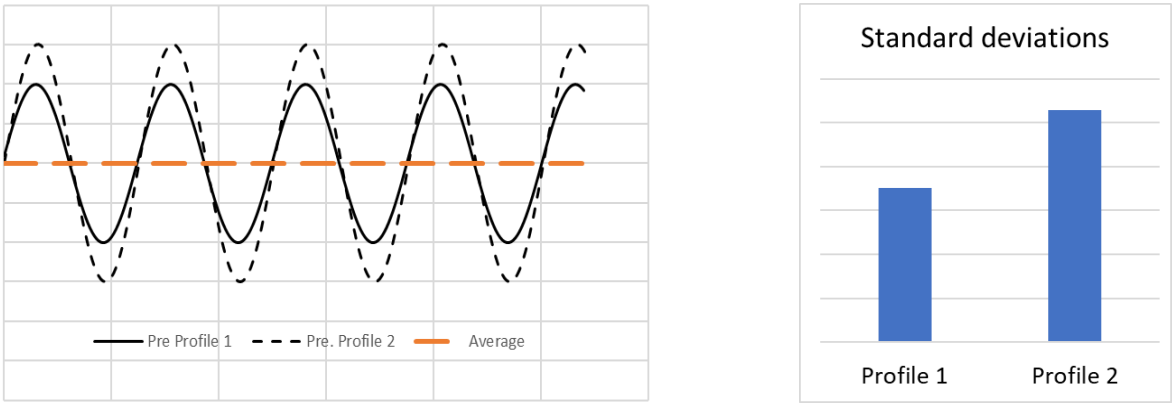

a) *b)*

Figure 2: Two pressure profiles (a) having the same average or nominal pressure (orange dashed line) but different amplitudes and standard deviations (b)

2.4 Analysis of pressure variation

Considering the geometrical characteristics of the corrugated board, we first took the average of the readings from the sensor cells in each row along the CD or the direction parallel to the flutes. The measured data was thus degenerated into one dimensional, e.g., pressure variation profile in MD. Figure 2 depicts two pressure profiles (Figure 2a) after the averaging in CD and their corresponding standard deviations (Figure 2b). Obviously, these two profiles have different amplitudes of pressure variation even though their nominal pressures (averages) are identical. For a sine-shaped periodic profile, the standard deviation of the profile is proportional to its amplitude. Thus, the variations can be well represented by their standard deviations. For meaningful compressions, pressure profiles corresponding to four nominal pressures, [50, 80, 110, 140] kPa, are presented in the next section.

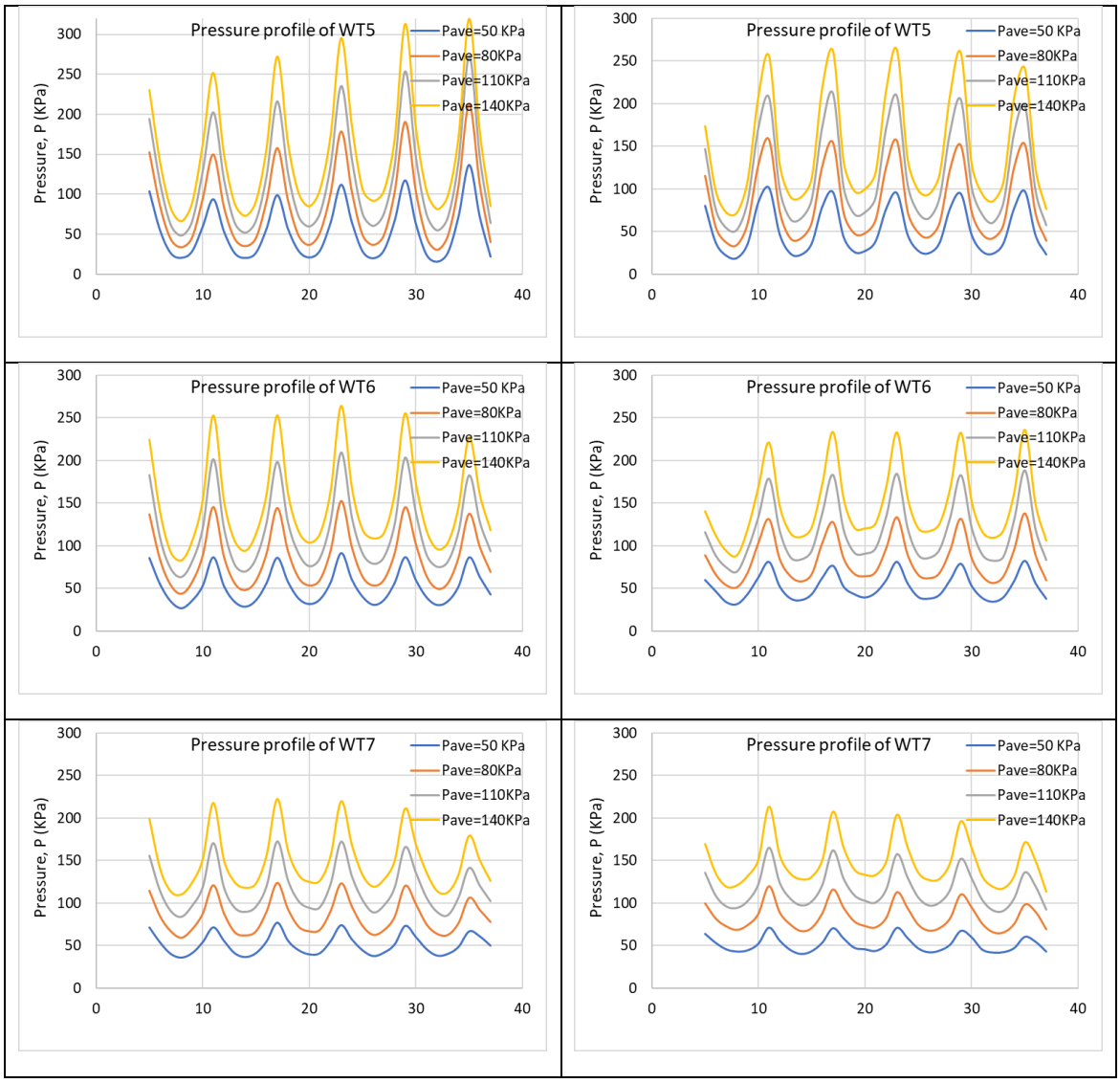

a) *b)*

Figure 3: Pressure profiles at four nominal (average) pressure levels, [50, 80, 110, 140] kPa; with the harder (Asahi) polymer plate (a); and with the softer (Flint) polymer plate (b)

3. Results and discussion

Figures 3 shows as an example of the pressure profiles of three corrugated boards, WT5 – WT7, at four nominal (average) pressures, [50, 80, 110, 140] kPa. Their corresponding standard deviations are shown in Figure 4. It is obvious that the amplitudes of the pressure variations increase with increasing nominal pressures. i.e. the higher the nominal pressure, the greater the pressure variation amplitude. Additionally, the amplitudes and the profiles differ significantly from one sample to another. As these samples were made of the same fluting medium but different topliners, one may thus attribute the differences to the topliners' properties. Furthermore, compared to the profiles in the right column (using the softer print plate, Figure 3b), the amplitudes of the pressure profiles obtained with the harder print plate (left column, Figure 3a) are generally higher. In other words, the pressure variation was reduced when the softer print plate was used.

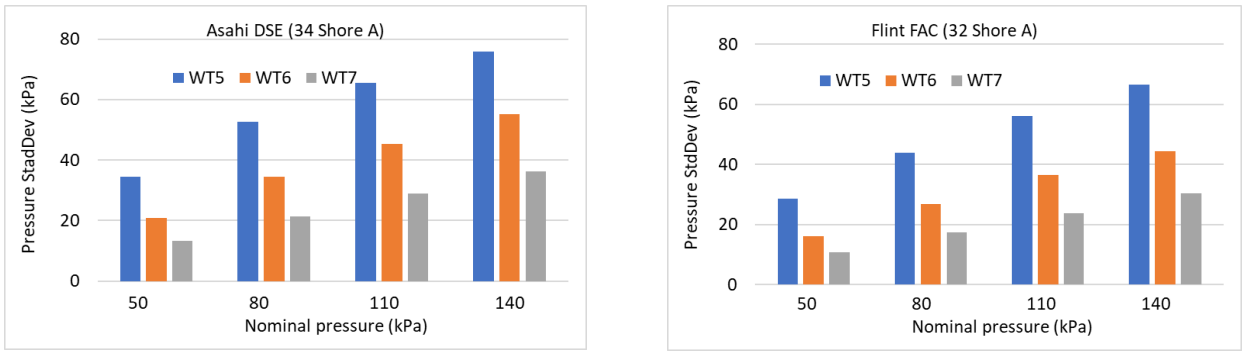

a) *b)*

Figure 4: Pressure variations (standard deviations) of the pressure profiles shown in Figure 3; with the harder (red) polymer plate (a), and with the softer (blue) polymer plate (b)

Figure 5 shows the relationships between the pressure variation and the short-span tensile stiffness of the top liners. The two figures correspond to experiments with two polymer plates. The four datasets in each of the subfigures, from bottom to top, correspond to four nominal pressure levels, [50, 80, 100, 140] kPa. The seven data points in each dataset correspond to the seven corrugated board products. The very high R^2 values indicate very strong correlation between the pressure variation and the short-span tensile stiffness of the top liners.

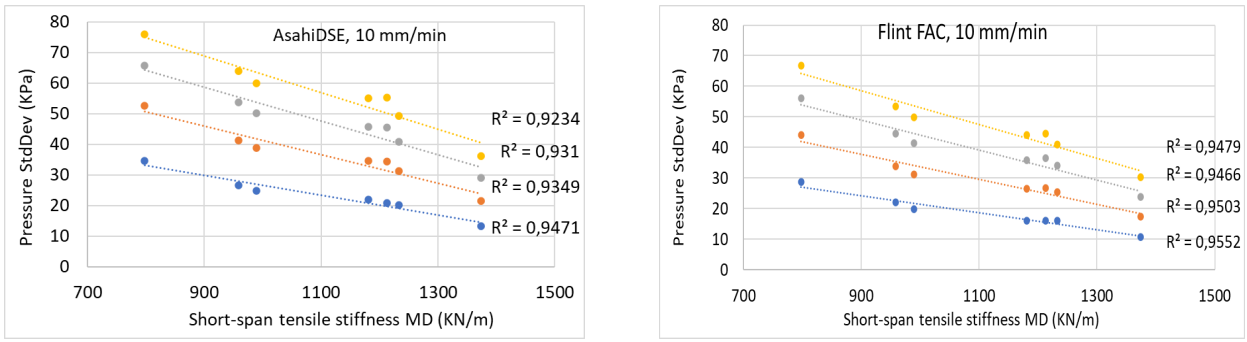

a) *b)*

Figure 5: Correlations of the pressure variation with the short-span tensile stiffness of the top liners; with the harder (Asahi) polymer plate (a), and with the softer (Flint) polymer plate (b); the dots and lines from bottom to top correspond to the nominal pressures [50, 80, 110, 140] KPa, respectively

4. Conclusion remarks

This study confirmed the hypothesis that the topliner's mechanical properties, particularly the short-span tensile stiffness, have indeed strong impacts on the lateral nip pressure variation in flexo post-print. The R^2 values ranging between 0.92 and 0.96 indicated extremely strong correlations between the lateral presser variation and the short-span tensile stiffness of the topliners, regardless the grades or detailed material compositions of the topliners. This is significantly higher that the R^2 values for the correlation with the topliners' grammage (not show), ranging between 0.64 and 0.78.

The precedingly stated findings have been further studied in the dynamic compression situation using an IGT-F1 lab press and verified by lab printing where stripiness propensity of the lab prints. Detailed results of these studies will be published elsewhere.

Acknowledgements

DS Smith, Metsä Board, Mondi, and Stora Enso are gratefully acknowledged for financial support and providing the corrugated boards samples.

References

Holmvall, M. and Uesaka, T., 2007. Nip mechanics of flexo post-printing on corrugated board. *Journal of Composite Materials*, 41(17), pp. 2129–2145. https://doi.org/10.1177/0021998307074135.

Holmvall, M. and Uesaka, T., 2008. Striping of corrugated board in full-tone flexo post-printing. *Appita Journal*, 61(1), pp. 35–40.

Holmvall, M., 2010. *Nip mechanics, hydrodynamics and print quality in flexo post-printing*. PhD thesis. Mid Sweden University, Sweden.

Hallberg Hofstrand, E., 2006. *Flexographic post-printing of corrugated board: contact mechanics and print quality*. PhD Thesis. Karlstad University, Sweden.

Thorman, S. and Sandin, S., 2020. *Technique for characterisation of lateral pressure variations of corrugated boards: Bioeconomy Report No: 80*. Stockholm: RISE.

DOI 10.14622/Advances_49_2023_16

Control of ink-water balance in offset lithography by machine learning

Eric Holle[1], *Felix Knödl*[2], *Martin Mayer*[3], *Tizian Schneider*[1], *Dieter Spiehl*[2], *Andreas Blaeser*[4,5], *Edgar Dörsam*[2] *and Andreas Schütze*[1]

[1] Saarland University, Faculty of Natural Sciences and Technology, Lab for Measurement Technology, Campus A5.1, 66123 Saarbrücken, Germany

[2] Technical University of Darmstadt, Department of Mechanical and Process Engineering, Institute of Printing Science and Technology, Magdalenenstr. 2, 64289 Darmstadt, Germany

[3] Heidelberger Druckmaschinen AG, Department for Research and Development, Gutenbergring 17, 69168 Wiesloch, Germany

[4] Technical University of Darmstadt, Department of Mechanical and Process Engineering, Institute for BioMedical Printing Technology, Magdalenenstr. 2, 64289 Darmstadt, Germany

[5] Technical University of Darmstadt, Center for Synthetic Biology, Schnittspahnstr. 10, 64287 Darmstadt, Germany

E-mails: e.holle@lmt.uni-saarland.de; knoedl@idd.tu-darmstadt.de; Martin.Mayer@heidelberg.com; t.schneider@lmt.uni-saarland.de; spiehl@idd.tu-darmstadt.de; blaeser@idd.tu-darmstadt.de; doersam@idd.tu-darmstadt.de; schuetze@lmt.uni-saarland.de

Short abstract

This paper presents a concept for recording relevant press parameters and parameters influencing the ink-water balance. The sensor technology for recording additional process parameters is explained and the installation of a measuring traverse in a sheetfed offset press is shown. A measurement campaign with variation of various printing parameters was carried out. The set press parameters and the sensor data were digitally documented and then evaluated using sensor data fusion and a machine learning toolbox developed at Saarland University. The sensor data consists of temperature, humidity and gas sensor data, which were synchronized with the recorded press parameters. The target variable to be investigated is the setting of the dampening potentiometer. It was shown that the algorithm is able to relatively accurately reconstruct the setting of the dampening potentiometer.

Keywords: gas sensor, printing, AI, model, sensor fusion

1. Introduction and background

Offset lithography is a flat printing process in which the image and non-image areas lie in one plane. During printing a thin film of fountain solution (for simplicity water and fountain solution represent the same terms) is first applied to the printing plate, which is clamped onto the plate cylinder so that the ink can only adhere to the image areas (Kipphan, 2000). This is a special feature compared to the other conventional printing processes, but makes the printing process all the more complex and susceptible to faults. This is one of the reasons why Teschner (1995) describes offset lithography as "... the most problematic and technically complicated of all printing processes."

Figure 1 illustrates the operating principle of offset lithography. The printing plate is clamped around the plate cylinder, which is first wetted with fountain solution via the water rollers of the dampening unit. The printing plate is then inked in the image areas by means of inking rollers from the inking unit. The ink is then transferred to the substrate via the blanket cylinder, onto which an elastic blanket is clamped. The impression cylinder provides the required back pressure to transfer the ink on the printing substrate.

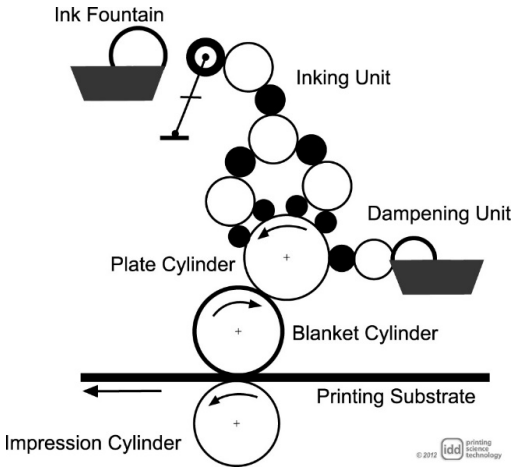

Figure 1: Operating principles of offset lithography

The ratio between ink and water is essential for high-quality printing. There is no process for automated control for the amount of water on the printing plate, yet. To this day it is still set and corrected manually several times during the printing process via the so-called dampening potentiometer, that controls the turning speed of the water rollers. Due to the noticeable decline in qualified printing personnel, the offset printing process must be further automated to regulate the ink-water balance. The approach is to control the ink-water balance based on sensor fusion and machine learning methods as suggested by Weber, et al. (2021).

The dampening potentiometer is set manually by the operator on the press at the control station for each printing unit individually. The value for the setting generally ranges between 0 and 100 percentage points. If the dampening potentiometer is set too low, scumming can occur, i.e., ink also reaches non-image areas on the printing plate. If the dampening potentiometer is set too high, the dampening solution may migrate into the ink duct; this is also known as emulsification, i.e. the ink exceeds its water absorption capacity (Knödl, et al., 2022).

In a first approach, machine learning is used to reconstruct the setting of the dampening potentiometer, that was controlled by an experienced operator and, thus, to mimic the operator`s know-how. A change in the dampening potentiometer set point leads to an increased or decreased supply of fountain solution. Fountain solution is mainly composed of osmosis water, additives, and isopropanol. Isopropanol can be detected in the gas phase by metal oxide semiconductor (MOS) gas sensors. In general, these gas sensors record the resistance of one or more gas sensitive layer which react to changes in the composition of the surrounding atmosphere. For this reason, among others, MOS sensors are used in the experiments presented here for the first time. In order to achieve a higher selectivity, a temperature-cycled operation (TCO) is implemented (Lee and Reedy, 1999). Here, the sensor layers are periodically heated to different temperatures resulting in a characteristic pattern for different gases (Wagner, 2014). Furthermore, TCO also improves the stability by desorbing or burning gas residues from the sensor layer at high temperature (Schütze and Sauerwald, 2020).

In some cases, glycerol is used as a substitute for isopropanol. The structural formula of glycerol is suitable for detection with semiconductor gas sensors. Due to the lower vapor pressure of glycerol results may differ. Fountain solutions without isopropanol are not part of these investigations.

The data evaluation is based on a tool for automated feature extraction and feature selection (Schneider, Helwig and Schütze, 2018). This tool is used in condition monitoring and related cases, but can also be used for novelty detection or to detect errors like sensor offset or drift. Basically, the Matlab-based toolbox offers individual feature extraction per sensor combined with sensor data fusion and rigorous validation

of the obtained machine learning (ML) models (ML-Toolbox, 2023). The toolbox is modular and allows combining different algorithms for feature extraction, selection and classification or regression to select the best performing combination. It is also possible to add further algorithms in the form of modules, e.g., further extractors or selectors, but also transformers or regression algorithms.

2. Materials and methods

2.1 Sheet offset press, printing parameters and design of experiment

The experiments were carried out on a *Speedmaster XL 106* print press (Heidelberger Druckmaschinen AG, Germany) with 8 printing units, where only the last 4 printing units before the delivery were used. During the tests, the parameters printing speed, inking, printing form and the dampening potentiometer setting were systematically varied. Two different printing forms were used with high and low area coverage, inking was either −15 % or +15 % and printing speed was 12 000 sheets/h or 16 000 sheets/h. Half of the variations involved setting the machine to the scumming limit by carefully adjusting the dampening potentiometer. The other half consisted of increasing the dampening potentiometer setting by 5 percentage points starting from the scumming limit. From one variation to the next, only one of the above-mentioned parameters was changed at a time and a total of 24 variations were carried out, including 8 repetitions of variation. The individual variations were held for 4.5 minutes and 3.5 minutes at printing speeds of 12 000 sheets/h and 16 000 sheets/h, respectively, in order to be able to collect measured values in the stationary printing process. All experiments were performed in a closed environment at a temperature of 23 °C ± 0.5 °C and a relative humidity of 55 % ± 2.5 %.

2.1 Additional sensors

To record additional relevant process parameters, measuring traverses were developed in cooperation with Heidelberger Druckmaschinen AG, which were mounted on the delivery side in the 4 printing units. Gas, temperature and humidity sensors were mounted on the measuring traverses. Gas sensors *SGP40* (Sensirion, Schweiz), which contains four different gas sensing layers, and *ZMOD4450* (Renesas, Japan) as well as a combined temperature-humidity sensor *SHT35* (Sensirion, Schweiz) were integrated with the required control electronics in a 3D-printed housing with openings centered along the rollers. A suitable temperature cycle (TC) for detecting and quantifying isopropanol was identified in preliminary lab experiments, the TC parameters are given in Table 1.

Table 1: Temperature cycle parameters used for all gas sensors

Cycle segment	Duration in s	Temperature in °C
1	4	400
2	6	175
3	4	400
4	6	300

In addition, PT100 temperature sensors were mounted on each of the measuring traverses. Finally, an infrared thermometer was mounted on one measuring traverse to record the temperature on the oscillating roller above the fourth ink form roller. Another PT100 temperature sensor was magnetically attached to the side walls of the printing units on the operator side. Figure 2 shows the sensors mounted on the measuring traverse and Figure 3 shows the installation situation in the printing unit.

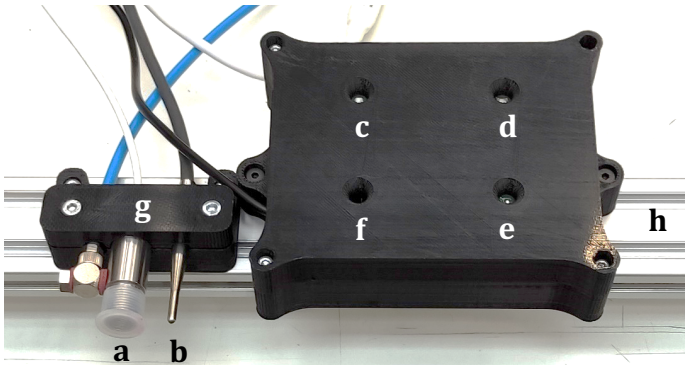

Figure 2: Mounted sensors on the measuring traverse (h); housing (f) with SGP40 (c), ZMOD4450 (d) and SHT35 (e); bracket (g) with PT100 (b) and infrared temperature sensor (a) with free blowing unit

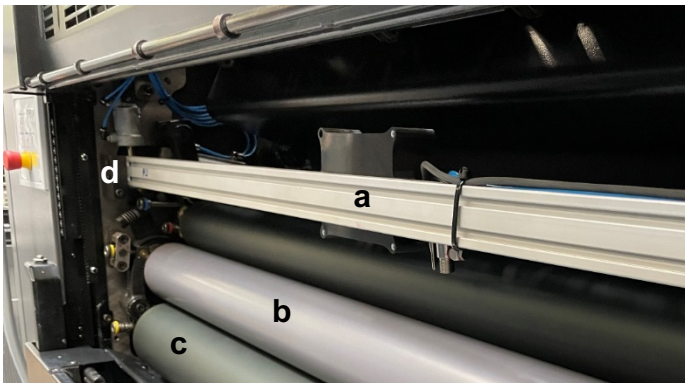

Figure 3: Measuring traverse (a) built into a printing unit with distributor roller (b), 4th ink form roller (c) and sidewall mounting (d)

2.2 Ink, fountain solution, substrate and printing plate

Four conventional offset printing inks, two black and two magenta, were obtained from two printing ink manufacturers. The fountain solution used had a content of 4.5 % isopropanol. A satin image printing paper with a grammage of 135 g/m^2 was selected as the substrate. The printing plates were *Saphira Thermal Plate PN 101* (Heidelberger Druckmaschinen AG, Germany). Figure 4 shows the two test printing plate images used in the experiments.

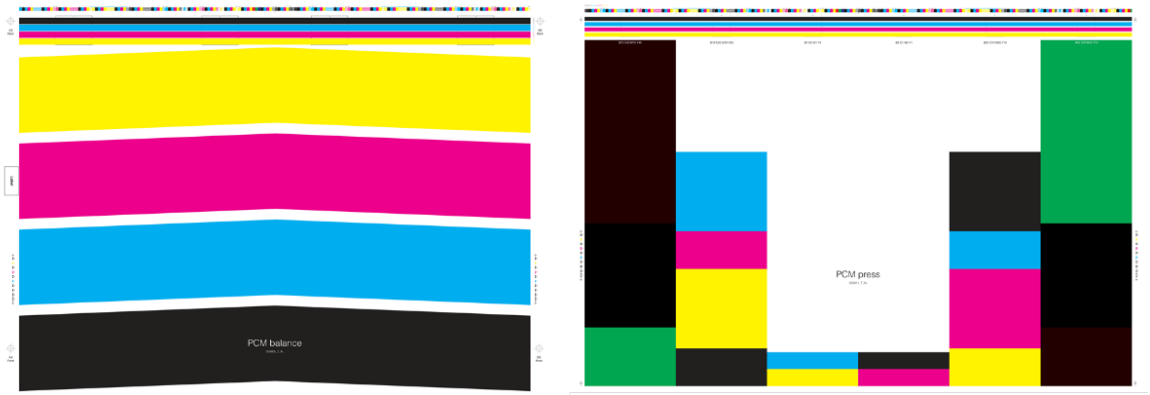

a) *b)*

Figure 4: Test printing forms (a) - high area coverage; (b) - low area coverage (Heidelberger Druckmaschinen AG)

2.3 Data preparation

After the implementation of the experiments with the different parameter variations, the collected sensor data as well as the machine data from the digital logbook were processed. For this purpose, the data were time-synchronized (all measurements were time-stamped) and sorted. Machine parameters that were not relevant were removed from the digital logbook and the sensor data was added. Finally, the data was structured in time so that a complete temperature cycle of the gas sensors with a duration of 20 s was specified as the smallest time increment and converted into the specific format for evaluation with the ML toolbox. All operations before inserting the data into the ML toolbox were performed with the program *Matlab* (The MathWorks, Inc., USA).

2.4 AI-generated model and training algorithm

For the generation of an ML-generated model, the ML toolbox explained in the introduction, is used which has a multi-stage structure. For feature extraction of the gas sensors, they are divided into segments of one second. For each segment, the mean and slope are calculated and were used as features. For humidity and temperature, the average over each 20-second cycle of the *SHT35* is included as a feature. The printing speed, inking, printing form, number of the printing unit are unchanged during each test and are also transferred to the model as a feature. Subsequently, a feature selection takes place in which the 20 features with the highest Pearson correlation coefficient in terms of amount are selected. These 20 selected features are correlated to the target variable by means of a partial least-squares regression. One observation is made per 20-second cycle that lies entirely within one experimental point of the experimental design. The leave-one-experiment-out methodology is used for validation. Each validation iteration 23 points of the experimental design are used to train the model and the remaining cycles of the last experimental parameter settings are used to validate the model. Choosing 20 for the number of features used gives the lowest validation error.

3. Results and discussion

3.1 Correlations between dampening potentiometer and varied parameters of the test plan

Multiple correlations can be identified in the data; here the Pearson correlation coefficient is evaluated unless noted otherwise. The correlation between the dampening potentiometer and the printing speed is 0.33. It should be noted here that the dampening potentiometer has a characteristic curve which is speed-dependent. This is used to control the amount of the fountain solution. The correlation coefficient between dampening potentiometer and inking is 0.27. For the printing form with the low area coverage, the dampening potentiometer was set slightly higher, with a correlation coefficient of 0.12. Since the temperature is lower on the second printing day on which the printing form with the low area coverage was used, a significant influence can be assumed. In addition, the setting of the dampening potentiometer increases the closer the printing unit is to the delivery, as can also be seen in Figure 5. The correlation coefficient for this is 0.57.

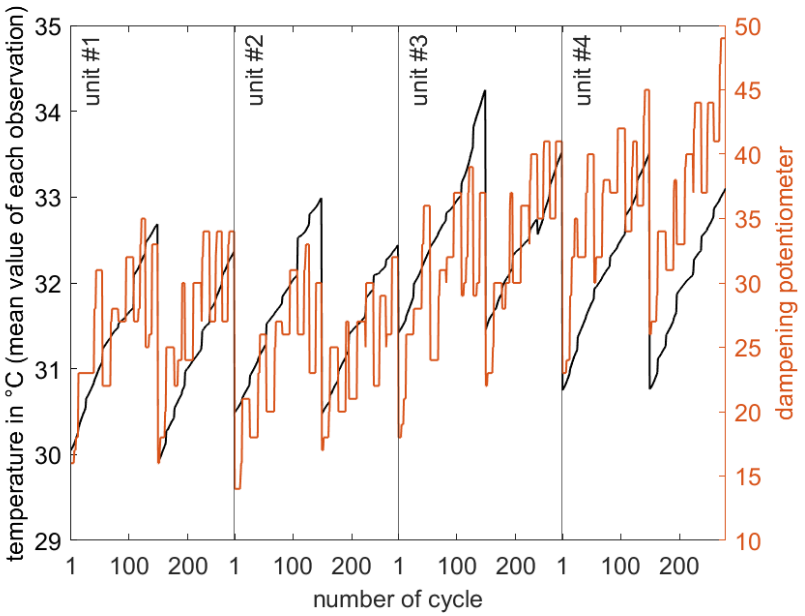

Figure 5: Number of cycles for printing unit vs. temperature and dampening potentiometer

3.2 Relationship between temperature and humidity to the dampening potentiometer

Figure 5 shows the strong influence between the setting of the dampening potentiometer and the temperature measured by the SHT35. On the abscissa axis, separated by the vertical lines within the graph, the four printing units are plotted. For each printing unit, one value per observation is plotted in chronological order. An observation period is 20 seconds each and lies entirely within the experimental period according to the experimental design and corresponds to a TC of the gas sensors. The values on the left ordinate axis (black) correspond to the average temperature, measured with the SHT35, during the respective observation period. The right ordinate axis (orange) shows the adjusted dampening potentiometer set point at the beginning of each observation period.

As the temperature rises, the set point of the dampening potentiometer is generally increased. The temperature jump at the approximate half of the cycles of each printing unit marks the beginning of the new test day and can be easily seen for each printing unit. For each printing unit, the first temperature values of the two test days shown here are very close together. Generally, the measured temperature increases during the course of the day while the press is running. Although the temperature tends to rise more on the first day of the trial than on the second day, the dampening potentiometer values are higher on the second day than on the first day of the trial, especially in printing units #3 and #4. Since the test plan is identical on both days, except for printing forms, the coverage seems to influence the selected set point. The most significant influencing factor on the selection of the dampening potentiometer set point is the temperature, as shown in Figure 5. As the temperature increases, the dampening potentiometer needs to be set higher. The printing press was not in use prior to the trials and warmed up during operation. Test points 13 through 24, corresponding to cycles 149 to 278, were performed on a subsequent day, so the machine cooled overnight.

The absolute humidity, calculated through the temperature and relative humidity, is closely correlated to the dampening potentiometer and whether the machine is currently printing. When the machine is switched off, the humidity always drops to approx. 12 g/m^3. Most of the drop in absolute humidity when the machine is switched off occurs within the first minute. When the machine is switched on, the humidity rises directly and levels off after about one minute. The value at which the absolute humidity settles depends on the dampening potentiometer set point. The higher this is, the higher the absolute humidity

value. A representative time window is shown in Figure 6. The black graph corresponds to the absolute humidity, the red graph to the dampening potentiometer set point and the green graph is high while the machine is printing and otherwise low.

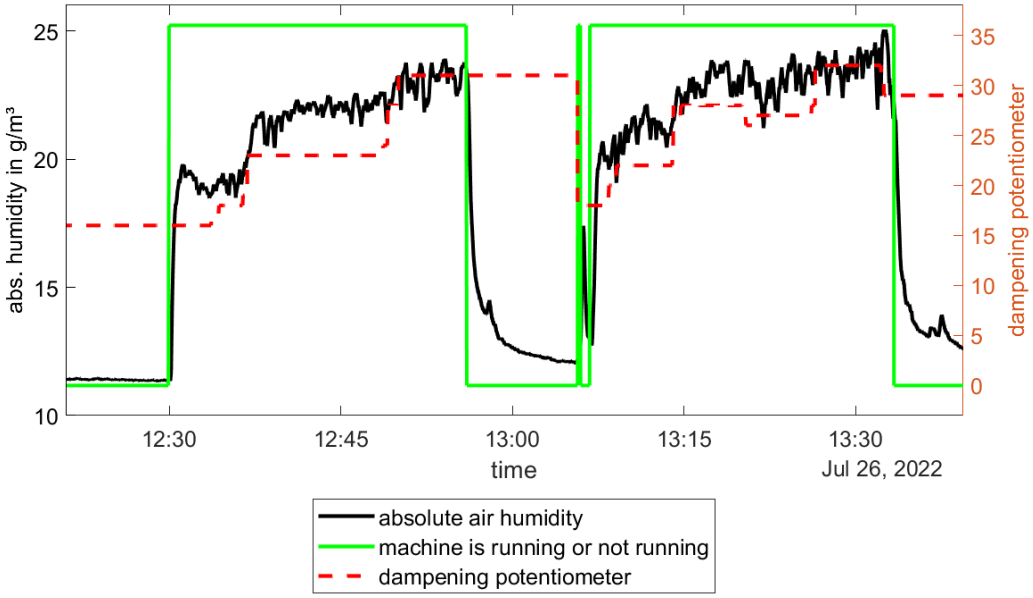

Figure 6: Representative example demonstrating the effect of the printing operation and dampening potentiometer set point on the absolute humidity

3.3 Machine learning model

In a first step, an ML model was built to predict the dampening potentiometer set point to demonstrate that the sensor data allow reproducing the experience of a printer. Later, a model should be trained allowing automatic adjustment of the dampening potentiometer based on the printing conditions and recorded sensor data.

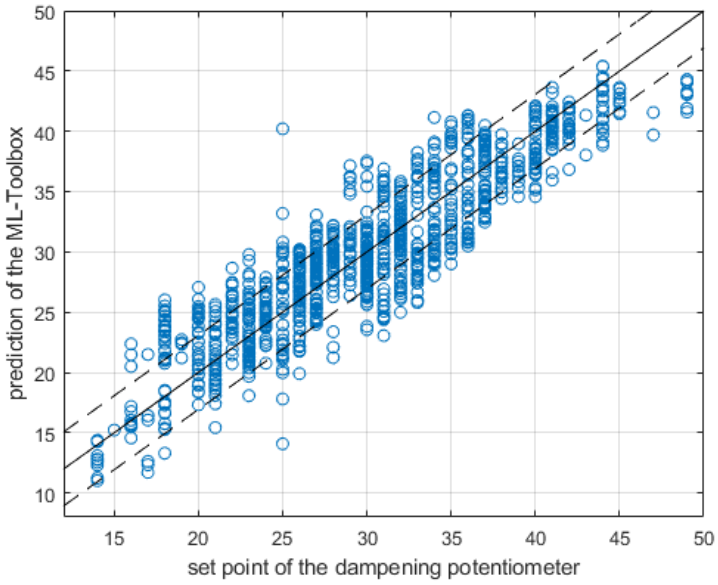

Figure 7: ML model showing dampening potentiometer set point vs. prediction of the ML toolbox

Figure 7 shows the result of one ML model. On the abscissa axis the actual dampening potentiometer set point is shown and on the ordinate axis the prediction by means of the ML toolbox. Optimally, it would run along the solid black line ($x = y$). The dotted lines indicate the root mean square error (RMSE) of the pre-

diction corresponding to ± 3 % of the dampening potentiometer set point. The mean relative error is 8.8 %, determined from the range of the dampening potentiometer set point, i.e. the difference between the lowest and highest values of 14 % and 49 %, respectively. Overall, the model is basically able to reflect tendencies in the setting of the dampening potentiometer, but with an error to be noted. The largest deviations, e.g., the highest and lowest values for the dampening potentiometer set point at 25 %, are usually the first observation during a trial point of the experimental design. The number of outliers could decrease in a real production operation, since abrupt major changes of the settings as in the present experimental design occur less frequently.

Further analysis shows that the slope of the resistance during the high temperature phases of sensor layer 2 of SGP40 correlate strongly with the dampening potentiometer, similarly the average resistance in the low temperature phase at 175 °C. The greatest correlation with the dampening potentiometer set point, however, is observed for the temperature recorded by the SHT35, followed by the absolute humidity. Since certain characteristics correlate similarly strongly or weakly with the dampening potentiometer in each of the four printing units, a causal relationship can be assumed. The setting of the inking and the printing speed are included in the model as additional factors while the selected printing form is not considered in the model for the regression algorithm.

4. Conclusions and outlook

With these first tests, it could be shown that with the help of additional sensors, which record temperature, relative humidity and information about the gas atmosphere in the individual printing units, it is possible to reconstruct the set point of the dampening potentiometer relatively accurately. An evaluation with a similar test setup and design of experiments is currently taking place at another printing press manufacturer, which will provide further insights into the subject. In addition, a two-week measurement campaign is currently being planned at a printing company where, as described in this paper, the additional sensor technology will also be installed and production will then be monitored in 3-shift operation. In particular, the temperatures in the individual printing units can be tracked and analyzed more precisely. Since a printing house wants to sell its print products, it can be assumed that high-quality print products will be produced in this environment. A particular challenge later on will be to define a sensible threshold value above which the dampening potentiometer should be adjusted in order to be able to maintain the ink-water balance. In addition, scattering of the data was also observed, which was presumably caused by human influence (manual setting of the press parameters at the control station).

In general, it must also be said that due to the limited test time and the limited amount of paper substrate, more data must be collected through further tests. Since the tests took place in a controlled environment, real conditions are also being investigated with two-week measurement campaign.

Acknowledgements

We would like to thank Heidelberger Druckmaschinen AG for the excellent cooperation and the provision of the printing press and needed materials for the experiments.

We would also like to express our sincere thanks to the AiF/IGF (Industrielle Gemeinschaftsforschung), which made this work possible through the research project No. 22060 N – *Kontrolle des Farb-Wasser-Gleichgewichts mittels Künstlicher Intelligenz*.

References

Kipphan, H. ed., 2000. *Handbuch der Printmedien: Technologien und Produktionsverfahren*. Berlin: Springer.

Knödl, F., Holle, E., Klein, S., Schütze, A. and Dörsam, E., 2022. Das Farb-Feuchtmittel-Gleichgewicht mit maschinellem Lernen in den Griff bekommen. *P3 Paper Print Packaging,* 1–2, [online] Available at: < http://www.p3-news.com/SubscriptionDe/Article/fc7522443c83c4c5aaf820e5#> [Accessed 14 April 2023].

Kohl, C.-D. and Wagner, T., 2014. *Gas sensing fundamentals*. Berlin, Heidelberg: Springer.

Lee, A.P. and Reedy, B.J., 1999. Temperature modulation in semiconductor gas sensing. *Sensors and Actuators B: Chemical*, 60(1), pp. 35–42. https://doi.org/10.1016/S0925-4005(99)00241-5.

ML-Toolbox, 2023. MATLAB toolbox for machine learning (v1.0.0). [computer program] ZeMA-gGmbH. Available at: < https://github.com/ZeMA-gGmbH/LMT-ML-Toolbox> [Accessed 13 April 2023].

Schütze, A. and Sauerwald, T., 2020. Chapter twelve - dynamic operation of semiconductor sensors. In: R. Jaaniso, and O.K. Tan, eds. *Semiconductor gas sensors.* 2nd ed. Cambridge: Woodhead Publishing, pp. 385–412. https://doi.org/10.1016/B978-0-08-102559-8.00012-4.

Schneider, T., Helwig, N. and Schütze, A., 2018. Automatic feature extraction and selection for condition monitoring and related datasets. In: *IEEE International Instrumentation and Measurement Technology Conference (I2MTC)*. Houston, TX, USA, 14–17 May 2018. IEEE, pp. 1–6. https://doi.org/10.1109/I2MTC.2018.8409763.

Teschner, H., 1995. *Offsetdrucktechnik: Informationsverarbeitung, Technologien und Werkstoffe in der Druckindustrie*. 9th ed. Fellbach: Fachschriften-Verlag.

Weber, T.E., Klein, S., Dörsam, E. and Schütze, A., 2021. *Vorstudie zur Kontrolle des Farb-Wasser-Gleichgewichts und der Schichtdicken im Offsetdruck durch Einsatz von maschinellem Lernen*: *Abschlussbericht*. Darmstadt.

DOI 10.14622/Advances_49_2023_12

Optimization of printable electrolyte

Gunter Hübner[1], *Marvin Graner*[1] *and Aakash Grewal*[1,2]

[1] Innovative Applications of the Printing Technologies (IAD), Stuttgart Media University, Nobelstr. 10, 70569 Stuttgart, Germany

[2] Franz Binder GmbH & Co., Raiffeisenstraße 53, 74906 Bad Rappenau

E-mails: huebner@hdm-stuttgart.de; mg202@hdm-stuttgart.de; A.Grewal@binder-connector.de

Short abstract

Based on previous studies, here the composition of the printable electrolyte of printed batteries was investigated further. In the stack design of a printed battery, the electrolyte layer is located between the anode and cathode and is responsible for ion transport. However, the anode and cathode must not touch each other, so a so-called separator is used. This separator usually is a porous fleece-like material where the pores are filled with electrolyte. If a gel-like electrolyte can be used that is also printable and additionally has the separating function, this would be extremely advantageous for the production process, e.g., in a web press with several printing units. By adding thickener agents such as agar-agar and spacer particles to the classical $ZnCl_2$-electrolyte solution it could be shown that this can be rendered in a paste that works well as a gel-like and printable electrolyte with separator function. The goal of this investigation is to find out the optimum amount of these ingredients.

Keywords: printed batteries, screen printing, printable electrolyte, thickeners, spacers.

1. Introduction and background

According to business analyses e.g., provided by the OE-A organisation (see the OE-A Roadmap, 2023) small, flexible power sources such as printed batteries used to power IoT devices (Internet of Things) will become a promising and well flourishing market in the coming years. Manufacturers such as VARTA have announced at the LOPEC 2023 trade fair that they will set up a production line for printed batteries by the end of 2025.

Whereas printed rechargeable batteries (secondary batteries) are challenging, the non-rechargeable zinc/manganese dioxide chemical system (primary battery) is comparingly simple and has been brought to market earlier by companies such as Enfucell (2019), Blue Spark Technologies (2023), and some more. One recent new player to enter the market of printed batteries in the sector of logistics is the company elmeric (n.d.) which co-operates with VARTA. The printing technique, and mechanical properties of these film batteries have been described earlier (Lanceros-Méndez and Costa, 2018; Hübner, et.al., 2015; 2021).

In this investigation, which is based on previous work (Hübner, et.al., 2022), the so-called stack design of a printed battery is used. Details and layer structure of the design are shown in the explosion drawing in Figure 1.

In printed batteries, the separator mostly is a kind of fleece, a monolayer microporous membrane placed between the electrode layers. One renowned manufacturer of such fleece materials is the company Celgard (2023). In a manufacturing process where several layers are printed subsequently the insertion of such a fleece soaked with electrolyte would be disruptive. Therefore, it would be desirable if the electrolyte could be printed and perform the separator function at the same time. A printable electrolyte fulfilling the separator function by itself would be a great cost saving factor, at least by eliminating the need for the fleece.

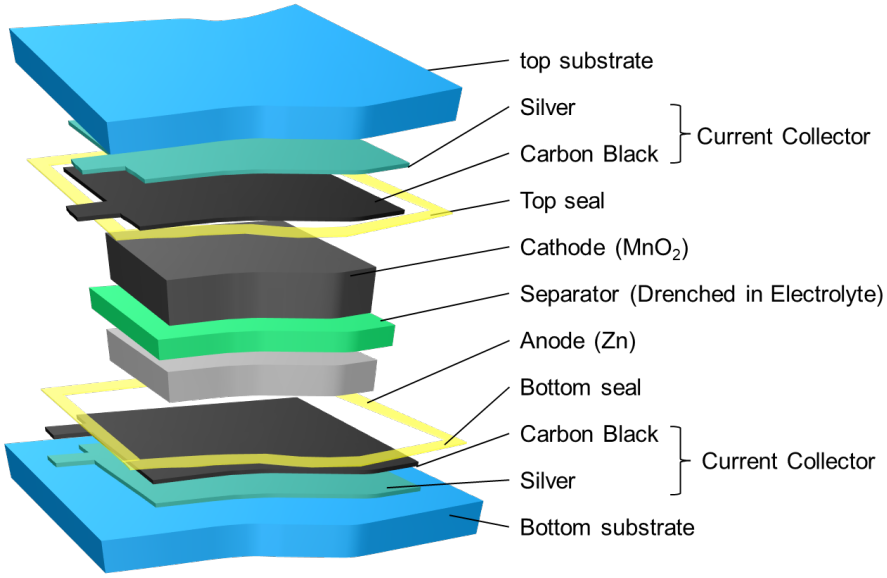

Figure 1: Explosion drawing of a printed battery in stack design

For the zinc/manganese dioxide electrochemical system that is used here, the electrolyte is a salt dissolved in water. According to common experience and previous investigations (Hübner, et al., 2022) the best choice is a 40 % zinc chloride solution.

- Distilled water 60 %.
- Zinc chloride ($ZnCl_2$) 40 %.

However, this solution is almost as liquid as water and therefore cannot be printed using the screen printing process, which produces all other layers, e.g. because of large particles in the electrodes.

The feasibility of making this electrolyte solution printable by adding a gelling agent, in this case agar-agar, and 50 µm PMMA beads as spacers has been shown previously (Hübner, et al., 2022). The idea is illustrated in Figure 2.

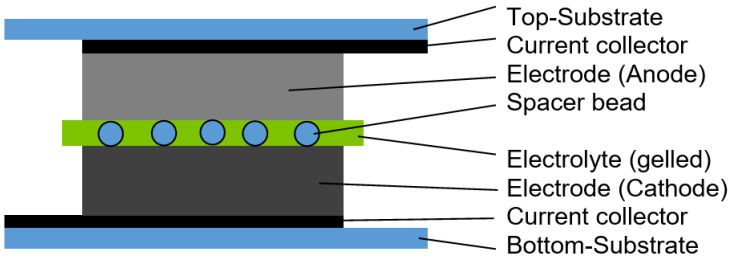

Figure 2: Side view of stack design with added spacers

Agar-agar is a food-safe gelling agent that can be found in many kitchens today. In Asia, the substance has been used for centuries to thicken food. The carbohydrate is made from the cell walls of algae such as red and blue-green algae. Agar-agar is a so-called multiple sugar, which consists of many simple sugars. The chemical structure of agar-agar is very similar to that of native fruits and vegetables. This fibre structure has very good swelling properties. Here, we dissolve agar-agar in the $ZnCl_2$-solution at room temperature and a few percent are sufficient to achieve a screen printable consistency. However, when agar-agar is dissolved in hot water, the liquid becomes even more viscous or even solid.

The aim of the current investigation is to optimise the concentration of agar-agar and PMMA spacers. The addition of these materials should be as low as possible in order not to influence the battery function

too much. At the same time, the printability (rheological properties that enable screen printing) must be maintained, and the spacers must ensure sufficient distance between the electrodes to avoid short circuits.

2. Materials and methods

The materials and measurement methods are the same as described detailed earlier in (Hübner, et al., 2022). We measured:

- Rheology of the mixed pastes with a Physica MCR 300 rheometer parallel plate geometry
- Conductivity of the mixed electrolyte pastes using a cup with two immersed nickel strips at a fixed distance and determining the impedance with a Bio-Logic SP-300 potentiostat (Biologic, 2022)
- Electrical characterisation of batteries
  - Capacity (derived from constant current discharge curves)
  - Impedance (inner resistance) with GEIS method Bio-Logic SP-300 potentiostat (Biologic, 2022)

2.1 Printing paste preparation

In comprehensive preliminary experiments it could be found that the interesting range of component additions is for agar-agar from 2 % to 5 % and for the PMMA beads from 3 % to 5 %. Thus, a matrix was set-up for the experiments, which is shown in Table 1. The weight proportion of the four ingredients is given to form 100 g of paste. The ratio 2/3 between ZnCl and H_2O is maintained for all solutions.

Table 1: Matrix of different mixtures, weight proportion in grams to result in total 100 g paste

			PMMA Beads		
			3 %	4 %	5 %
Agar-agar	2 %	ZnCl	38.0 g	37.6 g	37.2 g
		H_2O	57.0 g	56.4 g	55.8 g
	3 %	ZnCl	37.6 g	37.2 g	36.8 g
		H_2O	56.4 g	55.8 g	55.2 g
	4 %	ZnCl	37.2 g	36.8 g	36.4 g
		H_2O	55.8 g	55.2 g	54.6 g
	5 %	ZnCl	36.8 g	36.4 g	36.0 g
		H_2O	55.2 g	54.6 g	54.0 g

For the experiments, the highly pure BioScience agar-agar from vendor CarlRoth (2022) has been used. The poly methyl methacrylate, aka. acrylic glass (PMMA) particles are microspheres with a diameter of 50 µm from the vendor Coating Products OHZ e.K.

For the experiments with these 12 different solutions the following nomenclature is introduced:

- PxAy

where x and y are the percentages of the ingredients. For example, P5A3 means that there is 5 % of PMMA beads and 3 % of agar-agar contained in the paste.

The electrolytes were prepared in laboratory glass jars. The substances were added at room temperature in the following order: first the $ZnCl_2$-salt was stirred into the water, then the thickening agent agar-agar was added in several steps, until it reached the desired percentage. With constant stirring the PMMA beads were added.

2.2 Printing process

All prints were carried out on a semi-automatic laboratory screen-printing machine Ekra E2. The following settings were used:

- squeegee speed 100 mm/s
- squeegee pressure 136 N
- snap-off distance 2 mm.

The screen used was a PET mesh with 21-140 (n-d i.e., mesh count in threads per cm – thread diameter in µm). This is a quite coarse mesh providing a large mesh opening that the PMMA beads can easily pass through.

A two-stroke operation was used, meaning that the flood bar and the squeegee moved two times back and forth.

As in the previous study (Hübner, et al., 2022) pre-printed battery halves (current collectors and electrode materials) were used and only the electrolyte was printed onto both electrodes. For the sealing, a printable, heat and pressure activatable glue was used. Sometimes also a cut out frame of double-sided adhesive tape.

2.3 Conductivity and battery performance

The conductivity of the electrolyte mixtures was measured as described in Hübner, et al. (2022). To determine the battery performance constant current (CC) discharge curves were recorded and a galvanostatic electrochemical impedance spectroscopy (GEIS) performed. A typical discharge curve from which the battery capacity can be derived is shown in Figure 3.

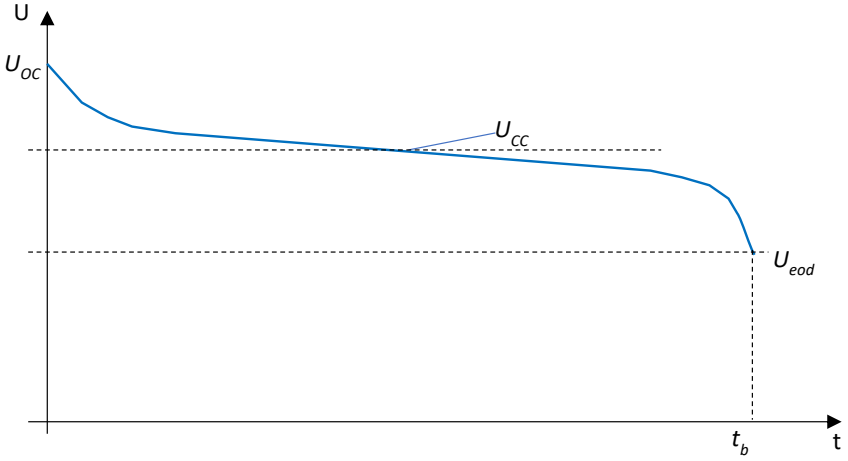

Figure 3: Typical CC-discharge curve of primary battery

For the Zn/MnO_2-system typical values are:

- U_{OC} = 1.6–1.7 V (open circuit voltage)
- U_{CC} = 1.5 V (nominal battery voltage)
- U_{EOD} = 0.9 V (end of duty)

For example, if the battery is discharged with 1 mA and t_b is 20 hours, then the resulting battery capacity is 20 mAh.

The GEIS measurements of the assembled batteries were performed before and after the discharge. The GEIS was conducted with a frequency sweep from 10 kHz to 1 Hz.

There are different possibilities to describe the GEIS behavior of a battery. One of the possible descriptions is an equivalent circuit diagram as shown in Figure 4.

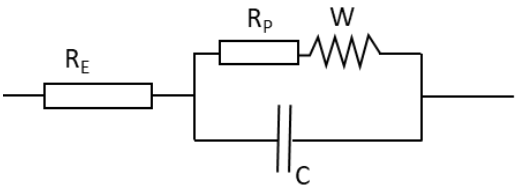

Figure 4: Equivalent circuit diagram

In the diagram, the inner resistances are named *R*. At high frequencies, the capacitor C plays no role and only the inner ohmic resistance R_E matters. At low frequencies C is blocking the current. Then the other resistances start to matter. W is a so-called Warburg impedance representing diffusion processes. The measurement curves of the fully assembled batteries should look like the idealized Nyquist plot depicted in Figure 5.

In the very best case there is no imaginary part at the ends of the half circle, the measurements however show a significant value.

As a measure for the inner resistance of the battery the values R_E and $Im(R_E)$ were considered.

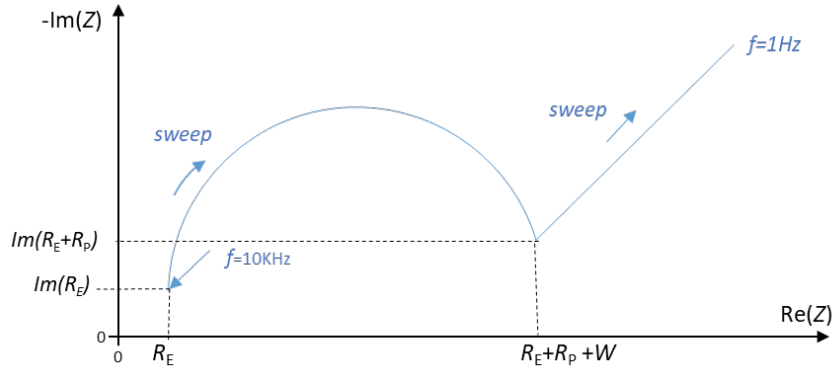

Figure 5: Idealized Nyquist plot of a printed battery

3. Results

3.1 Conductivity

The conductivity of the 12 different pastes have been measured and the result is shown in Table 2 and in a 3D representation in Figure 6.

Table 2: Conductivity of the electrolyte pastes

		PMMA beads		
		3 %	4 %	5 %
Agar-agar	2 %	108 mS·cm^{-1}	117 mS·cm^{-1}	84 mS·cm^{-1}
	3 %	135 mS·cm^{-1}	108 mS·cm^{-1}	123 mS·cm^{-1}
	4 %	124 mS·cm^{-1}	125 mS·cm^{-1}	120 mS·cm^{-1}
	5 %	114 mS·cm^{-1}	116 mS·cm^{-1}	114 mS·cm^{-1}

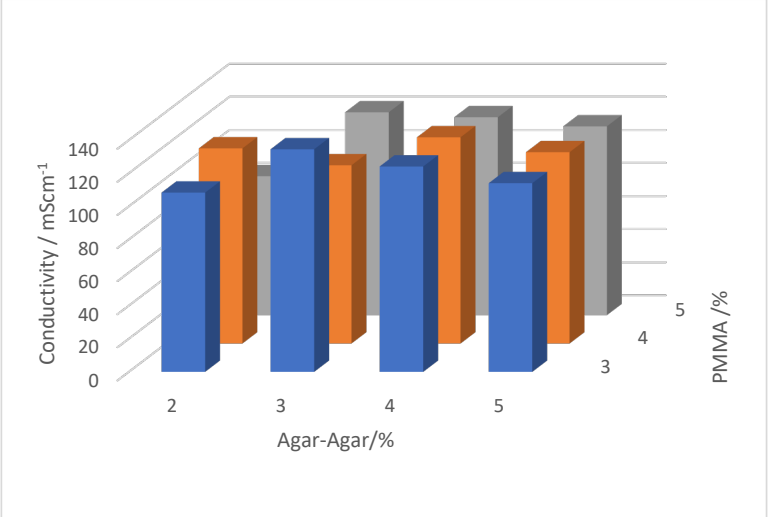

Figure 6: Conductivities of the different pastes

The measured conductivities of the electrolyte pastes are all in the same range between 107 mS·cm^{-1} and 135 mS·cm^{-1}, except for P5A2, which could be an outlier. It should be noted that the measurement method is not very accurate, an error of ±5 mS·cm^{-1} is likely.

For comparison, the pure 40 % $ZnCl_2$-solution has a conductivity of 110 mS·cm^{-1}, which is also in the same range.

It can be assumed that the influence of the agar-agar and PMMA bead content on the battery performance is not very large. In an earlier study (Hübner, et al., 2022), it was shown that the conductivity could even be improved by adding agar-agar. However, no spacer beads were added at that time.

3.2 Printability

The printability of the different pastes was observed during the screen printing process and the results were visually evaluated with regard to the homogeneity of the print and the appearance of bubbles. Some pastes showed very good results, while others had a pronounced tendency to bubble. The P3A2 had such a low viscosity that screen printing was not possible at all. The results are summarised in Table 3.

Table 3: Printability of the electrolyte pastes

		PMMA beads		
		3 %	4 %	5 %
Agar-agar	2 %	printing not possible	very good	very good
	3 %	very good	very good	good
	4 %	good	good	good
	5 %	poor	good	poor

3.3 Rheological behavior

Since the low and high addition levels of agar-agar and PMMA led to non printable mixtures the range of addition was refined. The additions were varied in 3 steps for both agar-agar and PMMA, namely 2.5 %, 3.5 % and 4.5 %. Since the different paste blends showed very similar pronounced shear thinning behavior,

shear rate sweeps were performed for comparison and viscosities were recorded at 50 and 100 reciprocal seconds. The resulting values are shown in Figure 7 for the 9 pastes.

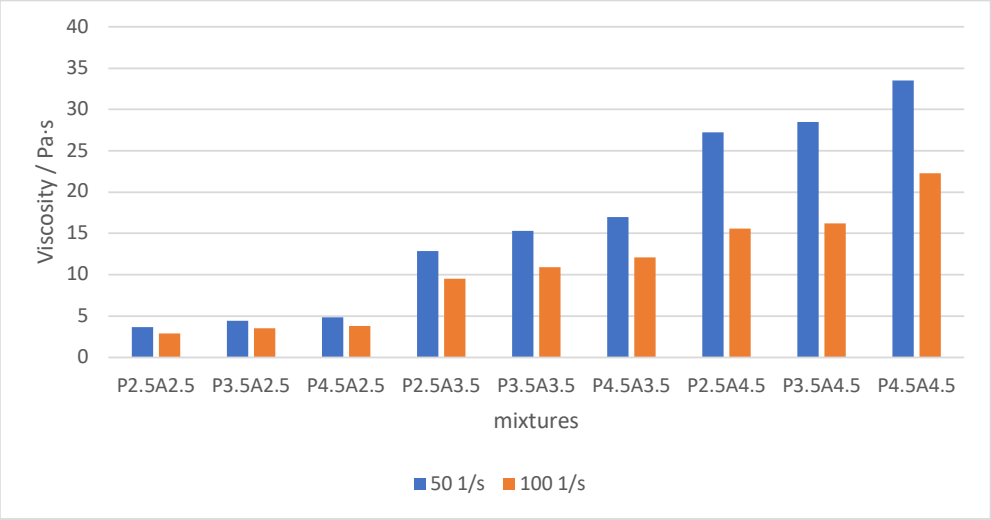

Figure 7: Viscosities of the different pastes

Figure 8 shows the results in a 3D-column chart.

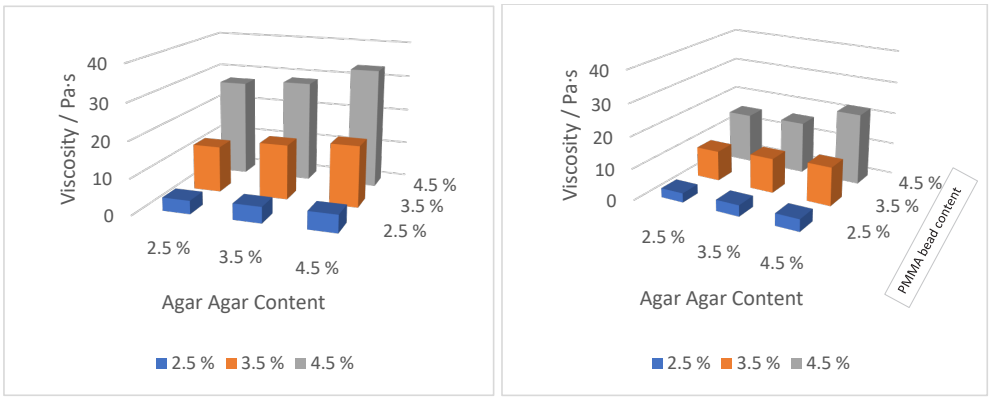

Figure 8: Viscosities of the different pastes left: at a shear rate of 50 s^{-1} and right at 100 s^{-1}

It is obvious and in accordance with the expectations that the viscosity increases with the addition of agar-agar and with the amount of PMMA beads. The optimum value for printability is at about 2.5 % to 3 % for each ingredient. However, printability is not the main focus, the main focus is the function, the battery performance.

3.4 Battery performance

Figure 9 shows the CC-discharge curve of a battery with the P3A5 electrolyte. The overall curve looks good. However, the voltage over the whole curve is too low. The open circuit voltage V_{OC} is only about 1.4 V and should be a little less than 1.7 V. The plateau-voltage V_{CC} is around 1.3 V and should be around 1.5 V. Finally, after reaching V_{EOD} (0.9 V), which is the point at which one can normally assume that the battery is empty and the load of 1 mAh is taken away, the voltage recovers to about 1.32 volts. This means nothing other than that the battery is not flat and still some capacity left over.

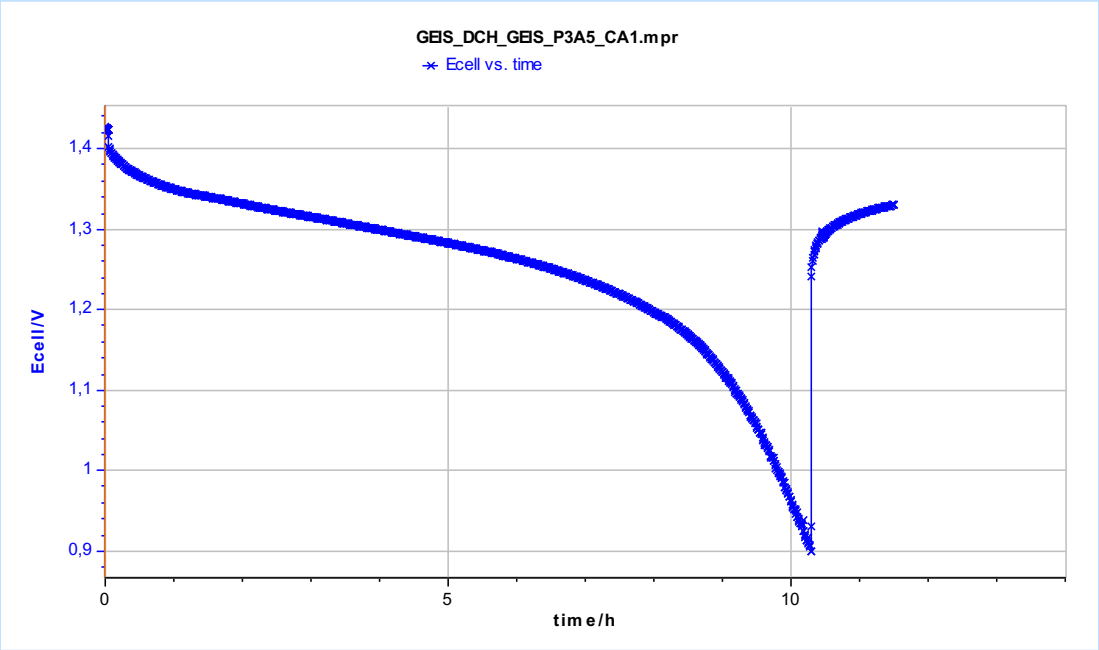

Figure 9: CC discharge curve of a battery with P3A5

Figure 10 shows the results of all assembled batteries. The only battery that achieves satisfactory results is the one with the electrolyte P4A4. As shown in previous reports such as (Hübner, et al., 2022) a capacity of 2 mAh·cm^{-2} is the target minimum value. With an area of 16 cm^2 and a discharge time of 40.3 h the P4A4 shows a quite good capacity of 2.5 mAh·cm^{-2}. As all others show poor or very poor performance. It can be assumed that something went wrong during assembly.

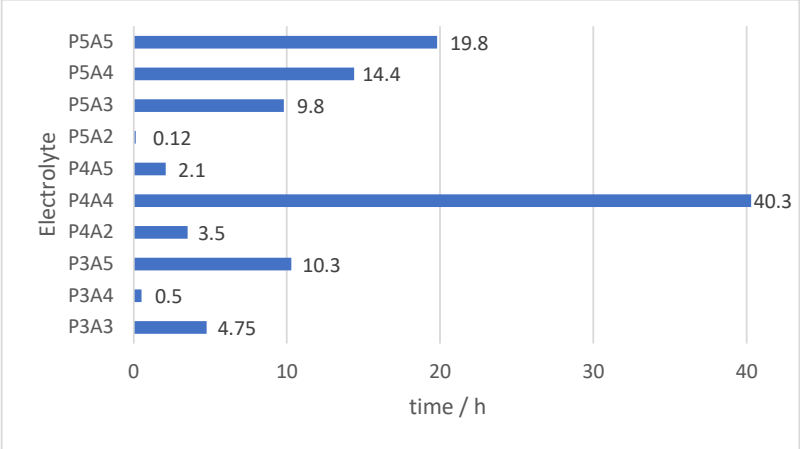

Figure 10: CC discharge results for batteries with different electrolytes

There are several possible reasons for the poor performance:

- Sealing is defective (leakages or even drying out)
- Electrolyte is in touch with the silver (e.g. because beads have punctured the passivation carbon)
- Electrolyte has degraded
- Overall too high inner resistance

The internal resistance (impedance) can serve as an indicator of poor capacitance performance and low voltage level. According to Figure 5 the value of R_E (real and imaginary part) are such indicators. As can be seen in Figure 11 only P4A4 has an acceptable low resistance level.

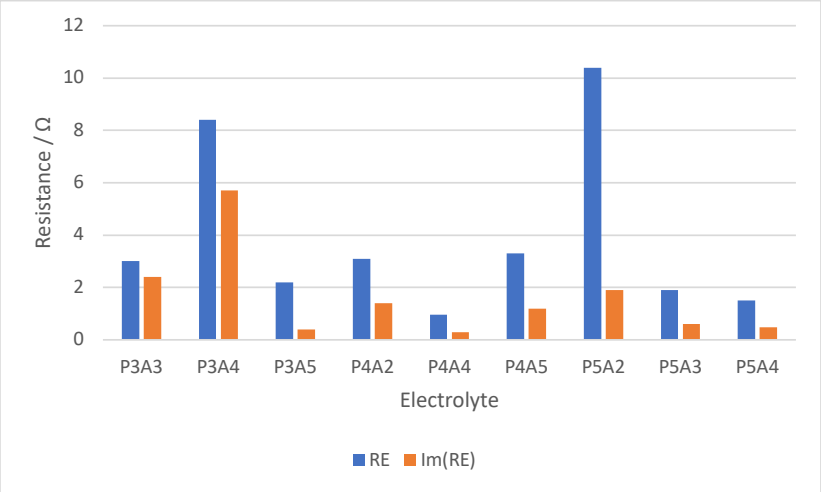

Figure 11: Inner resistances of assembled batteries (real and imaginary part of impedance)

The battery performance of the cells assembled with the intermediate 2.5 % to 4.5 % additions is ongoing and there are hints that one of the electrode layers caused the problem. There will be more investigations until the conference.

4. Conclusion

It could be shown that a printable electrolyte is possible by using a widely available and affordable ingredient agar-agar as thickener agent. By adding PMMA beads with 50 µm diameter the separator function can be realized. Solely printing techniques are the subsequent manufacturing steps avoiding the disruptive process of inserting a fleece soaked with liquid electrolyte.

Some assembled batteries showed very good results in terms of capacity and low inner resistance, however, unexpected results were found with most of the assembled batteries. These results must be verified in repeating the experiments. This is currently ongoing and will be finished with hopefully completely satisfying results until the conference in September.

Acknowledgements

The research was within the scope of the project OxiFlexIT, which is funded by the German Ministry of research and education.

GEFÖRDERT VOM
Bundesministerium für Bildung und Forschung

Thanks to all the partners in this project and especially VARTA Microbattery GmbH.

References

Biologic, 2022. *What is Electrochemical Impedance Spectroscopy (EIS)?* [online] Available at: <https://www.biologic.net/topics/what-is-eis/> [Accessed March 2023].

Blue Spark Technologies, 2023. *TempTraq® Early fever detection leads to better patient care*. [online] Available at: <https://www.bluesparktechnologies.com> [Accessed March 2023].

CarlRoth, 2022. *Technical info gelling agents in microbiology agar-agar*. [online] BioScience. Available at: <https://www.carlroth.com/de/en/agar/agar-agar-bioscience-granulated/p/1347.3> [Accessed March 2023].

Celgard, 2023. *At the center of membrane innovation*. [online] Available at: <https://www.celgard.com> [Accessed March 2023].

elmeric, n.d. *We link electrical engineering to print technologies*. [online] Available at: <https://www.elmeric.de/index.html> [Accessed March 2023].

Enfucell, 2019. *Enfucell SoftBattery*. [online] Available at: <https://www.enfucell.com/softbattery> [Accessed March 2023].

Hübner, G., Krebs, M., Rassek, P. and Willfahrt A., 2015. Printed batteries, overview, status, recent developments, future perspectives. In: P. Gane, ed. *Advances in Printing and Media Technology: Proceedings of the 42nd International Research Conference of iarigai*. Helsinki, Finland, September 2015. Darmstadt: iarigai, pp. 183–193.

Hübner, G., Krebes, M., Etzel, F., Nussbaum, L. and Thamm, S., 2021. Printed batteries, properties of substrates and components, regarding bendability and barrier. In: C. Ridgway, ed. *Advances in Printing and Media Technology: Proceedings of the 47th International Research Conference of iarigai*. Athens, Greece, 19–23 September 2021. Darmstadt: iarigai, pp. 29–42.

Hübner, G., Krebes, M., Cirstea, L. and Kolesova, A., 2022. Printable electrolyte for printed batteries. In: C. Ridgway, ed. *Advances in Printing and Media Technology: Proceedings of the 48th International Research Conference of iarigai*. Greenville, USA, 19–21 September 2022. Darmstadt: iarigai, pp. 156–170. https://doi.org/ 10.14622/Advances_48_2022_14.

Lanceros-Méndez, S. and Costa, C.M. eds., 2018. *Printed batteries: materials, technologies and applications.* Hobokem NJ, USA: John Wiley & Sons. https://doi.org/ 10.1002/9781119287902.

OE-A Roadmap, 2023. *OE-A roadmap for flexible, organic and printed electronics*. [online] OE-A. Available at: <https://oe-a.org/topics/oe-a-working-groups/roadmap> [Accessed March 2023].

DOI 10.14622/Advances_49_2023_10

Printing biocathodes: construction and characterization of an air breathing platform

Élise Bessac[1,2], Sébastien Solan[2], Bilal Demir[2], Nadège Reverdy-Bruas[1] and Anne Blayo[1]

[1] Université Grenoble Alpes, Laboratory of Process Engineering for Biorefinery, Bio-based Materials and Functional Printing (LGP2), CS 10065, 38402 Saint-Martin-d'Hères, France

[2] BeFC, F-38610 Gières, France

E-mail: elise.bessac@befc.fr

Short abstract

As a virtuous technology, printed biofuel cells are emerging as a promising way to supply low-power devices in the context of Internet of Things or healthcare, while addressing the environmental challenges of our century. The aim of this study is to produce a functional biosurface for an effective oxygen reduction as a fuel cell biocathode. The challenge of this technology is to neutralize the environmental impact of current power sources by introducing bio-based materials to a functional ink formulation for a printed biocathode. In this concept, cathodic enzymes need to be localized near the electroactive sites to optimize the Direct Electron Transfer (DET) thanks to an optimized percolation network. Another function of this novel biosurface is the increase of O_2 levels in the microenvironment of biocathode to improve the electrochemical activity. Hence, different parameters of the ink formulation were also studied: hydrophobicity/hydrophilicity control of printed biocathode surfaces via contact angle measurements, surface structure via microscopy after printing, total solid content, particle size, pH and rheological properties. Finally, a new environmentally friendly formulation has been developed, by using only bio-based components and water as solvent. After optimization, stable catalytic current above 1 mA/cm^2 has been achieved. In full cell configuration, maximum power reached is 75 µW/cm^2. This printable cathode ink is therefore promising for sustainable applications.

Keywords: biocathode, functional printing, enzymatic biofuel cell, biosensors

1. Introduction and background

The rise of connected and miniaturized devices has increased the need for flexible low power apparatus. These devices have a short life span, and they currently use batteries which contain toxic ingredients for the environment. Among them, lithium-ion batteries, known as one of the most used types for those connected devices, always end up in landfill or are incinerated. Moreover, incorrect disposal of this type of battery does not only contaminate the environment but also cause fire incidents (Mrozik, et al., 2021). Hence, the demand of alternative options for those batteries has increased and oriented to study biodegradable components as an alternative for the toxic ingredients in currently used batteries.

Fuel cells can be an alternative way to power connected devices. But they currently raise some issues due to the use of synthetic materials. For instance, to overcome the problem of oxygen accessibility and cathode flooding, fuel cell cathodes are using hydrophobic components made from fluorine chemistry. Indeed, Chi, et al. (2018) demonstrated that adjusting the ratio between hydrophobicity and hydrophilicity improved the performances. In fact, by adding polytetrafluoroethylene (PTFE) or Nafion™, they generate a balance between cathode flooding and system hydration for proton flow. In addition, fuel cells such as H_2-O_2, use metal catalysts such as platinum, an expensive and non-recyclable metal which is difficult to industrialize because of its chemical reactivity. Therefore, the drawback of this technology has been the presence of non-disposable components such as fluorinated binders or metallic catalysts.

Compared to standard fuel cell cathode, biocathode can work with natural catalyst such as enzymes to enable the O_2 reduction. Equation [1] represents the half-reaction that occurs at the cathode. To operate as a complete cell, a bioanode and a separator are required. For glucose-O_2 biofuel cell, glucose oxidation occurs at the bioanode side (Equation [2]).

$$\frac{1}{2}O_2 + 2e^- + 2H^+ \rightarrow H_2O \quad [1]$$

$$\text{Glucose} \rightarrow \text{Gluconolactone} + 2e^- + 2H^+ \quad [2]$$

Enzymes used for O_2 biocathode are usually multicopper oxidases. They can perform with Direct Electron Transfer (DET) approach, so they do not need any mediator or promoter to do the electron transfer. Several types of enzyme immobilization can be used on the electrode surface: adsorption, covalent bonding, cross-linking or encapsulation (Abreu, 2018). The selection of the enzymes and the way to immobilize it on the electrode surface have a significant impact on the biofuel cell performances in terms of power and/or current. Electrical transfer properties are also studied to improve performances by introducing highly conductive materials such as Carbon Nanotubes (CNTs), carbon nanodots or graphene oxide (Huang, et al., 2019). These enzymatic biocathodes are well known at lab scale with optimized enzyme immobilization. However, their industrialization is complicated to consider. Therefore, the use of printing technologies is investigated in this study to unlock scale up production.

Thus, the objective of this work is to formulate an ink for a biocathode which can be printable with screen printing or coating. Particle size measurements, rheological characterization and printing trials were carried out to demonstrate the printability of this ink. Moreover, characterization tests of the biocathode were performed in terms of ionic, electronic conductivity, enzyme activity and hydrophobic behavior. The new ink was also largely made up of biobased components and is likely to be biodegradable within a few weeks. Some of these components and specific process are confidential for the moment for reasons of intellectual property. They will not be mentioned in this extended abstract.

2. Materials and methods

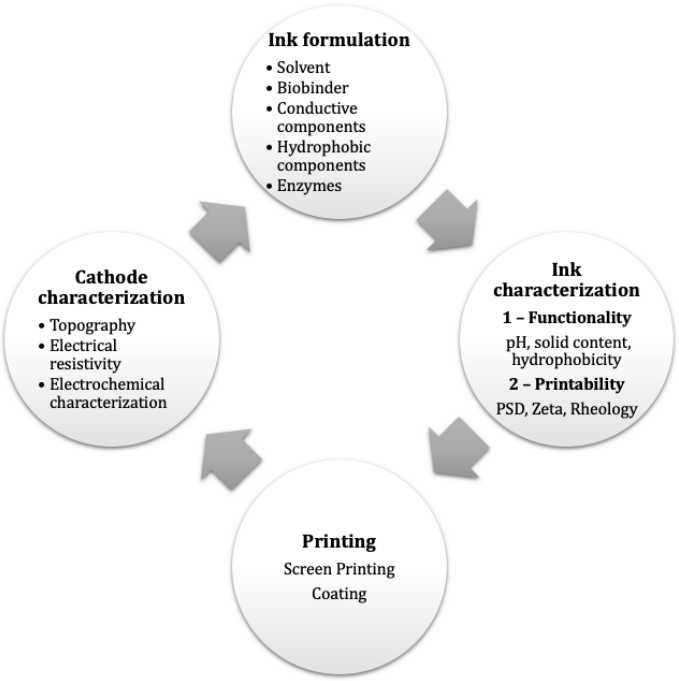

Figure 1: Development process of the cathode ink formulation and its printing

Figure 1 shows the process of ink formulation and printing implementation with associated characterizations. The material selection was done in coordination with the different characterizations. The ink formulation consists of a combination of bio-binders, conductive components, hydrophobic components and enzymes. The solvent used is MiliQ water. The ink samples were characterized by different methods.

The first objective is to allow biocathode functionality by choosing certain components:

- The pH has to be adjusted to allow the best enzyme activity and to allow a stable state of charged particles and polymers. It was measured with pH-meter from Mettler Toledo.
- Solid content is measured to estimate residual amount deposited on the substrate after printing. This measurement allows to calculate the deposited volumes by coupling this with thickness and topography measurements. Finally, layers density and microstructure can be estimated. It was measured with thermobalance HC103 from Mettler Toledo.
- Hydrophobic components have been developed to avoid cathode flooding and allow O_2 diffusion. They were characterized with Ossila's contact goniometer and its related software. It has been done for the biobinder blends, which is a mix between hydrophobic and hydrophilic components. Different ratios have been prepared. The polymer blend solutions were coated on glass and dried. A 10 µL droplet of distilled water was used to perform the contact angle measurement. Measured contact angle represents the angle between the solid interface and water. If this angle is superior to 90°, the solid is considered as hydrophobic.

The second objective of ink characterizations is to make the ink printable by adjusting the appropriate components and processes:

- The particle size distribution can affect the ink rheological behavior and the layer architectural nano and microstructure. Furthermore, D90 parameters is directly connected to mesh opening selection. It was measured with electroacoustic spectroscopy DT1202 from Dispersion Technology because of carbon suspensions opacity which excluded light scattering techniques.
- The residual charges of polymers and particles in inks play a role in suspension stability. The zeta potential is used to stabilize inks with adjusting the pH, double layer charge state and ionic forces. It was measured with electroacoustic spectroscopy DT1202 from Dispersion Technology.
- Rheological measurements are also essential to understand the behavior of the ink under shear rate induced by printing process. By modeling those printing steps, it is possible to adjust the formulation thanks to screen printing or coating requirements. They were performed with a rheometer (HR20 – TA Instrument) thanks to a parallel plate geometry with a diameter of 40 mm and a gap of 1 mm at 20 °C. Solvent cage was used to avoid sample evaporation. Flow curve was plotted to determine the rheological behavior of the inks. Oscillation tests were also conducted to determine the viscoelastic behavior of the ink (G' and G'' moduli).

After several iterations of formulation and characterization, suitable inks have been produced and printed. As a starting point, inks have been coated with a traditional coating table. Metal templates with 200 mm thickness were used on the substrate material as Gas Diffusion Layer (GDL). This substrate was chosen as a conductive, hydrophobic, and porous surface that allows oxygen diffusion (so called air breathing) and avoids cathode flooding. Additionally, it plays a current collector role since it is electrically conductive. Figure 2 represents the printed biocathodes on GDL.

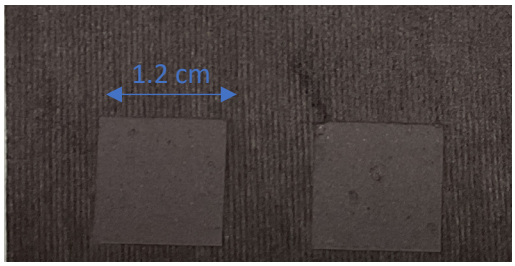

Figure 2: Coated cathodes on GDL

Finally, some characterizations were conducted on this cathode electrode:

- Surface reconstruction in 3D had been performed to study the topography of the printed layer. Microscopic surface characterization was carried out with an Axioscope 7 from Optic Concept Zeiss, with its associated software DeltaPix Insight.
- Electrical resistivity was measured with 4 points probe DAQ973A from Keysight. This ink was first coated on glass prior to measurement in order to remove substrate conductivity contribution.
- Electrochemical characterizations were finally performed to assess catalytic activity. Measurements were performed on a MPG2, Biologic™ potentiostat. Bioelectrodes were tested in a half-cell configuration with a 3-electrode setup including an Ag/AgCl reference electrode and a Pt counter electrode within GDL/Ink/Enzyme as working electrode. Open circuit voltage (OCV), which represents the potential reached without any applied current, and cyclic voltammetry (CV) were performed from 0.7 V to 0 V with a 1 mV/s scan rate. These electrochemical characterizations were repeated 10 times.
- For the characterization of full cell, a reference enzymatic bioanode was added but it will not be described in this study. Polarization tests were conducted with different current discharges from 0 µm to 500 mA.

3. Results and discussion

3.1 Ink characterization

Different characterization and optimization loops were performed for the biocathode to adjust the ink performances and printability:

- Conductive components ratio has been adjusted to control the ink rheological behavior and ink solid content (20 %, w/w).
- The polymer matrices have been made compatible by modifying the ratio of the dispersion polymers and the binder polymer, which have opposite charges.
- An optimal pH has been determined within the range 5 and 6 in regards of maximum enzyme catalytic activity and zeta potential stability. In the carbon dispersion, zeta potential is −14.32 ±0.13 mV, means that the global charge of carbon particle induces repulsive interactions that stabilizes the system. Steric stability given by the binder polymer also enhances overall dispersion stability (Tadros, 1991; Bajpai, et al., 2007).
- Particle size distribution shows a maximum particle size in the carbon dispersion at 36.40 ±0.12 nm. Thus, the opening diameter of the screen-printing mesh should not be less than three times this value.

3.1.1 Rheological characterization

Figure 3a represents the variation of G’ and G’’ moduli as a function of oscillation strain. Under strain of 40 %, G’ > G’’, meaning that the elastic behavior is preponderant, and the ink behaves as an elastic solid. Over 40 % of oscillation, the ink behaves as a viscous liquid.

Figure 3b shows the variation of viscosity as a function of shear rate. Ink viscosity decreases when the shear rate increases, and power law index is 0.35 which demonstrates the shear-thinning behavior of this ink.

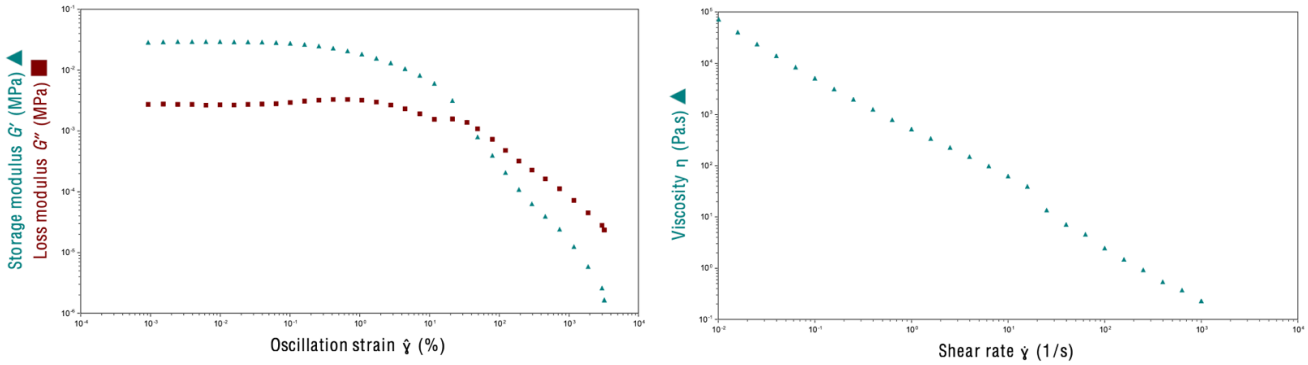

a) *b)*

Figure 3: (a) Elastic and viscous modulus and (b) flow curve of the ink

Screen printing process usually requires a high viscosity at low shear rate and a shear-thinning behavior, associated to pronounced thixotropy. In the first step, the ink is applied onto the screen. At this stage, the ink shouldn't spread and should stay under flow threshold. Secondly a high shear rate is applied to force the ink pass through the mesh screen: at 100 s^{-1}, the ink reaches low viscosity around 1 Pa·s. Ink should recover its solid behavior rapidly after screen unmold and material reconstruction properties are mandatory to reach homogenous layers. The viscoelastic behavior of the ink shows that ink can be reconstructed after printing. These rheological properties are compatible with the screen-printing process and are sufficient conditions for the ink to be printable. However, process parameters such as squeegee pressure and speed, and off-contact conditions will also have an influence (Kuscer, 2021).

3.1.2 Hydrophobic biobinder – O_2 accessibility

As Chi, et al. (2018) shown, balance between hydrophilic and hydrophobic components is an important parameter to avoid cathode flooding while promoting ionic conductivity. For this ink, hydrophobic microstructures have been developed to enhance O_2 diffusion near catalytic centers.

Contact angle measurements of the hydrophobic bio-binder have been carried out to select the best ratio of hydrophobic component in the bio-binder. Table 1 represents the results of contact angle measurements.

Biobinder A, with the lower amount of hydrophobic compound reaches an apparent contact angle of 71°. As this value is under 90°, it shows that it has a dominant hydrophilic behavior. Biobinders B, C and D which contain more hydrophobic compounds have reached an apparent contact angle higher than 90°, that confirms their macroscopic hydrophobic behavior. As expected, the higher the hydrophobic content, the higher the contact angle.

Table 1: Contact angle for different hydrophobic ratios

Biobinder name	Ratio of hydrophobic component	Contact angle (°)
A	-	71 ± 5
B	+	90 ± 2
C	++	98 ± 3
D	+++	100 ± 3

Biobinders B, C and D were incorporated in the ink formulation, printed and tested in full cell with an enzymatic anode reference. A control ink with PTFE was also printed and tested with the reference enzymatic anode. Polarization tests were done for each printed fuel cell. Table 2 presents the open circuit voltage (OCV) prior to polarization sequences. The higher the ratio of hydrophobic component in the hydrophobic biobinder, the higher the OCVs. As expected, the control PTFE ink reached the maximum OCV because the structure cannot be flooded by water at all. The maximum power achieved by the biofuel cells is impacted by the ratio of hydrophobic components in the biobinder. Indeed, the maximum power reached for ink with ratio D is much higher than for ratio B and C. Maximum power can be reached thanks to an optimized O_2 accessibility and a high ionic conductivity. The biobinder blend based on ratio D enhances oxygen diffusion and preserves ionic conductivity on the cathodic enzyme side allowing the printed biofuel cell to reach higher maximum power. In this study, a new natural biobinder component was developed, offering advantageous alternative compared to fluorinated binders such as PTFE.

Table 2: Polarization tests results for different printed fuel cells

Hydrophobic compounds	OCV (mV)	Maximum Power (µW)
B	654 ± 3	29 ± 5
C	672 ± 3	35 ± 5
D	684 ± 13	107 ± 14
PTFE	695 ± 8	95 ± 4

3.2 Biocathode characterization

3.2.1 Surface characterization

A 3D reconstruction of the cathode printed on Gas Diffusion Layer (GDL) allowed to evaluate the surface roughness of the electrode and the material organization on its surface. Therefore, the thickness is estimated as approximately 91 ± 3 µm.

3.2.2 Electrical resistivity

This electrical resistivity must be as low as possible to optimize the electron transfer. GDL substrate shows resistivity of about $3{\cdot}10^{-5}$ Wm, which is suitable for biocathode current collector applications. Conductive network has been optimized in the biocathode formulation by adjusting particle aspect ratio and particle size distribution. The optimal resistivity obtained is about $3{\cdot}10^{-3}$ Wm.

3.2.3 Electrochemical characterization

3 series of half-cells have been tested electrochemically: the bare substrate (GDL), the ink without enzyme printed on the substrate (GDL/Ink) and the ink with enzymes printed on the substrate (GDL/Ink/Enzymes).

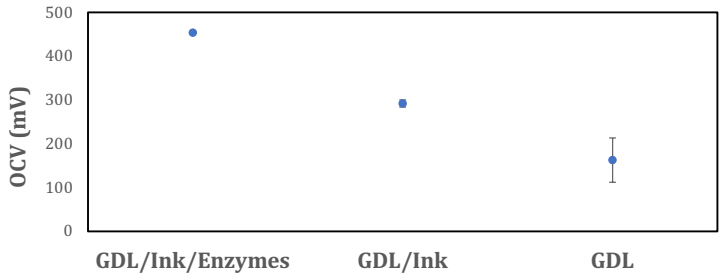

Figure 4: OCV results for printed inks and bare substrate

Figure 4 represents the Open Circuit Voltage (OCV) values measured by the potentiostat. For the bare substrate, the value is completely dispersed and means that there is no spontaneous dioxygen reduction possible in this surface. The OCV about 300 mV reached by the printed ink without enzymes shows that a moderate spontaneous dioxygen reduction can take place in the surface. Then, the OCV around 450 mV for the printed ink with enzymes shows typical OCV value observed for the type of enzymes used. It means that the O_2 catalytic reduction occurs on the surface of the electrode.

Figure 5 shows cyclic voltametric results. A scan from 0.7 V to 0 V is realized and a drop is observed around 0 V for the printed electrode with enzymes. It can be assigned to O_2 reduction, and the catalytic current reached is about 1 mA/cm^2. No signal apart from the capacitive envelope is observed for the printed layer without enzyme and the bare substrate. This result shows that the printed biocathode with enzymes can be used in a full cell configuration with an optimized power.

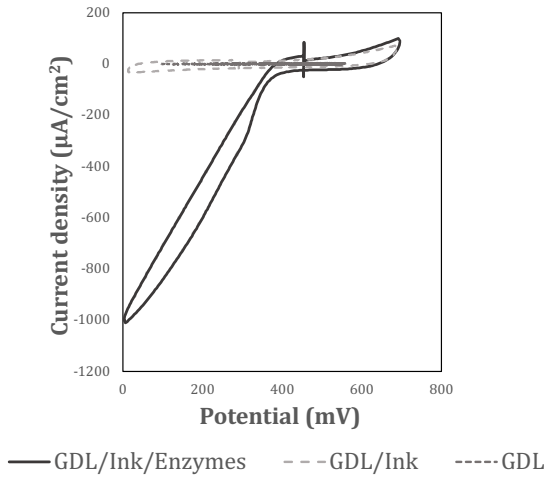

Figure 5: Comparison of the different surfaces via cyclic voltammetry; measurements were performed at a scan rate of 1 mV/s and ambient temperature

4. Conclusions

This study shows the development, characterization and optimization of a printed enzymatic biocathode. The ink components have been specifically studied for their biosourced and biodegradable properties. The new biocathode tackles the well-known challenges toward oxygen diffusion and cathode flooding in full cell technology. An optimized biobinder blend have been developed to manage the balance between hydrophobic region and ionic conductivity. Moreover, electrical conductivity and enzyme activity have been improved. Finally, the biocathode inks are suitable with screen printing process and are expected to have a low environmental impact due to their composition. Properties of cohesion, adhesion to the substrate and thermal drying impact should be studied to go forward a full industrialization.

References

Abreu, C., 2018. *Conception et optimisation de piles enzymatiques glucose-O_2 pour la gestion de puissance.* Dr. thesis. Université de Lyon.

Bajpai, S.K., Mohan Y.M., Bajpai, M., Tankhiwale, R. and Thomas, V., 2007. Synthesis of polymer stabilized silver and gold nanostructures. *Journal of Nanoscience and Nanotechnology*, 7(9), pp. 2994–3010. https://doi.org/10.1166/jnn.2007.911.

Chi, B., Hou, S., Liu, G., Deng, Y., Zeng, J., Song, H., Liao, S. and Ren, J., 2018. Tuning hydrophobic-hydrophilic balance of cathode catalyst layer to improve cell performance of proton exchange membrane fuel cell (PEMFC) by mixing polytetrafluoroethylene (PTFE). *Electrochimica Acta*, 277, pp. 110–115. https://doi.org/10.1016/j.electacta.2018.04.213.

Huang, X., Zhang, L., Zhang, Z., Guo, S., Shang, H., Li, Y. and Liu, J., 2019. Wearable biofuel cells based on the classification of enzyme for high power outputs and lifetimes. *Biosensors and Bioelectronics*, 124–125, pp. 40–52. https://doi.org/10.1016/j.bios.2018.09.086.

Kuscer, D., 2021. Screen printing. In: M. Pomeroy, ed. *Encyclopedia of materials: technical ceramics and glasses*. Oxford: Elsevier, pp. 227–232. https://doi.org/10.1016/B978-0-12-803581-8.12082-X.

Mrozik, W., Rajaeifar, M.A., Heidrich, O. and Christensen, P., 2021. Environmental impacts, pollution sources and pathways of spent lithium-ion batteries. *Energy & Environmental Science*, 14(12), pp. 6099–6121. https://doi.org/10.1039/D1EE00691F.

Tadros, T.F., 1991. Steric stabilisation and flocculation by polymers. *Polymer Journal*, 23(5), pp. 683–696. https://doi.org/10.1295/polymj.23.683.

DOI 10.14622/Advances_49_2023_06

Influence of atmospheric plasma polymerisation on the printability of polycarbonate and poly (methyl methacrylate)

Mansi Vivek Puro[1], *Dhia Ben Salem*[2] *and Michael Dattner*[1]

[1] Berliner Hochschule für Technik (BHT)

[2] Plasmatreat GmbH

E-mails: mansipuro@gmail.com; dhia.bensalem@plasmatreat.de; michael.dattner@bht-berlin.de

Short abstract

Polycarbonate and poly (methyl methacrylate) are very promising materials with generally extremely critical and challenging printability. Polycarbonate finds extensive utilization in the fields of food packaging, aircraft components and medical applications. Poly (methyl methacrylate) is a prevalent alternative for inorganic glass with its shatter-resistance and it is utilized in electronic instrument displays as well as in the medical sector. Despite their excellent characteristics, mentioned above, these polymers require surface modification prior to the printing process to improve wettability and therefore ink adhesion. Plasma polymerisation is a special possibility to enhance this adhesion by depositing an ultra-thin film of organic monomers on the surface of the substrate. An experiment was conducted with UV inkjet printing on the mentioned substrates by using a plasma system to improve printability. This plasma process includes one process gas, three process speeds and two power levels for plasma generation. The adhesion properties were compared with untreated samples by crosscutting tests (according to DIN EN ISO 2409) and surface characterisation by surface energy analysis combined with polymerisation film thickness measurements and FTIR analysis. All four analyses show coherent results and lead to a most promising set of parameters at the plasma process for long lasting inkjet prints on polycarbonate and poly (methyl methacrylate).

Keywords: plasma polymerisation, polycarbonate, PMMA, printability, print-adhesion, inkjet

1. Introduction and background

The printing industry often deals with a variety of substrates that possess unique physical and chemical features. To achieve first-class output, it is important to understand and consider substrate properties. Amongst the many properties, surface energy holds great significance for achieving desirable print quality by facilitating the adhesion of ink onto substrates (Lahti, et al., 2004).

In this context, it is important to achieve a best match in surface energy of substrate and ink as well as further, the printing process positively affecting, surface characteristics. Various surface treatment technologies are established since many years. There are techniques for improving surface properties like corona discharge, flame treatment and chemical primers (Lahti, et al., 2004). But conventional treatment methods have quite often drawbacks related to their impact on the environment and the ejection of harmful volatile organic compounds that affect human health and surroundings.

Recent advancements in nanotechnology have led to the development of plasma surface treatment technology that offers improved performance as well as sustainability (Friedrich and Hidde, 2015). This process can also ensure more uniform and longer-lasting results compared to traditional surface modification approaches (Pykönen, et al., 2007). As printing systems are frequently adopting new technologies for modified surfaces, this study aims to examine the effect of plasma polymerisation on the surface characteristics and printing performance of polycarbonate (from now on written PC) and poly (methyl methacrylate) (PMMA).

The main-focus of this study is to enhance the adhesion quality of inkjet printed UV-ink on PC and PMMA by identifying the optimal combination of parameters in the atmospheric plasma polymerisation. Finally, the durability of the treatment results is determined by measurements with samples printed immediately after plasma treatment, 24 and 48 hours after plasma treatment.

Related work has been conducted to obtain printability on different polymers by focusing on the process parameters of different surface modification methods:

- Izdebska-Podsiadly (2021) examined the effects of cold plasma surface modification on the print quality of two different types of biodegradable polylactide (PLA) films with flexographic water-based and solvent-based inks.
- Pykönen, et al. (2007) conducted an experiment for determining the effects of atmospheric dielectric barrier discharge (DBD) plasma activation at inkjet print quality with paperboard, polyethylene and polypropylene films. Three black inks (solvent-based pigmented, solvent-based dye ink and water-based pigment ink) were used with paperboard. With polyethylene and polypropylene films, solvent-based black ink was used.

In wider field of research in the context of plasma treatment further work has been conducted:

- Dimić-Mišić et al. investigated the influence of dielectric barrier discharge nitrogen plasma treatment on the transfer of solvent-based photovoltaic (PV) inkjet printing inks (IP) onto enzyme-pretreated fibre-derived micro/nanofibrillated cellulose (MNFC) films. The drop-on-demand inkjet printing process was utilized for the visual inception of the printability of plasma-treated and untreated films (Dimic-Misic, et al., 2019).
- In addition to the aforementioned research, Dimić-Mišić et al. conducted an extensive study examining the effect of oxygen, nitrogen and oxygen followed by nitrogen DBD plasma as well as different treatment exposure time (120 s and 240 s) on MNFC film surfaces. The surface characteristics were determined by surface energy calculations and assessing material composition, surface roughness. The investigation aimed to further evaluate printability and print uniformity by transferring a highly polar functional ink with yellow-orange tint on treated and untreated films (Dimić-Mišić, et al., 2021).

In this study, atmospheric pressure plasma processes will be considered to prepare two different polymer surfaces PC and PMMA prior printing . Moreover, the influence of plasma power and deposition speed will be studied in order to improve the adhesion to the UV-curable ink.

2. Materials and methods

To achieve the results, the surface of PC and PMMA plates with dimensions of 180 mm × 550 mm × 2 mm, density of 1.20 g/cm^3 to 1.22 g/cm^3 and toughness from 140 °C to −20 °C, were plasma-treated and printed.

2.1 Equipment

The plasma activation and plasma coating of the polymer surfaces were realized with an atmospheric plasma treatment system provided by Plasmatreat GmbH (Plasma Scanner PS700; Figure 1a). The plasma scanner is equipped with two different rotational jets, one for activation and one for the coating, both suitable for large surface treatment. The reference plates, the plasma-activated plates, and the plasma-coated plates were printed with a flatbed UV-curable inkjet printer (Mimaki UJF 3042 MKII Ex; Figure 1b) using corresponding UV-inks (LUS-120 (C, M, Y, K, W, Cl)).

a) *b)*

Figure 1: Plasma treatment system (a) (Plasmatreat, 2023), and flatbed UV-curable inkjet printer (b) (Mimaki, 2023)

Further equipment consisted of a contact angle measurement device (OCA; Figure 2a) for surface energy analysis, a spectrophotometer (x-rite i-1 pro Rev) for colour analysis, an interference reflectometer (Ocean optics Nano calc 2000) for coating thickness measurements and a FTIR setup (Tensor II Bruker optics; Figure 2b) for chemical information concerning the plasma induced coating.

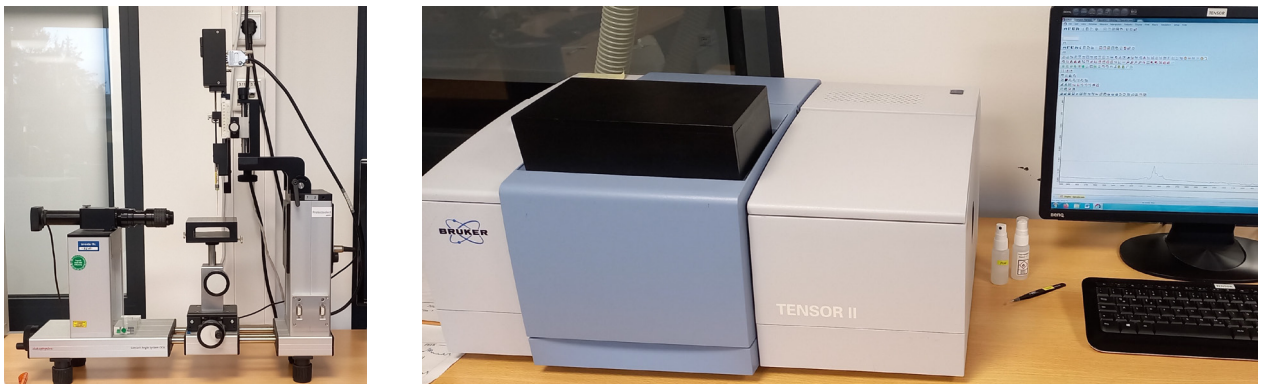

a) *b)*

Figure 2: Setup for contact angle measurements (a) and an ATR-FTIR setup (b)

2.2 Test chart designs

Three test chart designs were printed on the plates and used for large area analysis with CMYK solids (Figure 3a), ink superpositioning analysis with a CMYK image (Figure 3b) and colorimetric halftone analysis with various area coverages of CMYK (Figure 3c).

a) *b)* *c)*

*Figure 3: CMYK solids (a), CMYK image (b) (Mimaki, 2023),
and halftone patches with various area coverages in CMYK (c)*

2.3 Experiment

All the experimental trials were performed at constant room temperature (21 °C). All samples were cleaned with isopropyl alcohol before being exposed to the plasma surface treatment. The surface tension of all inks was 29 mN/m (min. 27.2 mN/m, max. 30.1 mN/m), calculated corresponding to the algorithm of Daerr and Mogne (2016).

2.3.1 Plasma polymerisation

The plasma polymerisation was carried out at two power levels (450 W and 550 W) and three process speeds (5, 10 and 15 m/min). All the other parameters, like ionisation gas (air), ionisation gas flow (72 L/min), heater- and evaporator-temperature (520 °C and 270 °C) as well as the distance between the plasma setup jethead and the substrate (2 mm), remain the same for all trials.

2.3.2 Printing and analysing PC and PMMA

Following the treatment, the plasma-modified plates were printed immediately with the mentioned UV inkjet printer and analysed concerning surface energy, print adhesion and colour values:

- Surface energy is estimated via contact angle readings (mean value out of five measurements) by using three test liquids (water, ethylene glycol and diiodomethane) on treated and untreated samples. Considered are the surface tensions and their relevant dispersive and polar component using the Owens, Wendt, Rabel, and Kaelble's (OWRK) method (Yu, et al., 2020).
- Print adhesion was analysed via cross cutting tests in accordance with DIN EN ISO 2409 (Deutsche Institut für Normung, 2020) for treated and untreated samples.
- Colour density values according to DIN 16536-1 (Deutsche Institut für Normung, 1997) of the solids as well as CIE $L^*a^*b^*$-colour-coordinates (CIE, 1971) of halftones were derived from the measured spectral data (mean value out of five measurements) concerning the treated and untreated samples.
- Colour deviation analysis was operated with the colour values of the print on untreated samples as reference in the ΔE_{00} formula (CIE, 2001) to identify potential colour changings due to treatment.

2.3.3 Further surface characterisation

To achieve additional chemical information concerning the plasma induced coating, an ATR-FTIR analysis was performed by using treated and untreated copper plates (because PC interferes the signal within the utilised infrared wavelength range) (Munshi, et al., 2018). The treatment was realised with the same plasma polymerisation parameters as with the PC and PMMA plates.

To get information concerning the thickness of the plasma induced ultra-thin film coating, spectroscopic reflectometry was used to measure the corresponding SiO_2 layer on a silicon wafer, which was also treated with the same plasma polymerisation parameters as the PC and PMMA plates.

2.3.4 Durability test

Finally, the durability of the treatment is determined by analysing the contact angle and the print adhesion additionally for samples printed 24 and 48 hours after the plasma treatment. The samples were heated up to 80 °C for three hours and kept the rest of the time in constant humidity- and temperature-conditions or kept in water for the complete time.

3. Results and discussion

First, the numbers for the surface energy analysis are presented in diagrams, followed by the adhesion results, that clearly show – using images of the crosscut results – the positive effect of the plasma polymerisation for both substrates at different process speeds and different power levels.

Colorimetric analysis shows the impact of the treatment on the colour reproduction up to 4.5 ΔE_{00} units and the ATR-FTIR combined with the layer thickness measurements confirm the speed and power level related trends, found in the surface energy analysis.

Finally, the durability results show the significant influence of power level and process speed on the print-adhesion (even if the samples were kept in water), which leads to a most promising parameter setting at the plasma system.

3.1 Surface energy effects due to plasma polymerisation

Figure 4 shows the strongest decreasing of surface energy due to plasma polymerisation with 550 W power level in the dispersion component at the slowest process speed (5 m/min) in the plasma setup. With higher speed, this effect is reduced again. The polar component is increased compared to the untreated sample but is decreasing again with higher process speed. The surface energy is only slightly modified due to plasma polymerisation and remains nearly unchanged.

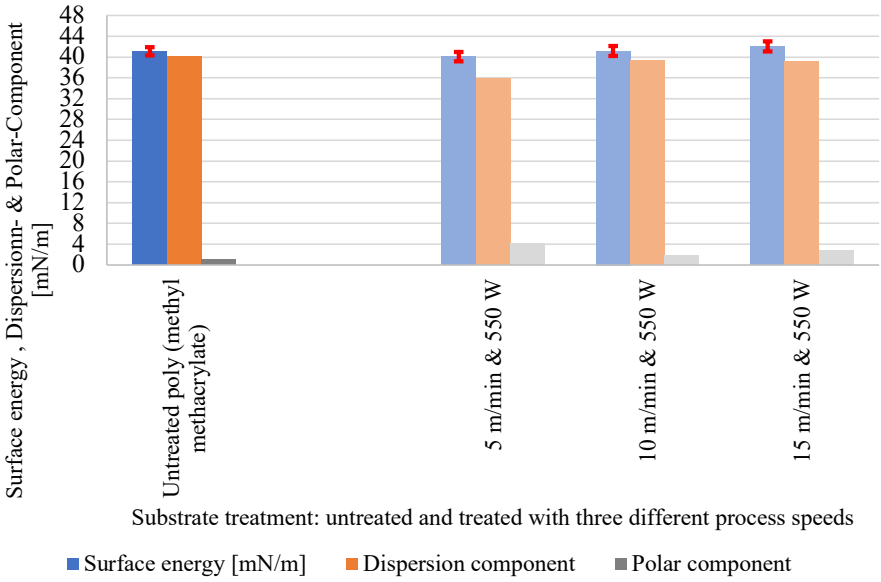

Figure 4: Surface energy at untreated and with 550 W plasma treated PMMA at different process speeds.

The same behavior was also observed with a lower plasma power of 450 W on PMMA and PC but is not presented in detail here.

This surface energy effects, caused by the plasma treatment, lead to significant improvements in print adhesion at the samples. Figure 5 shows the crosscutting test results for untreated samples (Figure 5, top) and samples that were treated with power levels 450 W (Figure 5, middle) and 550 W (Figure 5, bottom) at process speed 5 m/min printed immediately after the treatment.

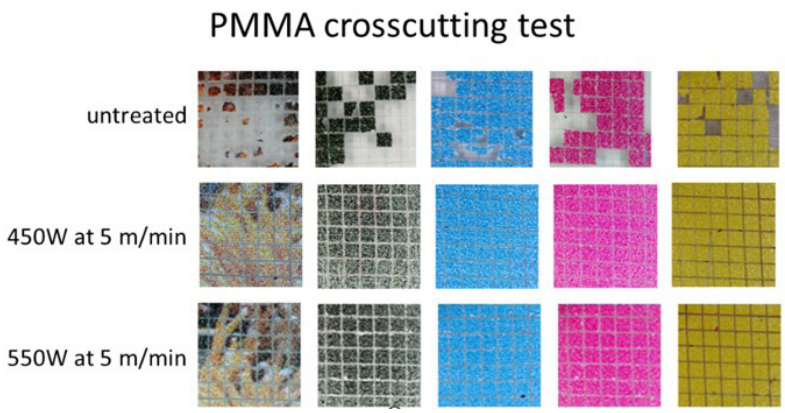

Figure 5: Crosscutting test at PMMA after plasma coating: untreated (top), 450 W (middle) and 550 W (bottom) power level at process speed 5 m/min

3.2 Colorimetric analysis

Concerning print density analysis, it can be seen that the surface modification of samples with plasma polymerisation showed mainly a 0.1 higher print density as compared to untreated surfaces.

Since the print-adhesion is perfectly given with these plasma parameter settings (when printed immediately after treatment), all halftones colour values are clearly affected by the treatment. Since the solids (100 % area coverage) show minor effects due to the treatment (< 2 ΔE_{00} at 100 % black & cyan, compared to the colour values determined at untreated samples), there are strong effects up to 4.5 ΔE_{00} at the halftones with lower tonal values (50 % black and cyan at 550 W power level with 10 m/min process speed (Condition 2)). Figure 6 shows the effects on trapping for the inks with the most uniform effects with 5 m/min (Figure 6, Condition 1) process speed for all area coverages. At process speed 15 m/min (Figure 6, Condition 3) the effect decreases with increasing tonal values. The treatment with 10 m/min (Figure 6, Condition 2) show inhomogeneous effects, which must be double checked.

For perfect colour reproduction results, it is obviously necessary to adapt the printer profile to the plasma induced changed situation including the inks that are not included in this figure.

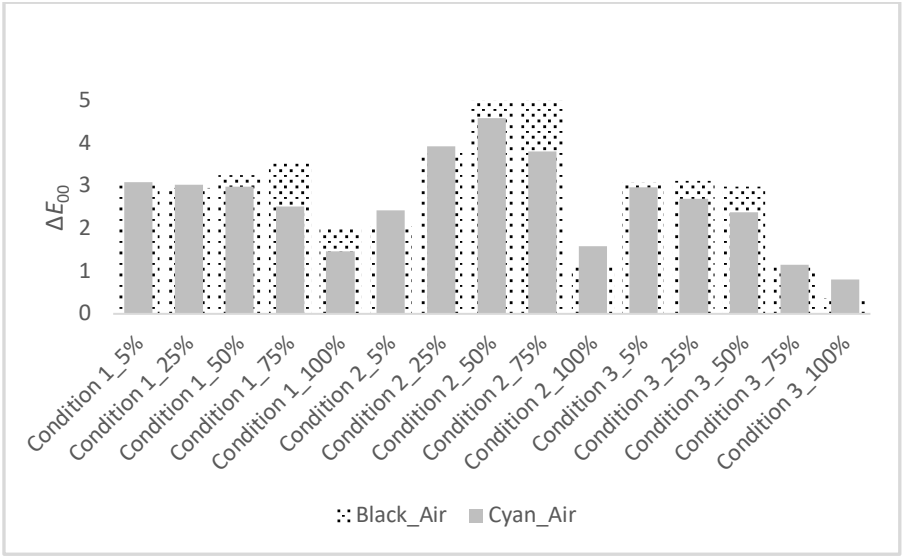

Figure 6: Colorimetric results for halftones of cyan and black printed on PMMA treated with 550 W, printed immediately after treatment; power level at 5, 10 and 15 m/min process speed (Condition 1, Condition 2, Condition 3)

3.2 Thickness measurements of the plasma induced ultra-thin coating

Referring to the reduced effects at the surface energy due to increasing speed at both power levels and to the reduced effect on the ink transfer (especially with black and cyan) it is predictable, that the coating thickness would be reduced in the same manner with both power levels, as it is shown in Figure 7. The ultra-thin thickness of the coating was representative measured on a silicon wafer, which is necessary due to the spectroscopic reflectometry technology with model Siox and refractive index 1.4571.

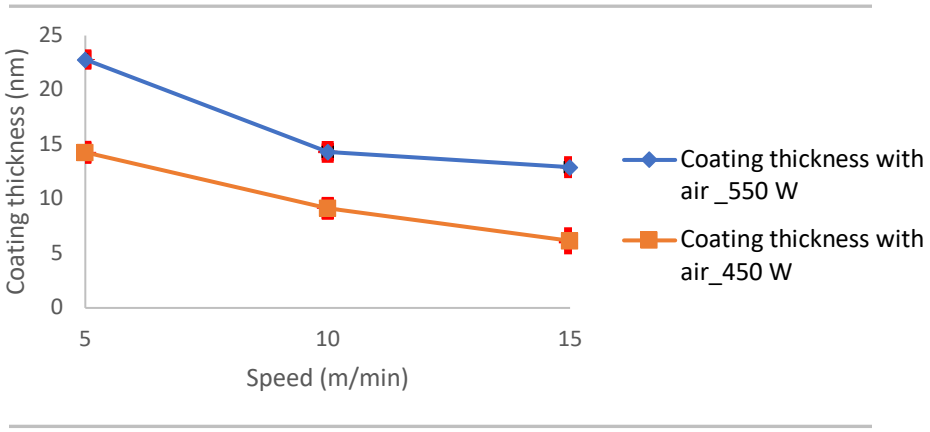

Figure 7: Plasma induced coating thickness at different speed, and two power levels 450 W and 550 W

3.3 ATR-FTIR analysis for more chemical information of the plasma induced coating

Referring to the effects identified at the surface energy and the coating thickness analysis, the same speed-depending characteristics should be obvious also with the functional groups within the coating. Figure 8 confirms this with higher absorbance values in all relevant areas at 5 m/min process speed compared to the values at 10 m/min or 15 m/min concerning a copper plate (Figure 8a). Relevant functional groups with corresponding wavenumbers are shown in Figure 8b. A Silane precursor was introduced in the plasma discharge, the FTIR confirmed the plasma polymerization mechanism with SiO bands clearly identified around 1200 cm^{-1}.

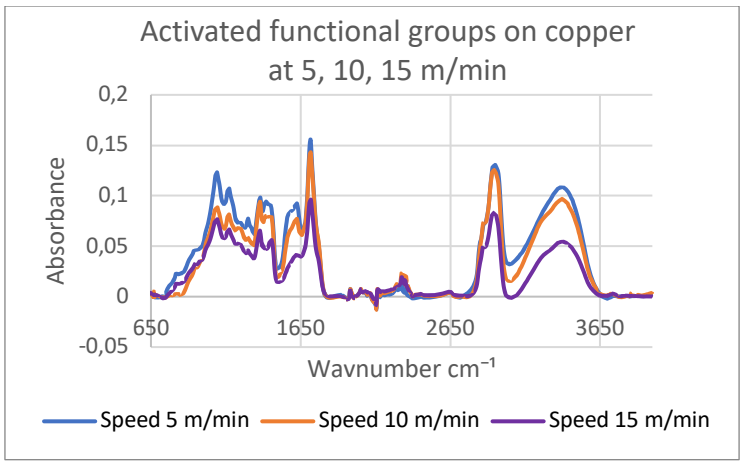

a)

Wavenumber	Functional group
951 cm^{-1}	Vinyl C-H out-of-plane bend
1123 cm^{-1} 1176 cm^{-1}	Alkyl substituted ether, C-O Stretch
1303 cm^{-1}	Vinylidene C-H in-plane bend
1721 cm^{-1}	C=O stretching vibration of ester groups
2868 cm^{-1}	Methyne C-H Stretch
2957 cm^{-1}	Methylene C-H asym./ sym. Stretch
3200-3570 cm^{-1}	Hydroxyl group, H bonded OH stretch

b)

Figure 8: ATR-FTIR chart for plasma coatings with 5, 10 and 15 m/min process speed (a), relevant functional groups with corresponding wavenumber (b)

3.4 Durability of surface energy effects due to plasma polymerisation

Especially in the crosscutting test results with higher process speed (and lower power level), the reduced print-adhesion becomes obvious. Figure 9 shows the strongly reduced positive impact due to waiting 24, or 48 hours after treatment before printing: large areas of the print are removed during the test.

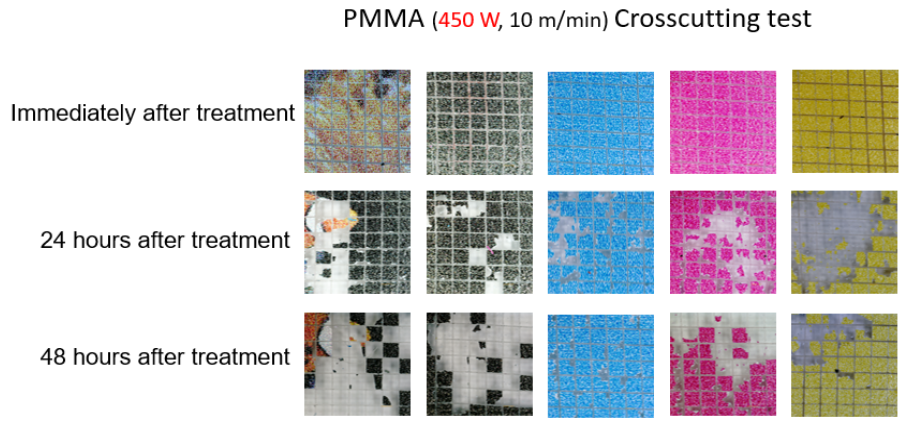

Figure 9: Crosscutting test at PMMA treated with 450 W power and 10 m/min and printed 24 / 48 hours after treatment

By reducing process speed and increasing the power level, the samples become more resistant, even if the samples are kept in extraordinary conditions like in water between treatment and printing. This can be seen in Figure 10 and 11.

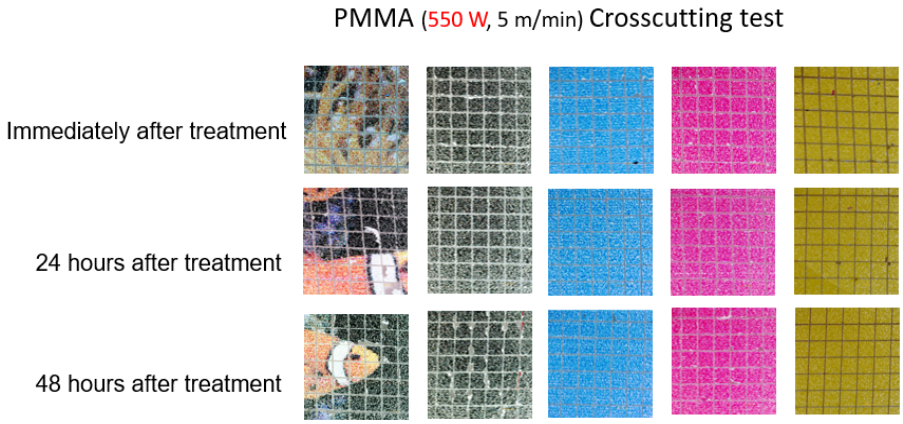

Figure 10: Crosscutting test at PMMA treated with 550 W power and 5 m/min, printed 24 / 48 hours after treatment

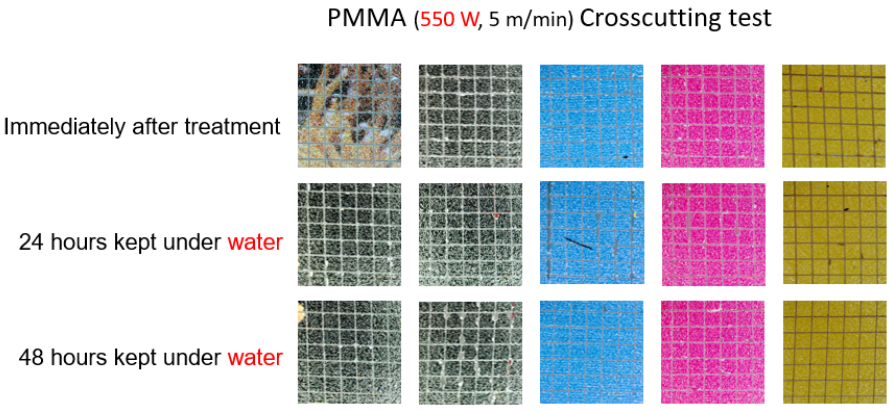

Figure 11: Crosscutting test at PMMA treated with 550 W power and 5 m/min, printed 24 / 48 hours after treatment and kept in water

Even if now, the print-adhesion is perfectly given for this plasma parameter setting, the colour perception of the printed halftones is affected by the treatment. Since the solids (100 % area coverage) show minor effects due to the treatment, there are increasing effects at the halftones with decreasing tonal value. Figure 12 shows this especially for black and cyan and indicates an effect on the trapping, which must be considered. For perfect colour reproduction results, it is necessary to adapt the printer profile to the plasma induced – and waiting-time depended – surface characteristics.

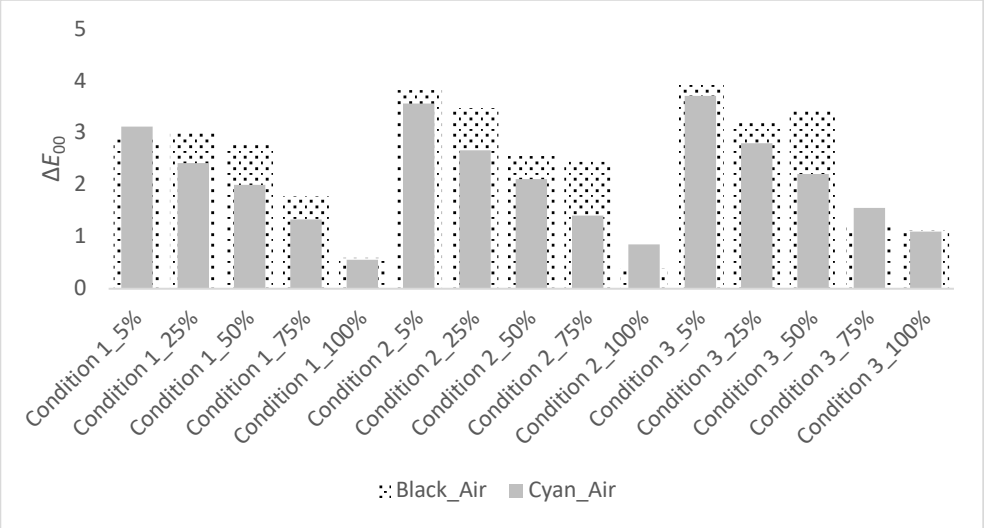

Figure 12: Colorimetric results for halftones of cyan and black printed on PMMA treated with 550 W power level at 5, 10 and 15 m/min process speed (Condition 1, Condition 2, Condition 3), 48 hours after treatment

4. Conclusions

Atmospheric plasma polymerisation ensures ink bonding on PC and PMMA by increasing the polar components and achieving optimum surface energy. Furthermore, the increased presence of functional groups supports covalent bonds between substrate surface and ink. This leads to stronger and more durable print-adhesion, which becomes obviously with the crosscutting test especially at PMMA samples that were treated with the identified process parameters and were kept 48 hours in harsh conditions before printing.

The plasma induced effects on the ink trapping can be easily considered in the printer-profile, to ensure first-class output with a high accuracy in the colour reproduction and high print-adhesion.

Acknowledgements

We would like to thank Magnus Buske, Head of Research and Development at Plasmatreat GmbH, for sensibilising us for this challenging and meaningful topic. Further thanks to Sebastian Guist and Hassan Schlee at Plasmatreat GmbH, especially for knowledge, guidance, and instrumentation assistance in the context of UV inkjet printing and plasma setup.

References

CIE, 1971. *Colorimetry: official recommendations of the International Commission on Illumination*. Paris: Bureau Central de la CIE.

CIE, 2001. *Improvement to industrial colour-difference evaluation: technical report: CIE 142:2001*. Vienna: CIE.

Daerr, A. and Mogne, A., 2016. Pendent_drop: an imageJ plugin to measure the surface tension from an image of a pendent drop. *Journal of Open Research Software*, 4(1): e3. http://dx.doi.org/10.5334/jors.97.

Dimic-Misic, K., Kostić, M., Obradović, B., Kramar, A., Jovanović, S., Stepanenko, D., Mitrović-Dankulov, M., Lazović, S., Johansson, L.-S., Maloney, T. and Gane, P., 2019. Nitrogen plasma surface treatment for improving polar ink adhesion on micro/nanofibrillated cellulose films. *Cellulose*, 26(6), pp. 3845–3857. https://doi.org/10.1007/s10570-019-02269-4.

Dimić-Mišić, K., Kostić, M., Obradović, B., Kuraica, M., Kramar, A., Imani, M. and Gane, P., 2021. Iso-and anisotropic etching of micro nanofibrillated cellulose films by sequential oxygen and nitrogen gas plasma exposure for tunable wettability on crystalline and amorphous regions. *Materials*, 14(13): 3571. https://doi.org/10.3390/ma14133571.

Deutsche Institut für Normung, 2020. *DIN EN ISO 2409, 2020. Paints and varnishes cross-cut test*. Berlin: Beuth-Verlag.

Deutsche Institut für Normung, 1997. *DIN 16536-1, 1997 Prüfung von Drucken und Druckfarben der Drucktechnik – Farbdichtemessung an Drucken – Teil 1: Begriffe und Durchführung der Messung*. Berlin: Beuth-Verlag.

Friedrich, J. and Hidde, G., 2015. Ultra-thin plasma polymer films as a novel class of adhesion promoters: a critical review. *Reviews of Adhesion and Adhesives*, 3(1), pp. 1–52.

Izdebska-Podsiadly, J., 2021. Effect of plasma surface modification on print quality of biodegradable PLA films. *Applied Sciences*, 11(17): 8245. https://doi.org/10.3390/app11178245.

Lahti, J. Savolainen, A., Räsänen, J.P., Suominen, T. and Huhtinen, T., 2004. The role of surface modification in digital printing on polymer-coated packaging boards. *Polymer Engineering and Science*, 44(11), pp. 2052–2060. https://doi.org/10.1002/pen.20209.

Munshi, M.U., Berden, G., Martens, J.K. and Oomens, J. 2018. Gas-phase infrared spectroscopy of metal-ligand redox pairs. In: *73rd International Symposium on Molecular Spectroscopy*. The University of Illinois, 18–22 June 2018. https://doi.org/10.15278/isms.2018.WI03.

Pykönen, M., Hakola, L., Eiroma, K., Lahti, J., Sundqvist, H., Kaukoniemi, O.-V., Tuominen, M,. Järnström, J., Peltonen, J., Fardim, P. and Toivakka, M., 2007. Effects of atmospheric pressure plasma activation on inkjet print quality. In: *NIP23: The 23rd International Conference on Digital Printing Technologies and Digital Fabrication. Anchorage, Alaska, 16-21 September 2007*. IS&T, pp. 404–409.

Yu, X., Hörst, S.M., He, C., McGuiggan, P, Kristiansen, K. and Zhang, X., 2020. Surface energy of the titan aerosol analog "Tholin". *The Astrophysical Journal*, 905(2): 88. https://doi.org/10.3847/1538-4357/abc55d.

DOI 10.14622/Advances_49_2023_17

The thermochromism of organic pigments dispersed in liquid phase

Tim Stiene

University of Wuppertal, School of Electrical, Information and Media Engineering, Rainer-Gruenter-Straße 21, D-42119 Wuppertal
E-mail: stiene@uni-wuppertal.de

Short abstract

Temperature is a known factor for colour appearance of both inks and dyes. This work investigates the temperature influence on the visible spectra of 43 organic pigments. The pigments are converted into solvent-based flexo inks and spectrally measured in transmission within a temperature range of 20–50 °C. After cooling down, up to two more heating and measuring cycles take place to assess reversibility. Significant thermochromic spectral effects and ΔE_{00} values > 1 can be observed for the majority of pigments. For most samples, spectral transmittance increases with increasing temperature. For peaks and gradients, a wavelength shift is observed usually. This leads to shifted hues and decreased chromaticities. The thermochromic effect can be described as linear with temperature increase, whereby the effect is only reversible from the second heating cycle onwards.

Keywords: thermochromism, UV-Vis spectroscopy, organic pigments

1. Introduction and background

The term 'thermochromism' describes colour changes as a function of changing material temperatures. Apart from known thermochromic effect colourants, which are subject to temperature-related changes in their crystal structure, this work is dealing with organic pigments, which are actually known as 'non-thermochromic'. Their thermochromism can be relevant for colour measurements in production processes such as printing presses using thermal dryers, coil coating or plastic injection moulding. It is known from industrial printing processes, that significant temperature differences can occur between inline and offline colour measurement. In one specific flexo print production, for example, a temperature difference ΔT of 15 °C and resulting colour differences which were of magnitudes of visual perception were measured. (Bohn, 2020)

From the perspective of thermochromics, however, it is difficult to put hard numbers on printing processes as many variables have an influence. For example, dryer temperature, substrate thickness, speed and material as well as the position of the inline colour measurement within the machine setup. For plastic injection with its ΔTs > 100 °C, Botos, et al. (2014) identified changes in colour values of up to 10 percent while measuring colour inline. Besides scientific interests, the thermochromism of organic colour pigments thus also has practical relevance.

As other factors, like concentration or solvent used, temperature is known for potentially having influence on UV-Vis measurements (Bamfield, 2001). Temperature, generally speaking, can be described as the average kinetic energy in a molecular system (Stierstadt, 2020). When energy is added to a system, it results in a stronger molecular vibration which could cause altered material properties. In an early study, Yarborough, Haskin and Lambdin (1954) have measured the absorption coefficient of various organic compounds as a function of temperature which was found to decrease with increasing temperature. Other studies were dedicated to the thermochromism of solids, started with ceramic tiles. Compton (1984) determined thermochromic effects for seven out of twelve tiles whereby red, yellow and green hues showed effects in contrast to blue and grey tiles. The effects had magnitudes of up to 0.9 ΔE_{00}/10 °C. Fairchild and Grum (1985) also investigated ceramic tiles in temperature ranges of 25–45 °C. The most intense thermochromic colour

changes were found for orange and red colours, successively decreasing with the wavelength of the main reflection for green and blue. Results that were fundamentally confirmed by Verrill, Comptom and Malkin (1986). Malkin, et al. (1997) pointed out that the reflectance decreases with increasing temperature, which affects particularly spectral bands with large gradients. For various sample materials and colours, Hiltunen, et al. (2002) marked principles for the thermochromic phenomena which can also be found in some of the sources already cited: the shift of transmittance or reflectance is described as being directly proportional to the temperature change; the greater the slope in a spectral curve the bigger the colour change; a rising edge of a spectrum tends to shift towards longer wavelength, whereby this shift became bigger with rising wavelength. Furthermore, valid for single absorption, spectral changes occur in such a way that the integrated absorption area remains constant. Piening (2006) has worked on methods for analysing art and made some statements on temperature influence in this course. Following his argumentation, the temperature-dependent distances within molecular orbitals are responsible for colour differences. Here should be remembered that the visible colour of organic materials is mostly based on electron transitions between molecular orbitals. Generally speaking, the distance between those orbitals corresponds with the necessary amount of absorbed energy and thus the absorption spectrum (Nassau, 1978). The number of possible locations and energy differences of an electron also increases with the temperature. That's what leads to sharper absorption bands of measurements on lower temperature. Griffiths (1976) and Song, et al. (2014) investigated the temperature-dependent absorption of *ß*-carotene in a solvent. For a temperature range of 18–81 °C, they determined a spectral red shift. They attributed this to the temperature-dependent reduction in conjugation length and thus increased μ-electron delocalisation.

Che, Li and Senanayake (2016), examined ceramic tiles for a range of 10–55 °C. They found almost no thermochromism for reflections without significant slopes, only little effects for blue tiles, and distinct thermochromism for yellow, orange and red tiles with values up to 1.8 $\Delta E_{00.}$ The authors hypothesize the following: the steeper the slope, the greater the red shift for positive slopes, reflections with only negative slopes don´t show thermochromic shifts, for reflections with both negative and positive slopes there is also no spectral shift. In another work, Che and Senanayake (2017) were able to confirm their previous results for a more diverse sample field with respect to colourimetric characteristics. For a temperature range of 20–60 °C, colour changes correlated linearly with the temperature change. According to them, the physical mechanism for the hue dependency of thermochromism is still unclear. Che (2018) again investigated only samples of thermochromic-sensitive hues including ceramic and plastic tiles, textile fabrics, ink-printed and paint-coated paper cards in a range of 20–60 °C. This investigation confirms the hue dependency. He locates a possible explanation for the greater temperature sensitivity of colours such as red, yellow and orange in their particle size.

Summarizing the main findings of past studies, it can be stated that the thermochromism intensities depend both on the particular colour material and the wavelength range of the main absorption region of a colourant. In this context, the degree of slope of a spectral curve also seems to be relevant. Moreover, the physical background of thermochromism is declared as unknown by some researchers, whereas others mention the temperature-dependent excitation energies as key factor.

Thermochromism is to be systematically investigated as part of an ongoing research project. For this purpose, a laboratory UV-Vis spectrometer for reflected light measurements of solid samples has been extended by a temperature-controlled sample holder, including an infrared thermometer for continuous monitoring of the sample temperature. However, in order to first examine the pigments without substrate influence, this work wants to characterise the thermochromic effect for organic pigments dispersed in liquids by conducting absorbance measurements. A special feature of absorption measurement is the need to dilute the samples so heavily that they appear only slightly coloured to human perception. In combination with the high layer thickness of 10 mm resulting from the cuvettes path length, this leads to very distinctive spectra.

2. Materials and methods

2.1 Organic pigments and ink components

An organic pigment is classified by its chemical type and identifiable through the established Colour Index (C.I.), following the listing in Hunger and Schmidt (2018). 43 pigments are obtained to cover a wide range of different types. Table 1 contains all pigments and Table 2 all components and respective concentrations used for the preparation of inks.

Table 1: All organic pigments used, listed following the systematic of the Colour Index, polymorphic modifications are characterised with additional Greek letter, P.V. 55 exists in dark (d) and bright (b) shade

C.I.		**C.I.**		**C.I.**	
P.B.	15:1	P.R.	122	P.Y.	83
	15:3		144		109
	15:4		168		110
	15:6		175		129
	60		176		139
P.Bl.	1		177		150
P.Gr.	7		179		151
	36		206		213
P.O.	61		254	P.V.	19 (α)
P.R.	9		254		19 (β)
	3		264		19 (γ)
	83	P.Br.	23		37
	83		25		55 (b)
	122	P.Y.	3		55 (d)

Table 2: Components and concentrations for ink and sample preparation

Component	**Function/Type**	**Concentration (%)**
Kraemer ERKAMAR 3120 (EK)	binder / maleic resin	28.5
BYK DISPERBYK-2013	dispersing agent	3
1-Methoxypropan-2-ol	diluent / solvent	37
Ethanol	diluent / solvent	28.5
Pigment	colourant	3
Kraemer ROKRAPOL 7495 (RK)	binder / polyester resin	only for dilution

2.2 Methods

A Cary 60 UV-Vis Spectrometer is employed to determine absorbance spectra of liquid samples which are filled in cuvettes made of optical glass. Cuvette path length is 10 mm. According to the usual procedure, it is assumed that the measuring device works with standard light D65. To enable temperature-variable spectral measurements in transmission, it is necessary to convert the inks in stable suspensions, as it is not suitable to measure the pigments in pure solvent only. Stability here means to minimise potentially absorbance-influencing phenomena such as sedimentation, agglomeration and other particle interactions.

Stability is even more important as the suspensions are heated up twice within the spectrometer, which lasts approx. 90 minutes for each sample. Eight suspensions are heated even three times.

The pigments are dispersed manually using a glass muller in a binder mixture of EK 3120, 1-Methoxypropan-2-ol and dispersing agent (ratio: 0.485 : 0.485 : 0.03). The resin is completely soluble in organic solvents and, according to the manufacturer, has good pigment wetting properties. The 1-Methoxypropan-2-ol with its high evaporation number (22 to 8, compared to ethanol) is used, to minimise solvent evaporation during dispersion. Ethanol is then used to reduce the pigment pastes viscosity, although the final viscosity of the inks produced in this way is never identical – due to the respective pigment properties.

For absorbance measurements, each suspension must be brought to an absorbance strength appropriate for the measuring instrument ($A < 1$) by means of a dilution series. Depending on the specific absorption strength of the pigments, dilution rates between 1 : 1 000 and 1 : 10 000 are generated. The experiments have shown that dilution with ethanol only leads to unstable samples. Therefore, the samples are diluted with a 1 : 1 mixture of Ethanol and RK 7495. RK is used here because, unlike the slightly yellowish EK, it has no inherent colouring. The mixing ratio of 1 : 1 has proven to be well suited to keep the samples stable for an adequate period of time. The relatively high viscosity η of the mixture should also contribute to this and is provided by Table 3. It is determined in shear tests deploying a cone-plate viscometer Anton Paar MCR 101. For shear rates of 0–100 s^{-1} the fluids viscosities were shown to be independent of the shear rate. All measurement values are the result of averaging three individual measurements.

All samples rested for at least 72 hours before measurement, as experience has shown that this time contributes to higher stability during measurement. The cuvette, binders and diluents do not have their own thermochromism. However, temperature-specific baseline corrections related to a cuvette only filled with the diluent are made since a slightly decreasing absorbance with increasing temperature can be observed.

Table 3: Viscosities of a 1:1 solution of RK 7495 binder and ethanol for temperatures of 20–50 °C

Temperature (°C)	Viscosity (mPa·s)
20	99
30	65
40	41
50	27

Applying Equation [1], all spectral absorbances measured with the UV-Vis spectrometer are converted to spectral transmittances and can then be further processed to colourimetric numbers.

$$T = (10^{-A}) \cdot 100 \qquad [1]$$

3. Results and discussion

3.1 Characteristic and reversibility

Figure 1 shows transmittance spectra for three samples in 20 °C resp. 50 °C ($\Delta T_{30°C}$) each. For most areas the transmittance increases with increasing temperature. But, deviations from this behaviour can be observed especially in areas with changing gradients. The peak of P.B. 15:1 (1.48 ΔE_{00} for 20 °C to 50 °C) is slightly shifted from 512 nm towards 514 nm while the regions of low transmittance on both sides of the peak show increasements. P.V. 19(β) (1.23 ΔE_{00}) shows increased transmittances and small peak shifts at around 550 nm. The distinct slopes of P.Y. 129 (1.71 ΔE_{00}) become somewhat blurred in areas of changing

gradients between 400 nm and 500 nm while one also sees a decrease at those blurred areas, in contrast to areas with higher transmittances.

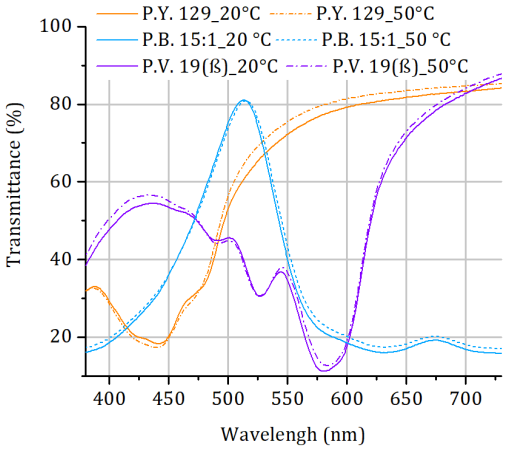

Figure 1: Transmittance spectra for three pigmented suspensions at two temperatures of 20 °C resp. 50 °C

The presence of a spectral red shift for blue and violet correspond to the findings of other researchers. Thermochromism does not seem to be limited to areas with changing gradients, a finding that differs from the ones in existing literature.

Except from Song, et al. (2014) and Yarborough, Haskin and Lambdin (1954) none of the mentioned authors have measured liquid suspensions but solid samples. It must be kept in mind that the temperature-dependent properties of a liquid phase have a potential influence on the measurements.

When a typical sample returns to 20 °C, the characteristic of its thermochromism is preserved in the spectrum, as Figure 2 shows. The 20 °C measurements already shown in Figure 1 are depicted with the spectra that are measured after the return to 20 °C. In this work, measurements of the second heating cycle are denoted with '_2'. In cases where the transmittance intensity increased due to heating, it remains and does not necessarily decrease during cooling. The peak shift of P.B. 15:1 recedes, but the areas off the peak only decrease slightly and remain on a level about two percentage points higher. P.Y. 129 at 400–500 nm loses even more transmittance intensity from 50 °C back to 20 °C and is clearly altered when it returns to 20 °C. Beside P.Y. 129, only P.V. 19(β) and 19(α) show a similar effect to some extent at 500 nm. Apart from such effects, the samples of this work are to be characterised as not fully reversible during their first heating and differ in this from the samples of other studies. Even after a rest period of three hours, the samples do not return to pre-first heating state.

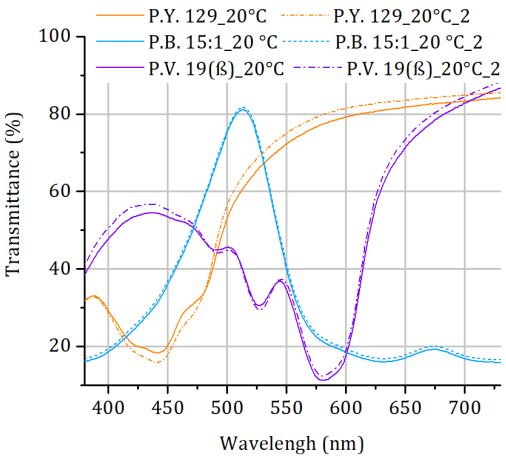

Figure 2: Transmittance spectra for three pigmented suspensions at 20 °C, before and after the first heating cycle

It could be shown that by heating up the samples initially, processes are initiated that affect the spectral characteristics. A subsequent second heating cycle leads to significantly different thermochromism, as Figure 3 illustrates. The visible spectral alterations are weakened. Unlike the first heating cycle, P.Y. 129 now shows an increased transmittance in areas of changing gradients. Again, one can observe a peak shift for the blue pigment, whereas violet no longer shows a shift at 550 nm. The spectra seem to follow the systematics of increased transmittance intensities and possibly slightly shifted peaks. Despite all the changes one can observe, the spectra at 50 °C are almost identical, regardless of whether they are measured during the first or second heating. P.V. 19(β) is among the samples heated up three times. Compared to the second cycle, both the 20 °C and 50 °C spectra of the third cycle are nearly identical to their temperature equivalent and do not indicate any other changes comparable to those determined for heating cycle one.

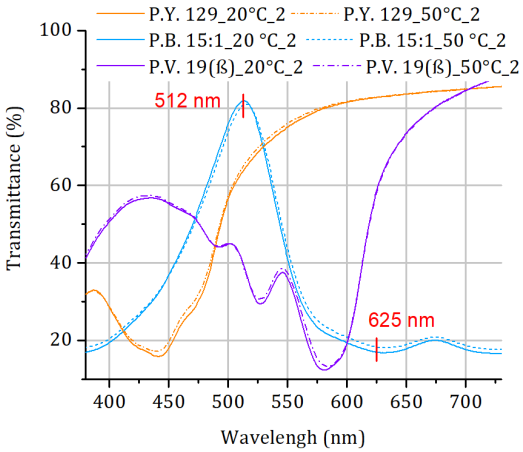

Figure 3: Transmittance spectra for three pigmented suspensions at 20 °C, second heating cycle

From this point on, the spectra reach a steady state and the thermochromism also appears to be completely reversible – as far it can be said for three measurement cycles. This reversibility is in accordance with results of other studies.

One conceivable explanation for the different results regarding reversibility in the heating cycles can be changes in absorption due to particle interactions. Agglomerations triggered by the first heating, for example, could change the particle size during the first phase. The viscosity changes due to heating can potentially facilitate these processes. However, particle interactions do not explain the opposed spectral effects for P.Y. 129 in the first cycle with decreasing (~ 430 nm) and increasing (~ 550 nm) wavelength areas. Considering that this behaviour is not observed in second heating phase, one can assume that structural changes occur in the pigment molecule during the initial heating.

3.2 Linearity

Other researchers described the linearity of thermochromism. The question whether the relationship between thermochromism intensities of the pigmented suspensions and temperature increases is linear or not can be answered by Figure 4. It shows the monochromatic transmittances for two wavelength intervals of P.B. 15:1 for seven temperatures from 20 °C to 50 °C. Depicted are the monochromaticities 512 nm and 625 nm in order to show a distinct peak as well as an area of high absorbance. The temperature-dependent rise reps. fall of the transmittance intensities shows a clear linear behaviour. Spectra from the second heating (cf. Figure 3) are used to check the linearity so that potential transformations during the first heating phase cannot falsify the outcome.

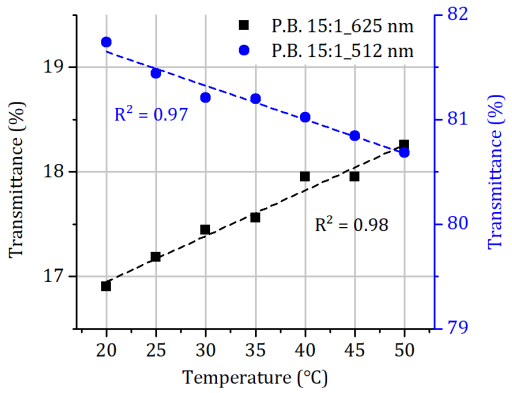

Figure 4: Transmittance intensities for PB 15:1 in wavelength intervals 512nm and 625 nm for seven temperatures, second heating cycle

3.3 Colourimetric

To give an impression of changes in colour characteristics, Figure 5 shows a polar chroma-hue plot of all 43 samples, again for 20 °C and 50 °C measurements (depicted as coloured resp. black bordered circles). The data pairs corresponding to the spectra depicted in Figures 1 to 3 are marked.

For the majority of samples, chromaticities decrease, recognisable by the fact that the circles tend towards the centre. Remarkable here as well are the shifts in hue, especially for blue and green shades. The hues become smaller, hence the shades move towards the yellow areas. The spectral anomalies characterised in Figure 1 are also reflected in the colourimetric coordinates, as one can see aberrations in the data set. This refers to data points that do not show decreasing but increasing chromaticity values due to temperature rise, for example data point 1 for P.Y. 129.

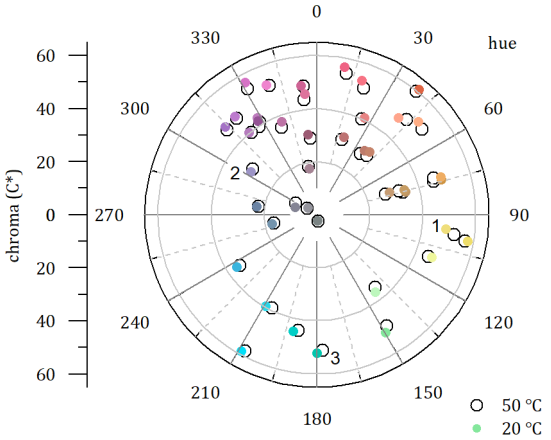

Figure 5: First heating cycle: Chroma (C) and hue values of 43 organic pigments for temperatures of 20 °C resp. 50 °C, P.Y. 129 (1), P.V. 19(β) (2) and P.B. 15:1 (3) are denoted*

Figure 6 shows a chroma-hue plot for the second heating cycle. The shifts in chroma and hue are consistent with those of Figure 1, except for the fact that the initial spectral changes during the first heating no longer occur in the second cycle. This is well illustrated by data point 1 that shows decreased chromaticities and is in line with the majority of the data. The magnitude of chroma loss tends to be smaller for colours with rather low initial chroma values than the loss of colours of high chromaticities. Other researchers found that green and especially blue have low thermochromism compared to red and orange tones. This observation also applies to our examination, considering only ΔE_{00} values. But if one looks at the spectral characteristics and also the chroma and hue indicators, this rule does not hold. The magnitude of the percentage

spectral changes is quite similar for different wavelength intervals. But for pure reds, for example, these spectral changes add up to larger ΔE_{00} values due to their long edge and low absorptions in the red range and suggests a hue dependency.

In order to sum up the findings, colour distance ΔE_{00}, differences in lightness ΔL^*_{ab}, chromaticity ΔC^*_{ab} and hue Δh_{ab} values are provided in Table 4. For the pigmented suspensions, ΔE_{00} values >1 are observed.

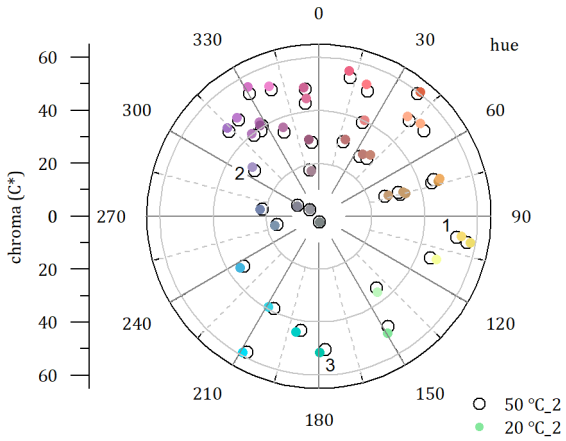

Figure 6: Second heating cycle: Chroma (C) and hue values of 43 organic pigments for temperatures of 20°C resp. 50 °C, P.Y. 129 (1), P.V. 19(β) (2) and P.B. 15:1 (3) are denoted*

Table 4: Colourimetric results: ΔE_{00}, ΔL^*_{ab}, ΔC^*_{ab} Δh_{ab} are given as arithmetic mean $\bar{x}$ and 90th percentile, related to measurements at 20°C and 50 °C ($\Delta T_{30°C}$) and two heating and measurement cycles

	First heating cycle ($\Delta T_{30°C}$)				Second heating cycle ($\Delta T_{30°C}$)			
	ΔE_{00}	ΔL^*_{ab}	ΔC^*_{ab}	Δh_{ab}	ΔE_{00}	ΔL^*_{ab}	ΔC^*_{ab}	Δh_{ab}
$\bar{x}$	1.05	0.72	1.35	1.36	0.95	0.64	1.37	1.00
$p = 0.9$	1.56	1.29	2.34	3.10	1.35	1.08	2.27	2.25

4. Conclusions

All pigment suspensions show temperature-dependent thermochromic effects whose linearity is in line with other researchers' findings. The spectral changes indicate alterations at the structural level between the first and subsequent heating cycles for three of the pigments. Apart from these phenomena, all samples aren´t reversible for the first measurement while there is reversibility for the subsequent measurements. This is either related to structural changes that affect all pigments or, more likely, to particle interactions triggered by the initial heating that lead to changes in absorbance strength. However, the study shows that even 'non-thermochromic' organic pigments show thermochromic behaviour, at least as liquid suspensions. Next steps in the thermochromism project are the use of further binders to put the absorption studies on a broader basis. In addition, the inks generated are to be applied and measured in order to investigate thermochromism in solid phase as well. In this work, thermochromism was measured at magnitudes well above 1 ΔE_{00}. If this is confirmed for printed samples, and the results of other studies suggest that it probably will be, thermochromism is a parameter that should be considered in temperature-variable production processes. Production tolerances of 2 ΔE_{00} are realistic for demanding print productions with inline colour measurement. A deviation from 1 ΔE_{00} merely due to temperature differences should not be ignored against this background.

Acknowledgements

The author would like to thank Shuhuai Wu for his active support in sample preparation and measurement. Thanks also to the companies Robert Kraemer GmbH & Co. KG and BYK-Chemie GmbH for their kind support with binders and additives.

References

Bamfield, P.,2001. *Chromic phenomena: the technological applications of colour chemistry*. Cambridge: Royal Society of Chemistry.

Che, J., 2018. Relative analysis of the dependency of spectrophotometric data on temperature using textiles, ceramics, plastics, paints, and printed materials. *Color Research and Application*, 43(6), pp. 922–927. https://doi.org/10.1002/col.22281.

Che, J., Li, R. and Senanayake, M., 2016. A comparative study of the dependency of colour measurement on surface temperature. *Coloration Technology*, 132(2), pp. 144–152. https://doi.org/10.1111/cote.12202.

Che, J. and Senanayake, M., 2017. A statistical analysis for correlation approach to compensate the measured CIELAB colorimetric data for temperature alterations. *Color Research and Application*, 42(6), pp. 726–739. https://doi.org/10.1002/col.22141.

Compton, J.A., 1984. The thermochromic properties of the ceramic colour standards. *Color Research and Application,* 9(1), pp. 15–22. https://doi.org/10.1002/col.5080090104.

Fairchild, M.D. and Grum, F., 1985. Thermochromism of ceramic reference tiles. *Applied Optics*, 24(21), pp. 3432–3433. https://doi.org/10.1364/AO.24.003432.

Griffiths, J., 1976. *Colour and constitution of organic molecules*. London: Academic Press.

Hiltunen, J., Silfsten, P., Jaaskelainen, T. and Parkkinen, J.P.S., 2002. A qualitative description of thermochromism in color measurements. *Color Research and Application*, 27(4), pp. 271–275. https://doi.org/10.1002/col.10062.

Hunger, K. and Schmidt, M.U., 2018. *Industrial organic pigments: production, crystal structures, properties, applications*. 4th ed. Weinheim: Wiley-VCH Verlag.

Malkin, F., Larkin, J.A., Verrill, J.F. and Wardman, R.H., 1997. The BCRA–NPL Ceramic Colour Standards, Series II – Master spectral reflectance and thermochromism data. *Journal of the Society of Dyers and* Colourists, 113(3), pp. 84–94. https://doi.org/10.1111/j.1478-4408.1997.tb01873.x.

Piening, H., 2006. *Mobile UV-VIS-Absorptionsspektroskopie: Einsatzmöglichkeiten zur zerstörungsfreien Materialanalytik in der Konservierung und Restaurierung von Kunst- und Kulturgut.* Dr. dissertation. Hochschule für Bildende Künste Dresden.

Song, W., Sun, C., Yin, W. and Men, Z., 2014. Influence of temperature on the vibration and electron absorption spectra of all-trans-β-carotene. *Optik*, 125(20), pp. 6131–6135. https://doi.org/10.1016/j.ijleo.2014.06.145.

Stierstadt, K., 2020. *Temperatur und Wärme – was ist das wirklich?: Ein Überblick über die Definitionen in der Thermodynamik*. Wiesbaden: Springer Fachmedien Wiesbaden.

Verrill, J.F., Compton, J.A. and Malkin, F., 1986. Thermochromism of ceramic color standards. *Applied Optics*, 25(18), p. 3011. https://doi.org/10.1364/AO.25.003011.

Yarborough, V.A., Haskin, J.F. and Lambdin, W.J., 1954. 'Temperature dependence of absorbance in ultraviolet spectra of organic molecules. *Analytical Chemistry*, 26(10), pp. 1576–1578. https://doi.org/10.1021/ac60094a012.

DOI 10.14622/Advances_49_2023_01

The fate of synthetic polymers – an analysis on the future of plastic waste

Volker Jansen

Hochschule der Medien, Stuttgart
E-mail: jansen@hdm-stuttgart.de

Short abstract

Synthetic polymers have been indispensable since the 1950s and have long been under scrutiny from an environmental perspective. However, there is a lack of reliable global information, especially on the fate of plastics at the end of their life. By identifying and aggregating scattered data on the production, use and disposal of polymer resins, synthetic fibres and additives, the first global analysis of all plastics ever produced was conducted in 2017 by Geyer, Jambeck and Lavender Law. It is estimated that between 7.3 and 8 billion tons of plastics have been produced to date. Disposal, however, remains problematic. Different studies speak of a global recycling rate of mere 9 %. This paper examines the amounts of waste, the amounts of plastic added to the different recycling methods. After a short review of polymer history this paper analysis global waste management systems, waste treatment in compliance with production data, life cycles of synthetic polymers and raises pressing questions for the future.

Keywords: plastic waste management, live-cycle of synthetic polymers, recycling, primary plastics, secondary plastics, micro plastics

1. Introduction and background

1933 Polyethylene was created in England by *Imperial Chemical Industries* for ICI in short. At that time, the chemical structure was a well-kept secret, as it was used to insulate radar cables (Britannica, 2022). World War II demanded a fast development of the plastics industry and made new products a requirement. The invention of polyethylene was followed by polymers like polystyrene (PS) and nylon, which DuPont released in 1939. It was readily used for military products such as parachutes and ropes. Polymers were increasingly used during the war for the production of weapons and numerous auxiliaries to support the war machine. In a Time magazine article, it was noted that because of the war, 'plastics have been turned to new uses and the adaptability of plastics demonstrated all over again' (Nicholson and Leighton, 1942).

During the 1950s then plastic manufactures turned to making consumer and packaging products. High Density Polyethylene or HDPE for short was already developed during the 1940s, however with inconstant results (Science History Institute, 2022). The production methods improved during the early 1950s, which led to the Hula Hoop craze when HDPE was introduced to a greater amount and the plastic version of the Hula Hoop became popular in 1958 when the Wham-O toy company introduced it to the market (Holmes, 2022).

In 1965 polysulfones, a family of thermoplastics were introduced for technical applications. The wide working temperature range of −100 °C to 200 °C, that allows polysulfone to go from a deep freezer directly to a steam table or microwave oven. This was the time when plastic debris in the oceans was first observed, a decade in which Americans and Europeans became increasingly aware of environmental problems.

The reputation of polymers fell in the 1970s and 1980s as anxiety about waste increased. The United States used to be dangerously polluted. Before 1970 the environment and its well-being were not a federal pri-

ority and in 1970 President Richard Nixon inaugurated the Environmental Protection Agency to promote environmental protection and waste management.

Eventually, during the 1980s and 1990s the first 'bioplastics' were developed to respond to the growing concerns of environmental conversation (Spierling, et al., 2019). Research continued and bioplastics as a class have resurged in production, however to a small degree, which is due to the specific properties, which limit their use.

Supermarket plastic bags quickly developed into a target for activists looking to ban one-use, disposable plastic sacks, and many cities in the US passed bag bans (Science History Institute, 2022). At the turn of the century the ultimate symbol of the problem of plastic waste was the Great Pacific Garbage Patch, which has often been described as a swirl of plastic garbage the size of Texas floating in the Pacific Ocean.

Today, major concerns focus on additives such as bisphenol in BPA for short. This is a class of chemicals which belongs to the group of phthalates. These compounds make the polymer products more flexible, durable and transparent (Muñoz Meneses, et al., 2022). Phthalates pose a risk especially to the health of children. Despite rising concerns plastics and their components have long become an indispensable material in our lives.

Despite growing mistrust, plastics are critical to modern life, and today plastics have outgrown most man-made materials. They are regularly used to a great amount in packaging, construction, for computers and smart phones, in machines and for consumer products, just to name the most important applications.

The majority of synthetic monomers used to make polyethylene, propylene, polystyrene, and other plastics are derived from fossil hydrocarbons. None of the commonly used plastics are biodegradable. As a result, they accumulate, rather than decompose, in landfills or the natural environment. There is now an estimated 30 million tons of plastic waste in seas and oceans, and a further 109 million tons has accumulated in rivers. 'The build-up of plastics in rivers implies that leakage into the ocean will continue for decades to come, even if mismanaged plastic waste could be significantly reduced' (OECD, 2022). According to the OECD (2022) the world is producing twice as much plastic waste as two decades ago, with the bulk of it ending up in landfill and incinerated, which mean converted into CO_2, or leaking into the environment. On a global scale only 9 % are reported to be recycled for reuse. Contamination of freshwater systems and terrestrial habitats is also increasingly reported. Consequently, contamination of the natural environment with near permanent plastic waste is a growing concern, which include synthetic polymers, additives such as plasticizers and synthetic fibres. According to Geyer, Jambeck and Lavender Law (2017) 'Plasticizers, fillers, and flame retardants account for about three quarters of all additives. The largest groups in total non-fibre plastics production are PE (36 %), PP (21 %), and PVC (12 %), followed by PET, PUR, PS and PA (< 10 % each)'. It is assumed that these seven polymer groups account for 92 % of all plastics ever made, whereas polyester, most of which is PET, accounts for 70 % of all synthetic fibre production. Approximately 42 % of all non-fibre plastics have been used for packaging, which is predominantly composed of PE, PP, and PET. The building and construction sector, which has used 69 % of all PVC, is the next largest consuming sector, using 19 % of all non-fibre plastics (2017).

When synthetic polymers and fibres are not biodegradable, the question of the fate of discarded plastic products arises, which includes the consideration of appropriate recycling or downcycling methods and energy recovery. The following paper examines the current fate of polymer waste and its treatment based on an analysis of available data.

2. Materials and methods (methodology)

Most information on the global fate of plastics at the end of their life cycle is unreliable. The search for reliable data and the analysis of such data is the core element of the methodological approach introduced for this research project. Many of the sources found on the internet or in the literature are ambivalent and do not provide the required information about the origin of the data used. The results presented in this paper are based on data-driven information from various official sources and research projects that can present and identify the source situation. Hence, only data that indicate a reliable source situation are used. Incomplete or ambivalent sources are excluded from this paper.

Major data for the end of use management in Europe and the United States has been obtained by the OECD and from several research related environmental projects (ReportLinker, 2022). Some of the data on waste management for the rest of the world is based on data from the World Bank, as this source is a reliable data basis. Detailed and comprehensive solid waste management data for the United States were obtained from the U.S. Environmental Protection Agency (EPA, 2014). European data were retrieved from several reports by PlasticsEurope (2008; 2016), which collectively cover 1996 to 2014. Chinese data were synthesized and reconciled from the English version of the China Statistical Yearbook (2021), translations of Chinese publications and government reports, and additional waste management literature. As recommended by Hoornweg and Bhada-Tata (2012) statistics on waste management for the rest of the world is based on figures released by the World Bank.

Concerning independent projects on the topic, the work of Geyer, Jambeck and Lavender Law (2017) provide a well-researched foundation for further analysis of the subject. They have examined the fate of plastics and presented a paper in Science Advance to shed light on the data of production, use and end-of-life management. In 2017 Geyer, Jambeck and Lavender Law developed the first global analysis of all mass-produce plastics ever manufactured. According to them, when including additives, which are used for the production of polymers, the amount of non-fibre plastics manufactured since 1950 increased to 7.3 billion tons. Synthetic fibres add another billion tons.

3. Results and discussion

Here we may raise the question of the lifetime of plastic products. According to Geyer, Jambeck and Lavender Law (2017) most of the plastics used for packaging and flexible films leave use the same year they are produced (Figure 1). However, construction plastics are employed for decades, and were manufactured when production quantities were much lower. It is estimated that 30 % of all plastics ever produced are still in use.

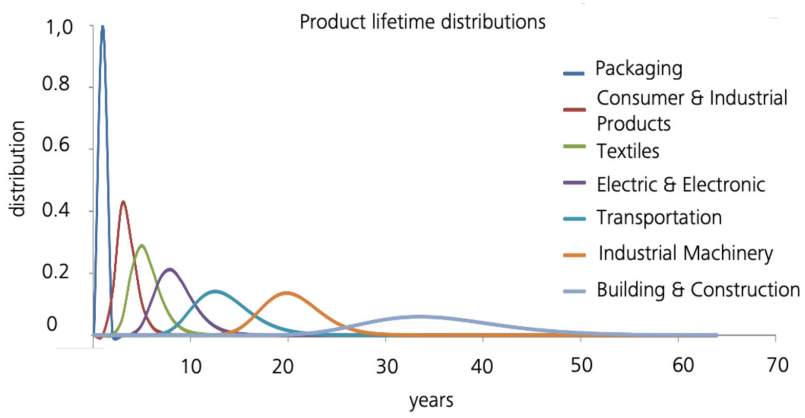

Figure 1: The lifetime of plastics in years (Geyer, Jambeck and Lavender Law, 2017)

Research suggests (Figure 2) that for example, in 2015, 42 % of primary non-fibre plastics produced (1.46 billion tons) entered use as packaging and 19 % (65 million tons) as construction, whereas non-fibre plastic waste leaving use was 54 % packaging (1.41 billion tons) and only 5 % construction (12 million tons). Similarly, in 2015, PVC accounted for 11 % of non-fibre plastics production (38 million tons) and only 6 % of non-fibre plastic waste generation (16 million tons) (Geyer, Jambeck and Lavender Law, 2017).

In 2015, 407 million tons of primary plastics entered the use phase, whereas 302 million tons left it. Geyer, Jambeck and Lavender Law (2017) concluded 'that plastic waste generation in 2010 was 274 million tons, which was 10 % less than in 2017'. If we conservatively assume a linear rather than a (probably more realistic) dynamic growth, we determine for the year 2020 a plastic waste generation of 330 million tons, this is 10 % higher than in 2015 and about 20 % higher than in 2007.

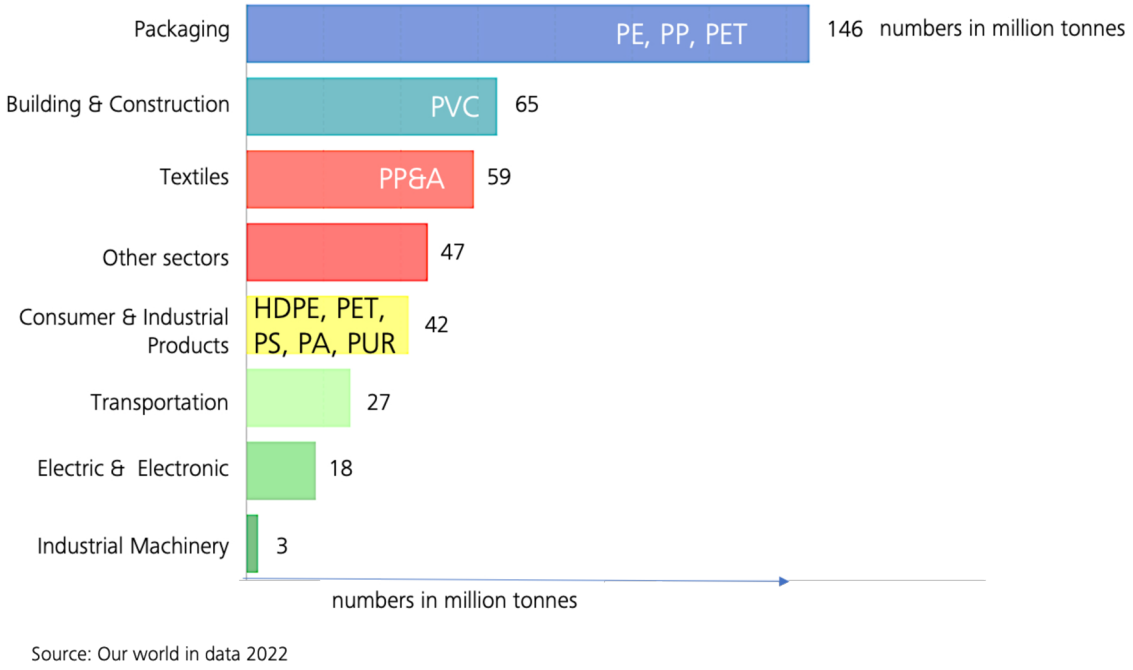

Figure 2: Primary plastic production by industrial sector (Our World in Data, 2022)

By the end of 2015 all plastic waste generated reached 5.8 billion tons of which 700 million tons were polyester, polyamide, and acrylic fibres, in PP&A for short (OECD, 2022).

Annual production of approximately 400 million tonnes of non-fibre plastics (Figure 3), of which 55 % is discarded, according to Ritchie and Roser (2022), has amounted to 7.3 billion tonnes of discarded plastics by end of December 2022 since the 1950s. If we include PP&A fibres the total amount of plastic waste will reach approx. 8.3 billion tons since 1950 of which 4.6 billion tonnes were discarded. Discarded means that the waste is not recycled, reused or incinerated; non-recycled discard includes waste that goes to closed or open landfill, littered, or lost to the environment.

According to the OECD (2022) 'global plastic waste set to almost triple by 2060'. Consequently, in 2060 humans would produce 660 million tons of plastic waste per annum compared to the roughly 400 million tons produced in 2022. If we consider this increase and assume that in 2022 220 million tons of plastic were discarded (55 %) that would lead to 330 million tons of global discarded non-fibre plastic in 2060 if waste management does not change and no drastic measures are taken to implement new methods of recycling, reuse or avoidance.

Barrett, et al. (2020) asserts that it is quite difficult to estimate and measure the amounts of microplastics entering the environment. Assumptions of the amounts of microplastics released and formed are uncertain due to the undefined sources and a lack of standards for sampling and measurement. All the same Boucher and Friot (2020) suggest in a paper titled *Primary Microplastics in the Ocean*, published by IUCN in Switzerland in 2020, that at any rate 14 million tons of microplastics have accumulated on the world's ocean floor so far and that an additional (approximately) 1.5 million tons enter the oceans annually. The release of microplastics occurs throughout the whole plastics value chain, during production, transport and use, and most importantly at the end of product life.

Microplastics can be divided into two major types, depending on the formation processes involved: primary and secondary microplastics. Primary microplastics are directly released into the environment as plastic particles, whereby secondary microplastics are formed from the breakdown of larger plastic items in the environment (EEA, 2022). Once a plastic item has a size of less than 5 mm, it is defined as microplastic (GESAMP, 2015). Due to their small but also microscopic size, microplastics are readily ingested by a wide range of marine organisms (Wright, Thompson and Galloway, 2013) and can have negative impacts on the health of marine life (Teuten, et al., 2009). 'Given the long residence time of such sequestered particles relative to the lifetime of the organism, even slow chemical release may cause low but chronic delivery within the animal' (GESAMP, 2015).

A number of national and international regulations (such as REACH) seek to identify and limit even small amounts of plastics that contribute to the problem of microplastic accumulation in the world's oceans. A good example is the focus on synthetic binders in printing inks, coatings and tie layers. The meaningfulness of these regulations is often questioned, as there is no globally binding enactment for the prevention of plastic waste entering the oceans. The European Chemicals Industry or ECHA (2023) for short recently launched their latest proposal concerning the formation of microplastics. They state that microplastics created by synthetic binders in printing ink, coatings and barrier layers cause considerable administrative burden, as for end-of-life purposes information must be provided concerning the identity of possible polymers used in inks, paints and coatings to give an estimate of the environmental impact. According to Verband der deutschen Lack- und Druckfarbenindustrie e.V. or Verband in short (Rommert, 2023) there is 'the possibility for enforcement authorities to request further information' regarding the nature of polymers used in inks and coatings. The Verband informs in their press release 4/2023 'Microplastics: Paints, coating and printing ink under pressure': 'In addition, the [enactment] provides for labelling obligation to prevent releases of microplastics into the environment. Entry into force of the restriction under REACH is planned for 2023'. Issued under the European chemical legislation REACH, the EU Commission's proposal follows the ECHA's findings 'that microplastics pose a risk to the environment that is not adequately controlled' (REACH, 2023). The aim of the new restriction is to reduce the microplastics released into the environment by printing inks and coatings by 0.2 to 0.6 per cent (Rommert, 2023). According to the Verband 'This is neither effective nor proportionate'. The definition of microplastics in REACH (2023) on which the proposed restriction is based is 'too broad'. In its definition it refers to most polymer-containing substances and mixtures (e.g. binding agents in paints, varnishes and printing inks). However, it is claimed by the Rommert (2023) that many of the polymeric binders used in paints, inks and coatings do not enter the environment as microplastics. It is assumed that the proportion entering the oceans will be negligible compared to the amount of microplastics formed annually. The layer thicknesses of printing inks and coatings (1 to 10 micrometers) are many times smaller than those of plastic containers (20 to 500 micrometers and even thicker materials). It should be noted that the additives used in plastics have more relevance when it comes to microplastics than the synthetic binders used in printing inks. In order to fulfil the new reporting obligations, the German paints, coatings and printing ink industry claims to have extra costs of 6 million euros per annum (Rommert, 2023).

Turning to another aspect, Geyer, Jambeck and Lavender Law (2017) compiled statistics from resin, fibres, and synthetic polymer additives from a number of industry sources and combined them according to type and sector. On average they found that non-fibre plastic contains 93 % polymer resin and 7 % additives by mass. If additives are included in the calculation, the amount of non-fibre plastics produced since 1950 increases from 7.3 to 7.8 billion tonnes in 2022. The scientists claim that 'Plasticizers, fillers, and flame retardants account for [roughly] three quarters of all additives.' (Geyer, Jambeck and Lavender Law, 2017).

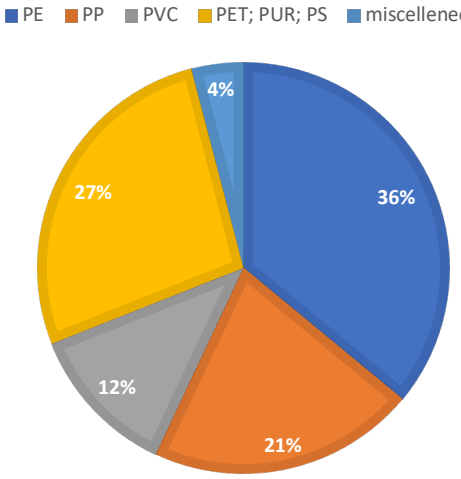

Figure 3: Major polymer types according to occurrence

They assert that 'before 1980 plastic recycling and incineration were negligible. On the basis of limited available data, the highest recycling rates in 2014 were in Europe (30 %) and China (25 %), whereas in the United States, plastic recycling has remained steady at 9 % since 2012'. According to a study by the OECD (2022) globally only 9 % of plastics waste is recycled, while 22 % mismanaged, 49 % ends up in landfills, and 19 % is incinerated.

The mismanaged plastic waste is highest in the Middle East and Africa. The OECD (2022) suggests that 64 % of plastic waste in Africa is mismanaged, which means littered or lost in the environment, whereas 30 % ends up in landfills. Recycling and incineration are negligible in Africa. In the Middle East 40 % of the plastic waste is mismanaged and 54 % ends up in landfills. The lowest figures of mismanaged waste is true for the EU and OECD Asia.

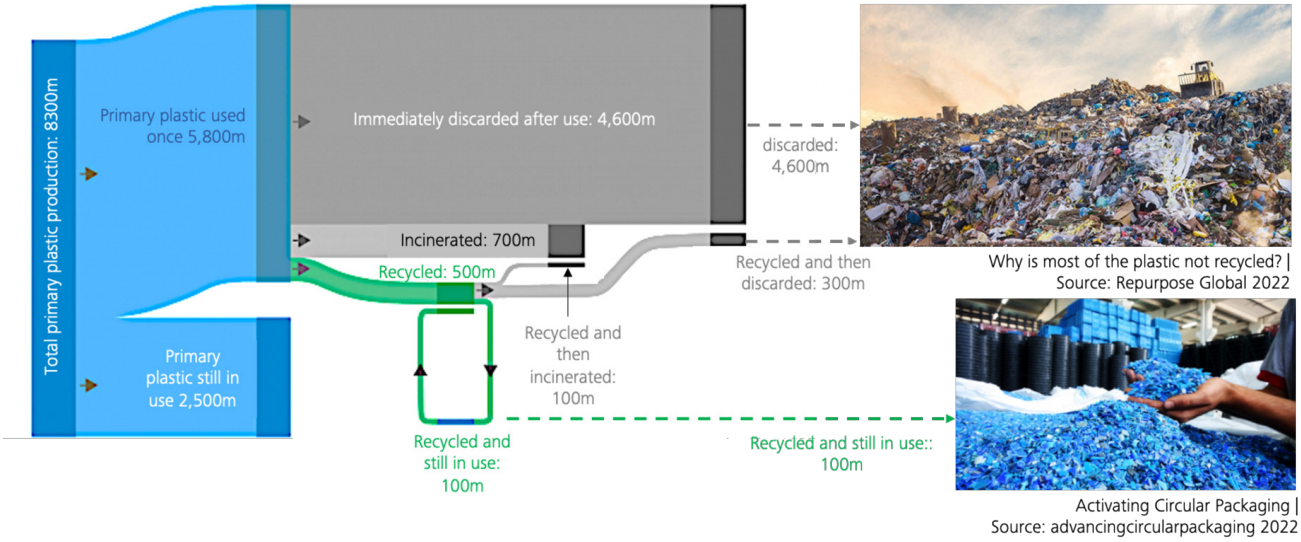

Figure 4: Production, use, and fate of all plastics ever made (Geyer, Jambeck and Lavender Law, 2022)

Most plastics in use today are primary plastics, made from crude oil or gas. Global production of plastics from recycled – or secondary – plastics has more than quadrupled, however, compared to discarded waste the recycling rate is still on a low level (Figure 4). According to the OECD (2022) the 'world community needs to create a separate and well-functioning market for recycled plastics, which are still viewed as substitutes for primary plastic'. They suggest that 'setting recycled content targets and investing in improved recycling technologies could help to make secondary markets more competitive and profitable' (OECD, 2022). However, the low costs for crude oil and the high investment and operations costs for sustainable recycling methods, which require an expensive system of curb side collection and waste management stand against each other, which brings us to the question of which methods underlie the recycling of plastics (Ceurstemont, 2020).

The industry distinguishes between primary recycling, which describes a closed-loop circle of pre-consumer plastic scrap, which is recovered via mechanical recycling or physical processing, and secondary recycling, which comprises a downgrading of post-consumer, post-commercial plastic waste. Secondary recycling comprises mechanical recycling processes and physical reprocessing. However, the quality of the resulting product is lower than with primary recycling due to the contamination of packaging.

For primary and secondary recycling every item must be collected, sorted, directed into defined streams or reclaimed. Collection is the first step of a multi-step procedure leading to downcycling, reuse, or disposal of flexible plastic packaging waste.

Residual postconsumer flexible plastic packaging shows the lowest recycling rates due to inefficient sorting technologies. Multilayer packaging is the most problematic material and can hardly be targeted by collection schemes. It is not currently recycled, 97 % of all post-consumer plastic films are incinerated or end up in landfills and oceans. The reason is that multilayer materials sport different barrier, carrier and tie layers of chemically different materials (Figure 5).

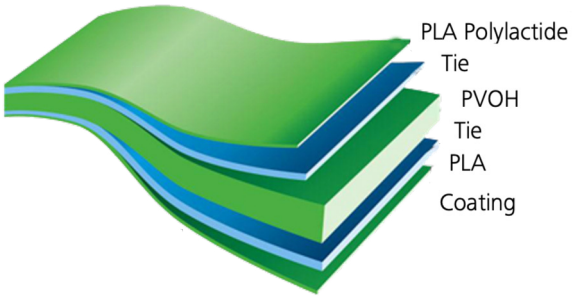

Figure 5: Multilayer film for Cheese or fresh pasta packaging (BIO4MAP, 2016)

Even if the film material is of single origin, for instance polyethylene, the recycling of film and flexible packaging still presents specific challenges and difficulties. According to Enrico Siewert, director at Stadler (2022) 'the first challenge is the low bulk density of these materials […]. [Plastic films and foils] tend to move around on a sorting plant's conveyors and wrap themselves around the bearings of the shafts, affecting the equipment's performance and maintenance. Also, these materials are susceptible to trapping moisture, they tend to crumple locking in the moisture, and it takes a lot of energy to clean them'.

Hence, flexible plastic packaging result in a disappointingly low recycling rate due to inefficient sorting technologies and the high percentage of multi-layer materials. For flexible packaging chemical or tertiary recycling seems a likely option.

Tertiary or chemical recycling (Figure 6) encompasses a depolymerization processes, hence referred to 'feedstock recycling' (Ceguide, 2022). It seems an attractive option for plastic products that are difficult

to recycle mechanically due to low quality, composite nature or low economic value. The monomers can be used as primary material alternatives in manufacturing new polymers. The syncrude generated via depolymerisation, however, is incidentally more costly than natural crude oil, which makes a widespread introduction of tertiary recycling less attractive. Consequently, tertiary recycling remains a small market. It can be achieved by pyrolysis, gasification and hydrogenation.

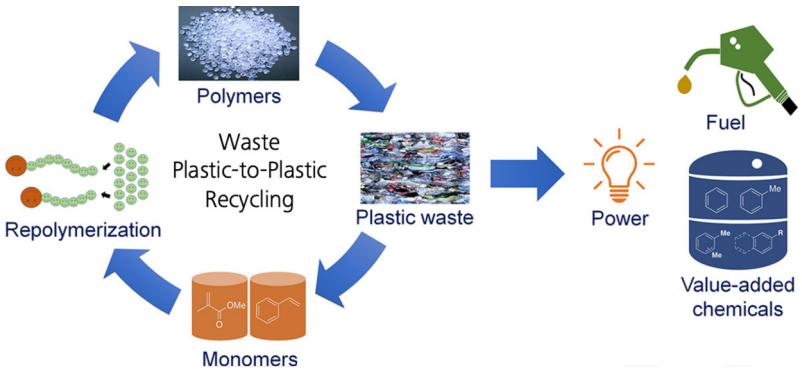

Figure 6: Thermochemical recycling of waste plastics by pyrolysis (Soni, et al., 2021)

The recycling methods discussed lead us to the question of renewable feedstocks of biological origin such as biomass, by-products derived from sustainable materials. Biological recycling involves the decomposition, physical fragmentation of an end-of-life product. The combination of moisture, temperature, mechanical action and microbial activity is responsible for the disintegration process.

According to European Bioplastics (2017) the current share of biodegradable plastics in the total plastic waste designed for organic recycling sold in the EU is comparatively small. The detected biodegradable plastic material is the waste stream is not higher than 0.3 %, that makes biological recycling less likely to become financially viable on an industrial scale (McDonald, 2019). However, we must not forget that the level of biodegradability is currently discussed and the available options are questionable concerning their biodegradability as they end up as micro plastics polluting the soil.

As primary and secondary recycling methods involve sorting, separating and classifying waste, which incurs high costs, a very common method is quaternary recycling, which is not recycling in the true sense of the word, as it involves energy recovery or mostly pure incineration with CO_2 emissions. According to the OECD (2022) the highest incineration rates are in OECD Asia and accounts for 72 % of the plastic waste. Good examples for countries who have widely introduced quaternary recycling are Singapore and Taiwan. In the EU 44 % of the entire plastic waste is incinerated whereas in the US only 19 % are burnt. In China about 24 % of the total plastic waste are incinerated (OECD, 2022) in comparison to 27 % of the waste, which is still unmanaged and littered. Quaternary recycling is mostly negligible in South America and Africa, the percentage of incinerated plastic waste ranges between 1 % and 5 % (OECD, 2022).

4. Conclusions

Due to the unavailability of reliable data for the period between 1950 to 2010, we can only reliably estimate global recycling rates from the last decade. According to PlasticsEurope (2016) the highest recycling rates in 2014 were in Europe (30 %) and as stated by the National Bureau of Statics of China (2021) in China (25 %). In the United States, plastic recycling has remained steady at 9 % since 2012. The reports suggest that in Europe and China incineration rates have increased over the last years. In the report, Annual Data, China Statistical Yearbook, 1996–2016 by the National Bureau of Statics of China (2021) the incineration was to reach 40 % and 30 %, respectively, in 2014. It is not clear whether these figures reliably base on the

entire production volume of plastics consumed in China. In any case, they differ significantly from the data obtained by the OECD (2022) (Figure 7).

The OECD has recorded much smaller recycling rates in China and Europe. Giving their findings in 2022 China has recycled only 13 % of its waste whereas 36 % of Chinas plastic waste ended up in landfills. For the United States figures for primary and secondary recycling of plastic waste ranges at 4 % in 2019 whereas OECD Europe is reported to recycle 8 % of and India 13 % of its plastic waste in 2022.

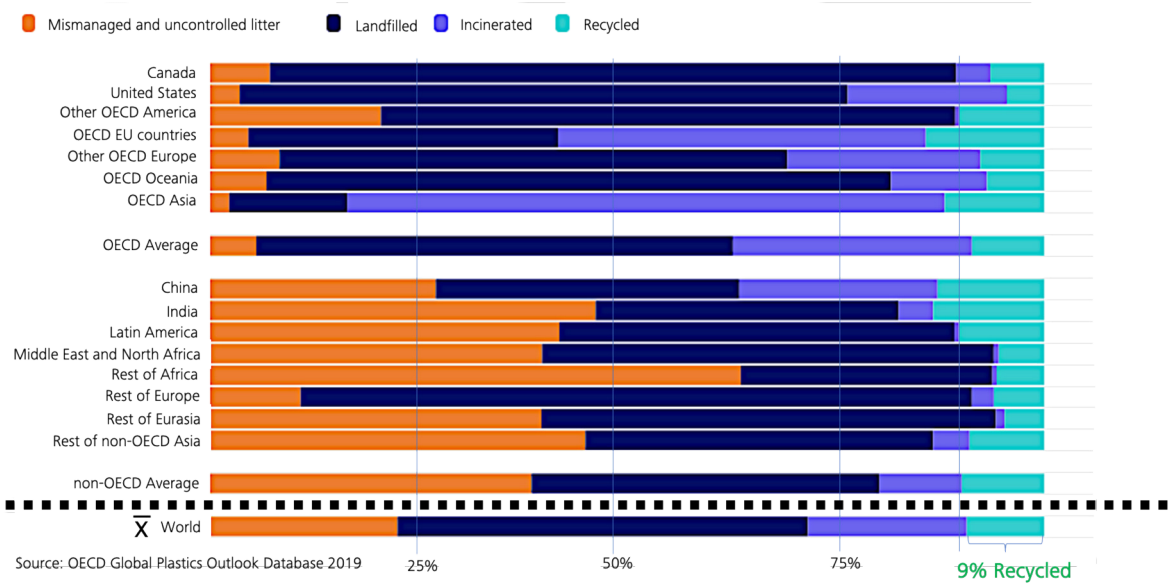

Figure 7: Wasted or recovered (graphic created in 2019) (OECD 2022)

Finally, it should not go unmentioned that since the 1990s the global recycling rate for non-fibres has increased 0.7 % per annum. Assuming that this (linear) trend continues, the global recycling rate would reach 44 % in 2050. With this assumption, the global discard rate would decrease from 58 % in 2014 to 6 % in 2050 (Geyer, Jambeck and Lavender Law, 2017).

Nevertheless, measured against global population growth and the steady increase in global prosperity, despite crises and wars, this is a rather sobering result. Also, there is currently no significant recycling of synthetic fibres (Geyer, Jambeck and Lavender Law, 2017). We can therefore assume that used textiles will continue to be incinerated and disposed of together with all other municipal solid waste in the future. If current trends in production and waste management continue, about 12 billion tons of plastic waste may end up in landfills or in the natural environment by 2050.

References

Barrett, J., Chase, Z., Zhang, J., Banaszak Holl, M.M., Willis, K., Williams, A., Hardesty, B.D. and Wilcox, C. 2020. Microplastic pollution in deep-sea sediment from the Great Australian Bight, *Frontiers in Maritime Science*, 7: 576170. https://doi.org/10.3389/fmars.2020.576170.

BIO4MAP, 2016. BIO4MAP develops sustainable food packaging to improve shelf life. *Food&Drink Business Europe* [blog] 15 August. Available at: < https://www.fdbusiness.com/bio4map-develops-sustainable-food-packaging-to-improve-shelf-life/> [Available November 2022].

Boucher, J. and Friot, D., 2020. *Primary microplastics in the ocean*. [pdf] IUCN, Gland, Switzerland. Available at: <https://holdnorgerent.no/wp-content/uploads/2020/03/IUCN-report-Primary-microplastics-in-the-oceans.pdf> [Accessed 3 November 2022].

Britannica, 2022. *Polyethylene*. [online] Encyclopedia Britannica. Available at: <https://www.britannica.com/science/polyethylene> [Accessed 28 October 2022].

Ceguide, 2022. *Feedstock recycling*. [online] Available at: <https://www.ceguide.org/Strategies-and-examples/Dispose/Feedstock-recycling> [Accessed 9 November 2022].

Ceurstemont, S., 2020. Bio-based? Recyclable? Biodegradable? Your guide to sustainable plastics. *Neste* [blog] 14 May. Available at: <https://journeytozerostories.neste.com/plastics/bio-based-recyclable-biodegradable-your-guide-sustainable-plastics?> [Accessed 10 November 2022].

ECHA, 2023. *Microplastics*. [online] Available at: <https://echa.europa.eu/hot-topics/microplastics> [Accessed 31 May 2023].

EEA, 2022. *Microplastics from textiles: towards a circular economy from textiles in Europe*. [online] European Environment Agency. Available at: <https://www.eea.europa.eu/publications/microplastics-from-textiles-towards-a> [Accessed 2 November 2022].

EPA, 2014. *Municipal solid waste generation, recycling, and disposal in the United States: tables and figures for 2012*. [pdf] U.S. Environmental Protection Agency. Available at: <https://www.epa.gov/sites/default7files/2015-09/documents/2012_msw_dat_tbls.pdf> [Accessed 5 November 2022].

European Bioplastics, 2017. *Biodegradable plastics needed to increase recycling efficiency*. [online] Available at: <https://www.european-bioplastics.org/biodegradable-plastics-needed-to-increase-recycling-efficiency/> [Accessed 11 November 2022].

GESAMP, 2015. *Sources, fate and effects of microplastics in the marine environment: a global assessment*. London: International Maritime Organization. https://doi.org/10.13140/RG.2.1.3803.7925.

Geyer, R., Jambeck, J.R. and Lavender Law, K., 2017. Production, use, and fate of all plastics ever made. *Science Advances,* 3(7): e1700782. https://doi.org/10.1126/sciadv.1700782.

Holmes, G.S., 2022. *Hula hoop*. [online] How products are made. Available at: <http://www.madehow.com/Volume-6/Hula-Hoop.html> [Accessed 23 October 2022].

Hoornweg, D. and Bhada-Tata, P., 2012. *What a waste: a global review of solid waste management*. [online] Washington, DC: World Bank, Urban Development Series: Knowledge Papers, no. 15. Available at: <https://openknowledge.worldbank.org/handle/10986/17388> [Accessed 11 November 2022].

McDonald, N., 2019. Biological recycling of biodegradable plastics. *BioCycle* [blog] 18 September. Available at: <https://www.biocycle.net/biological-recycling-biodegradable-plastics/> [Accessed 7 November 2022].

Muñoz Meneses, R.A., Cabrera-Papamija, G., Machuca-Martínez, F., Rodríguez, L.A., Diosa, J.E. and Mosquera-Vargas, E., 2022. Plastic recycling and their use as raw material for the synthesis of carbonaceous materials. *Heliyon*, 8(3): e09028. https://doi.org/10.1016/j.heliyon.2022.e09028.

National Bureau of Statics of China, 2021. *China Statistical Yearbook 1996–2016*. [online] Available at: <www.stats.gov.cn/ENGLISH/Statisticaldata/AnnualData/> [Accessed 11 November 2022].

Nicholson, J.L. and Leighton, G.R., 1942. Plastics come of age. *Harper's Magazine*, August 1942, p. 306.

OECD, 2022. *Plastic pollution is growing relentlessly as waste management and recycling fall short, says OECD*. [online] Available at: <https://www.oecd.org/environment/plastic-pollution-is-growing-relentlessly-as-waste-management-and-recycling-fall-short.htm> [Accessed 4 November 2022].

PlasticsEurope, 2008. *The compelling facts about plastics: an analysis of plastic production, demand and recovery for 2006 in Europe*. [pdf] PlasticsEurope. Available at: <https://plasticseurope.org/wp-content/uploads/2021/10/2006-Compelling-facts.pdf> [Accessed 10 November 2022].

PlasticsEurope, 2016. *Plastics – the facts 2016: an analysis of European plastics production, demand and waste data*. [pdf] PlasticsEurope. Available at: <https://plasticseurope.org/wp-content/uploads/2021/10/2016-Plastic-the-facts.pdf> [Accessed 10 November 2022].

REACH, 2023. REACH committee votes to restrict intentional microplastics. *European Commission* [blog] 27 April. Available at: <https://single-market-economy.ec.europa.eu/news/reach-committee-votes-restrict-intentional-microplastics-2023-04-27_en> [Accessed April 2023].

ReportLinker, 2022. *Plastic waste management global market report 2022*. [online] Available at: <https://www.reportlinker.com/p06319263/Plastic-Waste-Management-Global-Market-Report.html?utm_source=GNW> [Accessed 3 November 2022].

Ritchie, H. and Roser, M., 2022. *Plastic pollution*. [online] Our World in Data. Available at: <https://ourworldindata.org/plastic-pollution> [Accessed 3 November 2022].

Rommert, A., 2023. *Microplastics: paints, coatings and printing inks under pressure*. [pdf] Microplastics. Available at: <https://www.wirsindfarbe.de/fileadmin/user_upload/Dokumente/OnePager/2023/VdL-Onepager_Microplastics_2023.pdf> [Accessed 31 May 2023].

Science History Institute, 2022. *History and future of plastics*. [pdf] Philadelphia, PA: Science History Institute. Available at: <https://www.sciencehistory.org/sites/default/files/history-of-plastics.pdf> [Accessed 28 November 2022].

Soni, V.K., Singh, G., Vijayan, B.K., Chopra, A., Kapur, G.S. and Ramakumar, S.S.V., 2021. Thermical recycling of waste plastics by pyrolysis: a review. *Energy Fuels*, 35(16), pp. 12763–12808. https://doi.org/10.1021/acs.energyfuels.1c01292.

Spierling, S., Venkatachalam, V., Behnsen, H., Herrmann, C. and Endres, H.-J., 2019. Bioplastics and circular economy – performance indicators to identify optimal pathways. In: L. Schebek, C. Herrmann and F. Cerdas, eds. *Progress Life Cycle Assessment*. Cham, Switzerland: Springer Professional, pp. 147–154.

Stadler, 2022. Film and flexible packaging recycling. *Recycling Magazine*, 7 February 2022. [online] Available at: <https://www.recycling-magazine.com/2022/02/07/film-and-flexible-packaging-recycling/> [Accessed 9 November 2022].

Teuten, E.L., Saquing, J.M., Knappe, D.R.U., Barlaz, M.A., Jonsson, S., Björn, A., Rowland, S.J., Thompson, R.C., Galloway, T.S., Yamashita, R., Ochi, D., Watanuki, Y., Moore, C., Viet, P.H., Tana, T.S., Prudente, M., Boonyatumanond, R., Zakaria, M.P. Akkhavong, K., Ogata, Y., Hirai, H., Iwasa, S. Mizukawa, K., Hagino, Y., Imamura, A., Saha, M. and Takada, H., 2009. Transport and release of chemicals from plastics to the environment and to wildlife. *Philosophical Transactions of the Royal Society B: Biological Sciences*, 364(1526), pp. 2027–2045. https://doi.org/10.1098/rstb.2008.0284.

Wright, S.L., Thompson, R.C. and Galloway, T.S., 2013. The physical impacts of microplastics on marine organisms: a review. *Environmental Pollution,* 178, pp. 483–492. https://doi.org/10.1016/j.envpol.2013.02.031.

DOI 10.14622/Advances_49_2023_05

Organic solar cells with an inkjet printed P3HT:O-IDTBR layer based on a green solvent by utilizing a heatable printhead

Niklas Guhr and Holger Göbel

Department of Electronics, Helmut Schmidt University/University of the Federal Armed Forces,
Holstenhofweg 85, D-22043 Hamburg, Germany
E-mails: guhrn@hsu-hh.de; goebel@hsu-hh.de

Short abstract

In this study we present organic solar cells with an inkjet printed active layer based on a P3HT:OIDTBR bulk heterojunction with a PCE of 2.3 %. The green solvent 2-Methylanisol was used for the ink. The necessary steps for the creation of such cells are explained. The remaining problem of a significant sensitivity to UV radiation is studied. Steps for the improvement of photovoltaic parameters and lifetime of the solar cells are discussed.

Keywords: organic solar cells, inkjet printing, green solvent, UV induced degradation

1. Introduction and background

Organic photovoltaics are a research area that opens up many new fields of application compared to conventional solar cells. In particular they offer potential key features like transparency, flexibility and stretchability (Fukuda, Yu and Someya, 2020). A potential problem however might be that research is often focused on fabrication by spincoating. While this production method works well for lab-scale devices, reaching power conversion efficiencies (PCE) of up to 19 % (Cui, et al., 2021), it is inherently difficult to upscale for industrial applications. Consequently, it is crucial to explore alternative possibilities suitable for industrial production, primarily printing technologies.

In this work we use inkjet printing, which offers many advantages compared to other printing methods. While its throughput is lower than for example slot-die coating, the ability to freely create new patterns without the need for a mask makes it a potent contender for niche applications (Gertsen, et al., 2020).

Organic solar cells (OSCs) are built around a photoactive layer consisting of an acceptor and a donator polymer. In this study we used an inverted layout, which means that the substrate is serving as the cathode. This layout was shown to increase the lifetime and stability of the solar cells under ambient conditions (Hau, Yip and Jen, 2010).

We used an indium tin oxide (ITO) coated glass substrate as it is common in research and does not influence the studied active layer. OSCs require electron and hole transport layers to extract the charge carriers out of the active layer. In this study we used zinc oxide (ZnO) as the electron transport layer and molybdenum trioxide (MoO_3) as the hole transport layer. A schematic displaying the layers of our solar cell is shown in Figure 1.

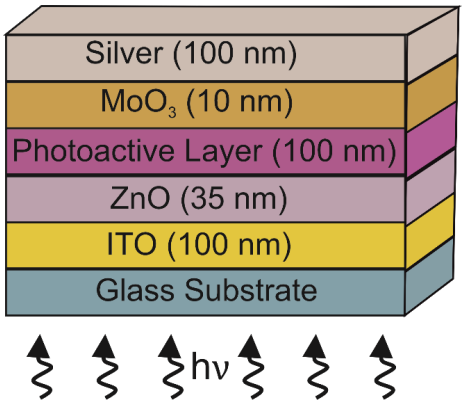

Figure 1: Schematic cross section of the used architecture for the studied solar cells

In the majority of OSCs the components of the active layer are intermingled to maximize the surface between the components, thus creating a bulk heterojunction solar cell. In recent years, new polymers were developed to increase the PCE with impressive results. The creation of nonfullerene acceptors (NFAs) significantly increased the PCE and stability of organic solar cells, since their absorption spectrum can be tailored to match with new highly efficient donators. However, from a commercial perspective, it would be preferable to combine specifically tailored NFAs with the well-researched donator poly(3-hexylthiophen-2,5-diyl) (P3HT) due to its low cost of production and high stability under ambient conditions (Li, McCulloch and Brabec, 2018). As such, for this work we used the NFA (5Z,5'Z)-5,5'-((7,7'-(4,4,9,9-tetraoctyl-4,9-dihydro-s-indaceno[1,2-b:5,6-b']dithiophene-2,7-diyl)bis(benzo[c][1,2,5]thiadiazole-7,4-diyl))bis(methanylylidene))bis(3-ethyl-2-thioxothiazolidin-4-one) commonly referred to as O-IDTBR because of its excellent stability and good synergy with P3HT (Holliday, et al., 2016).

Inkjet printing of OSCs based on P3HT was already demonstrated in the past, however mostly with toxic halogenated solvents (Hoth, et al., 2007). Even when the used solvents were halogen-free, they still had unwanted health effects like the narcotic properties of the often used o-xylene or toluene.

In this work we used an inkjet printer to fabricate a P3HT based OSC utilizing a truly green solvent, the food additive 2-Methylanisole (2-MA). While this solvent has successfully been used in other production methods like spincoating (An, Zhong an Ying, 2020), it has not yet been demonstrated to be compatible with inkjet printing. This is most likely due to the rapid clumping that occurs at low temperatures when in contact with even very small amounts of P3HT.

Thus, the aim of this study is to research the possibilities and difficulties of using 2-MA as the singular solvent for inkjet-printing of the active layer.

2. Materials and methods

2.1 Materials

Prepatterned ITO substrates (S211) were purchased from Ossila. ZnO was purchased in the form of a commercial ink (Helios'Ink H-SZ01034, semi conductive ink) from Sigma-Aldrich. These glasses have a transmittance of > 80 % for wavelengths between 400 nm and 750 nm. For wavelengths below 400 nm, the transmittance starts falling and is approximately 77 % at a wavelength of 350 nm. The active layer materials P3HT (molecular weight: 24 480, 93.6 % regioregularity) and O-IDTBR were acquired from Ossila. The 2-MA and silver pellets were ordered from SigmaAldrich. MoO_3 was purchased from Evochem.

2.2 Device fabrication

The ITO substrates were cleaned in acetone and isopropanol and then coated with 35 nm of the commonly used electron-injection layer zinc oxide, applied via inkjet printing of the commercial ink as received. For all the printing in this work a MD-P-826 printing system (one nozzle, printing speed 50 mm/s) from microdrop Technologies was used.

The active layer consisting of P3HT:O-IDTBR in a 1:1 weight ratio was prepared by dissolving each material in 2-Methylanisol. The concentration of P3HT was 4 mg/ml. The ink was heated to 85 °C and stirred overnight. Since the solution quickly hardened at room temperature the ink was kept printable by using a heatable printhead MD-K-801 (microdrop Technologies) with a heated storage container. High ink temperatures lead to a significantly reduced viscosity, which is unwanted since it causes the generation of satellite droplets. We used a printhead temperature of 85 °C as a compromise between viscosity and the risk of nozzle blocking. 2-MA proved well suited for this application because its viscosity (14.32 mPa·s at room temperature) is relatively high for a solvent, such preventing satellite droplets. The ink was printed in ambient atmosphere. Optimal substrate temperature during the printing process was determined to be 57 °C. In order to investigate the influence of the coating process on the characteristics of the OSCs, we produced additional samples by using a spincoater inside a glovebox to deposit the active layer. Those cells only serve as a reference and were not optimized in terms of electrical parameters.

For both production methods, the thickness of the active layer was approximately 100 nm. After both inkjet-printing and spincoating the samples were annealed for 5 minutes at 100 °C in vacuum. The back electrode consisting of a 10 nm MoO_3 and a 100 nm silver layer, was applied by physical vapor deposition.

The data of the cells with inkjet printed active layer is based on 5 ITO substrates with 8 solar cells produced on each substrate. Each cell had an active area of 4 mm^2. 7.5 % of the cells were unusable due to short circuits and thus are not included in the following discussion. 30 cells with spincoated active layers were used for comparison.

2.3 Measurements

For measuring the solar cell parameters a solar cell I-V test system (Ossila) in conjunction with a HAL-320 solar simulator, supplying an AM1.5G spectrum, was utilized. In this setup, an ultraviolet (UV) blocking PET film procured from Edmund Optics could be inserted, in order to investigate the UV sensitivity. It blocked wavelengths below 400 nm and its transmittance in the visible part of the spectrum was approximately 80 %. This reduction in light intensity was considered, when calculating the photovoltaic parameters PCE, J_{SC}, V_{OC} and *FF* based on the measured *J*-*V*-curves.

3. Results and discussion

By using the measurement setup described above, we determined PCEs of up to 3 % for the cells with inkjet printed active layer, which is a reasonable value for the used materials. However, most of the cells showed a massively reduced lifetime compared to the spincoated OSCs, when exposed to the light of the solar simulator. Further investigations revealed that placing a UV-filter in between solar simulator and solar cells prevented this effect, which indicates that wavelengths below 400 nm are the origin of the degradation.

To get a better understanding of the UV induced degradation of the inkjet printed cells we used the following procedure: First, a *J*-*V*-curve was measured, while the UV-filter was protecting the sample. Then the PCE was calculated and depicted in Figure 2 as M_0. Afterwards the UV filter was temporarily removed and

the sample exposed to UV light for 0.5 seconds. Now, a second *J-V*-curve was measured, while protecting the sample from UV by using the filter. Based on this measurement the PCE was calculated and plotted as $M_{0.5}$ in Figure 2. By removing the filter again for 0.5 seconds, the cumulated UV exposure was increased to 1 second, another *J-V*-curve was measured, and the result depicted as M_1. Following this procedure, measurements of up to 5 seconds of cumulated UV exposure were performed. These measurements were done for the printed cells as well as the spincoated cells, resulting in a plot of PCE vs. exposure time.

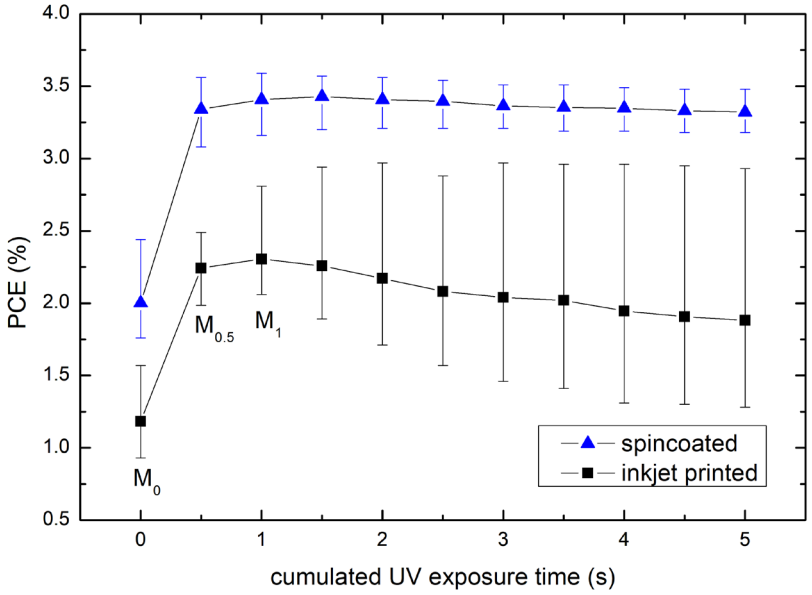

Figure 2: The average PCE of the inkjet printed and the spincoated solar cells versus cumulated UV exposure time; the error bars represent the maximal and minimal measured PCE

From Figure 2 it can be seen that for exposure times of up to approximately 1 second the PCE increases, a phenomenon well known as the light soaking effect (Kim, et al., 2012). This means that ZnO is dependent on regular exposure to UV radiation to maintain its functionality. Otherwise, a drastically reduced fill factor is observed. This effect is theorized to originate from the absorption of oxygen into the ZnO layer leading to a shift in the work function (Sundqvist, et al., 2016). Even short amounts of exposure to UV radiation leads to the ZnO adsorbing the oxygen and increasing the PCE of the cell.

The PCE of the cells with spincoated active layers remains almost constant for high UV exposure times. This behavior is expected, since the UV induced degradation of the cells usually happens on a larger time scale. For the inkjet printed cells however, the average PCE can be seen to quickly decrease. Since UV radiation is required to activate the ZnO, protecting the cells with a UV filter is not a viable option.

However, the upper ends of the error bars shown in Figure 2 reveal that it is possible to fabricate printed cells that do not show a significant degradation effect. This strongly suggests that it is possible to minimize efficiency losses by carefully optimizing the printing process.

The measured results are summarized in Table 1. Samples with a spincoated active layer showed an average PCE of 3.41 % after 1 second of exposure to UV radiation. It should be noted, that the used P3HT had a relatively low molecular weight to reduce aggregation and thus minimize the risk of nozzle clogging. However, Khan, et al. (2019) showed that a low molecular weight leads to a high loss of efficiency. As such the PCE of these unoptimized OSCs was expected to be lower than the efficiency of comparable cells in literature. The corresponding average PCE of the printed cells is 2.28 %, which is less than the PCE of the spincoated cells due to the different coating process.

Table 1: Averaged photovoltaic parameters of the inkjet-printed and spincoated OSCs after 1 second of UV exposure

Production method	PCE (%)	J_{SC} (mA/cm^2)	V_{OC} (V)	*FF* (%)
Inkjet printing	2.28	−5.44	0.69	48.07
Spincoating	3.41	−6.49	0.74	57.10

Additionally, it can also be seen from Figure 2 that it is possible to produce cells with an inkjet printed active layer able to achieve higher values of up to 3 % efficiency, while also minimizing degradation. To compare the photovoltaic parameters, averaged *J-V*-curves of the 4 best performing inkjet printed and the 5 best performing spincoated cells are shown in Figure 3. It can be seen that the V_{OC} and the J_{SC} of spincoated and inkjet printed cells are almost identical, indicating that these parameters will achieve high values for an optimized printing process. The current problems are likely occurring because only one line at a time can be printed with a singlenozzle system. This may result in drops drying separately instead of forming a homogeneous layer, which is highly relevant for the photovoltaic parameters and should be a focus of further research.

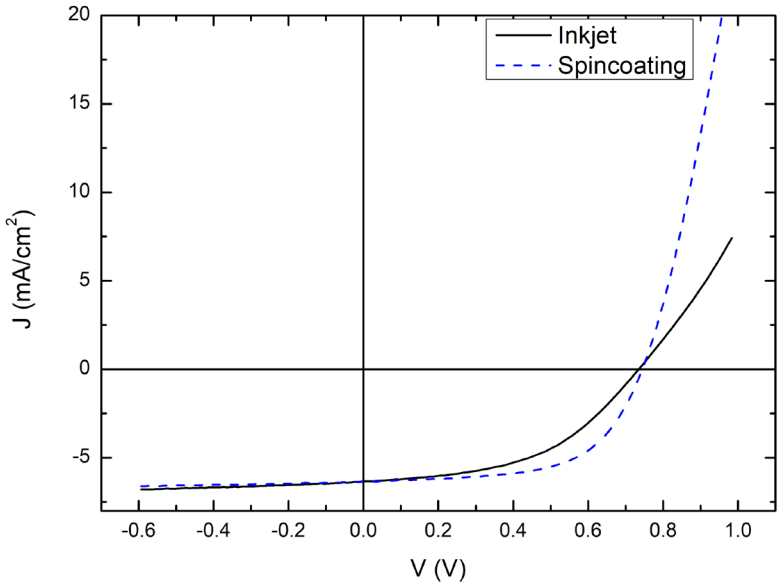

Figure 3: Averaged J-V-Curves of the 5 best performing devices for spincoated (dashed) and the 4 best performing devices for inkjet printed (solid) solar cells

4. Conclusions

We found that it is indeed possible to produce inkjet printed organic solar cells using a truly green solvent. The use of a printhead with a heatable storage bin and hose allowed us to print the 2-MA based ink without damaging the nozzle, producing cells of up to 3 % efficiency. However, the study revealed stability issues for the majority of our printed cells. While further research will be necessary to fully understand the problem, our results strongly suggest that it can be overcome by optimization of the printing process. Our best inkjet printed cells showed photovoltaic parameters and UV stability comparable to the fabricated reference cells, demonstrating the potential of inkjet printed OSCs from an environmental perspective. This shows a possible path towards industrialization for niche products, where the digital flexibility of inkjet printing might prove to be invaluable.

References

An, K., Zhong, W. and Ying, L., 2020. Enhanced performance of P3HT-based non-fullerene polymer solar cells by optimizing film morphology using non-halogenated solvent. *Organic Electronics*, 82: 105701. https://doi.org/10.1016/j.orgel.2020.105701.

Cui, Y., Xu, Y., Yao, H., Bi, P., Hong, L., Zhang, J., Zu, Y., Zhang, T., Qin, J., Ren, J., Chen, Z., He, C., Hao, X., Wei, Z. and Hou, J., 2021. Single-junction organic photovoltaic cell with 19 % efficiency. *Advanced Materials*, 33(41):2102420. https://doi.org/10.1002/adma.202102420.

Fukuda, K., Yu, K. and Someya, T., 2020. The future of flexible organic solar cells. *Advanced Energy Materials*, 10(25): 2000765. https://doi.org/10.1002/aenm.202000765.

Gertsen, A.S., Castro, M.F., Søndergaard, R.R. and Andreasen, J.W., 2020. Scalable fabrication of organic solar cells based on non-fullerene acceptors. *Flexible and Printed Electronics,* 5(1): 014004. https://doi.org/10.1088/2058-8585/ab5f57.

Hau, S.K., Yip, H.-L. and Jen, A.K.-Y., 2010. A review on the development of the inverted polymer solar cell architecture. *Polymer Reviews*, 50(4), pp. 474–510. https://doi.org/10.1080/15583724.2010.515764.

Holliday, S., Ashraf, R., Wadsworth, A., Baran, D., Yousaf, S.A., NIelsen, C.B., Tan, C.-H., Dimitrov, S.D., Shang, Z., Gasparini, N., Alamoudi, M., Laquai, F., Brabec, C.J., Salleo, A., Durrant, J.R. and McCulloch, I., 2016. High-efficiency and air-stable P3HT-based polymer solar cells with a new non-fullerene acceptor. *Nature Communications,* 7: 11585. https://doi.org/10.1038/ncomms11585.

Hoth, C.N., Choulis, S.A., Schilinsky, P. and Brabec, C.J., 2007. High photovoltaic performance of inkjet printed polymer:fullerene blends. *Advanced Materials*, 19(22), pp. 3973–3978. https://doi.org/10.1002/adma.200700911.

Khan, J.I., Ashraf, R.S., Alamoudi, M.A., Nabi, M.N., Mohammed, H.N., Wadsworth, A., Firdaus, Y., Zhang, W., Anthopoulos, T.D., McCulloch, I. and Laquai, F., 2019. P3HT molecular weight determines the performance of P3HT:O-IDTBR solar cells. *Solar RRL*, 3(8): 1900023. https://doi.org/10.1002/solr.201900023.

Kim, J., Kim, G., Choi, Y., Lee, J., Park, S.H. and Lee, K., 2012. Light-soaking issue in polymer solar cells: photoinduced energy level alignment at the sol-gel processed metal oxide and indium tin oxide interface. *Journal of Applied Physics*, 111(11): 114511. https://doi.org/10.1063/1.4728173.

Li, N., McCulloch, I. and Brabec, C. J., 2018. Analyzing the efficiency, stability and cost potential for fullerene-free organic photovoltaics in one figure of merit. *Energy & Environmental Science*, 11(6), pp. 1355–1361. https://doi.org/10.1039/C8EE00151K.

Sundqvist, A., Sandberg, O. J., Nyman, M., Smått, J.-H. and Österbacka, R., 2016. Origin of the S-shaped *JV* curve and the light-soaking issue in inverted organic solar cells. *Advanced Energy Materials*, 6(6): 1502265. https://doi.org/10.1002/aenm.201502265.

DOI 10.14622/Advances_49_2023_09

Cyanotype – from hand craft to industrial print

Thorsten Euler[1], *Jakob Feldmann*[1], *Dieter Spiehl*[1], *Edgar Dörsam*[1] *and Andreas Blaeser*[2,3]

[1] Technical University of Darmstadt, Department of Mechanical Engineering, Institute of Printing Science and Technology, Magdalenenstr. 2, 64289 Darmstadt, Germany

[2] Technical University of Darmstadt, Department of Mechanical Engineering, Institute for BioMedical Printing Technology, Magdalenenstr. 2, 64289 Darmstadt, Germany

[3] Technical University of Darmstadt, Centre for Synthetic Biology, Schnittspahnstr. 10, 64287 Darmstadt, Germany

E-mails: euler@idd.tu-darmstadt.de; feldmann@idd.tu-darmstadt.de; spiehl@idd.tu-darmstadt.de; doersam@idd.tu-darmstadt.de; blaeser@idd.tu-darmstadt.de

Short abstract

In this extended abstract, first, a history of cyanotype is presented. The aim of this research is to change the process of cyanotype from hand craft to industrial application. A test form is developed which serves as a photo mask for the cyanotype process. Printing experiments on an industrial, modular, label printing press Gallus RCS 330-HD are conducted at 5 m/min on foil and paper. The flexographic unit is used to apply the main components necessary for the cyanotype process, a UV curer is utilized for exposure and the gravure unit for washing out the remains with distilled water. This is a novel technique and application for the cyanotype process. Quality of the printed Prussian blue layers is evaluated using a spectrophotometer, measuring the CIE $L^*a^*b^*$ values of solid and halftone patches. The results show that the Prussian blue is homogeneously distributed over the printed area. As expected, small details are transferred well, since the cyanotype process has already been established for blueprints in the past. Future applications for cyanotype are discussed, as the presented industrial process gives the opportunity to fabricate, e.g., electrochromic (EC) devices, which can contain a Prussian blue layer within their layer stack. Thus, our process could serve as an alternative to coating processes for EC devices.

Keywords: flexography, rotogravure, gravure printing, blue print, Prussian blue

1. Introduction and background

The technique of cyanotype is a photographic process, which is known for at least 150 years. It can be traced back to its inventor, the English astronomer Sir John Herschel (Herschel, 1842). Cyanotype became first widely known trough Anna Atkins, who utilized the process to document plants in 1843 (Atkins, 1843, Figure 1a). Under the name of blueprint, the cyanotype was also used by Herreshoff Manufacturing Company for the first copies of technical drawings using the light tracing process (MIT Museum, 1919, Figure 1b).

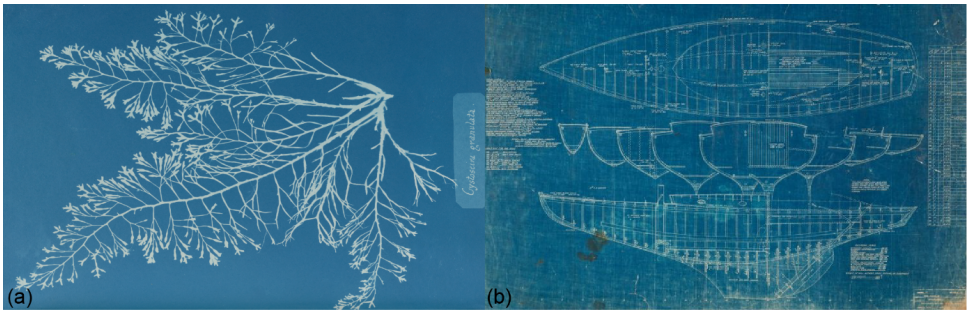

Figure 1: Examples for cyanotype: (a) artwork created by A. Atkins (1843) using cyanotype which shows plants like "Cystoseira granulata" from 1843 and (b) Historical blueprint of a "828 Class Knockabout" yacht (MIT Museum, 1919)

In this process a light blocking object is used or an original is first drawn onto a translucent substrate (Mrhar, 2013) which is then placed on a sheet of paper which was prepared with a layer of liquid containing light-sensitive iron(III) complexes. The arrangement is then exposed to light, so that the object or original serves as a photomask. Where exposed to the light the liquid is photodecomposed and reacts to form an insoluble, blue pigment, also known as *Prussian blue.* The remaining unexposed areas do not undergo this reaction and can therefore be washed out afterwards. On a white substrate, these areas then appear pale. Cyanotype can therefore be used to create multiple copies of an original. Today, cyanotype is still enjoying worldwide attention for artwork and illustrations and was added to the list of intangible cultural heritage by UNESCO in 2018 (Unesco, 2018).

Prussian blue is considered one of the earliest synthetic color pigments. It owes its deep blue color to an absorption of light in the yellow, reddish range and reflection of blue light as the complementary color. The principle of cyanotype is based on the photodecomposition of iron(III) complexes, which are e.g. contained in ammonium ferric citrate or ferric ammonium oxalate. In these, the light-sensitive iron(III) carboxylate is chemically reduced induced by UV-light to give iron(II). The iron(II) complexes can further react with also added potassium ferricyanide to give $Fe_4[F(CN)_6]_3$ or *Prussian blue*. While Prussian blue is not solvable in water the iron(III) containing chemicals (ammonium ferric citrate or ferric ammonium oxalate) are and can be washed out with water, so that only the distinctive blue colored Prussian blue remains. (Ware, 2003)

In printing or artwork application cyanotype can be considered as a mainly manual task. Firstly, potassium hexacyanidoferrate(III) is mixed with green ammonium iron(III) citrate or iron ammonium oxalate in the ratio 2:1 or 1:1 and dissolved in distilled water. The solution is applied to a watercolor paper e.g. using a brush. This paper appears now in a colored *Prussian green*. After the applied solution has dried, a photomask is placed on the coated watercolor paper and exposed to a source of UV radiation (e.g. direct sunlight or a UV lamp). When the photomask is removed, the unexposed areas are still Prussian green, the exposed areas contain reacted and unreacted parts and it appears in a *Prussian brown* tone. The coated watercolor paper must then be washed, using water to remove the unexposed components and fix the exposed areas. The fixed areas take on the Prussian blue hue, which becomes slightly darker when later on exposed to oxygen. This blue pigment is stable to light and insoluble in water. (Maehrle, 2020)

Although Prussian blue is also used in modern applications, such as automatic darkening of window panes by electrochromic (EC) devices, a modern printing process has not yet been established. The aim of this work is therefore to close this gap and find a suitable process for an automated printing of cyanotype with a modern printing setup. For this purpose, two proven conventional printing processes, flexography and gravure printing, are used. In this work, the transition from mainly manual tasks of the historical cyanotype printing to modern, industrial machines is developed and printing parameters are discussed. Furthermore, experiments are carried out to influence the saturation of the blue hue in the cyanotype in order to obtain further variation possibilities.

2. Materials and methods

2.1 Preliminary test

A test form was designed (see Figure 2) and printed on an overhead transparency foil (3561 overhead projector transparencies, thickness 0.13 mm**,** *Avery Denison*, Ohio, USA) using a laser printer (Bizhub C258, 1 800 × 600 dpi, *Konica Minolta Holdings K.K.*, Marunouchi, Japan) as a photomask for the manual task of cyanotype.

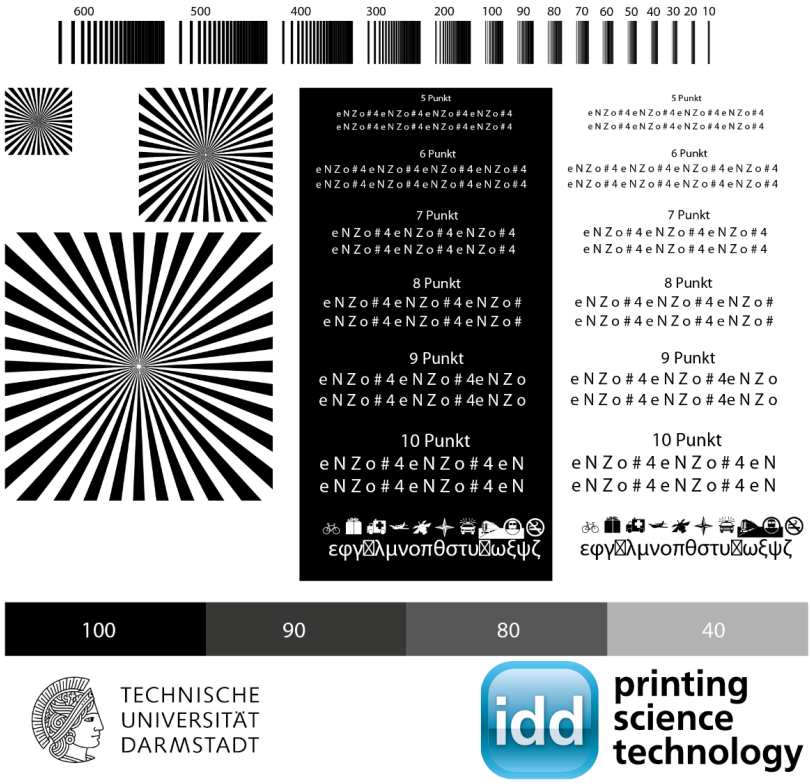

Figure 2: Layout of the test form with line spacing bars, siemens stars, negative and positive font field with fonts in 5 to 10 points size, a solid field (100 %) and halftone fields of 90, 80 and 40 %

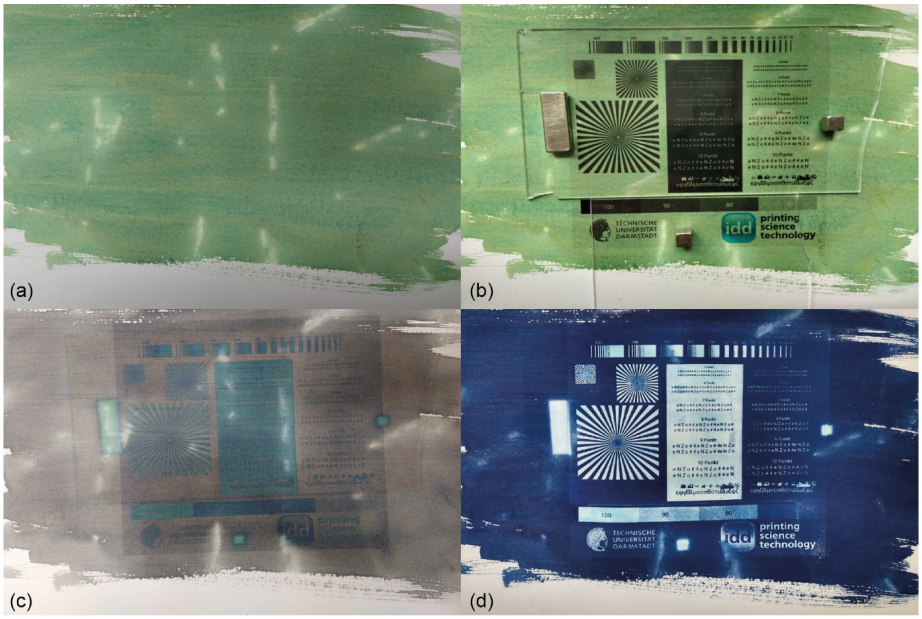

Figure 3: Preliminary test of the cyanotype workflow: (a) Prussian green after applying and drying of solution (A) onto paper, (b) overhead test form foil with quartz glass placed on (a), (c) Prussian brown after UV lightning and removing of the test form, (d) after washing Prussian blue developed

A solution (A) of 20 g potassium hexacyanidoferrate(III) red (*Kremer Pigmente*, Aichstetten, Germany) and 10 g green ammonium iron(III)citrate green (*Kremer Pigmente*, Aichstetten, Germany) with 200 ml distilled water was prepared. The aquarelle paper used was Mixed Media Universalblock (*Hahnemühle*, Dassel, Germany) in the size 30 cm × 40 cm in 310 g/m^2. Solution (A) was applied to the watercolor paper

with a brush and appears in Prussian green (Figure 3a). The test form printed on the overhead transparency foil was placed on the substrate coated with the dried solution (A), i.e. the iron (III) complex, (Figure 3b) and weighted down with a quartz glass. Afterwards, this setup was exposed with a UV dryer (*IST Metz GmbH*, Nürtingen, Germany) with a lamp power of 200 W/cm at a transport belt speed of 5 m/min. After exposure, solution (A) appears in a Prussian brown (Figure 3c). The watercolor paper was then washed out under running water and solution (A) now appears in Prussian blue (Figure 3, d).

It was noticed that the aquarelle paper curls after the application of solution (A) and the overhead transparency warps after UV exposure, which shows that the UV curing unit was set to strong. To prevent the paper from warping, it is recommended to mount the aquarelle paper on a frame before applying solution (A). Nevertheless, a result can be examined (Figure 4a). Characters are displayed well in the positive field (Figure 4b) up to a font size of 5 points. A very good resolution up to seven points can be seen in the font negative field (Figure 4c). The Siemens stars shows a very good line resolution down to the smallest resolutions. The line spacing bars (Figure 4d) also show a clean spacing, up to a spacing of 0.5 mm with a line width of 0.4 mm. Unfortunately, not all line distances can be evaluated because, as described above, the paper has warped in some areas. The solid field and the halftone fields (Figure 4e) still shows a good resolution in the 90 % and 80 % fields, but the 40 % field is completely closed and shows no halftone. So the tonal value curves show a convergence of the halftone dots towards a solid field, especially of the 40 % halftone field. But even in this field, an exact evaluation is not possible due to the warpage of the paper. However, this preliminary test shows that a Prussian blue is quite easy to produce and halftones can be achieved.

Figure 4: (a) Sample of the cyanotyped test form on aquarelle paper, (b) positive font field, (c) negative font field, (d) line spacing bars, (e) solid and halftone fields

After the success of this preliminary test, it was considered how the solution could be processed via an inline printing press.

2.1.1 Printing setup

A label printing press, Gallus RCS 330-HD (*Heidelberg Group Company*, Wiesloch, Germany), was selected for the inline process (Figure 5a) that has the following features: A large variety of printing methods (flexographic, gravure, rotary screen, offset and inkjet printing) can be used simultaneously and their sequence can be easily changed. Another degree of freedom is provided by the possibility of printing different colors or materials. The label printing press offers the possibility of UV, hot air or IR curing after each printing unit without changing the web guide of the substrate.

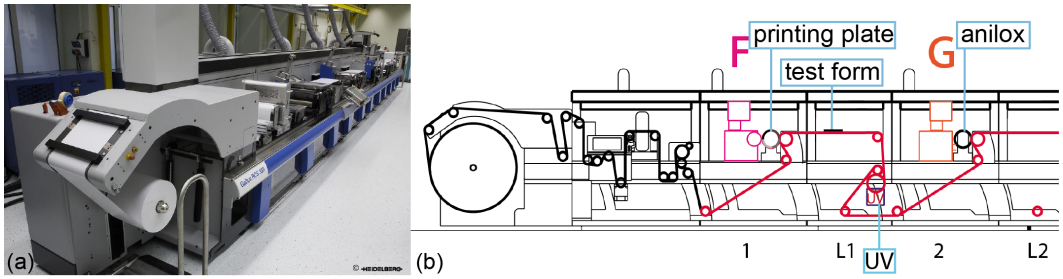

Figure 5: (a) Label printing press, (b) technical draw of the printing units Flexography (F) and Gravure (G) with web guide of the substrate in red and UV exposure

A corona treatment unit for conditioning the film web is also included. In our case, we decided to use the flexography and the gravure printing unit (Figure 5b). Flexography printing is a proven conventional printing process which plays an important role in the packaging industry (cardboard, foils, etc.) and is based on the letterpress technology (Nisato, Lupo and Ganz, 2016). We use this printing unit to apply the solution (A) with a solid and halftone flexographic printing plate which has 90 %, 80 % and 40 % patches (Figure 6). Gravure printing is a high volume mass production for catalogues, cardboards, etc. which provides high resolution and best edge definition in its printing form (Nisato, Lupo and Ganz, 2016). But these possibilities are not of interest in our case. We change the function of the Gravure unit and use it as a washing unit, to develop the Prussian blue.

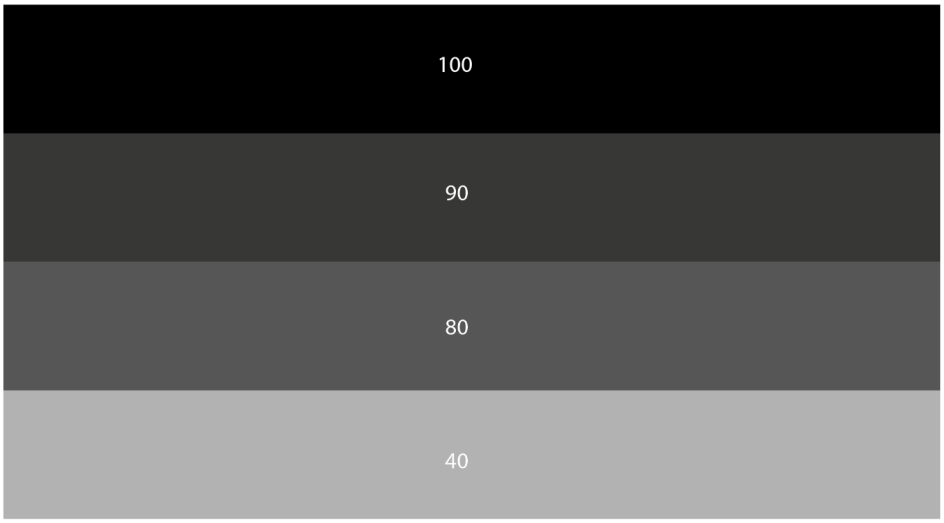

Figure 6: Layout of the flexographic printing plate used, showing the patches of solid (100 %) and halftones (90 % to 40 %)

2.1.2 Experimental setup

In the flexographic printing unit, an anilox roller (*Zecher GmbH*, Paderborn, Germany) with specifications of 7.9 cm^3/m^2, Haschur engraving, 160 l/cm and a Nyloflex ACE (Flint Group, Luxembourg) printing plate with the layout as shown in (Figure 6) were always used. The printing speed of 5 m/min was limited due to low viscosity (1 mPa·s) of the used solution (A) and was always used, for the printing tests. All other variated parameters are listed in (Table 1).

Table 1: Parameters used (marked with an "x") in the printing trials of this work for the different printing trials indicated by the trial number; the columns are marked in the Prussian green, Prussian brown and Prussian blue color results

Trial number	Substrate	Corona treatment	Test form printed on overhead foil	UV exposer	Gravure washing unit	Running water
Prussian green						
x2	natural coated offset paper 80 g/m²					
x5	natural coated offset paper 80 g/m²				x	
Prussian brown						
x1	natural coated offset paper 80 g/m²			x		
Prussian blue						
x4	natural coated offset paper 80 g/m²			x	x	
x3	natural coated offset paper 80 g/m²		x	x	x	
x6	natural coated offset paper 80 g/m²		x	x		x
x7	HOSTAPHAN PET film 125 µm	x		x	x	

Two substrates were used for the printing tests. A natural coated offset paper (*Igepa, Maxi Offset - FSC*®, 80 g/m², 0.1 mm thickness, Hamburg, Germany) and a PET film (*HOSTAPHAN*® GN 4600A PET film, *Mitsubishi Chemical Group Corporation*, 96 µm thickness, chemically treated on one side, Tokyo, Japan) which was treated with a corona pretreatment (*Arcotec GmbH*, Mönsheim, Germany) with a performance to a maximum of 3000 W with a performance of 40 % at 5 m/min. After applying solution (A) with the flexographic printing unit, the already known test form (Figure 2) printed on the overhead transparency foil, was fixed with tape onto the paper, as a photomask. This test form printed on the overhead transparency foil was removed after development by a UV Hg lamp, 120 W/cm (*Uviterno*, Berneck, Switzerland) at a power of 60 % at 5 m/min. For the gravure unit, another anilox roller (*Zecher GmbH*, Paderborn, Germany) with specifications 13.0 cm³/m², HIT engraving, 100 l/cm was used. The ink chamber of the gravure unit was filled with distilled water instead of a graphical ink to make it usable for a washout.

2.1.3 Measurement setup

The spectral densitometer *Spectrodens* (*Techkon*, Königstein, Germany) was used to determine the CIE *L*a*b** values. The spectral densitometer was used with the following measurement geometries: Illuminant D50, viewing angle 2°, no polarizing filter and white reference absolute. The printed solid and halftone patches were measured, each at five different points in one sample, to get a mean value difference (Δ) of the *L*a*b** values.

3. Results and discussion

Flexographic printing produced a uniform Prussian green (Figure 7a). After UV expose, the patches reached the Prussian brown (Figure 7b) state. Washing out the patterns with water, by the gravure printing unit or by rinsing under running water, resulted in the classic Prussian blue (Figure 7c) effect.

It was optically recognized, in the used natural coated offset paper, that the halftone patches achieved a more uniform printout compared to the solid area. This is due to the low viscosity and the slow printing speed. It was also recognized that the classic brush application achieved a richer color impression for the Prussian green, brown and blue, which was clearly due to the applied film thickness.

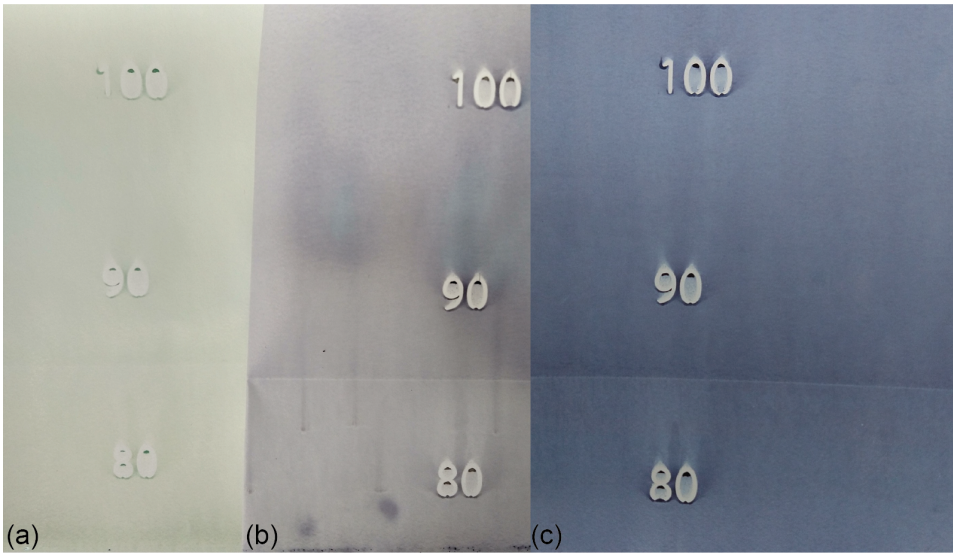

Figure 7: Printed results: (a) Prussian green, (b) Prussian brown and (c) Prussian blue

The Prussian green could be reproduced well on the offset paper and anchored well in the paper, with a mean value of about ±1 Δ in the $L^*a^*b^*$ measurement. Also washing out the substrates with water by using the gravure printing unit had no significant effect, only around one point in the Δ in brightness (L^*) and the color axes (a^*, b^*) (Table 2). Washing out by rinsing under running water removed the Prussian green layer.

Table 2: Prussian green in L, a* and b* values without (x2) and with washing (x5) of solid and halftone patches*

Trial number	x2	x5	x2	x5	x2	x5	x2	x5
Patches	100 %	100 %	90 %	90 %	80 %	80 %	40 %	40 %
L^*	92.51	91.22	91.83	90.02	90.76	88.95	92.78	92.19
a^*	−0.42	−0.71	−2.49	−3.37	−4.20	−5.05	0.82	0.26
b^*	−1.10	−1.45	3.51	4.02	7.46	7.17	−4.02	−3.27

However, a clear tendency was observed between the Prussian brown and the Prussian blue. In the mean value are only ±2 Δ in the $L^*a^*b^*$ measurement for the trial number x1 and x4. The Δ in brightness (L^*) decreased slightly after washing and generation of the Prussian blue. On the color axes (a^*, b^*) the Δ of the hue shifted to an obvious blue tone (Table 3). A color example for better visualization of trial number x1 and x4 (Figure 8) shows the Δ in $L^*a^*b^*$ between the shades of Prussian brown and Prussian blue in the 90 % patch.

Table 3: Prussian brown to Prussian blue L, a* and b* values of samples exposed to UV light without (x1) and with washing (x4) of solid and halftone patches*

Trial number	x1	x4	x1	x4	x1	x4	x1	x4
Patches	100 %	100 %	90 %	90 %	80 %	80 %	40 %	40 %
*L**	83.24	79.8	75.22	71.4	77.5	70.36	84.75	82.38
*a**	2.33	1.54	1.98	0.90	2.04	−0.31	2.53	1.26
*b**	−9.87	−13.16	−10.34	−15.4	−9.82	−16.56	−9.39	−11,50

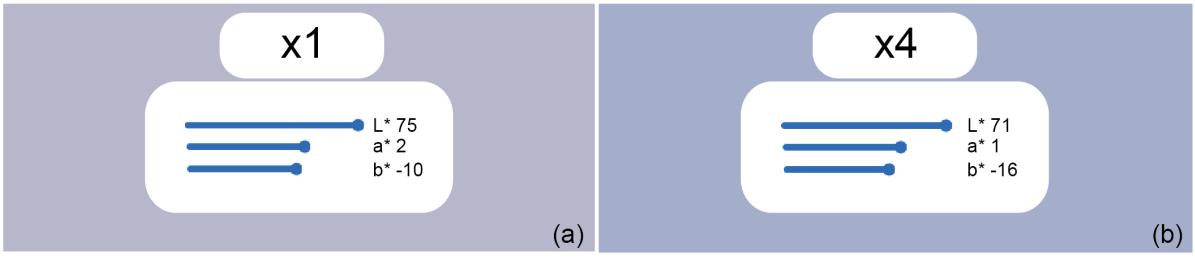

Figure 8: Color example between Prussian brown (a) and Prussian blue (b) in the 90 % patch

The Δ in the patches of the *L*a*b** values between washing out the samples by the gravure printing unit or by rinsing under running water are very small (Table 4). In the perceptual lightness (*L**) the Δ of *L** is only around 2–5 points of the solid and halftone patches. These appear slightly darker after washing out with the gravure unit. The Δ of green-magenta (*a**) axis (0.3–2.5 points in the (*a**) and the Δ of the blue-yellow axis (*b**) (0.4–3 points in the (*b**) are negligible. This is a good result, which shows that the gravure printing unit could be used instead of rinsing under running water. Also it shows that the mean value in the trials x3 and x6 is under ±2 Δ in the CIE *L*a*b** measurement. When using the test form printed on the overhead transparency foil, a residue of Prussian green (Sample x6, Figure 9a) was visually perceived in the gravure printed sample. The sample rinsed under running water shows no residue of Prussian green (Sample x6, Figure 9b). Since Prussian blue is even used as a drug to bind poisons (radioactive cesium and thallium), this should not cause a health problem.

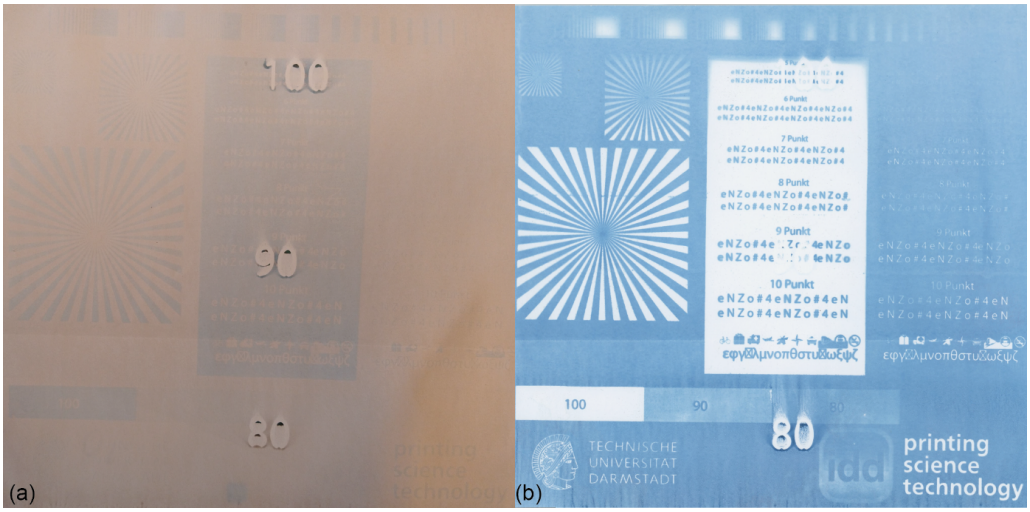

Figure 9: (a) Sample x6 of the test form exposed in Prussian brown with a residue of Prussian green, (b) Sample x6 of the test form by rinsing under running water with no residue of Prussian green

Table 4: The L, a* and b* values of samples washed using the gravure printing unit (x3) or rinsed under running water (x6) of solid and halftone patches*

Trial number	x3	x6	x3	x6	x3	x6	x3	x6
Patches	100 %	100 %	90 %	90 %	80 %	80 %	40 %	40 %
*L**	78.57	82.67	69.37	71.31	65.44	71.42	83.04	88.24
*a**	1.2	0.70	0.1	−1.58	−0.71	−3.18	1.77	1.41
*b**	−13.1	−13.53	−14.64	−18	−14.35	−17.65	−11.08	−9.12

When printing on HOSTAPHAN® PET film, only a slight Δ in the patches of the brightness (*L**) of the color tone, compared to printing on the natural coated offset paper, was observed (Table 5). The mean value in the trial number x7 was also under ±2 Δ in the CIE *L*a*b** measurement.

Table 5: Comparison of PET and offset paper; L, a* and b* values between solid and halftone patches*

Trial Number	x3	x7	x3	x7	x3	x7	x3	x7
Patches	100 %	100 %	90 %	90 %	80 %	80 %	40 %	40 %
*L**	78.57	85.22	69.33	80.93	65.44	82.54	83.04	82.298
*a**	1.12	−0.07	0.1	−2.19	−0.71	−3.05	1.77	0.61
*b**	−13.1	−10.78	−14.64	−14.54	−14.35	−14.66	−11.08	−11,37

4. Conclusions and outlook

Even in the preliminary tests, it was seen that lines, small fonts and other details could be reproduced very well. This is not surprising, since the blueprinting technique was used exactly for this purpose. But for the first time, a cyanotype process could be reproduced on an inline press. One can discuss whether the use of flexographic printing is suitable for printing the solution (A), or whether another printing process (gravure printing for a better edge definition, screen printing to generate a stronger Prussian blue) should be used for this purpose. Another option can be to make the solution (A) more viscous for flexographic printing with a thickener to achieve better printing results. This could allow to an application for screen printing. Also, parameters would need to be adjusted (e.g. optimal UV exposure, print speed) to refine the printing process. Converting the gravure unit to a washing out unit, however, was successful and showed that an inline printing process is possible. The spectralphotometric measurments in the mean value showed only small deviations in the trials of a maximum of ±2 Δ in the CIE *L*a*b** measurement. The Prussian blue of the offset paper and the PET foil shows only small differences, which brings us to the conclusion, that we can compare the gravure washing unit with a rinsing under running water. The Prussian blue can be used for two applications. Firstly, for battery systems as a cathode material and secondly, for electrochromic windows to achieve an efficient energy management of buildings, by allowing for a switchable window darkening. It should also be possible to print further stacked layers in order to be able to produce an electrochromic function exclusively with printing techniques. Conjugated electrochromic polymers for flexible EC devices generally lack a fully colorless bleached state (Macher, et al., 2019). Printing, so far, is only possible using screen printing while this gives a strong bleached state (Rueff, 2007). These are unsatisfactory results for EC devices.

Further work is pending to use additional printing technologies, speeds, optimal exposure and design elements for pattern generation for the cyanotype and electrochromic functions. Layer thickness of the Prussian blue layers shall be measured in future research.

Acknowledgements

We kindly acknowledge the financial support by the *Heidelberger Druckmaschinen AG.*

References

Atkins, A., 1843. Photographs of British algae: cyanotype impressions. *The New York Public Library Digital Collections*, [online] Avalable at: <https://digitalcollections.nypl.org/collections/photographs-of-british-algae-cyanotype-impressions#/?tab=navigation> [Accessed April 2023].

Herschel, J.F.W., 1842. On the action of the rays of the solar spectrum on vegetable colours, and on some new photographic processes. *Philosophical Transaction of the Royal Society*, 132, pp. 181–214. https://doi.org/10.1098/rstl.1842.0013.

Macher, S., Schott, M., Sassi, M. Facchinetti, I., Ruffo, R., Patriarca, G., Beverina, L. Pooset, U., Giffin, G.A. and Löbmann, P., 2019. New roll-to-roll processable PEDOT-based polymer with colorless bleached state for flexible electrochromic devices. *Advanced Functional Materials*, 30(6): 1906254. https://doi.org/10.1002/adfm.201906254.

Maehrle, M., 2020. *Blaue Wunder: Techniken und Projekte mit Cyanotypie*. Bern: Haupt Verlag.

MIT Museum, 1919. 828 class knockabouts. *MIT Museum: Haffenreffer-Herreshoff Collection*, [online] Available at: <https://mitmuseum.mit.edu/collections/object/HH.5.05572.1?query=828%20class&resultIndex=1> [Accessed April 2023].

Mrhar, P., 2013. *Cyanotype: historical and alternative photography*. CreateSpace Independent Publishing Platform, P. Mrhar.

Nisato, G., Lupo, D. and Ganz, S. eds., 2016. *Organic and printed electronics: fundamentals and applications*. Singapore: Pan Stanford Publishing.

Rueff, A.K.E., 2007. *Herstellung und Ansteuerung elktrochromer Anzeigeelemente*. Dr. Dissertation Universität des Saarlandes.

Unesco, 2018. Blaudruck/Modrotisk/Kékfestés/Modrotlač, resist block printing and indigo dyeing in Europe. *Unesco: Intangible Cultural Heritage*, [online] Available at: **<**https://ich.unesco.org/en/RL/blaudruck-modrotisk-kekfestes-modrotlac-resist-block-printing-and-indigo-dyeing-in-europe-01365**>** [Accessed April 2023].

Ware, M., 2003. A blueprint for conserving cyanotypes. *Topics in Photographic Preservation*, 10, pp. 2–18.

DOI 10.14622/Advances_49_2023_11

Development of a guideline for the engineering of a coherent, optimized packaging system based on the holistic systemic analysis

Veronika Schenk, Michael Herrenbauer, Christoph Haeberle and Maria Erxleben

Stuttgart Media University, Nobelstr. 10, 70569 Stuttgart, Germany

E-mails: schenkv@hdm-stuttgart.de; herrenbauer@hdm-stuttgart.de; haeberle@hdm-stuttgart.de; erxleben@hdm-stuttgart.de

Short abstract

During its life cycle a product experiences transformations in shape, consistency, place, and composition. The stresses which impact the product are various. The packaging as the interface of a product to its surroundings protects the product and covers the expectation of diverse stakeholders in the product supply chain, such as high protection, robustness, light weight, zero waste, low costs, attractiveness to customers and scalability. Science and Industry try to cope with these requirements' complexity by developing specific packaging manuals accordingly. However, quickly changing social and governmental conditions limit the applicability of such straightforward guidelines. A balanced scorecard model attempts to support packaging design considering a variety of influencing factors. The isolated measure of every factor however fails to consider the interconnections and dynamics in this complex field and thus remains one sided. A recent European Union bill towards Packaging and Packaging Waste Regulation (PPWR) aims for the reduction of packaging waste for example by minimizing the packaging size. It has triggered heated debates on feasibility and logic of the requirements. Packaging companies' associations as well as producers are concerned of being unable to meet a packaging's functionalities such as product protection with the proposed threshold. The question arose whether there can be a proper methodology on developing "efficient packaging" which ensures packaging to meet its purpose with minimal environmental impact. This paper describes a new approach to the analysis of packaging design which considers the complex environment and requirements towards packaging. It utilizes the "Malik Sensitivity Modell®Prof.Vester"– a methodology for the holistic consideration of complex systems. This first approach confirms the necessity of a holistic system theoretic analysis of the packaging design requirements.

Keywords: holistic analysis of packaging systems, sensitivity model, systems thinking

1. Introduction and background

Packaging systems are complex systems. This statement is founded in the variety of different packaging elements interdependent on each other (Schoeneberg, 2014). A complex system is characterized by variety, connectivity, and dynamics (Klabunde, 2003). The stakeholders of packaging make various, partially conflicting demands for the packaging which creates a field of tension. Packaging solutions fulfill some requirements better than others. There is however no instrument measuring the overall performance of a packaging system under consideration of all relevant variables which represent the complex packaging system and its environment. According to Bleisch, Majschak and Weiß (2011) and the German standard DIN 55405:2014-12 (Deutsche Institut für Normung, 2014) a multilayered packaging system consists of primary packaging which encases the product followed by several subsequent packaging layers. Those layers mutually influence the entire packaging system (Pfohl, 2018). The requirements of the different stakeholders are represented by a number of functions which a packaging system needs to fulfill, namely the product function, marketing function, usage function, handling function, protection function, storage function, transportation function, manipulation function and information function (Pfohl, 2018). The specifics of the product which needs to be packaged influence the packaging system strongly as well (Pfohl, 2018). Packaged goods' sensitivity towards stresses in the supply chain can be very different. The sensitiv-

ity of the packaged goods in combination with their shape and weight can lead to very specific packaging requirements. Packaging solutions differ with respect to the applied packaging materials. But not only the protective features, the production processes, the handling function, and the packaging costs are also influenced by the packaging material (Verghese, Lewis and Fitzpatrick, 2012). Companies are interested in applying economically efficient packaging systems, which means fulfilling maximal functional requirements using minimal material and personnel resources (Bleisch, Majschak and Weiß, 2011). The environmental impact of packaging is mainly driven by the packaging material, but it cannot be considered in isolation. The amount of packaging waste generated by different layers at different points in the supply chain (Pålsson, 2018) may or may not be increased by the selection of the wrong packaging material, the causes for the rising amount of packaging waste are various.

The Commission's proposal for a Packaging and Packaging Waste Regulation (PPWR), amending Regulation (EU) 2019/1020 and Directive (EU) 2019/904, and repealing Directive 94/64/EC, was published on 2022/11/30, is the inducement of the present analysis. The PPWR proposal stipulates that all packaging placed on the European market must be reusable or recyclable by 2030 and proposes specific measurement criteria (Karamfilova, 2022). The industry apprehends possible disproportionate effort for complying with the new regulation while insufficient overall environmental protection is achieved as a result. Consequently, a comprehensive holistic analysis was initiated.

Currently several regulations for the design and analysis of optimized packaging systems exist. The aim for the optimization varies, however. The EU Commission's PPWR contains requirements for packaging reuse, recyclability, recycled plastic content as well as packaging minimization and a maximum threshold of the proportion of empty volume between packing goods and packaging (Proposal /EC, 2022). Next to addressing barriers to circularity, the aim is to reduce the amount of packaging waste. Companies on the other hand require robust packaging which can protect the packaged goods and being handled along the supply chain until reaching the final customer. Amazon for example has implemented the so-called Frustration-Free Packaging Program and requires special ISTA test certificates. OEMs and suppliers in the automotive industry implement packaging manuals with specific requirements not only for their own packaging but also for the packaging of their suppliers with regard to part protection and handling optimization (Schaeffler Technologies AG & Co. KG, 2020). Logistics service providers, especially, focus on packaging requirements aiming for rapid and effective handling (Wackler Spedition & Logistik, 2022). Those examples underlay the problem at hand – despite the requirements' variety, the involved party implements specific packaging guidelines with partial view on the packaging design only. The Packaging Scorecard method from Olsmats and Dominic (2003) aims for the first time at a systematic evaluation of the measurement of packaging performance. The method takes under consideration all involved in the supply chain and their specific expectations toward the packaging (Olsmats and Dominic, 2003). This method aims a complex consideration of the problem at hand which plays out only partially. Although the analysis respects the *variety* of the problem, the subsequent analysis views the specific requirements only isolated with no regard to the *interdependence* among them and ignoring the *dynamic* changes within the packaging system as well as between the system and its surroundings.

The present paper will therefore for the first time apply a sensitivity model for the analysis of the overall packaging system performance – a method which considers the characteristics of *variety*, *connectivity*, and *dynamics* of complex systems.

2. Materials and methods

The sensitivity model is a system theoretical methodology which takes into consideration the specifics of complex systems: they consist of various elements which are dynamically interconnected and represent

a causal loop structure. The intervention in a complex system implies the understanding of its holistic behavior (Vester, 1999). The system theory and the methodology of the so called "systems thinking" postulated by Vester, Senge and other scientists emphasizes the danger of simplifying complex problems and inducing actions based on isolated and one-sided views of the system (Senge, 2017; Vester, 1999). The aim of system thinking is to capture the key components of a system (the so-called system variables) and their interactions and to develop an abstract model representing the system (Vester, 1999). This way, the system can be simulated, and its behavior can be examined.

The Sensitivity Model Prof. Vester® (since 2006 Malik Sensitivity Model®Prof.Vester) supports the systematic extraction and validation of the systems variables as well as the systems modeling and subsequent simulation of the systems response to different actions (Vester, 1999). The sensitivity modeling is executed in three main steps. Initially, the impact variables need to be extracted which represent the highest relevance to the system. In the second step the interaction between the variables as well as their characteristics are analyzed which implies the analysis of the system behavior. Ultimately, a cybernetic approach based on simulation of different impact scenarios is conducted which enhances the system understanding and helps in deriving appropriate controlling strategies (Vester, 1999).

3. Results and discussion

Relevant systems variables were collected. A first summary initially based on results of preliminary investigation of the industry partner with regard to influencing factors towards efficient packaging was enriched in several workshops with the involved experts. The resulting variables were then further examined regarding their interdependencies using a Cross-Impact-Matrix (Table 1). In order to underline the different influences from one variable towards the other, the relations were additionally subdivided depending on the strength of the impact (from 0 to 3) and the direction of the impact (proportional "+" and inversely proportional "–"). When one variable impacts one other variable and the connection is positive (or proportional), this would mean that the increase of the impact variable will trigger an increase of the affected variable. If the connection between the variables is negative (inverse proportional), then the increase of the impact variable will trigger a decrease of the second variable. The numbers 0 to 3 mark how strong the positive or negative impact might be in the complex system.

Table 1: Cross-Impact-Matrix developed together with the industry partner

Effect of ↓ on →		B	C	D	E	F	G	H	I	J	K	L	M	N	O	P	Q	R	**AV sum**	**P Product**
Material selection	B		+/-3	+/-3	0	0	0	0	0	+/-3	0	+/-3	0	0	+/-3	0	2	+/-3	20	660
Demand of resources	C	+/-2		2	0	0	0	0	0	0	0	0	0	0	0	0	0	0	4	92
Emissions	D	0	0		0	0	0	0	0	0	0	0	0	0	0	0	0	0	0	0
Packaging applicable for re-use	E	-3	-2	+/-1		-3	0	0	0	-3	0	2	2	3	-2	0	2	+/-1	24	288
Amount of packaging waste	F	0	0	2	0		0	0	0	0	0	0	0	0	0	0	0	-3	5	110
Product dimensions	G	-3	3	3	-2	-3		0	2	-3	0	3	1	0	-2	-2	1	0	28	0
Product shape	H	-2	0	0	0	3	0		2	-3	0	3	0	-2	-3	0	0	0	18	0
Fragility of the packaged product	I	-3	3	0	1	3	0	0		-3	0	2	1	0	-3	0	0	0	19	76
Structural packaging design	J	-3	-3	0	-2	-3	0	0	0		-3	-2	1	-3	3	0	0	3	26	884
Complaint rate	K	-1	3	0	0	0	0	0	0	-3		0	0	0	0	0	2	-3	12	108
Packaging dimensions	L	-2	3	0	-1	3	0	0	0	-3	0		1	0	-2	-2	-2	0	19	399
Information and communication	M	-1	0	0	0	1	0	0	0	-1	0	3		0	+/-2	0	0	+/-2	10	80
Standardization and modularization	N	-2	1	0	1	0	0	0	0	-2	-2	1	0		3	0	-2	0	14	140
Manufacturing process	O	-3	-2	-3	0	-1	0	0	0	+/-3	0	0	0	0		0	-2	0	14	350
Mode of transportation	P	-3	0	3	-3	1	0	0	0	-3	2	2	0	-2	0		3	0	22	88
Number of handling stages	Q	-3	0	0	0	1	0	0	0	-1	0	0	2	0	0	0		0	7	112
User experience	R	-2	0	0	+/-2	0	0	0	0	-3	2	0	0	0	-2	0	0		11	165
PV sum		33	23	17	12	22	0	0	4	34	9	21	8	10	25	4	16	15		
Q Quotient		0.61	0.17	0.00	2.00	0.23	-	-	4.75	0.76	1.33	0.90	1.25	1.40	0.56	5.50	0.44	0.73		

The in-depth investigation of the Cross-Impact-Matrix shows besides interferences between the variables, the main character of the relevant variables within the complex system – some variables impact many other variables directly or indirectly and thus their behavior influences the whole system strongly (active variables), and other variables are impacted by many others in the system while providing limited or no impact themselves (passive variables). In the present system for example there is the variable of "Product dimension" – an active variable which impacts almost every other relevant variable. Through the further influence of the impacted variables "Product dimension" shows not only direct but also indirect (belated or long range) influence on the whole system. A further variable "Amount of packaging waste" occurs passively as it does not have any impact on the rest of the variables besides on "Emissions" and "User experience". Such variables react sensibly to the behavior of the system and cannot be controlled easily and quickly simply by inducing one action because they are impacted by more than one impact variable. One action (e.g. reduction of "Packaging dimensions") might lead to a short reaction in the desirable direction (reduction of "Packaging waste"), through belated and long range effects in the system (reduction of "Material selection", increase of "Number of handling stages", decrease of "Mode of transportation" etc.), the desired holistic result will not last long and thus the one-sides action will not be sustainable.

In extreme cases variables can have an impact on the system that is so strong that they can be indicated as "critical", and on the other hand, other variables can be impacted by multiple other variables by giving no further impact back to the system. Such variables indicate a "buffer" attitude. An overview in Figure 1 shows the intensity of the involvement of the relevant influencing variables in the system behavior. Variables with a strong impact on the system are located in the "active" area of the portfolio, they execute a strong and direct impact on the whole system. Those variables can be used as control variables for the regulation of the system development in one desired direction. These variables are the levers for the system control and in the specific system we can define the variables "Product dimensions", "Product shape", "Packaging applicable for re-use", "Standardization and modularization" or "Mode of transportation" as such levers.

On the opposite side of the portfolio, we can locate the reactive variables, e.g. "Manufacturing process", which cannot be reached easily by direct actions but which act on many variables themselves. They boost certain impacts into the system. For strategic decisions these variables are important as their reaction into the system might enhance or reduce the desired result.

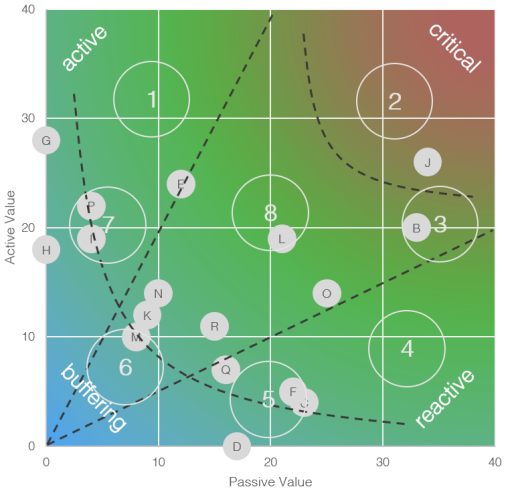

Material selection	B
Demand of resources	C
Emissions	D
Packaging applicable for re-use	E
Amount of packaging waste	F
Product dimensions	G
Product shape	H
Fragility of the packaged product	I
Structural packaging design	J
Complaint rate	K
Packaging dimensions	L
Information and communication	M
Standardization and modularization	N
Manufacturing process	O
Mode of transportation	P
Number of handling stages	Q
User experience	R

Figure 1: The roles of the variables in the system

The complexity in the interactions between the relevant system variables can be illustrated best using a causal loop diagram (Figure 2). It visualizes the holistic network representing a packaging system and its interconnections to the outer world. This model takes account of the variety and the connectivity of complex systems and represents the holistic field of tension of the packaging and its environment.

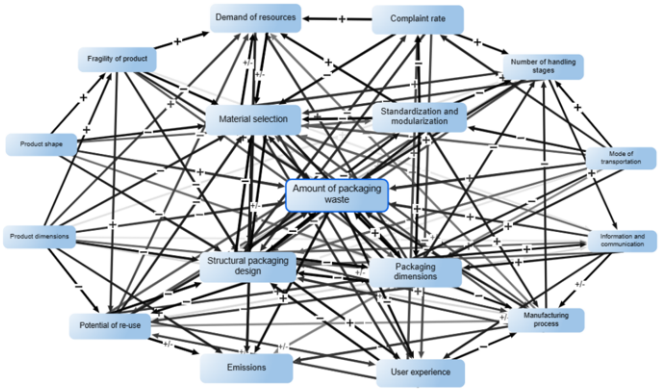

Figure 2: Causal Loop Diagram of a packaging system

The initial evaluation targeted the optimization of the packaging system for the product portfolio of the industry partner. The results of this first investigation show a holistic causal loop diagram, considering the connectivity and dynamics based on complex packaging systems of the company example. This approach expands the one-sided analysis of the Packaging Scorecard Model which considers the variety only. However, a further collection, in depth analysis, and validation of the influencing systems variables in line with the guideline of Malik Sensitivity Modell®Prof.Vester needs to be completed. To prove the holistic approach and exclude possible subjectivity in the variables, further investigation in industry and science is necessary. The revision of the system variables will lead to a new model which will be simulated and analyzed. Subsystems and submodels will help to dive into specific questions without ignoring the environmental impact of the overall system.

With regard to the Commission's proposal for a Packaging and Packaging Waste Regulation, the initial analysis has shown that the planned requirements cannot be put into effect without major side-effects on the product quality, logistics system efficiency, packaging material usage as well as the surrounding packaging system, meaning the underlayer and the next layer of the specific packaging. The variety of products, packaging materials and designs as well as dynamic changes in the logistics processes and customer needs make the measurement of the overall packaging performance through one key performance indicator impossible. A limitation such as this of the system's complexity to one metric might only provoke one-sided actions of the industry such as the usage of more material, of material with more robust characteristics, less recyclable packaging, heavier packaging, longer process times or even higher rates on damaged products. Without a systems analysis, there can be no guarantee that space reduction in the packaging will decrease or even increase packaging waste, and even if this goal is met there is no guarantee that it is not met at the expense of higher CO_2 emissions, pollution through damaged goods, and packaging materials requiring higher energy for production and recycling.

4. Conclusions

Packaging systems are complex and thus only a holistic analysis with a systems-theoretical approach is appropriate to make recommendations for the development of optimized packaging systems. Isolated considerations of individual influencing factors on the field of tension of the packaging, such as from a legal or from a company perspective, neglect the complexity of systems and are therefore not effective. Even the packaging scorecard does not meet all the complexity criteria required to view the packaging system holistically. A systems-theoretical approach such as the Malik Sensitivity Model®Prof.Vester helps to analyze the variety, connectivity, and dynamics of the overall packaging system. As a result, recommendations for the development of optimized packaging systems can be derived after implementation of further research requirements.

Future work should include validation, revision, and completion of the variables for exemplary packaging systems. Industrial partners and experts in the field of packaging life cycles should be consulted and involved in further research, creating working groups, which will contribute to the establishment of requirements for packaging systems including practical insights. The wide revision of the variables and their interdependencies aims to reduce subjectivity to build up an increasingly universal model for packaging systems.

Acknowledgements

The authors are grateful for the support and feedback provided by our industry partner.

References

Bleisch, G., Majschak, J.-P. and Weiß, U., 2011. *Verpackungstechnische Prozesse: Lebensmittel-, Pharma- und Chemieindustrie*. Hamburg: Behr.

Deutsche Institut für Normung, 2014. *DIN 55405:2014-12 Verpackung – Terminologie – Begriffe*. Berlin: DIN, Beuth-Verlag.

Karamfilova, E., 2022. *Revision of Directive 94/62/EC on packaging and packaging waste*. [pdf] Available at: <https://www.europarl.europa.eu/RegData/etudes/BRIE/2022/734698/EPRS_BRIE_734698_Revision_Directive_Packaging.pdf> [Accessed 8 March 2023].

Klabunde, S., 2003. *Wissensmanagement in der integrierten Produkt- und Prozessgestaltung: Best-Practice-Modelle zum Management von Meta-Wissen.* Wiesbaden: Deutscher Universitäts-Verlag.

Olsmats, C. and Dominic, C., 2003. Packaging scorecard - a packaging performance evaluation method. *Packaging Technology and Science,* 16(1), pp. 9–14. https://doi.org/10.1002/pts.604.

Pålsson, H., 2018. *Packaging logistics: understanding and managing the economic and environmental impacts of packaging in supply chains*. London, New York, New Delhi: Kogan Page.

Pfohl, H.-C., 2018. *Logistiksysteme: Betriebswirtschaftliche Grundlagen*. 9th ed. Berlin: Springer Vieweg.

Proposal 2022/0396 */EC of 30 November 2022 for a regulation of the European parliament and of the council on packaging and packaging waste*.

Proposal /EC of 30 November 2022 for a regulation of the European parliament and of the council on packaging and packaging waste, amending Regulation (EU) 2019/1020 and Directive (EU) 2019/904, and repealing Directive 94/62/EC.

Regulation (EU) 2019/1020 of the European Parliament and of the Council of 20 June 2019 on market surveillance and compliance of products and amending Directive 2004/42/EC and Regulations (EC) No 765/2008 and (EU) No 305/2011.

Schaeffler Technologies AG & Co. KG, 2020. *Verpackungshandbuch für Lieferanten*. [pdf] Available at: <https://www.schaeffler.de/de/news_medien/mediathek/downloadcenter-detail-page.jsp?id=87657920> [Accessed 10 March 2023].

Schoeneberg, K.-P. ed., 2014. *Komplexitätsmanagement in Unternehmen: Herausforderungen im Umgang mit Dynamik, Unsicherheit und Komplexität meistern.* Wiesbaden: Springer Gabler.

Senge, P.M., 2017. *Die fünfte Disziplin. Kunst und Praxis der lernenden Organisation*. 11th ed. Stuttgart: Schäffer-Poeschel Verlag.

Verghese, K., Lewis, H. and Fitzpatrick, L. eds., 2012. *Packaging for sustainability*. London: Springer.

Vester, F., 1999. *Die Kunst, vernetzt zu denken: Ideen und Werkzeuge für einen neuen Umgang mit Komplexität*. Stuttgart: Deutsche Verlags-Anstalt.

Wackler Spedition & Logistik, 2022. *Informationsbroschüre Verpackung*. [pdf] Available at: <https://www.wackler.de/wp-content/uploads/sites/52/2022/01/Informationsbroschuere_und_Checkliste_Verpackung.pdf> [Accessed 10 March 2023].

DOI 10.14622/Advances_49_2023_13

Ink spreading in gravure printing

Armin Weichmann, Thomas Sprinzing and Matthias Galus

Hochschule der Medien Stuttgart, Institut für Angewandte Forschung (IAF), Nobelstr. 10, 70569 Stuttgart, Germany
E-mails: weichmann@hdm-stuttgart.de; sprinzing@hdm-stuttgart.de; galus@hdm-stuttgart.de

Short abstract

Even though gravure printing is a process that has been known for a long time, it is rare to find a consistent model in the literature of what happens during the doctoring of the ink and the ink transfer. This article deals with the aspect of ink spreading on substrates and its influencing factors. A model on the basis of the Murray-Davies formula and Lambert-Beer's law is presented that can explain essential effects of the ink spreading in gravure. Within a large-scale gravure printing trial on an industrial-scale web press a subset of the varied parameters were chosen to expose the influencing factors: printing velocity (120, 180, 240 m/min), ink viscosity (high, medium, low), electrostatic assist (ESA) (on, off) on film with organic solvent based ink. The effect of ink spreading is measured by spot colour tonal value (SCTV). The results show that the factors behave completely differently in the tonal range of single dots, where spreading plays a role as opposed to the tonal range with a closed ink layer. With single dots viscosity plays the major role as it influences ink spreading most.

Keywords: rotogravure, ink spreading, parameter study, quality control

1. Introduction and background

Commercial rotogravure is actually a long-established process. On the other hand, fluid transfer in gravure printing is a complex process. In the last decades, researchers like Kunz (1975), Hübner (1991), Kumar (2015), Grau, et al. (2016) and Schäfer, et al. (2019) have contributed to a deeper understanding. More recently, Brumm, et al. (2021a; 2021b) tried to classify transfer patterns on the basis of a neural network.

Nevertheless, the scientific literature rarely provides an overall view of how individual steps in the process influence the print result. A comprehensive view is offered in trade journals, e.g. as a guide to troubleshooting in gravure printing (Beilenhoff, 2011a; 2011b). Joshi (2016) conducted an extensive Design of Experiments aimed at the optimising of mottle and missing dots. This article uses a similar approach to proof the different factors and their strength of influence on the gradation of a gravure print with an especial distinction between the area of single dots and the area after the flooding, where a closed layer of ink is printed.

This is a result in the frame of a large-scale gravure printing trial, that was conducted to systematically investigate the influence of seven major printing parameters (printing velocity, type of ink, ink viscosity, type of substrate, electrostatic assist (ESA) and doctor blade angle) on hydrodynamic pattern formation and gravure print quality. The trial itself is described in detail in Brumm, et al. (2022).

2. Model and assumptions to ink spreading

2.1 Effect of ink spreading on the tonal value of a print

A dot in a regular grid is assigned a space that corresponds to the size of a unit cell of the grid and is bounded by the neighbouring cells. Let the area reserved for each dot be A (see Figure 1). Two dots are consid-

ered that have the same ink volume and the same ink composition, i.e. the same amount of pigment. One of the two spreads more than the other. Let the proportion of covered area for the less spreading dot D be φ = area(D)/A, its layer thickness $h/2$, φ' = area(D')/A be the proportion of covered area for the more spreading, i.e. larger, but flatter dot D', $h'/2$ its thickness. ($0 < \varphi, \varphi' < 1$)

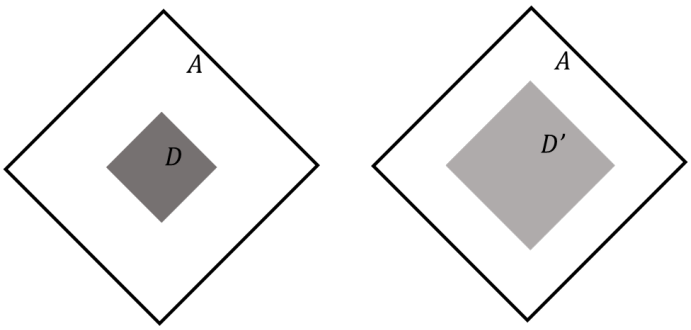

Figure 1: (a) Gravure dot D within its elementary cell of area A; (b) the more spreading dot D' within its elementary cell of area A

In a simplified model, the printed ink layer is regarded as a colour filter with a first passage of light, then the reflection by the surface and a second passage of light. In this approximation the surface is assumed to be perfectly reflective. As the light passes the layer twice the overall layer thickness can be assumed to be $h/2 + h/2 = h$. Additionally, the ink layer of the dot is considered to have the same thickness everywhere. If the dot spreads more, then it becomes larger. Nevertheless, it is considered to have a reduced but still homogeneous thickness.

Since the volume V_{dot} of the transferred ink remains the same, the following applies:

$$A\,\varphi\,h = A\,\varphi'\,h' = V_{\mathrm{dot}} \qquad [1]$$

With Equation [2] $\Delta a = \dfrac{\varphi' - \varphi}{\varphi}$ one can express the area coverage φ' as

$$\varphi' = \Delta a\,\varphi + \varphi = \varphi(1 + \Delta a) \qquad [3]$$

where Δa represents the relative increase in area due to the increased spreading. Δa = 10 % means, for example, an increase in area of 10 %. With Equation [3] the layer thickness of the more spreading point is then calculated from Equation [1] as:

$$h' = h\frac{\varphi}{\varphi'} = \frac{h}{1 + \Delta a} \qquad [4]$$

The absorption of light occurs through the pigments in the ink and can be described by Lambert-Beer's law.

$$I_{\mathrm{F}} = I_0\,e^{-\tau h} \qquad [5]$$

with I_{F} : light intensity after passing the ink layer, I_0 : incident light intensity, τ : absorption coefficient, and h : ink layer thickness.

Thus the intensity for the dot together with its reserved area:

$$I_{\mathrm{P}} = (1 - \varphi)\,I_0 + \varphi\,I_{\mathrm{F}} = (1 - \varphi)I_0 + \varphi e^{-\tau h} I_0 = (1 - \varphi + \varphi e^{-\tau h})\,I_0 \qquad [6]$$

The first part is essentially the Murray-Davis formula in intensity notation. $(1 - \varphi)\ I_0$ describes the light intensity generated by the uncovered surface that has no absorption. $\varphi\ I_F = \varphi\ I_0\ e^{-\tau h}$ describes the light intensity that is added by the residual intensity after absorption by the dot. The ratio of the light intensities from the two dots is given by:

$$R_A = \frac{I_D{}'}{I_D} = \frac{I_0\left(1 - \varphi' + \varphi' e^{-\tau h'}\right)}{I_0(1 - \varphi + \varphi e^{-\tau h})} = \frac{1 - \varphi(1 + \Delta a) + \varphi(1 + \Delta a) e^{-\frac{\tau h}{(1+\Delta a)}}}{1 - \varphi + \varphi e^{-\tau h}} \quad [7]$$

Further

$$R_A = \frac{1 - \varphi(1 + \Delta a) + \varphi(1 + \Delta a) e^{-\frac{\tau h}{(1+\Delta a)}}}{1 - \varphi(1 + \Delta a) + \varphi \Delta a + \varphi e^{-\tau h}} = \frac{\varphi_T + \varphi(1 + \Delta a) e^{-\frac{\tau h}{(1+\Delta a)}}}{\varphi_T + \varphi(\Delta a + e^{-\tau h})} \quad [8]$$

where $\varphi_T = 1 - \varphi\ (1 + \Delta a)$ describes the area within A that remains uncovered at the more spreading dot D' (see Figure 1) and thus has no absorption. This term is the same for both dots. It is therefore sufficient to look at the remaining term to prove that the more spreading dot D' has a lower residual intensity and thus a higher colour intensity. Without φ_T and by reducing the factor φ the quotient R_D results from Equation [8] in

$$R_D = \frac{(1 + \Delta a)\ e^{-\frac{\tau h}{(1+\Delta a)}}}{\Delta a + e^{-\tau h}} \quad [9]$$

This quotient describes the brightness ratio of the two dots alone, i.e. it refers to the area occupied by the more spreading dot D'. The completely ink covered area of the larger point D' is compared with the combination of the thicker but smaller dot D and the additional uncovered area, which together give the area of dot D'.

As an example a typical absorption for the ink layer of density 1.0 is assumed. This density results from an absorption of 90 % of the light, while 10 % remains. Thus acc. to Equation [5]

$$\frac{I_F}{I_0} = 0.1 = e^{-\tau h} \text{ and } \tau d = 2.3 \quad [10]$$

This is conservative, at least for process colours, which usually have a reasonably higher density. If we now evaluate the Equation [9] for this density, we get

$$R_D = \frac{(1 + \Delta a)\ e^{-\frac{2.3}{(1+\Delta a)}}}{\Delta a + e^{-2.3}} \quad [11]$$

For $\Delta a = 0$ ... 40 % the following Table 1 is calculated for R_A and R_D. For the calculation of R_A, a medium-sized (first) dot D with an area coverage $\varphi = 40$ % is assumed.

It can be clearly seen that $R_D < 1$ for $\Delta a > 0$, i.e. the numerator of R_D is also always smaller than the denominator. Thus the residual intensity of the more spreading dot is smaller than that of the less spreading dot. For R_D this is a massive effect with 6 % decrease in intensity with only 1 % more spreading. For the entire grid cell, the decrease in intensity is smaller, but the effect is still significant.

Table 1: Brightness ratio R_D of the two dots D and D' and brightness ratio R_A of the two dots D and D' together with uncovered area of their grid space A against the relative spreading Δa of D'

Δa	R_D	$R_A(\varphi = 40\ \%)$
0 %	100 %	100.0 %
1 %	94 %	99.6 %
2 %	89 %	99.2 %
3 %	85 %	98.8 %
4 %	81 %	98.4 %
5 %	78 %	98.0 %
10 %	68 %	96.0 %
15 %	62 %	94.1 %
20 %	59 %	92.3 %
25 %	57 %	90.5 %
30 %	55 %	88.8 %
35 %	55 %	87.2 %
40 %	54 %	85.7 %

2.1 Influences of process parameters on ink spreading

Various factors of printing influence the spreading of the ink on the substrate. A well-founded assumption is, that dot spreading is enhanced by lowering the ink viscosity, as this promotes the "mobility" of the ink and the increased solvent content means that the ink remains liquid for longer when drying and thus has more time to spread.

Further our assumption is that spreading of the dots is enhanced by the application of ESA, which promotes the emptying of the cells and draws the ink onto the substrate. Therefore, the electrostatic force supports the capillary forces, the emptying of the cells is more complete and more ink is transferred.

Slower printing speed is assumed to reduce the ink loss doctored out of the cells. As a result, more ink remains in the cells and more ink is transferred, leading to a higher colour intensity. This effect should be effective across the entire gradation, i.e. both in the area of visible dots and after flooding in the area of the fully covered ink layer. However, since more ink leads both to a directly higher ink thickness and to more spreading, the effect is stronger in the dot area. On the other hand, the slower printing speed leads to increased drying of the ink in the cells before transfer, which in turn can lead to less ink transfer or reduced spreading due to the higher viscosity.

From these assumptions it can be deduced that in the area of dot transfer, i.e. before flooding, a reduced viscosity and the use of ESA should play the most significant roles. Both factors, on the other hand, should no longer or considerably less be visible in the area of the fully covered ink layer.

3. Materials and methods

3.1 Gravure printing trial

3.1.1 Printing form layout

We used an electromechanically engraved, chrome-plated printing form (circumference 700 mm, engraving width 590 mm). The printing form was engraved on a Hell K500 engraving system (Hell Gravure Systems GmbH & Co. KG, Kiel, Germany) with a stylus angle 120°. The relevant raster angle for this article is Hell engraving angle 0 with raster frequency 80 lines/cm displayed in cyan. Angle 0 realises a compressed cell shape with a raster angle of 36.87° and an effective raster frequency of 80 lines/cm. The wedge with 28 tonal values (0, 1, 2, 3, 4, 5, 8, 10, 15, 20, 25, 30, 35, 40, 45, 50, 55, 60, 65, 70, 75, 80, 85, 90, 93, 95, 98, 100 %) in the lower part of area (C) is the relevant part in the print form layout for this article, see Figure 2. The print form layout was developed for use with the analysing methods as described in Brumm, et al. (2022).

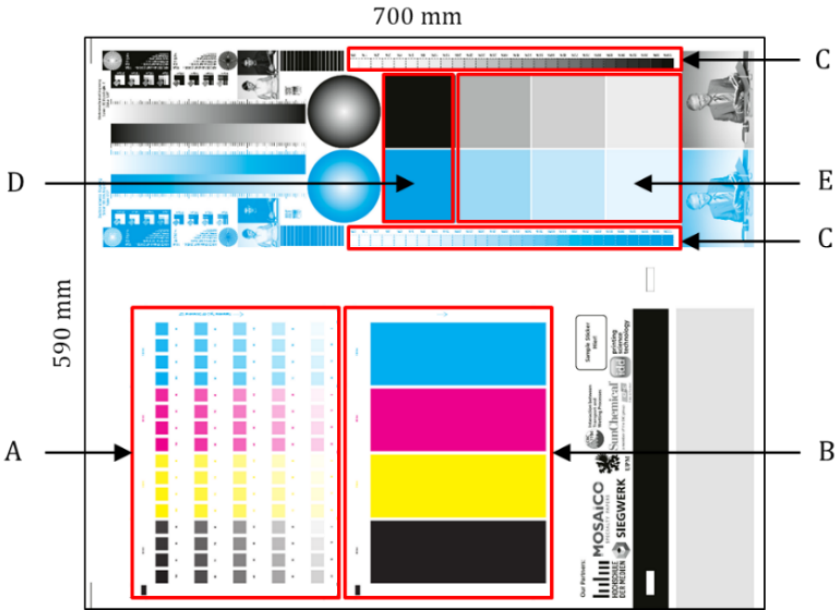

Figure 2: Print form layout; lower part of C is used for gradation measurements

3.1.2 Design of experiments

A 3-day printing trial was conducted on an industrial-scale gravure printing machine Bobst Rotomec MW 60 (Bobst, Mex, Switzerland) with a printing form cylinder of 700 mm circumference and 700 mm face and a maximum printing speed of 300 m/min. The design of experiments uses seven factors, which are varied during the trial. The trial itself is described in detail in Brumm, et al. (2022). The design of experiments was based on ascending velocity ramps with the printing velocities 15, 30, 60, 90, 120, 180 and 240 m/min as target velocities. ESA was always turned off for 15 m/min and 30 m/min and was turned both off and on for the other printing velocities. Furthermore, the ink viscosity and the angle of the doctor blade were varied in three steps (high, medium, low). The water-based ink was prepared using four different viscosities (base, high, medium, low). For diluting the solvent-based inks, a nearly azeotropic mixture of ethanol (30 %) and ethyl acetate (70 %) was used. The water-based ink was diluted with tab water. The ambient temperature and humidity were recorded and the ink temperature was monitored during the printing trial. Printing ink viscosity was measured with a 4 mm ISO flow cup and was controlled with a Fasnacht Viscopoint IL CPS viscosity sensor in combination with a viscosity control system Fasnacht pentasmart. Doctor blade pressure (1.5 bar), impression roller pressure (1.5 bar) as well as impression roller hardness (80 Shore A) were kept constant. In total, 17 velocity ramps were performed with 12 parameter combina-

tions each. For each parameter combination, 20 sheets (each 600 mm × 700 mm) were manually cut out, which results in over 4 000 sheets in total. The sheets were post-processed and evaluated according to the chosen analyzing method which mostly required further cutting as well as digitization steps. The areas A and B were used for classification of patterns with deep learning and Fourier analysis of ribbing patterns. The areas C were used for gradation measurements. With areas D and E mottle values and missing dots were evaluated.

For this article, only a small section of the large DoE is used, which is described below, considering factors:

- Printing velocity: Three different velocities from the trial, 120, 180 and 240 m/min, were used for this DoE.
- ESA: Two settings were used: off and on with 1 mA current (Enulec, Trittau, Germany, ESA1000compact), which is nearly maximum.
- Ink viscosity: Three different viscosities were used with the solvent based inks: high = 24 sec ISO#4, medium = 20 sec ISO#4, low = 17 sec ISO#4 (DIN EN ISO 2431) (Deutsches Institut für Normung, 2019).

Solvent based ink optimised for film (NC 133-15, magenta, Siegwerk, Siegburg, Germany) was printed on film (WSS 20 BoPP solid white film, both sides heat sealable, treated, Taghleef Industries, Dubai, United Arab Emirates). The patches with Hell gravure angle 0 (cyan colour in Figure 2) were measured for the evaluation. The ambient temperature and humidity were recorded and the ink temperature was monitored during the printing trial.

3.2 Sample analysis – gradation measurements

A measure of colour intensity is the Spot Colour Tonal Value (SCTV) according to ISO 20654:2017 (International Organization for Standardization, 2017), which is calculated from the CIE $L^*a^*b^*$ values in relation to the 100 % solid tone and normalised to paper white. The higher the SCTV, the stronger the colour of the measured field. For investigating the ink spreading this number, like dot gain, is especially advantageous, as both calculations reference to the solid tone. This leaves the relative colour intensity of the different tonal values in respect to the solid.

The gradation measurements were performed on the tonal value wedge over the whole tonal range (28 steps, see Section 3.1.2) of part C (Figure 2). The spectral values were measured by a Techkon SpectroDens spectro-densitometer (TECHKON GmbH, Königstein im Taunus, Germany) and stored as a spectrum and as CIE $L^*a^*b^*$ values.

Three substrate sheets were evaluated for each test point. Each colour wedge was measured three times so that measurement errors could be identified and corrected immediately. The resulting nine CIE $L^*a^*b^*$ measurements per colour field were averaged. From these SCTV were calculated and subtracted from the nominal tone values. The resulting curve, called dSCTV, should ideally be a horizontal line with the value 0.

4. Results and discussion

4.1 Tonal area evaluation

The factors speed, ESA and viscosity (see 3.1.1) result in 18 different factor combinations. As an example of the effect of the factors on spreading a section of the 50 % tonal values patches of EFMvhamV180E0, EFMvmamV180E0 and EFMvlamV180E0 (= all three samples at 180 m/min and ESA off, with high, medium and low viscosity) are shown in Figure 3. The increase in dot area is clearly visible, as is the reduction in intensity.

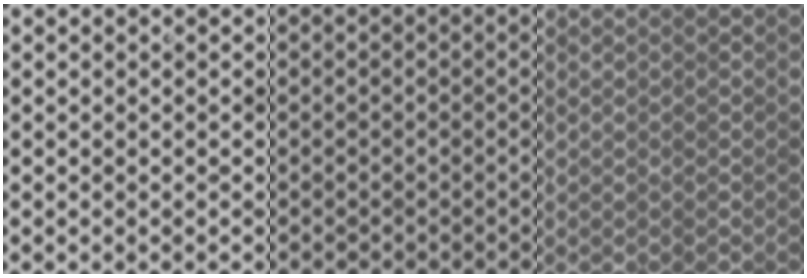

Figure 3: 50 % tonal values patches of EFMvhamV180E0, EFMvmamV180E0 and EFMvlamV180E0 (organic solvent based ink on film with 180 m/min and ESA off, high viscosity left, medium viscosity middle, low viscosity right picture) Hell gravure angle 0, 80 lines/cm, scanned with 1 200 dpi

The dSCTV curves of this configuration are shown in Figure 4.

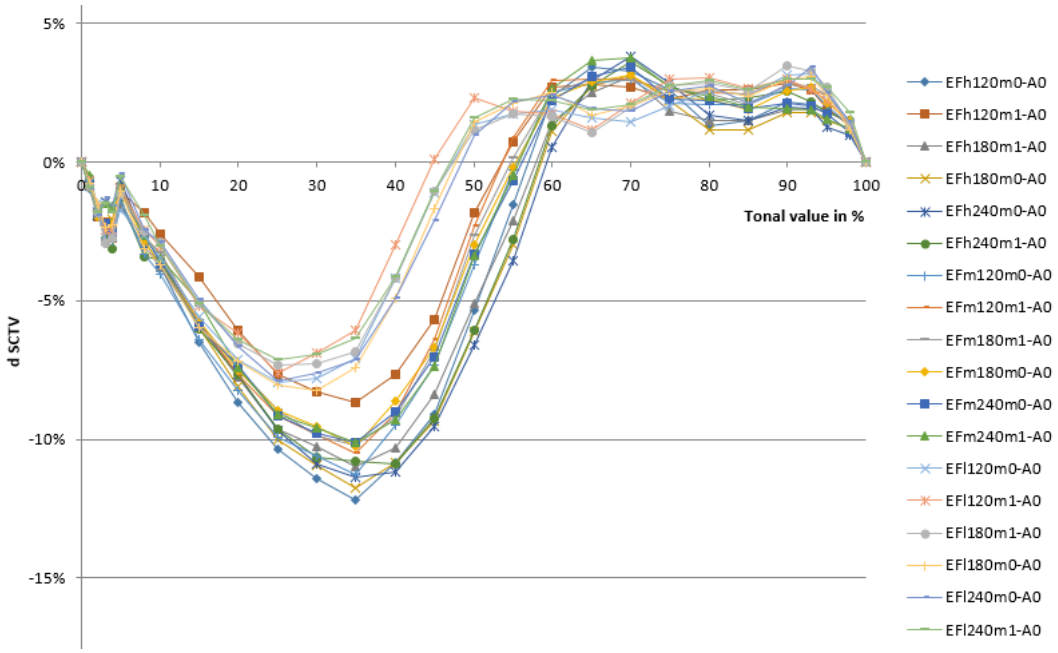

Figure 4: The dSCTV (= SCTV – TV) curves for different test points (legend for EFvsssme-A0: E – ethyl-based ink, F – film, v – viscosity (l, m, h), sss – speed (120, 180, 240), m – middle blade angle, e – ESA (0/1))

The dSCTV values in the area of the single dots (low tonal values up to ca. 60 %) are significantly negative, as the gradation used was not optimally adapted for these printing conditions. Nevertheless, there are clear differences for the different printing conditions. To further elaborate these differences, the centre point of the DoE was taken as reference (EFm180m1: viscosity = m, speed = 180 m/min, ESA = 1) and all values were related to this reference. Then the curves in Figure 5 result.

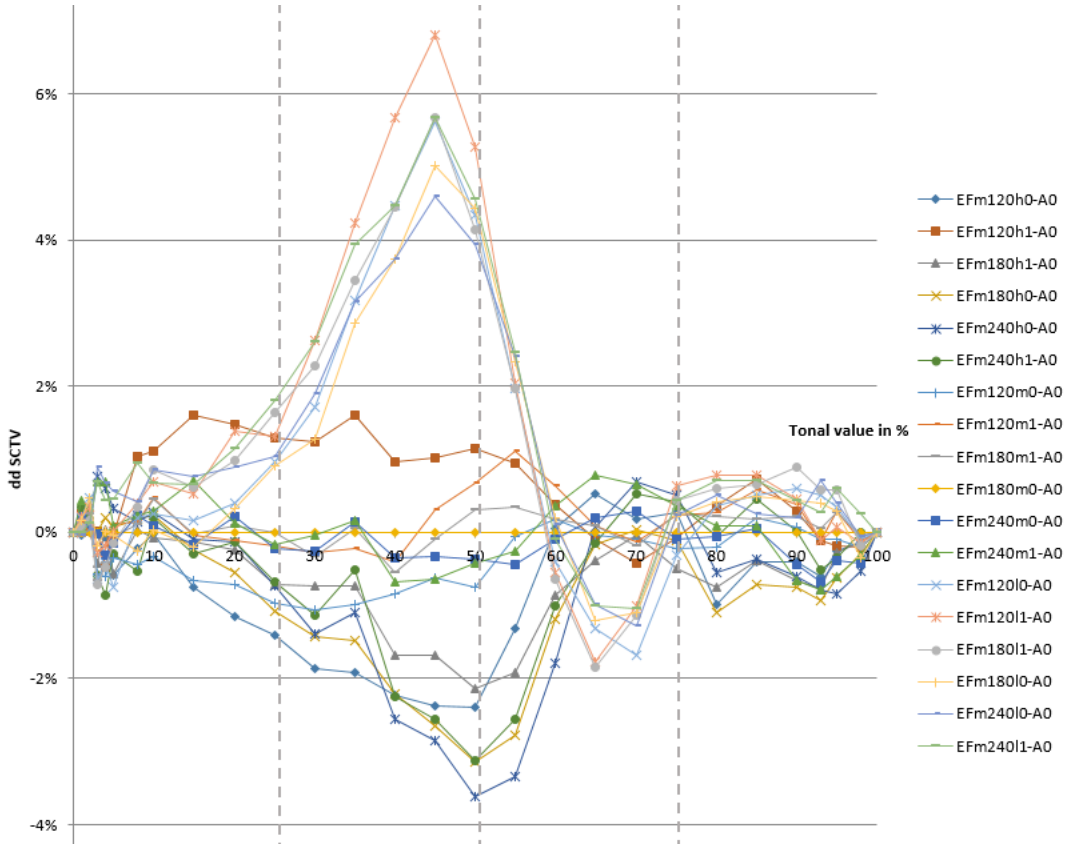

Figure 5: The ddSCTV (= SCTV – TV referenced to EFm180m1) curves for different test points; the dashed lines indicate the 3 tonal values used in the ANOVA evaluation (legend fo EFvsssme-A0: E – ethyl-based ink, F – film, v – viscosity (l, m, h), sss – speed (120, 180, 240), m – middle blade angle, e – ESA (0/1))

The four curves with the highest values in the 50 % range belong to the low viscosity, the four with the lowest values to the high viscosity. This already shows that viscosity plays the most important role and it works in different directions for the dots and the homogeneous areas.

To further illustrate these facts, the colour deviation in dE (DE2000) and the chromaticity differences dC (ΔC^*_{ab}) of the 50 % tonal value fields as well as the 75 % tonal values in relation to the trial point Efm180m0 (medium viscosity, medium speed – 180 m/min, ESA off) are plotted in Table 2 for tonal value 50 % and in Table 3 for tonal value 75 %. In contrast to 50 % tonal value, which is within the dot area, the 75 % tonal value is in the range where in rotogravure a more or less homogeneous ink film covers the complete grid cell.

Table 2: Left: dE values and right: dC values of patches in relation to patch with medium viscosity, medium speed – 180 m/min, ESA off for the 50 % tonal value; the value of EFm120h1 for 50 % was measured an outlier and is omitted for clarity

dE	ESA	off			on		
50%	Visco.	h	m	l	h	m	l
Speed	120	1,58	0,23	2,75		0,76	3,09
	180	2,26	**0,00**	2,72	1,21	0,41	2,67
	240	2,80	0,38	2,33	2,21	0,52	2,67

dC	ESA	off			on		
50%	Visco.	h	m	l	h	m	l
Speed	120	-3,99	-0,63	4,70		1,27	5,45
	180	-4,96	**0,00**	4,49	-2,89	0,43	4,35
	240	-6,49	-0,94	3,45	-4,94	-1,55	4,05

Table 3: Left: dE values and right: dC values of patches in relation to patch with medium viscosity, medium speed – 180 m/min, ESA off for the 75 % tonal value

dE	ESA	off			on		
75%	Visco.	h	m	l	h	m	l
Speed	120	1,14	0,24	2,20	1,14	0,37	1,85
	180	0,63	**0,00**	1,98	0,54	0,25	2,07
	240	0,70	0,26	2,39	0,49	0,29	2,35

dC	ESA	off			on		
75%	Visco.	h	m	l	h	m	l
Speed	120	0,68	0,04	-1,78	0,92	0,05	-1,69
	180	0,55	**0,00**	-1,83	0,50	-0,09	-1,93
	240	0,45	-0,12	-1,89	0,41	-0,12	-1,90

As can be seen the dE values are overall smaller with 75 % and the viscosity change makes the biggest difference in both tonal values. However, dE is not sensitive to directions. So dC is more interesting. For dots the chroma increases very significantly towards lower viscosity with dC at least +7 and up to +10 between high and low. This matches with the described model. For the homogeneous area the chroma does not increase, but in the contrary decreases in the range of dC = −2.5. This is due to the lower pigment content and the lack of the possibility for spreading. In the dot area, the actual difference in chroma due to spreading should therefore be even greater, as the pigment concentration also decreases there with lower viscosity. From the values for the 75 % tonal value, this additional chroma difference should be also more than 2.

4.2 Evaluation by ANOVA multivariance analysis

These results can be quantified by a multivariance analysis. This was done with a Java program written by Weichmann (2015) according to Montgomery (2021) and Backhaus, et al. (2018). The programme is specifically designed to handle multiple factor subsets of a Design of Experiments with a variety of effects to be used in the evaluation of the whole trial. The effects used here are in accordance to 4.1 the SCTV value of the 50 % tonal value field and the 75 % tonal value field and additionally the 25 % tonal value field for a second value in the dot area.

The Pareto diagram of the effects and the main effects plot are used to graphically display the significance of the different factors. In the Pareto diagram the factors are standardized to the critical value of the *F*-distribution for an error probability of 5 %. The *x*-axis shows the ratio of the factors' effect and the critical *f*-value for the degrees of freedom for this effect for an error probability of 5 %. So the value 1 (green dashed line in Figures 4 and 5) represents the critical value for the effect. Values above 1 are significant and values below are not significant in respect to the 5 % error probability. The higher the value, the more significant the factor for this effect. A value of 2.5 e.g. means that this factor exceeds this critical value by a factor of 2.5 and is therefore clearly significant. On the *y*-axis the factors and the interactions of two factors are listed.

The diagram of the effects' mean values for each level of each main factor shows the reaction of the effect to the variation of the factor. The *y*-axis plots the dSCTV value, the *x*-axis marks the different settings of the factor.

The following diagrams (Figures 6, 7 and 8) show the results of the dSCTV values for the three tonal values 25 %, 50 % and 75 %.

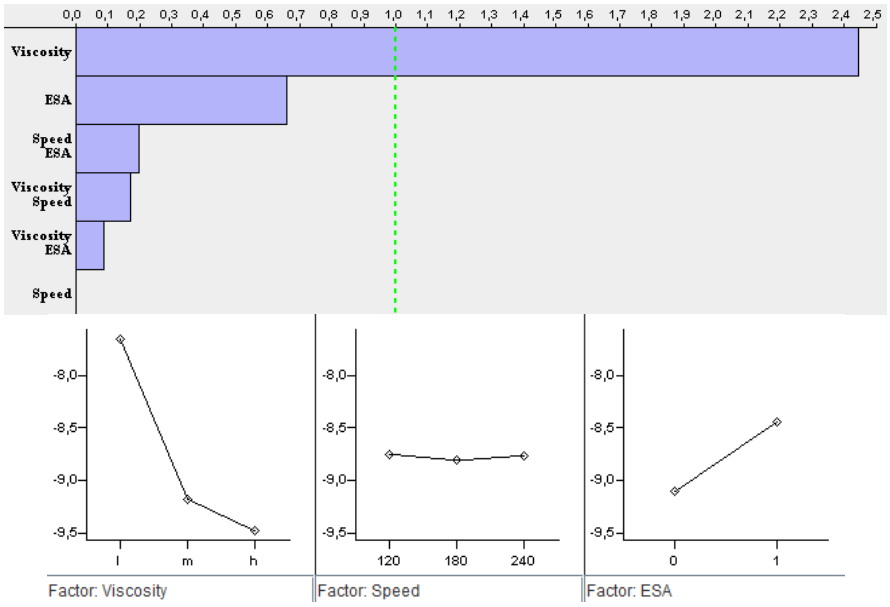

Figure 6: ANOVA evaluation of SCTV for TV = 25 %
Pareto diagram (x-axis: ratio between critical value of f-distribution and factor's value) and mean values of the test points with respective factor level (y-axis: dSCTV value, negative for 25 % tonal value)

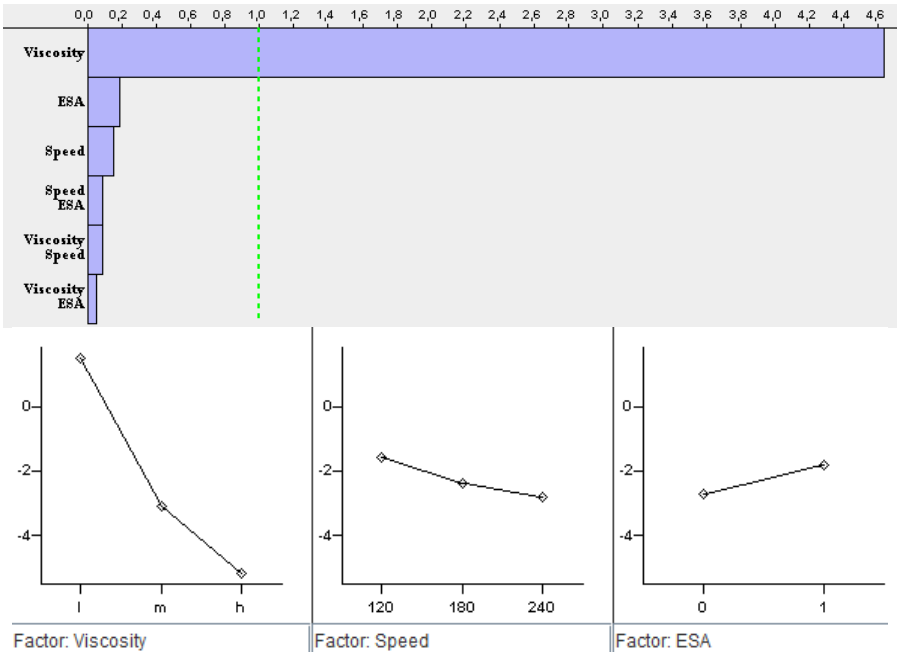

Figure 7: ANOVA evaluation of SCTV for TV = 50 %
Pareto diagram (x-axis: ratio between critical value of f-distribution and factor's value) and mean values of the test points with respective factor level (y-axis: dSCTV value)

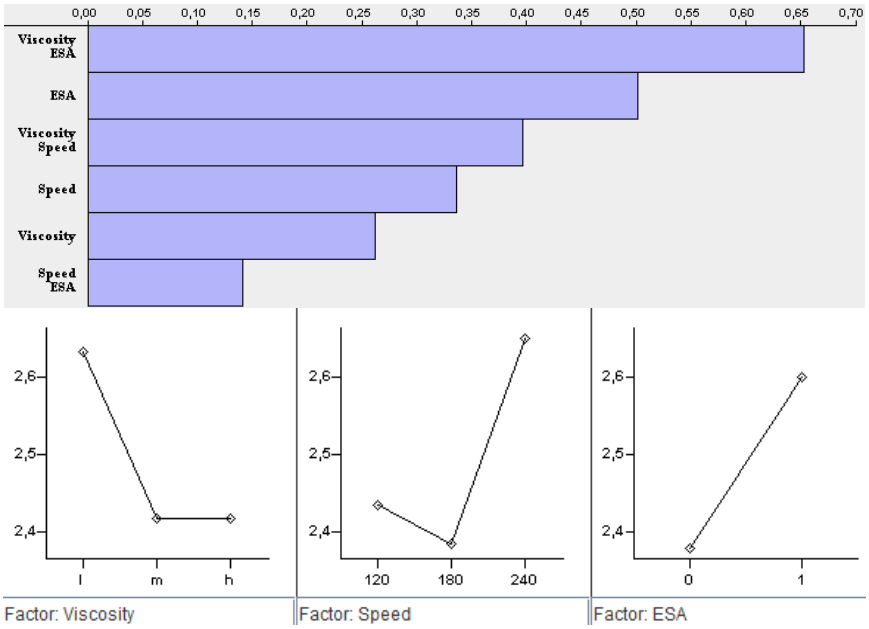

Figure 8: ANOVA evaluation of SCTV for 75 %
Pareto diagram (x-axis: ratio between critical value of f-distribution and factor's value) and mean values of the test points with respective factor level (y-axis: dSCTV value)

The statement from 4.1 that the viscosity has by far the highest influence, is reflected by this evaluation for 25 % and 50 %. It is indeed the only significant factor. ESA seems to be of slightly higher importance than speed, however both are not significant. The mean values show this finding directly. The slope between the averaged dSCTV values of the factor levels is maximal with viscosity. This is, however, different on paper substrates, where ESA plays a much more pronounced role due to the higher roughness of the paper compared to film.

The 75 % tone value offers a completely different picture. As in this range spreading no longer plays a role because no additional white areas can be covered, the effects are indeed all well below the significance threshold with an interaction of viscosity and ESA still as the strongest factor. Please note the much smaller spread of the mean values in the mean value diagram.

5. Conclusion and outlook

A model for the effect of different degrees of spreading of a dot was presented, based on the Murray-Davies formula and the Lambert-Beer absorption law, as well as on geometric considerations for spreading. With the help of this model, it can be shown that a more spreading dot with the same ink volume absorbs more and thus appears darker than a less spreading dot. The effect of different printing conditions, changed viscosity, strength of ESA and printing speed on dot gain i.e. SCTV were discussed. Ink viscosity was assumed to be the strongest factor, followed by ESA and printing speed. This could be quantified with the help of a design of experiment, where viscosity showed to be the only factor of major significance.

Further interesting dependencies could be demonstrated in the evaluation of the print test. However, the details of these are beyond the scope of this article.

Acknowledgements

We kindly thank Pauline Brumm, Thorsten Euler and Lara Philipp for their contribution in this elaborate print trial and their part of the sample and data preparation. We kindly thank Siegwerk for providing printing inks.

References

Backhaus, K., Erichson, B., Plinke, W. and Weiber, R., 2018. *Multivariate Analysemethoden: Eine anwendungsorientierte Einführung.* 16th ed. Berlin, Heidelberg: Springer.

Beilenhoff, S., 2011a. Troubleshooting im Verpackungstiefdruck. *Flexo+Tiefdruck*, 22(5), pp. 14–16.

Beilenhoff, S., 2011b. Troubleshooting im Verpackungstiefdruck. *Flexo+Tiefdruck,* 22(6), pp. 22–24.

Brumm, P., Lindner, N., Weber, T.E., Sauer, H.M. and Dörsam, E., 2021a. A deep learning approach for the classification task of gravure printed patterns. In: C. Ridgway, ed. *Advances in Printing and Media Technology: Proceedings of the 47th International Research Conference of iarigai.* Athens, Greece, 19–23 September 2021. Darmstadt: iarigai, pp. 2–9. https://doi.org/10.14622/Advances_47_2021.

Brumm, P., Weber, T.E., Sauer, H.M. and Dörsam, E., 2021b. Ink splitting in gravure printing: localization of the transition from dots to fingers. *Journal of Print and Media Technology Research*, 10(2), pp. 81–93. https://doi.org/10.14622/JPMTR-2016.

Brumm, P., Sprinzing, T., Euler, T., Galus, M., Weichmann, A. and Dörsam, E., 2022. *Creation of a comprehensive high-resolution image data set on an industrial web press to investigate hydrodynamic pattern formation in gravure printing.* In: C. Ridgway, ed. *Advances in Printing and Media Technology: Proceedings of the 48th International Research Conference of iarigai.* Greenville, USA, 19–21 September 2022. Darmstadt: iarigai, pp. 109–115. 10.14622/Advances_48_2022_08.

Deutsches Institut für Normung, 2019. *DIN EN ISO 2431 Paints and varnishes – Determination of flow time by use of flow cups (ISO 2431:2019, Corrected version 2019-09)*. Berlin: ISO.

Grau, G., Cen, J., Kang, H., Kitsomboonloha, R., Scheideler, W.J. and Subramanian, V., 2016. Gravure-printed electronics: recent progress in tooling development, understanding of printing physics, and realization of printed devices. *Flexible and Printed Electronics*, 1(2): 023002. https://doi.org/10.1088/2058-8585/1/2/023002.

Hübner, G., 1991. *Ein Beitrag zum Problem der Flüssigkeitsspaltung in der Drucktechnik.* Dissertation. Technische Hochschule Darmstadt. https://doi.org/10.25534/tuprints-00013550.

International Organization for Standardization, 2017. *ISO 20654:2017 Graphic technology – Measurement and calculation of spot colour tone value*. Geneva: ISO.

Joshi, A.V., 2016. Effect of electrostatic assist and gravure process parameters on voids and dot skips reduction in shrink PVC film. *Journal of Coatings Technology and Research*, 13(3), pp. 527–543. https://doi.org/10.1007/s11998-015-9774-0.

Kumar, S., 2015. Liquid transfer in printing processes: liquid bridges with moving contact lines. *Annual Review of Fluid Mechanics*, 47(1), pp. 67–94. https://doi.org/10.1146/annurev-fluid-010814-014620.

Kunz, W., 1975. Ink transfer in gravure process. In: *TAGA Proceedings 1975: Annual meeting of the Technical Association of the Graphic Arts*. Toronto, Ontario, 1975. Rochester, NY, USA: TAGA, pp. 151–176.

Montgomery, D.C., 2021. *Design and analysis of experiments.* 10th ed. Hoboken, NJ, USA: Wiley.

Weichmann, A., 2015. *GravureQ: commercially available software for mottle and missing dots analysis*. Hochschule der Medien Stuttgart, Germany.

DOI 10.14622/Advances_49_2023_15

Investigation on an alternative printing plate for offset lithography

Felix Knödl[1], *Hans Martin Sauer*[1], *Jakob Feldmann*[1], *Dieter Spiehl*[1], *Andreas Blaeser*[2,3] *and Edgar Dörsam*[1]

[1] Technical University of Darmstadt, Department of Mechanical and Process Engineering, Institute of Printing Science and Technology, Magdalenenstr. 2, 64289 Darmstadt, Germany

[2] Technical University of Darmstadt, Department of Mechanical and Process Engineering, Institute for BioMedical Printing Technology, Magdalenenstr. 2, 64289 Darmstadt, Germany

[3] Technical University of Darmstadt, Center for Synthetic Biology, Schnittspahnstr. 10, 64287 Darmstadt, Germany

E-mails: knoedl@idd.tu-darmstadt.de; sauer@idd.tu-darmstadt.de; feldmann@idd.tu-darmstadt.de; spiehl@idd.tu-darmstadt.de; blaeser@idd.tu-darmstadt.de; doersam@idd.tu-darmstadt.de

Short abstract

This work investigates wetting properties of thermo and waterless printing plates commonly used in offset lithography with the goal to analyse the potential of a new printing plate making process by surface laser structuring. Measurements of the surface free energy of thermo, waterless and laser-structured aluminum samples are presented and compared. Also, the surface tension of fountain solutions and inks are measured. Laser-structured aluminum samples reached a comparable surface free energy like the waterless offset printing plate. With the help of microscopic measurement, the topography of the printing plates and the laser-structured aluminum samples were evaluated. In addition, wetting envelopes are presented which can be used to predict the wetting of a substrate with a liquid whose surface tension is known.

Keywords: wetting, laser, structure, texture, surface free energy, surface tension, wetting envelope

1. Introduction and background

Offset lithography is a commonly used printing technique that involves transferring ink from a printing plate to a rubber blanket and then onto paper. It is a highly precise and efficient process that allows for the creation of high-quality prints in large quantities. Offset lithography is widely used in the printing of books, magazines, brochures, and other commercial materials like packaging. The wetting and de-wetting properties of this printing plate play an essential role in offset lithography because it is a flat printing process and therefore the whole surface of the printing plate is in contact with the substrate. Here, non-image and image areas virtually lie in the same plane on the printing plate (Kipphan, 2000). The differentiation of ink and fountain solution is mainly controlled by chemical-physical wetting conditions. Accordingly, printing plates have different surface properties in the image and non-image areas. Particularly important is the surface free energy (SFE) of the printing plate, which can be expressed by the sum of the disperse and polar components (see Equation [4]). Equation [1] shows the regularities in contact angle determination which is the basis to further calculate the SFE;

$$\sigma_{sg} = \sigma_{lg} \cdot cos\ \theta + \sigma_{ls} \qquad [1]$$

where σ_{lg} is the liquid surface tension, σ_{sg} is the solid surface tension, σ_{ls} is the liquid-solid interfacial tension and θ is the angle of contact for smooth surfaces defined by Young (1805). In Figure 1 the factual situation is schematically displayed.

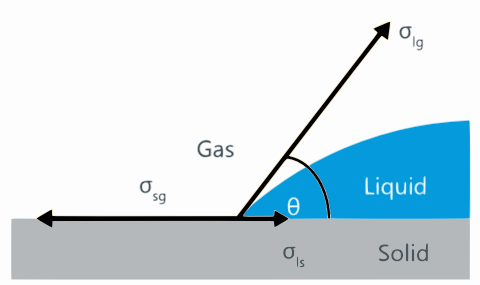

Figure 1: Wetting of a smooth solid surface with liquid surrounded by gas (Krüss, n.d.); θ: angle of contact (liquid-solid); σ_{lg}: liquid surface tension; σ_{sg}: solid surface tension; σ_{ls}: liquid-solid interfacial tension

To determine the SFE of a solid surface usually test fluids with known surface tensions are used and their angle of contact on the solid surface is measured. Typical fluids are water, ethanol, ethylene glycol, diiodomethane or glycerol. At least two fluids are needed to calculate the SFE of the solid surface to further create a wetting envelope. With the help of a wetting envelope, the wetting prediction of other fluids with known surface tension (SFT) on this solid surface can be estimated. The following Equation [2] describes the model according to Owens, Wendt, Rabel and Kaelble (OWRK) for calculating the SFE of a solid surface with disperse σ^D and polar σ^P components (Owens and Wendt, 1969; Thomsen, 2008). There are also other models but OWRK method is most suitable for this work.

$$\sigma_{lg}(1+\cos\,\theta) = 2\left(\sqrt{\sigma_{sg}^{D}\cdot\sigma_{lg}^{D}} + \sqrt{\sigma_{sg}^{P}\cdot\sigma_{lg}^{P}}\right) \quad [2]$$

For calculating the Radius $R(\theta)$ of the wetting envelope, Equation [3] and Equation [4] is used.

$$R(\theta) = \left[\left(\frac{2}{1+cos\theta}\right)\left(\frac{\sqrt{\sigma_{sg}^{D}\cdot cos\theta} + \sqrt{\sigma_{sg}^{P}\cdot sin\theta}}{cos\theta + sin\theta}\right)\right]^2 \quad [3]$$

$$\sigma_i^P + \sigma_i^D = \sigma_i \quad [4]$$

Ink and fountain solution are matched to these values for the SFE, so that the fountain solution preferably adheres to the non-image areas and the ink to the image areas. The better the disperse and polar components match, the higher are the adhesion forces between printing plate (image area) and ink or printing plate (non-image area) and fountain solution (dataphysics, 2012). In general, the terms oleophilic (image area) and hydrophilic (non-image area) are used in this context, but these explicitly represent a simplified use of terms, since fountain solution does not consist exclusively of water and, in addition, the ink forms an emulsion with the fountain solution during the printing process.

Offset printing plates are approximately 0.15 mm to 0.6 mm thick anodized aluminum plates coated with a polymer. In the case of waterless offset printing plates, they have an additional silicone layer. By exposing the polymer or silicone layer with light from laser diodes, the printing and non-printing areas are created on the printing plate. In conventional printing plates, fountain solution adheres to the anodized areas and the printing ink to the remaining polymer layer. In waterless offset printing, no fountain solution is required. The ink does not adhere to the areas with a silicone layer, but likewise only to the polymer layer. For every kind of printing plate and wetting mechanism used, the printing plate, fountain solution and ink must interact perfectly (Tian, Mao and Shen, 2009).

In the early years of offset lithography, bi- or tri-metal plates were used instead of anodized and polymer coated aluminum plates (mono-metal plates). Bimetallic plates (chrome-brass) were used in web offset

and trimetallic plates (chrome-copper-aluminum/iron) for sheetfed offset. Here, the metals copper and brass are considered ink-receptive, which are exposed by selectively etching the chrome layer. In small offset machines, waterproof plastic or paper printing plates were also used (Aull, 2001). Nowadays, thermal printing plates are mostly used, which are exposed with the help of infrared laser diodes. There are also special printing plates that do not require a washout process with chemicals. These are also known as *chem-free* or *process-less* printing plates, as the uncured polymer residues on the printing plates are removed by the inking and dampening rollers from the printing plate at the start of the printing process. However, these only represent a global market share of around 10 % (Nicolay, 2012).

The influence of laser-structuring on the wetting behavior of metal surfaces is currently being investigated at many research institutes and many scientific disciplines. In most cases, aluminum and steel but also other metals are processed using various laser-structuring methods (Kietzig, Hatzikiriakos and Englezos, 2009). The surface is then characterized by measuring the contact angle with water. The SFE of the manufactured samples are not carried out, but chemical analyses of the surfaces are performed and it has been recognized that the wetting properties (surface chemistry) of the metals can be altered. This can be done in common air (Dongre, et al., 2021), but can also be accelerated by using chemical treatment fluids (e.g. fluorine compounds, silicone oil). After initial laser structuring of the surface, all metals exhibit superhydrophilic wetting properties (contact angle towards less than 10°). Aging can change the wetting properties to the opposite. The surface becomes (almost) superhydrophobic (contact angle greater than 150°) (Tran and Chun, 2021).

If rough surfaces are considered, there are two possible wetting scenarios: Wenzel (1936) and Cassie-Baxter (Cassie and Baxter, 1944). Figure 2 shows these two wetting states.

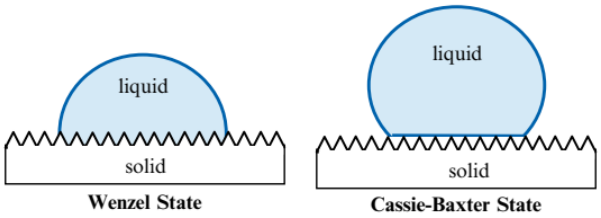

Figure 2: Illustration of the Wenzel and Cassie-Baxter state (Law and Zhao, 2016)

In the Wenzel state, the surface is completely wetted. The decisive factor here is whether the starting material is hydrophilic or hydrophobic. With hydrophilic materials, a superhydrophilic surface, i.e. spreading wetting with water, is achieved by roughening the surface. If, on the other hand, the starting material is moderately hydrophilic or hydrophobic, the wetting property increases in the direction of superhydrophobicity and water is repelled from the surface. Sometimes a metastable state in between these two states occurs, additionally vibration can transfer a hydrophobic surface to hydrophilic one (Wenzel, 1936). Equation [5] is used to calculate the contact angle θ_W in the Wenzel state:

$$\cos \theta_w = r \cdot \cos \theta \qquad [5]$$

with $r = \frac{\text{actual surface area}}{\text{projected surface area}}$

In the Cassie-Baxter state, air is trapped between the rough surface and the liquid during the wetting process, and a kind of interface of air cushion is formed between the two media. This condition results in a large contact angle and the surface is superhydrophobic or even superoleophobic when wetted with water (Cassie and Baxter, 1944). Currently, a wide variety of topographic structural elements are being investigated so that the Cassie-Baxter state becomes as stable as possible and remains therefore under pressure.

As an example, the well-known *Lotus Effect* is based on the Cassie-Baxter state. Equation [6] is used to calculate the contact angle θ_{CB} in the Cassie-Baxter state:

$$\cos\theta_{CB} = f \cdot \cos\theta + (f - 1) \quad [6]$$

where f is the solid-area fraction. The aim of this work is first to determine the SFE of two common printing plates (thermo printing plate and waterless printing plate) with the help of contact angle measurement using three test fluids. Additionally, the SFT of two inks and two fountain solutions are determined and set in context to the results of the two printing plates and already published literature. Laser-structured aluminum samples with varying laser parameters are fabricated and the SFE is also be determined and examined for analogies to the printing plates. A future goal is to produce printing plates that are not based on a layer construction principle (polymer/silicone on aluminum) but can be imaged directly with a laser. For this purpose, only pure aluminum or other compatible materials are to be used.

Finally, an analogy that is already successfully used in the printing sector should be mentioned. In the flexographic printing sector, targeted surface structuring of printing plates (Kodak Flexcel NX Systems, USA and Miraclon, Belgium) has already been used for several years. This has considerably improved the uniform ink application density, dot gain and edge sharpness of the printed products, thus enhancing print quality. In Figure 3, the surface structure of one letter to be printed is shown with increasing magnification (a to d). AED stands for Advanced Edge Definition, one of the latest technologies for improving edge sharpness in flexography (James, 2021).

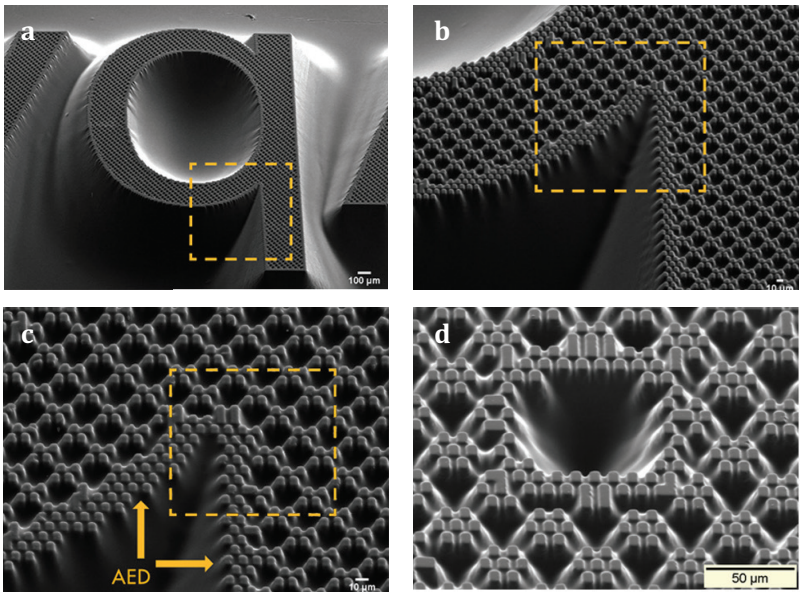

Figure 3: Detailed surface structure of a flexographic printing plate, Kodak Flexcel NX System, Miraclon's Advanced Edge Definition with surface structuring (James, 2021)

2. Materials and methods

In the following sections, the materials used and the methodology are presented. This includes the explanation of the determination of the SFT of fluids as well as the SFE of the printing plates and laser-structured aluminum samples, which were determined using contact angle measurements and a bubble pressure tensiometer. Process parameters and post-treatment of the laser-structured aluminum samples are presented and the measurement of topology of the printing plates and aluminum samples are shown.

2.1 Printing plates, inks and fountain solution

Two printing plates were investigated: a thermal printing plate *Azura TS* (Agfa, Belgium) and a waterless printing plate *Zahara Elite* (Verico Technology LLC, CT, USA). The inks tested were *Novavit 2 F100 magenta* (Flint Group, Luxembourg) and *Nevada PC cyan* (Classic Colours, Great Britain), which is used in waterless offset lithography. The fountain solutions tested were *Fluid Rotaprint* (Reiner Gräflich, Germany) with an IPA content of 10 % and *Fluid* (Roto International, Germany). Based on the odor development, it can be assumed that considerably less isopropanol is mixed in the fountain solution fluid from Roto International.

2.2 Laser structuring of aluminum samples and post-treatment

For fabrication of laser-structured aluminum samples a nanosecond fiber laser *F-9020* (KBA, Germany) was used, which has a wavelength of 1 062 nm, a spot diameter of 53 µm, a range of frequency from 20 kHz to 80 kHz, a max. laser power of 20 W, a focal length of 200 mm and a work area of 100 mm × 100 mm. Laser parameters are shown in Table 1.

Table 1: Laser parameters for fabrication of the laser-structured aluminum samples

Parameter	**Values**
Hatching distance	0.05; 0.10; 0.15; 0.20; 0.30 or 0.40 mm
Laser scan speed	125; 250; 500; 1 000; 1 500 or 2 000 mm/s
Laser power	20 W
Frequency	34.5 kHz
Hatching strategy	Cross-pattern with one pass

A total of 11 samples were prepared. Aluminum 3.0205 (99 % Al) with a material thickness of 0.15 mm was used for sample fabrication. Squares of 50 mm × 50 mm were cut and an area of 20 mm × 20 mm was laser-structured. After the laser structuring process, the aluminum samples were boiled in water for 10 min. Subsequently, the structured and dry surface was covered with a silicone oil *KF-96* (Shin-Etsu Chemical Co., Ltd., Japan) and heat treated in an oven at 200 °C for 10 min. Finally, the samples were cleaned in an isopropanol ultrasonic bath for 10 min. This procedure was performed according to Tran and Chun (2021). In this work, water contact angles of up to 170° were reached with this method.

2.3 Contact angle measurement and bubble pressure tensiometer

DSA 100 (Krüss, Germany) was used for contact angle measurement of test fluids on the printing plates and laser-structured aluminum samples (Krüss, n.d.; Thomsen, 2008). Test fluids were water, ethylene glycol and diiodomethane which were dispensed from the automatic dosing unit of the machine. The SFT for these fluids (Table 2) with disperse and polar fractions were taken from Ström, Fredriksson and Stenius (1987) for water and diiodomethane, and from Gebhardt (1982) for ethylene glycol. All drops had a volume of 2 µl and were applied by the sessile drop method. *Interpolation* algorithms to determine the contact angles were *tangent* (contact angle of 20° to 180°) and *circle* (contact angle of 0° to 20°).

Table 2: The SFT of three common test liquids including disperse and polar parts at 20 °C

SFT in mN/m	SFT (total)	SFT (disperse)	SFT (polar)
Water	72.80	21.80	51.00
Ethylene glycol	47.70	26.40	21.30
Diiodo-methane	50.80	50.80	0.00

The results of the contact angle measurement were then used to create the wetting envelopes according to the featured OWRK method, so that a prediction can be made about the wettability of the printing plates and laser-structured aluminum samples.

Since offset printing ink has a very high viscosity of 10 000 to 30 000 mPa·s (Leach, et al., 1988), the surface tension of the ink cannot be determined using a bubble pressure tensiometer (max. 500 mPa·s). The ink was therefore rolled thinly onto a coated cardboard, which was then directly examined with the three test liquids. The results are therefore analogous to the determination of the SFE of the two printing plates and the laser-structured aluminum samples.

The SFT of the fountain solutions were determined with a bubble tensiometer *BP 100* (Krüss, Germany). For this purpose, the capillary diameter of the capillary used was first determined in a beaker containing approximately 8 ml ultrapure water. Subsequently, the two damping solutions were measured with the capillary diameter determined. This is necessary because fountain solutions are surfactants that exhibit different surface tensions according to the bubble age. In order to also determine the disperse and polar components of the surface tension, the fountain solutions were subsequently analyzed by means of contact angle measurement on a polytetrafluoroethylene (PTFE) substrate, since this is a theoretically purely disperse material. For this purpose, the SFE of PTFE was predetermined via the three test fluids on the *DSA 100*.

All tests for contact angle measurement as well as bubble pressure were performed at a temperature of 21 °C ± 1 °C and a relative humidity of 30 % ± 5 %.

2.4 Microscopic measurements

The confocal profilometer PLu Neox from the company Sensofar was used for topographical examination of the printing plates and the laser-structured aluminum samples. The following settings were used for the printing plates: Objective DI 50X, threshold 5 % and light 10 %. For the characterization of the laser-structured aluminum samples, the best results were obtained with the following settings: SLWD 50X objective, threshold 0 % and light 4.5 %.

3. Results and discussion

In the following sections, the results on the measurements of the printing plates, the laser-structured aluminum samples, and the inks and fountain solutions are presented and then discussed. For the sake of simplicity, only a selection of the laser-structured aluminum samples is presented in detail with graphs. The selection includes the following samples:

- S1 (Scanning speed: 500 mm/s; Hatching distance: 0.20 mm)
- S2 (Scanning speed: 500 mm/s; Hatching distance: 0.15 mm)
- S3 (Scanning speed: 500 mm/s; Hatching distance: 0.10 mm)
- S4 (Scanning speed: 500 mm/s; Hatching distance: 0.05 mm)

3.1 Results of microscopic measurements of printing plates and laser-structured aluminum samples

Figure 4 shows the topographic examinations of the two printing plates. In addition, a section of a photograph of both printing plates has been added for illustration purposes. As mentioned in the introduction, offset lithography is a flat printing process in which image and non-image area lies on the same plane. However, this is technically not correct, as microscopic observation reveals that there is actually a height difference of about 2 µm to 4 µm between image and non-image areas. For the thermal printing plate (Azura TS), the image area is higher and for the waterless printing plate, the imaging area is lower com-

pared to the non-imaging area. This is plausible because the layer structure of the printing plates differs. It can also be seen that the thermal printing plate has a much rougher surface than the waterless offset printing plate. This is also supported by the scientific work of Pavlović, Novaković and Cigula (2012) and Shen, et al. (2008), among others.

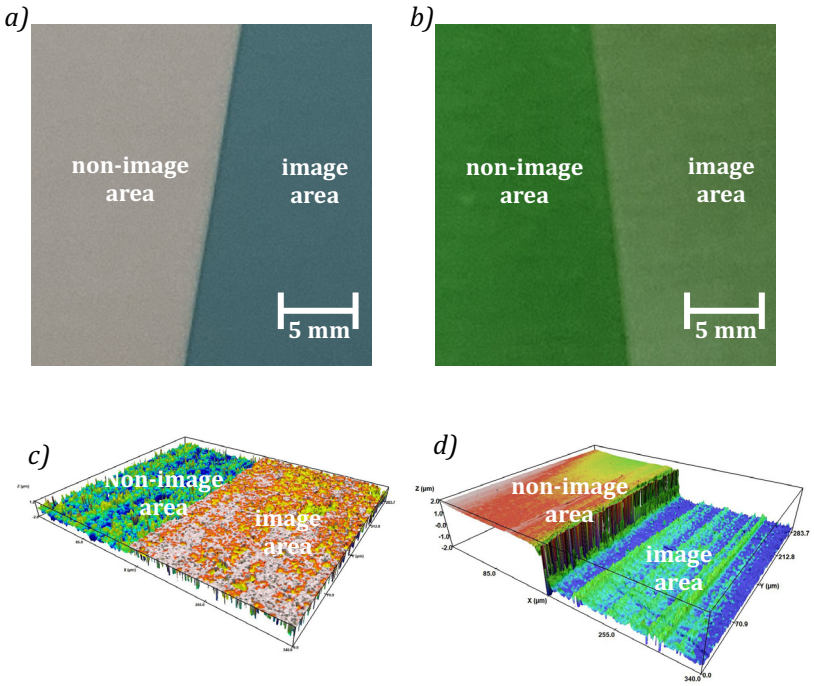

Figure 4: Image detail of thermal offset printing plate (a); image detail of waterless offset printing plate (b); microscopic topography of thermal offset printing plate (c); microscopic topography of waterless printing plate (d)

Photographs were also taken of the laser-structured aluminum samples, which can be seen in Figure 5. Up to a hatching distance of 0.20 mm, the built hatching structures are still visible to the unaided eye. From a hatching distance of 0.10 mm to 0.05 mm, they can no longer be easily identified.

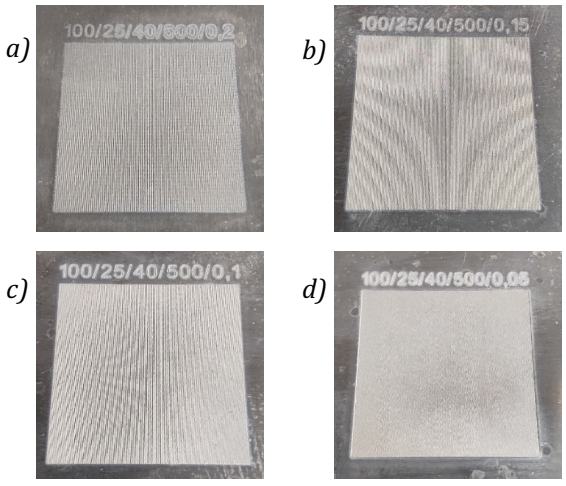

Figure 5: Image detail of selected laser-structured aluminum samples: S1 (a); S2 (b); S3 (c); S4 (d)

It should be noticed that in image detail on Figures 5a to 5c a Moiré effect appears which is not due to the laser-structuring or post-treatment rather it is of the nature from the taken pictures.

Figure 6 shows the topological analysis of the four selected laser-structured aluminum samples. The path of the laser beam is clearly visible and the hatching distance is reflected very accurately in the spacing of

the valleys (blue areas). In contrast to the two printing plates, the samples have a much higher roughness. The height differences from mountains to valleys are about 50 µm to 70 µm. In sample S1, a plateau can be seen in the center, which shows the original roughness of the untreated aluminum sample.

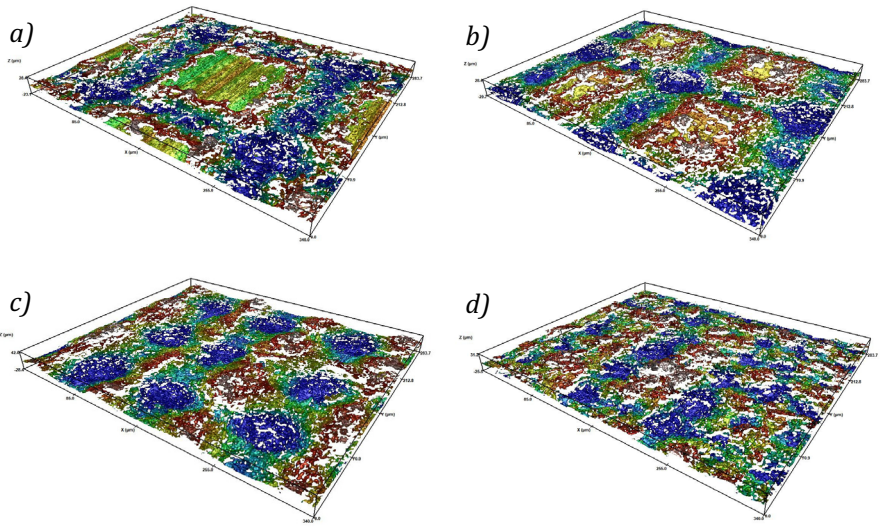

Figure 6: Topographic analysis of selected laser-structured aluminum samples: S1 (a); S2 (b); S3 (c); S4 (d)

In the following, a selection of the areal roughness parameters of the investigated surfaces of laser-structured aluminum specimens and of the imaging and non-imaging surfaces of the waterless and conventional printing plate are presented in accordance with ISO 14405-1 (Deutsches Institut für Normung, 2016). The roughness values S_a, S_z, S_k and S_q are presented in Table 3. It can be seen that the roughness parameters of the two typically used printing plates are much lower than those of the laser-structured aluminum samples. It can also be seen that the roughness values within the aluminum samples as well as the printing plates remain approximately the same.

Table 3: Surface roughness data of aluminum and printing plate samples

Sample	in µm	in µm	in µm	in µm
S1	2.04	36.75	4.67	2.91
S2	2.90	33.76	8.56	3.65
S3	3.40	38.16	10.15	4.36
S4	3.41	36.90	11.03	4.28
Zahara Elite image area	0.09	1.92	0.27	0.12
Zahara Elite non-image area	0.01	0.29	0.03	0.01
Azura TS image area	0.26	4.88	0.73	0.36
Azura TS non-image area	0.34	4.31	1.04	0.44

3.2 Contact angle measurement, SFT/SFE calculation and modelling of wetting envelopes

In this section, the contact angle measurements and the resulting SFE as well as SFT are presented. Finally, selected wetting envelopes are shown and placed in the scientific context. Figure 7 shows an example of how contact angle measurements were performed with the test fluids mentioned in the materials and methods section on the laser-structured aluminum specimens that were post-treated with silicone oil and heat. Contact angles are not explicitly listed because the later presented wetting envelopes can be used to predict the wetting with liquids for which the SFT with disperse and polar fractions is known or has been determined experimentally.

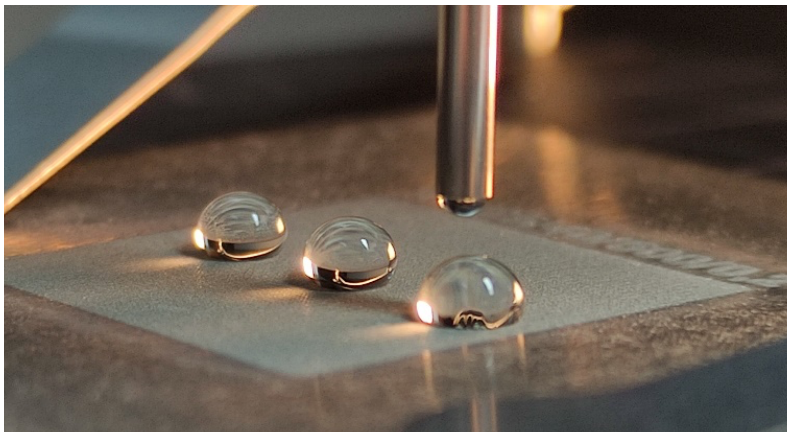

Figure 7: Contact angle measurement of laser-structured aluminum sample with ethylene glycol

The results for determining the SFE of the printing plates are listed in Table 4. In general, it can be seen that the *Azura TS* thermal printing plate has a significantly higher SFE than the *Zahara Elite* waterless printing plate. In addition, it can be seen that the Azura TS has approximately equal polar and disperse fractions. In contrast, the waterless printing plate Zahara Elite exhibits almost exclusively disperse fractions in the SFE. The results are in line with scientific work already carried out to determine the SFE of printing plates. In this context, Deshpande (2011); Cigula, et al. (2010); Tian, Mao and Shen (2009) and dataphysics (2012) can be mentioned. The results of the tests on inks and fountain solutions, which are listed in Table 4, can also be confirmed with the just mentioned scientific work. MacPhee (1998) investigated various relevant SFE and SFT of an offset printing press. The imaging area of a printing plate showed an SFE (total) of 39.4 mN/m with a disperse fraction of 36.5 mN/m and a polar fraction of 2.9 mN/m. For the non-imaging area of the printing plate, an SFE (total) of 69.4 mN/m with a polar fraction of 44.6 mN/m and a disperse fraction of 24.8 mN/m was determined. These values are comparable in magnitude to those found in this work for the Azura TS thermal printing plate. The properties of the non-imaging areas agree well. The properties of the imaging areas are further apart. This could be due to the fact that it is not clear which type of printing plate was investigated.

Table 4: SFE of thermo printing plate and waterless printing plate incl. polar and disperse parts

SFE in mN/m		SFE (total)	SFE (disperse)	SFE (polar)
Printing plate Zahara Elite	Image area	21.02 ± 1.11	21.01 ± 1.09	0.01 ± 0.01
	Non-image area	12.48 ± 1.29	11.96 ± 1.09	0.52 ± 0.21
Printing plate Azura TS	Image area	57.73 ± 1.60	36.03 ± 0.22	21.70 ± 1.38
	Non-image area	74.09 ± 0.30	33.78 ± 0.11	40.31 ± 0.19

The results for the determination of the total SFT of the fountain solution by bubble pressure tensiometer and the subsequent determination of the disperse and polar fractions by contact angle measurement on Teflon are shown in Table 5. The following values for the SFE were determined for the PTFE substrate:

- SFT (total): 17.57 ± 1.11 mN/m
- SFT (disperse): 17.02 ± 0.92 mN/m
- SFT (polar): 0.56 ± 0.20 mN/m

These were the basis for determining the polar and disperse fractions of the fountain solutions.

Table 5: SFT of inks and fountain solutions incl. polar and disperse parts

SFT in mN/m	SFT (total)	SFT (disperse)	SFT (polar)
Novavit® 2 F100 magenta	57.50 ± 0.10	50.51 ± 0.08	6.98 ± 0.01
Nevada PC cyan	51.33 ± 2.22	50.38 ± 1.82	0.94 ± 0.40
Roto Fluid	60.01 ± 1.04	36.46 ± 2.69	23.55 ± 2.88
Rotaprint R37	38.84 ± 0.64	31.51 ± 2.28	7.33 ± 2.37

Table 6 shows the results of the determined SFE of the laser-structured aluminum samples S1 to S4 as well as the results of the other aluminum samples with varying laser parameters. In particular, it can be seen that samples S2 and S3 are close to the determined SFE (overall as well as the polar and disperse fractions) of the *Zahara Elite* waterless printing plate and would therefore be suitable for further investigation. This aspect will be discussed in more detail in section 4. The two samples with 1 500 mm/s and 2 000 mm/s laser scanning speed with a hatching distance of 0.10 mm have basic tendencies towards the SFE of the *Azura TS* printing plate and should also be further investigated. The samples with laser scanning speed of 125 mm/s, 250 mm/s and 1 000 mm/s have extremely low SFE's. It may be possible that these samples could be suitable as non-imaging areas for waterless printing plates. Only further experiments and investigations can show to what extent these samples should be followed up. Finally, it must be added that no contact angle measurement and the corresponding determination of the SFE could take place for purely laser-structured aluminum specimens, since, as addressed in the introduction, without a silicone and heat treatment the specimens formed non-measurable contact angles with the test liquids (contact angles towards 0°). In particular, they showed superhydrophilic wetting behavior for water, which in turn could be an argument for using these untreated surfaces as non-imaging areas for a printing plate that works with fountain solution.

In order to achieve extreme wetting properties, the interaction of topology (microstructures) and the chemical compounds on the micro-structured surface is crucial. The surface chemistry initially determines whether the material is hydrophobic or hydrophilic, and the surface structure further enhances the effect so that superhydrophilicity or superhydrophobicity can be achieved. The extremely low SFE (< 10 mN/m) of some aluminum samples originate from strongly hydrophobic CH_3-groups observed after silicone oil/heat treatment by Tran and Chun (2021). After laser patterning and boiling water treatment, their study also found that hydrophilic pseudo-boehmite (AlOOH) had accumulated on the surface.

Table 6: SFE of laser-structured aluminum samples including polar and disperse parts

SFE in mN/m	SFE (total)	SFE (disperse)	SFE (polar)
Alu 125/0.20	2.02 ± 0.30	1.91 ± 0.08	0.11 ± 0.22
Alu 125/0.30	1.46 ± 0.16	1.37 ± 0.13	0.09 ± 0.04
Alu 125/0.40	2.45 ± 0.14	2.34 ± 0.05	0.11 ± 0.09
Alu 250/0.20	7.00 ± 3.16	5.82 ± 2.15	1.18 ± 1.01
Alu 500/0.05 (S4)	9.24 ± 1.23	7.29 ± 0.56	1.95 ± 0.66
Alu 500/0.10 (S3)	17.62 ± 3.28	13.56 ± 1.05	4.06 ± 2.23
Alu 500/0.15 (S2)	18.66 ± 3.11	15.55 ± 2.33	3.12 ± 0.77
Alu 500/0.20 (S1)	8.51 ± 2.21	7.50 ± 1.47	1.01 ± 0.74
Alu 1 000/0.10	8.50 ± 2.68	7.62 ± 1.11	0.87 ± 1.56
Alu 1 500/0.10	34.02 ± 1.04	32.65 ± 0.76	1.38 ± 0.29
Alu 2 000/0.10	50.41 ± 2.34	39.32 ± 1.25	11.09 ± 1.08

As an example for the prediction of wetting with liquids for which the SFT with the corresponding polar and disperse fractions is known, the wetting envelopes for the two printing plates (imaging as well as non-imaging areas) are shown in Figure 8. It should be noted that the three test fluids are drawn in the diagrams. The colored curves represent specific contact angles that would be formed for a corresponding SFT constellation of the liquid to be wetted. The dashed line represents the ratio of polar to disperse fractions and the solid line reflects a polar fraction of 100 %. With the help of these wetting envelopes, a substrate to be wetted can be specifically tested with various different liquids without having to perform a manual contact angle measurement. In this sense, laser-structured aluminum samples can also be theoretically tested with different fountain solutions and inks. Due to the scope, the wetting envelopes of the laser-structured aluminum samples are not shown.

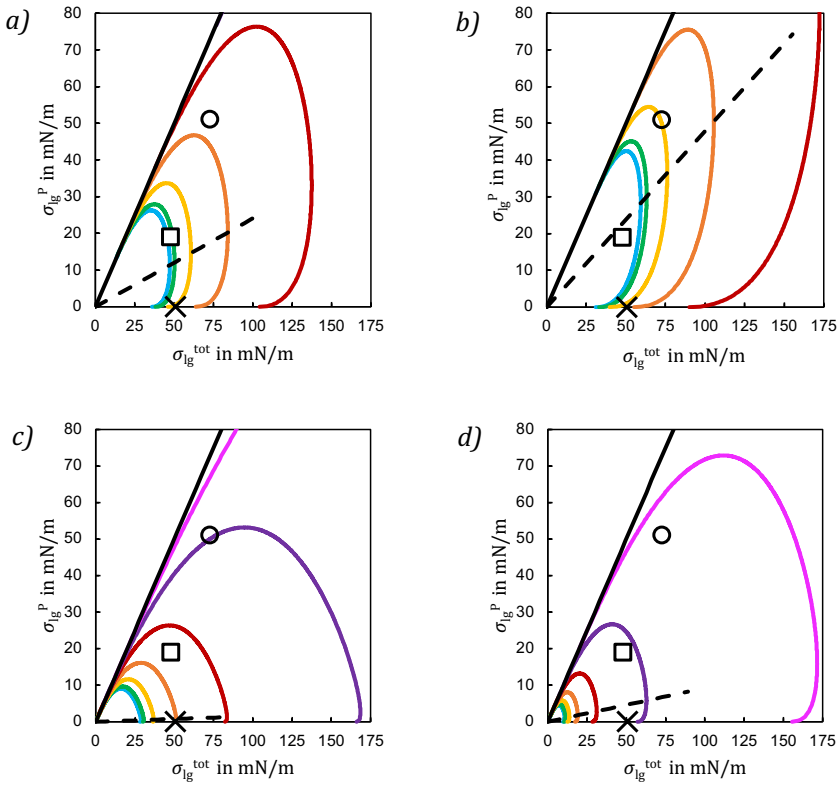

Figure 8: Wetting envelopes of thermo printing plate: (a) printing area; (b) non-printing area; and waterless printing plate: (c) printing area; (d) non-printing area (legend for contact angles of curves: light blue – 0°, green – 20°, yellow – 40°, orange – 60°, red – 80°, purple – 100°, pink – 120°; and for marks: circle – water, square – ethylene glycol, cross – diiodo-methane)

4. Conclusions

In these preliminary investigations of the laser-structured aluminum samples, it is shown that their SFE have an approximately similar value with the corresponding disperse and polar fractions of the investigated printing plates. However, the previous findings apply only to the case of static wetting. Further investigations should show whether the laser-structured aluminum surface is also compatible in the dynamic wetting case, as it occurs in offset printing presses. The influence of the surface roughness and the considerably larger height difference of the laser-structured aluminum surfaces must also be investigated in this course, since printing plates, as presented at the beginning of this chapter, have a very low surface roughness as well as height difference between imaging and non-imaging areas. Future tests should also include other metals in the investigations, such as copper, brass or bronze. Furthermore, a more suitable laser system, such as that already successfully used by Milles, et al. (2021), is to be used for surface struc-

turing of the metal samples. With this system, hierarchical surface structures can also be created and the high resolution generally required for offset lithography can be achieved. Furthermore, the first highly dynamic wetting tests are to be started in a small-format offset press.

References

Aull, M., 2001. *Lehr- und Arbeitsbuch Druck*. 6th ed. Itzehoe: Verlag Beruf und Schule.

Cassie, A.B.D. and Baxter, S., 1944. Wettability of porous surfaces. *Transactions of the Faraday Society*, 40, pp. 546–551. https://doi.org/10.1039/TF9444000546.

Cigula, T., Pavlović, Ž., Gojo, M. and Risović, D., 2010. Wetting of offset printing plate's nonprinting areas as a function of print run. In: *Proceedings of 5th International Symposium on Graphic Engineering and Design, Grid '10*. Novi Sad, Serbia, 11–12 November 2010. Novi Sad, Serbia: University of Novi Sad, pp. 9–18.

dataphysics, 2012. *Application note 3: determination of the surface tension between a printing ink and fountain water during the offset printing process*. [pdf] Available at: <https://www.dataphysics-instruments.com/Downloads/3_Interfacial_tension_between_a_printing_ink_and_fountain_water.pdf> [Accessed April 2023].

Deshpande, S.S., 2011. Fountain solution in lithographic offset printing. *Journal of Engineering Research and Studies*, 2(2), pp. 82–88.

Deutsches Institut für Normung, 2016. *ISO 14405-1:2016-08 Geometrische Produktspezifikation (GPS) – Dimensionelle Tolerierung – Teil 1: Lineare Größenmaße*. Berlin: DIN, Beuth Verlag GmbH.

Dongre, G., Rajurkar, A., Raut, R. and Jangam, S., 2021. Preparation of super-hydrophobic textures by using nanosecond pulsed laser. *Materials Today: Proceedings*, 42(2), pp. 1145–1151. https://doi.org/10.1016/j.matpr.2020.12.497.

Gebhardt, K.F., 1982. *Grundlagen der physikalischen Chemie von Grenzflächen und Methoden zur Bestimmung grenzflächenenergetischer Größen.* Stuttgart: Fraunhofer-Institut für Grenzflächentechnik IGB.

James, A., 2021. *Enhancing print contrast.* FTA [online] Available at: <https://www.flexography.org/industry-news/enhancing-print-contrast/> [Accessed April 2023].

Kietzig, A.-M., Hatzikiriakos, S.G. and Englezos, P., 2009. Patterned superhydrophobic metallic surfaces. *Langmuir: the ACS Journal of Surfaces and Colloids*, 25(8), pp. 4821–4827. https://doi.org/10.1021/la8037582.

Kipphan, H. (ed.), 2000. *Handbuch der Printmedien: Technologien und Produktionsverfahren*. Berlin. Springer.

Krüss, n.d. *Contact angle.* [online] Available at: <https://www.kruss-scientific.com/en/know-how/glossary/contact-angle> [Accessed 12 April 2023].

Law, K.-Y. and Zhao, H., 2016. *Surface wetting: characterization, contact angle, and fundamentals*. Cham: Springer International Publishing AG.

Leach, R.H., Armstrong, C., Brown, J.F., Mackenzie, M.J., Randall, L. and Smith, H.G. eds., 1988. *The printing ink manual*. 4th ed. Wokingham, UK: Van Nostrand Reinhold.

MacPhee, J., 1998. *Fundamentals of lithographic printing: volume 1 :mechanics of printing*. Pittsburgh: GATF Press.

Milles, S., Vercillo, V., Alamri, S., Aguilar-Morales, A.I., Kunze, T., Bonaccurso, E. and Lasagni, A.F., 2021. Icephobic performance of multi-scale laser-textured aluminum surfaces for aeronautic applications. *Nanomaterials,* 11(1): 135. https://doi.org/10.3390/nano11010135.

Nicolay, K.-P., 2012. CtP und Platten: als Einheit zu betrachten. *Druckmarkt COLLECTION*, 10, pp. 3–25.

Owens, D.K. and Wendt, R.C., 1969. Estimation of the surface free energy of polymers. *Journal of Applied Polymer Science*, 13(8), pp. 1741–1747. https://doi.org/10.1002/app.1969.070130815.

Pavlović, Ž., Novaković, D. and Cigula, T., 2012. Wear analysis of the offset printing plate's non-printing areas depending on exploitation. *Tehnički Vjesnik*, 19(3), pp. 543–548.

Shen, W., Mao, Y., Murray, G. and Tian, J., 2008. Adhesion and anti-adhesion of viscous fluids on solid surfaces – a study of ink transfer mechanism in waterless offset printing. *Journal of Colloid and Interface Science*, 318, pp. 348–357. https://doi.org/10.1016/j.jcis.2007.10.016.

Ström, G., Fredriksson, M. and Stenius, P., 1987. Contact angles, work of adhesion, and interfacial tensions at a dissolving hydrocarbon surface. *Journal of Colloid and Interface Science*, 119(2), pp. 352–361. https://doi.org/10.1016/0021-9797(87)90280-3.

Thomsen, F., 2008. *Krüss technical note TN315e: practical contact angle measurement*. [pdf] Available at: <https://warwick.ac.uk/fac/cross_fac/sciencecity/programmes/internal/themes/am2/booking/dropshapeanalyser/practical_contact_angle_measurement_5.pdf> [Accessed April 2023].

Tian, J., Mao, Y. and Shen, W., 2009. Ink transfer and refusal mechanisms in waterless offset printing. *Journal of Adhesion Science and Technology*, 23(2), pp. 281–296. https://doi.org/10.1163/156856108X389442.

Tran, N.G. and Chun, D.-M., 2021. Green manufacturing of extreme wettability contrast surfaces with superhydrophilic and superhydrophobic patterns on aluminum. *Journal of Materials Processing Technology*, 297: 117245. https://doi.org/10.1016/j.jmatprotec.2021.117245.

Wenzel, R.N., 1936. Resistance of solid surfaces to wetting by water. *Industrial & Engineering Chemistry*, 28(8), pp. 988–994. https://doi.org/10.1021/ie50320a024.

Young, T., 1805. III. An essay on the cohesion of fluids. *Philosophical Transactions of the Royal Society of London*, 95, pp. 65–87. https://doi.org/10.1098/rstl.1805.0005.

DOI 10.14622/Advances_49_2023_07

The future is now: opportunities and challenges of integrated technology in graphic communications for Industry 5.0: a Systematic mapping of the literature

Lucille Trepanier, Areej Syeda and Reem El Asaleh

School of Graphic Communications Management, Toronto Metropolitan University, Toronto, ON, Canada
E-mails: lucille.trepanier@torontomu.ca, areej.syeda@torontomu.ca, reem.elasaleh@torontomu.ca

Short abstract

This study provides a holistic overview of Integrated Technologies, such as Automation, Artificial Intelligence (AI), the Internet of Things (IoT), Big Data, Machine Learning (ML), and Augmented Reality (AR), and their applications within the Graphic Communications Industry. By leveraging a systematic literature review utilizing both quantitative and qualitative publications, this study aims to answer the following question, *"In the Graphic Communications Industry, do the implementations of Integrated Technologies have an impact on the quality of performance of organizations and the users who have adopted them in the previous 10 years?".* Identified publications were selected in order to contain a variety of different perspectives from a myriad of authors to make it abundantly clear that new approaches containing unprecedented use of integrated technologies are bringing continuous development and change, both positive and negative. They will reshape our current approach to technology in the Graphic Communications Industry and will therefore transform the way lives are lived. A pilot study was conducted by Syeda and El Asaleh in 2022 about the integrated technology available in the graphic communication industry. This study expands on previous existing research, including a more in-depth analysis to continue to shed light on existing implementation. These new opportunities and existing limitations will aid in determining the path the future of the Graphic Communications Industry will take in the Industry 5.0 revolution. This paper is part of ongoing research at The Creative School of Toronto Metropolitan University (Formerly known as Ryerson), 2022, and will serve as a basis on which further research will be conducted, as it's a neglected research topic and one that's lacking within the field of Graphic Communications.

Keywords: artificial intelligence, automation, integrated technology, graphic communication, Industry 5.0

1. Introduction and background

Automation, Artificial Intelligence (AI), the Internet of Things (IoT), Big Data (BD), Machine Learning (ML), Virtual Reality (VR), and Augmented Reality (AR), are more than modern terms, these technologies have created new potential innovations within the workplace, and it has been ruling many aspects of our daily life. Essentially, automation substitutes mundane or physically difficult labor by limiting human involvement. This technological-industrial integration has been, once again, revolutionizing our means of production, increasing productivity as never before. Businesses and economies worldwide can benefit from this technological-industrial integration into their workplaces. The results will not be immediate, but the long-term benefits are significant for companies. McKinsey (2019) stated that "the automation of activities can enable businesses to improve performance by reducing errors, improving quality and speed, and in some cases achieving outcomes that go beyond human capabilities". For instance, VIZIT, as a packaging mockup tool, provides a practical demonstration for consumers looking for a front-back-end automated solution. By delivering virtual prototypes for packaging design visualizations, VIZIT enables users to customize, personalize and view their mockup in real time.

Industry 4.0 is here and it's growing, however, it also brings certain concerns for the general population. The substitution of workplace labor by machines has unshackled workers to focus on higher-value tasks or

establish new ones, which leaves an uncertain future scenario for the availability of work. Many employees fear that there will not be enough jobs with the increasing integration of automation and artificial intelligence in the workplace or that some jobs will become obsolete. Seeking this, many individuals are already looking forward to the Fifth Industrial Revolution. Nahavandi (2019) defines it as "where robots are intertwined with the human brain and work as collaborators instead of competitors". Increased efficiency and intelligence systems are combined with human labor, which comes back to the fold 10 times over, to create revolutionary machinery in Industry 5.0. This research study will go deeper into the transition between Industry 4.0 and Industry 5.0, examining the challenges and opportunities that these technologies present to businesses in the Graphic Communications Industry, and will more specifically, discuss whether industry 5.0 will see a balance of cobots, and the impact of them.

This Paper will showcase background information about promising technologies that are already taking place in the industry nowadays and discuss their use within Industry 5.0, a new production model that emerges as a favorable alternative for the future of our society. A systematic literature review will be employed in order to construct a base from different authors and perspectives and draw conclusions based on the evidence presented. The paper employs a systematic review to critically evaluate relevant literature and focus on contemporary applications in various Graphic Communication Industry Sectors such as Graphic Arts, Graphic Design, Packaging, Printing, and others. This information will benefit those within the Graphic Communications Industries and those who are considering the implementation of integrated technologies within their respective businesses. It will explore the numerous benefits and drawbacks associated with the usage of Integrated Technologies, as well as their impact within the Graphic Communications Industry, focusing on performance quality and customer experience.

Given the scarcity of previous research on the subject, this study is especially important because it expands on previous research that's the first of its nature, thereby contributing to further research in this field. It provides a systematic review with clear definitions of emerging technologies such as Automation, AI, IoT, ML, VR, AR, and BD, as well as a holistic approach to discussing the implementation of Integrated Technologies in the Graphic Communications Industries, thereby making available evidence more accessible and advancing the Graphic Communications Industry forward.

1.1 Back-end and Front-end interrelation

Technologies in the current industry are diverse, from AI to IoT, and they all connect to each other in the automated production process, as seen in Figure 1. In many cases, they are not all employed at the same time, yet this whole process and information flow are leveraged by automation as it improves over time. Artificial intelligence enables the workflow to evolve as long as it learns, depending less on humans and manual programming to perform daily tasks in the production process. As technology continues to evolve rapidly, the merger of robotics and the human mind is causing huge breakthroughs in artificial intelligence, which will play a machine-independent role in Industry 5.0 allowing for a collective synergy between humans and autonomous machines.

Figure 1: Information process of back-end & front-end integrated technologies

2. Materials and methods

A systematic literature review was conducted based on PICO guidelines to showcase background information and current implementations of promising integrated technologies already taking place in the indus-

try and discuss their use and challenges within Industry 5.0. The study was considered to showcase the benefits and drawbacks of the implementation of relevant integrated technologies, such as Automation, AI, IoT, VR, AR, BD, and ML. The current challenges faced, barriers, and the road to Industry 5.0 are also discussed.

The study pulls over 463 academic papers, from thesis' to conference publications, to research reports. The available literature was gathered from unique sources, such as the Toronto Metropolitan University Library, Web of Science, ScienceDirect, Communication & Mass Media, Google Scholar, and the OpenDOAR database. The team took five main steps as we aimed to gather all empirical data that fit our pre-specified criteria to answer the research question posed.

The first step was to identify and frame the research question using the PICO method to strategize the Population, Intervention, Comparison, and Outcome. The second step was to define the inclusion and exclusion criteria, allowing the team to focus on the keywords that would be used throughout the literature search. The third step was to manually filter and extract data from the aforementioned resources, after which the fourth step was to select studies that fit our inclusion criteria. Using the keyword database created, the team used the Boolean logic technique of using both and/or to track down literature. The secondary screening was followed for final inclusion in the review, determining if the studies met the pre-determined criteria, and thereby limiting any biases. The final step was data extraction from the selected studies to report findings and conclusions. Any disagreements were discussed openly allowing the team to assess and compromise.

While this approach is not a unique research method, the singularity of this study is that it's one of the only available studies that cover the wide scope of sectors in the Graphic Communications field and hence bridges a research gap that was previously present. The findings that have been analyzed will benefit those within the Graphic Communications industries as well as those who may be thinking about integrating these technologies within their businesses and are focused on performance quality and customer interactions. The exploration of benefits and drawbacks associated with the implementation of integrated technologies within a workplace setting allows a basis for industry professionals to consider the use of these technologies, and how it may impact process optimization, quality control, decision making, user satisfaction, creativity, production, and management.

3. Results and discussion

Worries that emerged with Industry 4.0 and past industrial revolutions are embraced by Industry 5.0 solutions. Unfortunately, and inevitably, others remain and new ones appear. Industry 5.0 certainly has good premises, but it's important to understand its limitations and all the parts involved in the process to make it what it's expected to be in the future. Tech companies, technology fair access, and ethical questions are examples of important subjects to be addressed in order to prepare a safe path to the next industrial revolution.

A question that was already brought up by the Fourth Industrial Revolution: who would benefit the most from industrial technology innovations? The answer seems easy: larger companies have always been ahead when it comes to new technologies employment, with more structured data and access to resources. Even though these are expected to become more accessible through time and development, they must be guaranteed to keep a fair market share among different businesses. Industry tech owners must keep an effort to provide solutions for small firms. There are already semi-automated systems (in contrast to the larger full ones) available in the market that could be adopted by small-scale businesses. According to Moore's

Law, electronic devices tend to get smaller over time, which could contribute to the growth of new tech employment by small-scale firms.

New technologies should also be seen through the ethics lens, in order to identify the implications that come along. AI bias, for example, is one major problem that has been drawing a lot of attention recently, resulting in many studies by researchers and technologists. Therefore, AI bias must be taken into consideration to ensure that algorithms work in favor of all humans in all conditions, promoting the harmonic collaborative workforce expected. Generative AI can be difficult to accept as it provides a limited explanation when formulating a result. As long as these integrated technologies like Tilia Labs' Phoenix AI, CHILI publish, and Adobe Sensei are fed ethical data and correct criteria, companies can generate respectable outputs.

The most important question is: would machines replace humans, would the increased adaptation and integration to those emerging technologies replace the human factor and expertise? Several studies were focused on exploring human-machine interactions (Abbass, 2019; Albrecht, 2018; Nahavandi, 2019), while others concluded that while using emerging technologies would provide real-time solutions and enhance the decision-making process, the need to have human involvement and expertise is an asset (Verganti, Vendraminelli and Iansiti, 2020; Doehling; 2019; Krafft, Sajtos and Haenlein, 2020). With programming tools like Adobe Firefly, Tilia Labs, and CHILI publish, there is a tendency in society to associate these technologies in the workplace with negative consequences. The fear and uncertainty of these technologies have led to a reluctance to learn about the potential these mechanisms can offer to the workplace. Understanding that industries driven by creativity, such as the Graphic Communication sector, are subjective and dependent on catering to the needs of a consumer, human involvement remains a necessity. AI's role is not to substitute human labor but rather to foster opportunities for human participation to engage in higher-order thinking activities, such as supervising and project managing client expectations to deliver the most effective creative solutions.

The final question is: will there be smart enough technologies available in the next future? Cobots and the idea of a perfect collaborative synergy between machines and humans will require a high level of automation and advancements never seen before. Industry 5.0 intentions are achievable, however, they rely on technological progress that requires time and investment. At the present moment, technology has been providing contributions to industrial automation, this ultra-connected environment is a significant step toward integrating humans with machines. AI, IoT, VR, AR, BD and many others are the beginning of the future for the Next Industrial Revolution.

3.1 Findings

To study how integrated technology impacted organizations and users who adopted them, articles were sorted into 3 categories reflecting the graphic communications workflow: ideation, production, and customer satisfaction. These categories covered process optimization, quality control, decision-making, and user satisfaction in graphic arts.

3.1.1 Creativity

The Graphics Arts industry relies heavily on creativity, which involves various processes and workflows. However, with the emergence of immersive technologies like AI, IoT, VR, AR, and BD is transforming traditional creative professions. This subcategory of articles explores how integrated technologies reinvent and optimize processes, leading to new outputs and results. Adopting technology for creative purposes involves various tasks and procedures, including generating and preparing materials, simplifying projects, making decisions, and solving problems. However, limitations and technical challenges arise when tech-

nology leads the creative process, leading to copyright infringement and protection concerns. Adopting intelligent algorithms could transform the design industry, but creative-based firms may require a cautious implementation to preserve their human capital. Larger organizations could strategically leverage these technologies to streamline processes and boost efficiency in areas where the creative process has a lower impact on the final output.

3.1.2 Production management

Creating successful customer experiences and interactions requires the implementation of robust production and management practices. This subcategory delves into how immersive technologies like AI, IoT, VR, AR, and BD transform organizations' production and management processes. By incorporating intelligent algorithms, companies can optimize their operations for human and machine inputs, enhancing efficiency, quality, and cost-effectiveness. For example, Kodak PRINERGY Workflow, Esko Automation Engine, and HP PrintOS are AI-driven software that provides practical production management to help administrate files and eliminate redundant and tedious mundane tasks. However, digitizing processes also pose challenges such as job security, investments, and training. The articles also explore the impact of these technologies on employee relationships and management practices, focusing on safety, well-being, health, and training procedures. Ethical and moral judgments are crucial in evaluating the adoption of integrated technology, with deep learning employed to manage these protocols. While these technologies have brought significant benefits, they raise concerns about ethical implications, governance, privacy, and politics.

3.1.3 Customer interaction/experience

Selected papers focused on a customer-centric approach and output, particularly in the User Satisfaction, customer interaction, and experience subcategories. Companies must decide how their integrated technology benefits frequent consumer desires to improve their product, process, or organization. Consumer decision-making and evaluations of whether to adopt or not are based on the technology's benefits, experience, and final product results. ML has been utilized to enhance customer experiences in various settings, such as retail markets, creative environments, and learning environments. However, customers also have technological anxieties and may distrust integrated technologies, such as VR glasses, leading to negative attitudes and perceptions related to ethical and robotic relationships.

4. Conclusions

The main aim of this study is to provide a snapshot of the existing technologies in the last decade and how that impacted human perspectives and engagement with these technologies. It explores the pros and cons as well as challenges and future improvements. Overall, studies showed the positive impact of integrating various technologies in enhancing workflow automation, decision-making, consumer design, and engagement with products or services from AI art, prepared packaging compositions, and preflight software. On the other hand, certain articles discuss challenges such as recognizing the hesitancy and fear from the older generation in engaging with cutting-edge technology such as VR, AR, ChatGPT, and other AI-related technologies due to various factors such as the fear of the unknown. Along with the rise of automation and the adaptation of novel AI technologies such as Generative AI applications, the question of ethical consumption and the legal source of the training data used in various ML algorithms fed by those applications was also elaborated on in other articles. A successful adaptation must be accompanied by a substantial change management policy to ensure the sustainability of the service provided. Now we live in a competitive era where an organization's awareness of available technologies is recognized as significant to keep up with IT infrastructure and technology to stay on top of the mind of consumers. If you miss the wave, you miss the younger generation's profit.

As ongoing and current research at the Toronto Metropolitan University's (TMU) (formerly known as Ryerson), The Creative School, 2023, this paper will serve as the basis on which further research will be conducted to cover broader sectors in the Graphic Communications and the Creative Industries that were not addressed in this current research, as well as contribute to providing clear and accessible evidence of a neglected research topic and one that's severely under-addressed within the field of Graphic Communications. In addition, this study would benefit from identifying gaps in the available literature and implementing keyword co-occurrence and cross-fertilization of selected field analysis techniques. For example, some machine learning technologies were used to enhance overall performance optimization which lead to better decision-making. Analysis such as these would aid in the holistic approach considered in this paper to advance the Graphic Communications industry even further.

Acknowledgments

Special thanks to *Ella Tadmor from Cal poly university,* and *J*únior Yuki Morimoto from Education and Communication Arts, who were hired as part of the 2021 MITACS *Globallink program*. Also thanks to *Naomi Eichenlaub*, and *Cecile Farnum* at Toronto Metropolitan University (formerly known as Ryerson) who have helped make this study possible. Their support, engagement, and expertise have allowed this paper to become what it is today. Thank you for your contributions.

References

Abbass, H.A., 2019. Social integration of artificial intelligence: functions, automation allocation logic and human-autonomy trust. *Cognitive Computation*, 11(2), pp. 159–171. https://doi.org/10.1007/s12559-018-9619-0.

Albrecht, A., 2018. *Printed sensors for the internet of things*. Dr.-Ing. Dissertation. Technische Universität München.

Doehling, R.M., 2019. *Automation in graphic design*. Honors thesis. Georgia Southern University.

Krafft, M., Sajtos, L. and Haenlein, M., 2020. Challenges and opportunities for marketing scholars in times of the fourth industrial revolution. *Journal of Interactive Marketing*, 51(1), pp. 1–8. https://doi.org/10.1016/j.intmar.2020.06.001.

McKinsey, 2019, February. Driving impact at scale from automation and AI. *Digital/McKinsey*, [online] Available at: <https://www.mckinsey.com/business functions/mckinsey-digital/our-insights/driving-impact-at-scale-from-automation-and-ai> [Accessed April 2023].

Nahavandi, S., 2019. Industry 5.0-a human-centric solution. *Sustainability*, 11(16): 4371. https://doi.org/10.3390/su11164371.

Verganti, R., Vendraminelli, L. and Iansiti, M., 2020. Design in the age of artificial intelligence. *Harvard Business School*, [pdf] Available at: <https://www.hbs.edu/ris/Publication%20Files/20-091_3889aa72-1853-42f8-8b17-5760c86f863e.pdf> [Accessed April 2023].

DOI 10.14622/Advances_49_2023_04

TaxoCatalog: costless workflow integration of an expert system environment to personalize product catalogs in omni-channel context

Heiko Angermann

Hochschule Darmstadt – University of Applied Sciences, Faculty of Design
E-mail: heiko.angermann@h-da.de

Short abstract

Taxonomies are a formal method to semantically structure information using hierarchical ordered concepts. Those play a crucial role in omni-channel retailing to publish product catalogs across media channels, i.e. digital (portal-, paper-based) and print media (paper-based). Portal-based media use taxonomies to structure product-related content by concepts to facilitate customers navigating through the e-commerce site. That are the product categories. Paper-based media require taxonomies for automatic layout setting using data-driven publishing software. To achieve consistency, all media use the identical product taxonomy as basis. When additionally using recommender systems, products are published individually on the e-commerce site. Paper-based media, in contrast, show content regardless of dynamic preferences. Limited personalization takes place using sub-catalogs to only show products of, or specific categories. However, the resulted information loss may result in sales loss, as preferences change. An approach to produce paper-based catalogs without information loss is not available. This is, as individual layout setting and printing is uninteresting, if automating the required processes cannot be achieved. With TaxoCatalog, an expert system environment is presented, which can automatically process customers' preferences for producing individual product catalogs without information and automation loss. Using TaxoCatalog, a semantic personalization is computed, before the layout is set. The first component of TaxoCatalog is semantically analyzing the initial product taxonomy using natural language processing (NLP). The second component is analyzing customers' preferences to create a personalized taxonomy based on the NLP outcome. The third component is used to scale the personalized taxonomy, depending on the desired volume of the catalog. The fourth component is used to perform the rule-based layout setting using standard data-driven publishing software. All decision processes are achieved using background knowledge to allow a cost-less integration into standard workflows. A comprehensive evaluation using two public and one private database provided by a German retailer underline TaxoCatalogs' efficiency.

Keywords: data driven publishing, expert systems, content flow, premedia, workflows

1. Introduction

Today, products are advertised on different media channels (Hänninen, Kwan and Mitronen, 2021). Digital media channels in the form of internally and externally operated e-commerce portals, digital media in the form of paper-based documents, and paper-based print media products can be used (Gao, Melero and Sese, 2020). All have own benefits, but when using e-commerce, retailers can derive customers' preferences in real-time using recommender systems (Chen, et al., 2022; Gil-Gomez, et al., 2020). As a result, products can be shown individually to customers based on its order probability (Behera, et al., 2020). For example, suitable products are shown at the bottom of product sites, known as cross- and up-selling (Norvell, Kumar and Contractor, 2018). Paper-based digital product catalogs, in contrast, show static content, even if its appearance is dynamic. Here, formats like EPUB, or (interactive) PDF are used. Printed product catalogs, also show static content, as individualization affects de-automation of processes (Hoffmann-Walbeck, 2022). Usually, the specific format PDF/X is used for printing. Minimal individualization is enabled for paper-based product catalogs using proven methods of print-on-demand, variable data printing, sub-catalogs, and programmatic printing.

Using print-on-demand, the catalog is produced based on customers' interaction, e.g. an order. Using variable data printing, single pages of the catalog are individualized, e.g. an individual name (Lin, 2006). Using sub-catalogs, catalogs containing only a selection of products or categories are produced, e.g. for a season (Angermann and Ramzan, 2016). Using programmatic printing, a combination of the before-mentioned techniques and paradigms is achieved, which is possible since the advent of non-impact digital printing. A typical use-case is: the customer interacts on an e-commerce site, the preference is analyzed, the media is produced and shipped to the customer. For example, when a shopping cart is not ordered, the customer receives a mailing showing the products or alternatives, and a promotion code. Hereby, programmatic printing is not limited to print media, or to a specific range of print media products. The media can also be sent digitally.

Of course, programmatic printing is a major step forward, as it enables sharing knowledge across channels, e.g. customers' preferences. However, the decisive factor is that produced media shows a certain selection of products based on preferences. This leads to an information loss, as a large amount of products is not shown. This in turn, leads to a potential loss of sales. Sending the standard main catalog or a predefined sub-catalog instead, has no added value either. A discount could be provided here as well, but the rest of the content would be regardless of preferences.

To provide a fully-automatic solution for producing paper-based product catalogs without information loss, the expert system environment TaxoCatalog is presented. The main difference compared to existing works is that the structure of the catalog is semantically personalized based on the underlying product taxonomy, before the layout setting is performed. Four independent components that are based on using background knowledge, are part of TaxoCatalog. All have in common that the initial taxonomy can remain. The first component is aimed to semantically analyze correspondences of the concepts being part of the taxonomy, i.e. the product categories. The second component is analyzing the customers' individual preferences based on the order history. The third component is automatically modifying the taxonomy based on the computed preferences and correspondences, as well as the desired level of personalization. The fourth component is finally using the personalized taxonomy to automatically generate the personalized product catalog using standard data-driven publishing software. In summary, TaxoCatalog provides three contributions to the field of data-driven publishing and the printing industry:

- TaxoCatalog provides the first omni-channel application that is capable of using complex knowledge for producing paper-based product catalogs. The approach further advances the interlinking of portal-based digital media, and paper-based digital and print media.
- TaxoCatalog provides the first solution for personalizing paper-based product catalogs without resulting an information loss. This is achieved by semantically personalizing the content structure based on the underlying product taxonomy, before layout setting.
- TaxoCatalog provides the first solution that is able to dynamically but still fully-automatically scale the level of desired semantic personalization.

2. Background

This section succinctly describes the underlying concepts necessary to develop TaxoCatalog and to understand the used method explained in the next section. Four concepts are explained briefly: omni-channel retailing, taxonomy applications, expert systems, and data-driven publishing.

2.1 Omni-channel retailing

The retailing industry has been significantly influenced by the digitization of media channels. Today, retailers use omni-channel retailing, which allows that all channels are supplied by one single publishing

source, but the digital channels can nevertheless be networked with each other (Verhoef, Kannan and Inman, 2015). In this way, the retailer can explore knowledge about the customer's preferences in real-time to display product-related content in a personalized manner on the digital portal-based channels. To acquire those preferences, recommender systems are used. Such systems use and combine different statistical methods to measure order probability of products.

2.2 Taxonomy applications

Taxonomies are a formal methodology to semantically structure information using hierarchical ordered concepts (Angermann and Ramzan, 2017). The underlying concept can be described as a two-tuple $\tau = \{\varphi,\rho\}$, where ρ is a set of edges for connecting partially ordered concepts of φ. Each edge represents a semantic hypernym-hyponym (is-a) relationship between the concepts. For example, a "printed book" is-a "printed product" is-a "media product". Each concept is defined by a label and the position in τ. The deeper its position, the more specific the concept is. Taxonomies have many applications in information and content management (Angermann, 2017):

- In Product Information Management a taxonomy is used to hierarchically structure concepts in the form of product categories. These are used to group similar products, and to assign category-specific (e.g. attributes) and -unspecific (e.g. title) content to products.
- In Media Asset Management, the above-mentioned product categories are used to structure product-related media (e.g. images), and to assign those to the products.

In omni-channel retailing, the taxonomies are the most essential tool for publishing content across channels (Angermann, 2022). The data stored in the content management systems, is transferred via interfaces to the e-commerce portal. Same for transferring products to external marketplaces. And, the taxonomy is also required for enabling data-driven publishing. Its structure is used by the templates to automatically fill the pages with dynamic content provided using interfaces.

2.3 Expert systems

Expert systems are one kind of intelligent systems that aim to acquire new knowledge based on existing knowledge (Oleshchuk and Fensli, 2011). The main purpose of the systems is to derive decisions as done by a human expert (Mirmozaffari, 2019). In contrast to machine learning, the initial knowledge is acquired from domain experts, and not from training. Formally, this is known as background knowledge (BK) (Angermann and Ramzan, 2017). These can be internally or externally generated from different sources and in different formats, e.g. taxonomies, thesauri, etc.

2.4 Data-driven publishing

Data-Driven publishing is a rule-based technique for automatically setting the layout for paper-based documents using a layout generator software. This software provides different data interfaces to databases of different formats (e.g. SQL, XML), and a graphical interface for a designer, to set the data connection, and to create the needed master pages and templates:

- The master page defines the dimensions of the document, and of the page frame. That is the area of the paper that actually contains content (document minus margins).
- The (layout) template defines the position and size of static content to be included in a page frame using content frames, as well as the rules for formatting dynamic content.
- A data source finally provides the different content for the content frames as a data stack.

The most distinguish feature compared to earlier attempts is, that now content types are used (Enlund and Andersin, 2007). Those content types (e.g. for title, description, etc.) are also assigned with rules for

positioning and sizing, but also with rules for formatting the dynamic content. Thus, the dynamic content can be independently designed for producing various documents. Both, the needed structure of the data, and the included content types, is enabled using taxonomies.

Another criteria is that the content frames of the templates can be filled automatically by the above-mentioned stack. To do so, two conditions must be met (Gundougan, 2022): separation of the (media neutral) content from the layout, metadata assignment to the content. Both is achieved using single source publishing, which is already required when providing omni-channel retailing. Most retailers fulfill all criteria and conditions by using the hierarchical database format XML. It has the advantage that the data is already structured hierarchically, and the metadata can be individually specified in the form of so-called tags (van der Vlist, 2002). In addition, the required hierarchy and metadata can be validated using the data format Doctype Definition (DTD).

3. TaxoCatalog

In this section, the use-case of TaxoCatalog is discussed, before the components are explained. The implementation of the program will be shown at the conference.

3.1 TaxoCatalog use-case

The main difference compared to existing works is that the proposed use-case is semantically personalizing the product taxonomy, before the layout is set. A current order does not necessarily have to be an authoritative interaction to start the workflow of the system (see Figure 1):

1. The initial product taxonomy is analyzed with regard to semantic correspondences.
2. The customers' preferences are analyzed based on the order history. Orders that have been placed longer in the past are viewed at a correspondingly lower rate. The expert of the retailer can dynamically define to what extent part orders are taken into account.
3. The semantic correspondences and the preferences are taken into account to compute a personalized product taxonomy. The expert can define how strongly the taxonomy is semantically personalized. Theoretically, categories (and products) can be excluded, but this is not the focus of TaxoCatalog, since it results in a loss of information as explained.
4. The personalized taxonomy defines the structure of the catalog to be layout to fill the layout template with the dynamic content, as required for data driven publishing.
5. Finally, the file is exported according to a media-specific format, e.g. EPUB, PDF, or PDF/X.

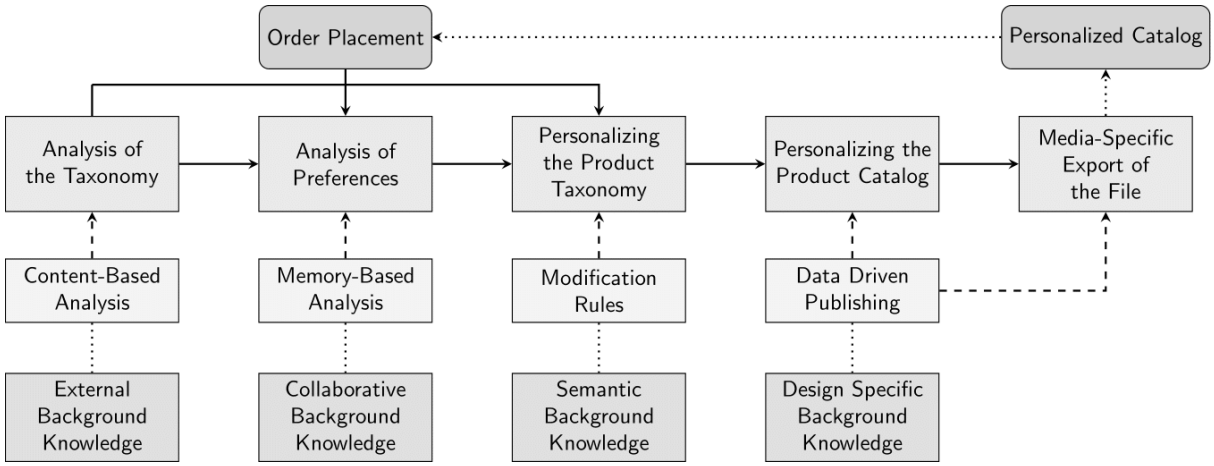

Figure 1: Use-case and workflow of TaxoCatalog, its components, and used background knowledge

3.2 TaxoCatalog components

Four components form TaxoCatalog. All decisions are automated using background knowledge to allow a cost-less integration into print media workflows (see Figure 1) (Angermann and Ramzan, 2016).

The first component is aimed to semantically analyze correspondences of concepts, i.e. the product categories of the initial product taxonomy. Its computation results a four-tuple δ for all possible combinations of φ: $\delta = (\varphi_1, \varphi_2, \rho, \varepsilon)$, where ρ states if two concepts $\varphi_{1,2}$ sharing the same is-a relationship are semantically similar or not. This is resulted through a computed value ε (between 0 and 1) and its comparison with a dynamic threshold. The computation of δ is performed using content-based natural language processing techniques. To increase the quality of the computation, external background knowledge is used as suggested in relevant literature (Angermann, Pervez and Ramzan, 2017).

The second component is analyzing the customers' individual preferences based on the order history. Here, a memory-based approach is used. This means that past orders are taken into account, as well as collaboratively acquired background knowledge, i.e. the analysis of other customers (Angermann and Ramzan, 2016). Its computation results a two tuple $\omega = (\varphi_{1,2}, \beta)$, where $\varphi_{1,2}$ are two semantically similar concepts, and β states the level of preference.

The third component is modifying the taxonomy based on δ and ω using different taxonomic operations, e.g. combining concepts and extending concepts. Each modification is performed in such a way that the semantics are adapted, but not corrupted. If a concept is extended, e.g., by further concepts, then this gets another label if necessary. This is particularly important, otherwise the customer may not be able to interpret the categories correctly. Since the new taxonomy was created on the basis of the initial taxonomy, the products can be assigned to the new categories without major hurdles. And, the expert can further define the semantic volume of the personalized taxonomy. This is performed using rules stored as background knowledge.

The fourth component is finally using the modified taxonomy to automatically generate the personalized product catalog using data-driven publishing.

4. Results

The efficiency of TaxoCatalog was evaluated with regard to a wide range of criteria and databases (see Table 1). The results for the two most relevant are summarized in this section. These are the *F*-Measure of the recommender system, and the semantic flexibility of personalizing taxonomies.

Table 1: Characteristics and parameters of the databases used for experimental results

Criteria	Adventureworks	Northwind	Festool
N Customers	700	93	500
N Orders	31 464	829	1 400
N Products	320	77	118
N Concepts	42	31	53

The *F*-Measure score states the decision quality of the system to analyze customers' preferences, compared to a human expert. A score of 1 means that in all test cases, the right decision has been made. The average *F*-Measure score of TaxoCatalog is 0.93 for all three databases: 0.92, 0.88, and 0.98. It is particularly noteworthy that the good score is similar for all three databases. Thus, an equally good result can be achieved

for a variety of products and publications. The Semantic Flexibility is measured to verify the flexibility when using the taxonomy as main instrument for personalizing the catalog. Two scores are measured. Firstly, the reduction flexibility is computed by identifying the maximum possible decrease of the taxonomy. Secondly, the enlargement efficiency is computed to verify a maximum possible decrease of the taxonomy. The average reduction flexibility score is 48.10 %. The average enlargement flexibility score is similar: 51.26 %. This states that the taxonomy provides a great solution in terms of semantic flexibility.

4. Conclusions

This work presented TaxoCatalog, the first taxonomy driven expert system environment for automatically personalizing paper-based product catalogs. Compared to related works, TaxoCatalog does the personalization without information and automation loss. As future work, the content types will be taken into account to also individualize the included graphic design.

Acknowledgements

Thanks to the Festool GmbH & Co. KG and the InBetween Deutschland GmbH for providing data and software for the presented research.

References

Angermann, H. and Ramzan, N., 2016. TaxoPublish: towards a solution to automatically personalize taxonomies in e-catalogs. *Expert Systems with Applications*, 66, pp. 76–94. https://doi.org/10.1016/j.eswa.2016.08.058.

Angermann, H., 2017. *Manager's guide to SharePoint Server 2016: tutorials, solutions, and best practices*. Berkeley: Apress/Springer.

Angermann, H. and Ramzan, N., 2017. *Taxonomy matching using background knowledge*. Cham: Springer.

Angermann, H., Pervez, Z. and Ramzan, N., 2017. *Taxo-Semantics*: assessing similarity between multi-word expressions for extending e-catalogs. *Decision Support Systems*, 98, pp. 10–25. https://doi.org/10.1016/j.dss.2017.04.001.

Angermann, H., 2022. TaxoMulti: rule-based expert system to customize product taxonomies for multi-channel e-commerce. *SN Computer Science*, 3(2): 177. https://doi.org/10.1007/s42979-022-01070-8.

Behera, R. K., Gunasekaran, A., Gupta, S., Kamboj, S. and Bala, P. K., 2020. Personalized digital marketing recommender engine. *Journal of Retailing and Consumer Services*, 53: 101799. https://doi.org/10.1016/j.jretconser.2019.03.026.

Chen, Y., Li, M., Song, J., Ma, X., Jiang, Y., Wu, S. and Chen G.L., 2022. A study of cross-border E-commerce research trends: based on knowledge mapping and literature analysis. *Frontiers in Psychology*, 13: 1009216. https://doi.org/10.3389/fpsyg.2022.1009216.

Enlund, N. and Andersin, H.E., 2007. The early days of computer aided newspaper production systems. In: J. Impagliazzo, T. Järvi and P Paju, eds. *History of Nordic Computing 2: Second IFIP WG 9.7 Conference – HiNC 2*. Turku, Finland, 21–23 August 2007. Springer, pp. 238–249.

Gao, L.-X., Melero, I. and Sese, F.J., 2020. Multichannel integration along the customer journey: a systematic review and research agenda. *The Service Industries Journal*, 40(15-16), pp. 1087–1118. https://doi.org/10.1080/02642069.2019.1652600.

Gil-Gomez, H., Guerola-Navarro, V., Oltra-Badenes, R. and Lozano-Quilis, J.A., 2020. Customer relationship management: digital transformation and sustainable business model innovation. *Economic Research-Ekonomska Istraživanja*, 33(1), pp. 2733–2750. https://doi.org/10.1080/1331677X.2019.1676283

Hänninen, M., Kwan, S.K. and Mitronen, L., 2021. From the store to omnichannel retail: looking back over three decades of research. *The International Review of Retail, Distribution and Consumer Research*, 31(1), pp. 1–35. https://doi.org/10.1080/09593969.2020.1833961.

Hoffmann-Walbeck, T., 2022. *Workflow automation: basic concepts of workflow automation in the graphic industry*. Cham: Springer.

Lin, X., 2006. Active layout engine: algorithms and applications in variable data printing. *Computer-Aided Design*, 38(5), pp. 444–456. https://doi.org/10.1016/j.cad.2005.11.006.

Mirmozaffari, M., 2019. Developing an expert system for diagnosing liver diseases. *European Journal of Engineering and Technology Research*, 4(3), pp. 1–5. https://doi.org/10.24018/ejeng.2019.4.3.1168.

Norvell, T., Kumar, P. and Contractor, S. (2018). Assessing the customer-based impact of up-selling versus down-selling. *Cornell Hospitality Quarterly*, 59(3), pp. 215–227. https://doi.org/10.1177/1938965518762836.

Oleshchuk, V. and Fensli, R., 2011. Remote patient monitoring within a future 5G infrastructure. *Wireless Personal Communications*, 57(3), pp. 431–439. https://doi.org/10.1007/s11277-010-0078-5.

van der Vlist, E., 2002. *XML schema: the W3C's object-oriented descriptions for XML*. Sebastopol, CA: O'Reilly Media.

Verhoef, P.C., Kannan, P.K. and Inman, J.J., 2015. From multi-channel retailing to omni-channel retailing: introduction to the special issue on multi-channel retailing. *Journal of Retailing*, 91(2), pp. 174–181. https://doi.org/10.1016/j.jretai.2015.02.005.

DOI 10.14622/Advances_49_2023_14

Robust method for printed pattern classification and creation of fluid splitting regime maps for gravure printing

Pauline Rothmann-Brumm[1,2] *and Edgar Dörsam*[1,2]

[1] Technical University of Darmstadt, Department of Mechanical Engineering, Institute of Printing Science and Technology, Magdalenenstr. 2, 64289 Darmstadt, Germany

[2] Collaborative Research Center (CRC) 1194 – Interaction between Transport and Wetting Processes, Project C01, Germany

E-mails: rothmann-brumm@idd.tu-darmstadt.de; doersam@idd.tu-darmstadt.de

Short abstract

Hydrodynamic pattern formation in gravure printing is not yet completely understood. Classification of printed patterns serves as a data-driven tool for finding cause-effect-correlations between printing parameters and printed patterns and thus helps to gain a deeper insight into pattern formation phenomena. The focus of this study is hydrodynamic pattern formation that originates from fluid splitting during fluid transfer. We aim to develop a method for pattern classification that is robust against printing defects. Our study is based on a comprehensive image data set created with an industrial web-press. First, a representative data subset is chosen and image preprocessing is performed. Second, classification of printed patterns into three fluid splitting classes, namely point splitting, transition regime and lamella splitting, is conducted by a human observer. The used classification method is optimized compared to previous methods. The main advantage of the new method is that the definition of the transition regime is tunable and thus is more robust against printing defects. Third, the results of the classification are used for the creation of exemplary regime maps which show the regimes of fluid splitting in printing parameter space.

Keywords: rotogravure, pattern formation, fluid splitting, regime maps, robust classification method

1. Introduction and background

Understanding hydrodynamic pattern formation during fluid transfer in printing processes is key for obtaining high-quality printed layers. The quality requirements for the printed layers are usually defined by their application such as graphical printing, printed electronics, functional coatings or bioprinting. An ideal printed layer thus can look very different. Some ideal layers are dominated by dot patterns as in many graphical applications, some ideal layers are smooth and do not have any pattern at all like large-area printed electronics and some ideal layers exhibit a stochastic, biomimetic finger pattern like in printed vascular networks for bioprinting applications. To forecast the printed pattern and to choose the correct printing parameters for each application, a detailed knowledge of cause-effect-correlations between printed patterns and printing parameters is crucial. This knowledge is, e.g., generated by conducting systematic printing experiments and then collect and visualize the results in fluid splitting regime maps. Regime maps in general are a common tool in fluid mechanics for the characterization of fluid flow regimes.

To create fluid splitting regime maps from printing experiments, it is necessary to classify the printed patterns into several types of fluid splitting. From Hübner (1991), we know two types of fluid splitting classes: point splitting and lamella splitting. Brumm, et al. (2021) extended this view to three classes and proved the existence of a transition regime class. In this study, we aim to develop a method for pattern classification that is robust against printing defects. Therefore, we use a large image data set and perform a data-driven analysis on it.

2. Materials and methods

2.1 Image data set

2.1.1 Complete data set

The image data set that serves as a basis for this research was created by Brumm, et al. (2022) on an industrial gravure web-press Bobst Rotomec MW 60-600/250 (Bobst, Mex, Switzerland). The experiments were conducted at printing velocities from 15 to 240 m/min, with water-based and solvent-based gravure inks with four different viscosities on foil and paper substrates, using an electromechanically engraved printing form decorated with full-area patches ("fields") with raster frequencies of 60, 70, 80 and 100 lines/cm and tonal values from 5 % to 100 % in 5 % steps. After high-resolution, color-calibrated scanning at 2 400 dpi and automated digital cutting of the printed samples in the programming language Python, a data set of 48 960 images of size 1 040 px × 1 040 px (11 mm × 11 mm) is obtained. This data set shows a great variety of hydrodynamic pattern formation phenomena from dot raster patterns resulting from "point splitting" to viscous fingering patterns, also called ribbing, resulting from "lamella splitting", see Figure 1. The transition between both types of patterns ("transition regime") is also represented in the data set. The aim of this research is to classify the printed patterns to be able to create fluid splitting regime maps in printing parameter space from the pattern classes and the available metadata in form of printing parameters.

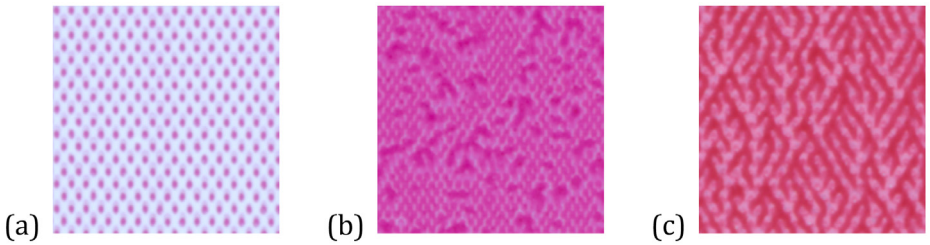

Figure 1: Examples for printed patterns assigned to different fluid splitting classes: point splitting (a), transition regime (b) and lamella splitting (c); each patch has the size 260 px × 260 px (2.75 mm × 2.75 mm)

2.1.2 Data preprocessing

Since in further studies from Brumm, et al. (2021), the manual classification scheme was not very robust against printing defects and thus tended to over exaggerate the amount of samples classified as transition regime, we develop an optimized, robust classification scheme (see section 2.2.). The robust classification scheme requires a simple preprocessing of the data. Each image of size 1 040 px × 1 040 px (11 mm × 11 mm) is divided into 16 equal parts of size 260 px × 260 px (2.75 mm × 2.75 mm). In this way, the data subset is increased from 48 960 images to 783 360 (smaller) images, which are called "subfields" in the following. No other preprocessing steps are performed.

In this study, the fields are divided into 16 subfields, because this results in a good viewing size of each subfield on a 14-inch computer screen such that no zoom-in is needed to observe the printed patterns. This simplifies the manual classification process. A division into 4, 9 or 25 and more subfields would theoretically also be possible. However, a smaller number of subfields per field might need a zoom-in during manual classification to properly see the printed patterns and a larger number of subfields would probably require a higher amount of time for the manual classification, since more subfields would have to be classified.

2.1.3 Selection of a representative data subset

The complete data set is very large so that manual classification of all samples is too time-consuming. Thus, a representative data subset is selected from the complete data set. Only the representative data subset is used for manual classification. The selection is aimed at considering at least samples with extreme values, e.g., with highest, lowest and a medium printing velocity, with the highest and lowest viscosity and with exemplary samples on all substrates and from all printing inks. In total, 26 880 of 783 360 images (3.4 %) were selected for the representative data subset.

2.2 Manual classification

2.2.1 Classification scheme for subfields

Manual classification of the subfields is conducted based on the definition of dot and finger patterns and the manual classification scheme of point splitting, lamella splitting and transition regime as presented in Brumm, et al. (2021). According to their manual classification scheme, a field that only shows "dots", is classified as point splitting (see Fig. 1a), and a field that only shows "fingers" is classified as lamella splitting (see Figure 1c). Fields that show dots and fingers are classified as transition regime (see Figure 1b). Hereby, one single dot among many fingers or one single finger among many dots is already enough to classify a field as transition regime, making the classification scheme rather harsh. A dot is an "isolated droplet on the printing product on a raster dot position" and a finger is a "liquid ink bridge resulting from viscous fingering on the printed product" and "the smallest finger is as long as the distance between two neighbouring raster dots" (Brumm, et al., 2021).

For this study, we made some changes to the described manual classification procedure to tune its harshness and thus to make it more robust against printing defects. In this work, a printing defect is regarded as a phenomenon that locally changes the pattern within a subfield or a field. This local change of the pattern can lead to a different classification of the subfield or the field, i.e., it corrupts the classification decision. The ideal situation would be to have a data set without any printing defects. In reality, printing defects are common, see Figure 2. Exemplary printing defects include missing dots, "donut" dots, dirt particles, drying patterns, pinholes, inhomogeneous ink distribution, doctor blade stripes etc.

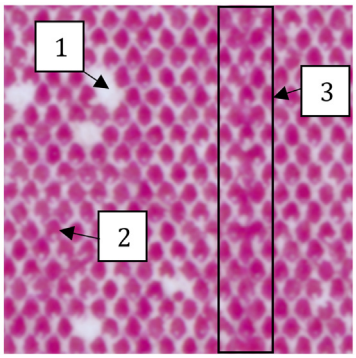

Figure 2: Exemplary printing defects: missing dot (1), "donut" dot (2) and doctor blade stripe (3); the patch has the size 260 px × 260 px (2.75 mm × 2.75 mm)

As an imaginary example, picture a doctor blade stripe that causes an accumulation of printing ink on a printed field. We assume that without the doctor blade stripe, the pattern on the field would be classified as "point splitting", since the pattern only consists of "dots". However, in the local region of the doctor blade stripe, the accumulation of ink leads to the formation of "fingers". This changes the classification decision of the field to "transition regime", since "dots" as well as "fingers" are present within the field. Consequently, the printing defect corrupted the classification decision of the field.

In Brumm, et al. (2021), classification was performed directly on the fields, whereas in our study, classification is performed on the subfields. The class of the field is then determined from the classification of the subfields using the algorithm from section 2.2.2. Another improvement is the use of an assistance software for the manual classification. This software is an adaption of the Python code "image-sorter2" from Arsenov (2019) and fosters an efficient classification process. Before, a lot of time was lost during organizational tasks during manual classification like opening the correct file and documenting the result in the correct cell in a spreadsheet software. Now, the assistance software automatically shows the next image after an image was classified and it automatically moves the classified image to a folder with the class name. The classification process can be paused and resumed at any time.

2.2.2 Algorithm for classification of fields

The main improvement for increase of robustness against printing defects is the algorithm that determines the class c of a field from the class c_i of its 16 subfields, see Figure 3. Therefore, each c_i is assigned a value a_i according to Equation [1]. All 16 values for a_i are added up for one field and yield a according to Equation [2]. The class c of the field is 1 (point splitting), 2 (transition regime) or 3 (lamella splitting), depending on a and the predefined lower and upper thresholds $a_{\text{tresh},l}$ and $a_{\text{tresh},u}$, see Equation [3].

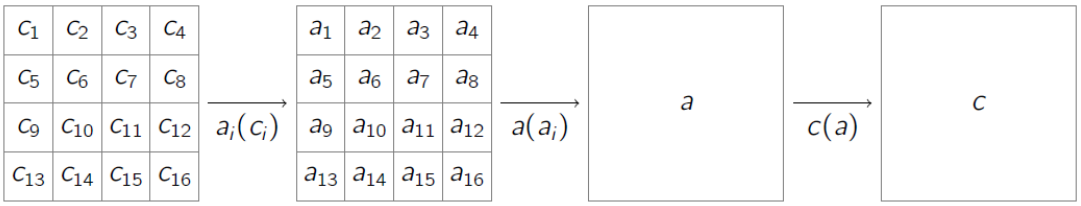

Figure 3: Schematic representation of the algorithm for determining the class c of a field based on the class c_i of its 16 subfields

$$a_i(c_i) = \begin{cases} -1, & c_i = 1 \text{ (point splitting)} \\ 0, & c_i = 2 \text{ (transition regime)} \\ 1, & c_i = 3 \text{ (lamella splitting)} \end{cases} \quad [1]$$

$$a(a_i) = \sum_{i=1}^{16} a_i \quad [2]$$

$$c(a) = \begin{cases} 1, & -16 \le a < a_{\text{thresh},l} \\ 2, & a_{\text{thresh},l} \le a \le a_{\text{thresh},u} \\ 3, & a_{\text{thresh},u} < a \le 16 \end{cases} \quad [3]$$

with $a_{\text{tresh},l} \in \{-15, -14, -13, ..., 0\}$ and $a_{\text{tresh},u} \in \{15, 14, 13, ..., 0\}$

The threshold values $a_{\text{tresh},l}$ and $a_{\text{tresh},u}$ can be used for tuning of the classification decision for the fields. If the thresholds are chosen close to −15 and 15, respectively, the transition regime is very large, whereas the transition regime narrows down for thresholds near zero. With thresholds going towards zero, the majority of subfields must be classified as "transition regime" to make the complete field be classified as "transition regime" as well. This likely eliminates the influence of corrupted classification decisions due to printing defects. However, when choosing a threshold near zero, there might not exist a transition regime any longer, since the criterion is too harsh.

2.3 Creation of exemplary regime maps

From the manual classification of a selected number of subfields from the data subset, we create exemplary fluid splitting regime maps. The regime maps are available in a raw and a processed form. We compare

the influence of the upper and lower thresholds on the appearance of the regime maps, especially on the appearance of the transition regime.

3. Results and discussion

3.1 Classification

3.1.1 Distribution of fluid splitting classes within the representative data subset

Within the representative data subset, 9 362 subfields (34.8 %) are classified as point splitting, 3 725 subfields (13.9 %) as transition regime and 13 793 subfields (51.3 %) as lamella splitting.

3.1.2 Distribution of fluid splitting classes within fields

All subfields from the representative data subset were manually classified. When analyzing the class of a subfield over the subfield's position within the field, we observe an inhomogeneity of the distribution of fluid splitting classes within the fields, see Figure 4. It shows how often the subfields of a field were classified as point splitting (Figure 4a), transition regime (Figure 4b) and lamella splitting (Figure 4c). It turns out that the four lower subfields within a field are more often classified as point splitting and transition regime and less often classified as lamella splitting than the rest of the field. Therefore, we assume that the four lower subfields are printed with a lower amount of ink, since a higher ink volume leads towards lamella splitting. We assume that the inhomogeneity originates due to the time dependent excess volume available in the printing nip.

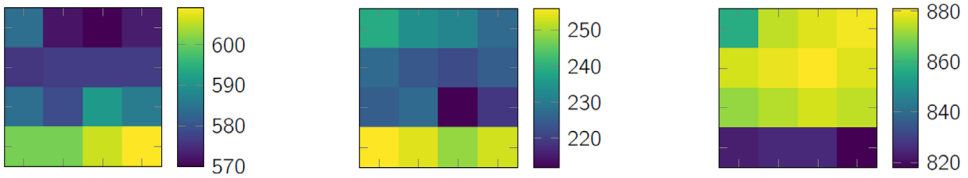

(a) Point splitting (b) Transition regime (c) Lamella splitting

Figure 4: Number of classifications of the 16 subfields into point splitting (a), transition regime (b) and lamella splitting (c) within the fields; the printing direction goes from bottom to top

The printing direction in Figure 4 goes from bottom to top, thus the excess ink volume builds up from bottom to top until it reaches a steady-state. We tried to avoid edge effects and resulting inhomogeneity by discarding the outer 1 mm of each printed field during digital cutting out of the fields, however, 1 mm turns out not to be sufficient.

3.1.3 Tuning the classification of fields

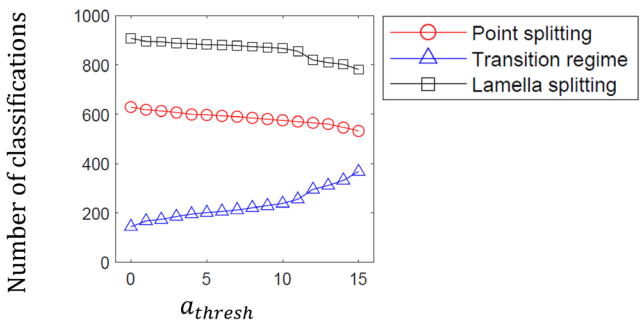

Figure 5: Number of classifications of fields into point splitting, transition regime and lamella splitting over threshold a_{tresh}

As already mentioned, the classification decision of a field based on the classification of its 16 subfields can be tuned via the lower and upper threshold $a_{tresh,l}$ and $a_{tresh,u}$. Figure 5 shows the number of classifications of fields into point splitting, transition regime and lamella splitting over the threshold value $a_{tresh} = |a_{tresh,l}| = a_{tresh,u}$. For simplification reasons, both thresholds are chosen equal in amount. A threshold closer to 15 leads to a higher amount of subfields classified as transition regime.

3.2 Exemplary regime maps

Figure 6 shows exemplary regime maps in raw and processed form for different threshold values. The processing is mainly based on linear interpolation and averaging of regime borders. On the *x*-axis, we see the printing velocity in m/min and on the *y*-axis, we see the tonal value of the printing form in %. The axes span the chosen printing parameter space and the plotted data points show the location of the three fluid splitting regimes: point splitting (red circle), transition regime (blue triangle) and lamella splitting (black square).

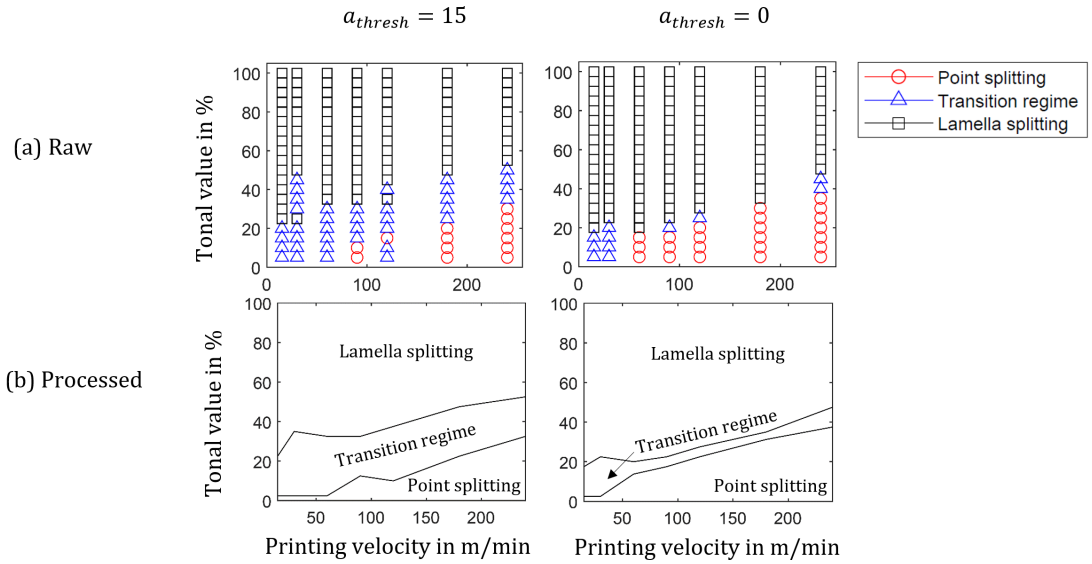

Figure 6: Exemplary regime maps in raw (a) and processed form (b) for two different threshold values

Regime maps with other axes are also possible, e.g., we could use non-dimensional numbers like the capillary number *Ca* on one axis. The regime maps in Figure 6 are based on classified image data from a printing run with id "B3-05" by Brumm, et al. (2022) on coated paper with water-based ink without electrostatic assist. Viscosity of the ink was determined as 17 s with a 4 mm ISO flow cup after DIN EN ISO 2431 (Deutsches Institut für Normung, 2020). Doctor blade angle is 55°. Engraving angle of the electromechanically engraved printing form is HELL engraving angle #2 (59.35°), stylus angle is 120° and raster frequency is 60 lines/cm. A fraction of the data was manually classified by a human observer as explained in section 2.2.1; another fraction was classified using machine learning methods, which is outside the scope of this paper.

From Figure 6 it becomes clear that with a threshold value closer to 15, the transition regime appears much larger than with a threshold value of zero. Thus, the appearance of the regime map can be tuned to the needs of the application. If the printer wants to avoid the transition regime, a threshold value of 15 might be suitable, since the transition regime reaches its biggest extent there. However, if the printer wants to print inside the transition regime, a threshold of zero might be better, since it gives a more precise location of the core of the transition regime.

Apart from tuning the appearance of the transition regime, the threshold leads to a robustness of the transition regime against printing defects when chosen near zero. In case of threshold $a_{tresh} = 0$, a field is only

classified as transition regime if all subfields are classified as transition regime ($a_i = 0$) or if all subfields except an even number of subfields are classified as transition regime. The even number of subfields must be half and half point splitting ($a_i = -1$) and lamella splitting ($a_i = 1$) so that their a_i-values add up to zero. As an example, we take a field, of which 14 subfields are classified as lamella splitting and two subfields are classified as transition regime due to a printing defect. This results in $a = 14$. Despite from the printing defects, this field will be classified as lamella splitting, if a_{tresh} is chosen between 0 and 13.

4. Conclusions and outlook

We were able to develop an algorithm for the classification of a field according to the classification of its 16 subfields. We showed that the threshold value a_{tresh} can be used to tune the appearance of the transition regime within fluid splitting regime maps. Besides, threshold values near zero lead to a robustness of the transition regime against printing defects. Exemplary fluid splitting regime maps were created. In future research, the algorithm shall be applied to the complete, available data set and fluid splitting regime maps for a broad variety of printing runs shall be created. The regime maps shall give further insights on the gravure printing process, e.g., on the influence of doctor blade angle, viscosity, substrate, electrostatic assist etc. on hydrodynamic pattern formation and on the resulting fluid splitting class. Moreover, the described methods and algorithms for pattern classification could be transferred to other printing processes.

Acknowledgements

We kindly acknowledge the financial support by the Deutsche Forschungsgemeinschaft (DFG, German Research Foundation) – Project-ID 265191195 – SFB 1194 'Interaction between Transport and Wetting Processes', project C01.

We thank F. Rothmann for fruitful discussion on the developed algorithm.

References

Arsenov, N., 2019. *image-sorter2: one-click image sorting/labeling script*. Github [online] Available at: <https://github.com/Nestak2/image-sorter2> [Accessed 12 April 2023].

Brumm, P., Weber, T.E., Sauer, H.M. and Dörsam, E., 2021. Ink splitting in gravure printing: localization of the transition from dots to fingers. *Journal of Print and Media Technology Research*, 10(2), pp. 81–93. https://doi.org/10.14622/JPMTR-2016.

Brumm, P., Sprinzing, T., Euler, T., Galus, M., Weichmann, A. and Dörsam, E., 2022. Creation of a comprehensive high-resolution image data set on an industrial web press to investigate hydrodynamic pattern formation in gravure printing. In: C. Ridgway, ed. *Advances in Printing and Media Technology: Proceedings of the 48th International Research Conference of iarigai. Greenville, SC, USA, 19–21 September 2022*, pp. 109–115. https://doi.org/10.14622/Advances_48_2022_08.

Deutsches Institut für Normung, 2020. *DIN EN ISO 2431:2020 DE Beschichtungsstoffe – Bestimmung der Auslaufzeit mit Auslaufbechern*. Berlin: DIN.

Hübner, G., 1991. *Ein Beitrag zum Problem der Flüssigkeitsspaltung in der Drucktechnik.* Dissertation. Technische Hochschule Darmstadt. https://doi.org/10.25534/tuprints-00013550.

DOI 10.14622/Advances_49_2023_19

Influences of mesh and glass surface types on the quality and adhesion of screen-printed elements

Sandra Rosalen and Ulrich Jung

University of Wuppertal, School of Electrical, Information and Media Engineering
E-mails: srosalen@uni-wuppertal.de; ujung@uni-wuppertal.de

Short abstract

This study investigates the impact of mesh screen geometry, surface pre-treatments (hydrophilization and hydrophobization) and the glass side, i.e. air-side or tin-side resulting from the float glass manufacturing process, on the reproduction (line width, roughness and ink thickness) of printed elements in screen printing process and the adhesion of ink on glass. It has been shown that the mesh screen has a stronger influence on the reproduction of the printed elements than the pre-treatment of the glass, and that this has a stronger influence than the side of the float glass. It was also demonstrated that screens with a higher mesh screen (165-030) yield thinner ink films and better adhesion to the glass as compared to screens with a lower mesh screen (120-030).

Keywords: screen printing, float glass, surface treatments, adhesion, reproduction's quality

1. Introduction and background

Screen printing on glass is a widely used method for decorating and functionalizing glass surfaces. The choice of screen and the surface treatment can have a significant impact on the final print quality and ink adhesion. Using a finer mesh screen can result in more precise and detailed prints, while a coarser mesh screen may be more suitable for larger areas or more textured designs. Hydrophilization and hydrophobization are surface treatments that can improve ink adhesion and reduce the amount of ink needed for printing. They are used to change the surface energy of the glass, making it more or less receptive to the ink.

The side of the glass on which the print is applied can also have an impact on print quality. In float glass manufacturing process, the fire side of the glass is formed on the side that faces the flame, while the tin side is formed on the side that faces the tin bath. The tin-side of the glass is usually smoother and has fewer defects than the air-side, which can result in a higher quality print. In some cases, surface defects and roughness can have an impact on ink adhesion. This leads to the common recommendation to use the fire side for sensitive applications.

The aim of the experiments presented here is to understand the influence of these variables (mesh screen, pre-treatment and glass side) on screen printing with UV ink on float glass. For this purpose, solid tone areas and lines were printed on the glass and subsequently the line width, the roughness of the printed area, the thickness of the ink film as well as the adhesion of the ink were measured. These are quality parameters in functional structures. Their variation determines e.g. the resistance or even the proper functioning of displays, integrated smart systems, electronics and components like memories, antennas and batteries.

To reduce the complexity of the experiments, only one type of UV ink was used.

2. Materials and methods

2.1 Materials

The materials used in this work are listed in Table 1.

Table 1: Materials used (Qty. – quantities used per batch)

Material	**Data** (manufacturer between brackets)	**Qty.**
Substrate	Float glass, transparent, size: 120 mm × 50 mm	28
Ink	UVGS/N50 (Sun Chemical)	50 g
Laboratory dishwasher cleaner (LDC)	Powder, mildly alkaline Neodisher Labo GK (Dr. Weigert) surfactant-free, contains phosphate and chlorine (< 30 % / >5 %)	17.2 g
Silylating agent (SA)	1,1,1,3,3,3-Hexamethyldisilazan CAS no.: 999-97-3 (Carl Roth)	600 ml
Cleaning agents	Ethanol 99.9 % CAS-no.: 64-17-5 (Chemsolute)	3 ml
	Distilled water CAS-no.:7732-18-5 (Wittig Umweltchemie)	5 l
Drying agent	Silica gel CAS-no.:1327-36-2 (Carl Roth)	150 g
Adhesive tape	Adhesive 4204 (Tesa) 25 mm wide, 59 µm thickness	-

2.2 Instruments / equipment

The instruments / equipment used in this work are listed in Table 2.

Table 2: Instruments / equipment used

Instruments / equipment	**Data and settings** (manufacturer between brackets)
Screen printer	AT PAB45 (ATMA ESC), snap off: 2 mm, print speed: 30 mm/s, distance to frame: 344 mm left and 183 mm right
Screen 1 (120)	L-120-030-305PW (NBC), frame 30 mm × 30 mm slope, mesh angle 22.5°
Screen 2 (165)	L-165-030-420PW (NBC), frame 30 mm × 30 mm slope, mesh angle 22.5°
Flood squeegee	165 mm wide, angle 0°, micrometer screw setup 7 mm
Print squeegee	145 mm wide, angle 10°, micrometer screw setup 10 mm
UV conveyor dryer	UN50059 (Technigraf)
Washing machine	MMD 37004 (Medion), washing program P2
Magnetic stirrer	PRSM-10HP (Phoenix Instrument)
Desiccator	DN 200 (Duran)
Scanner for image capture s. ISO/IEC 24790:2017	Perfection 4990 PHOTO (Epson), 1 200 dpi, 24 bits, photo modus
Microscope for surface roughness/ink layer thickness measurement	3D laser scanner microscope VK-X160K (Keyence), surface profile modus, standard 1024 × 768 pixel, RDP on, high accuracy quality, double scan off, ND-filter 30 %, noise removal on, image sharpening off, automatic exposure time, gamma correction value 0.45
Peel tester for adhesion measurement	Peel testing machine VPA-2S (Kyowa), pull-off angle 90°, speed 300 mm/min, measuring length 199 mm, start force 0 N
Adhesive tape applicator	(in-house development), applied tape length: 199 mm

2.3 Software

The software used in this work are listed in Table 3.

Table 3: Software used

Software	**Data and settings** (editor / developer between brackets)
TS24790_Tool 1.5.2a	Version 1.5.2a (ISO) for analysis of line elements – ISO/IEC 24790:2017
Epson Scan	Version 1.0 (Epson) for printed elements scanning – ISO/IEC 24790:2017
Image J	Version 1.53k (NHI) section of the ROI in the scanned elements – ISO/IEC 24790:2017
Multi File Analyser	Version 1.3.1.120 (Keyence) for analysis of microscope captured images
VPA	Version 2.3.2 (Kyowa) for adhesion measurement

2.4 Methods

The methods were divided into 3 groups: cleaning of the surface of the float glass plates, modification of the surface of the float glass plates and analysis of the printed elements. The first two methods were presented in a previous study (Patejdl, Jung and Freieck, 2022) and demonstrate high repeatability.

2.4.1 Cleaning of the surface of the float glass plates (Hydrophilization – HI)

Glass is naturally hydrophilic, which means it has a high surface energy that tends to make it more prone to environmental contamination. Thus, it is necessary to clean them to achieve a homogenous and comparable surface properties, as manufacturing and cutting processes deposit contaminants on the surface. The cleaning procedure requires immersing the plates in a 60 °C distilled water bath with LDC for 60 minutes. The bath should be stirred continuously. The plates are then washed with distilled water with the program P2 in the washing machine (wash at 50 °C, rinse at 65 °C and dry for one hour). Then the glasses were stored in dustproof containers for 1 week.

2.4.2 Modification of the surface of the float glass plates (Hydrophobization – HO)

Surface hydrophobization was performed with hexamethyldisilazan (HMDS), that has two well-known mechanisms to modify the surface. Firstly, it reacts with the adhered water molecules on the glass surface and thus removes the water layer. Secondly, it binds to the now free oxygen atoms of the silicon oxide on the glass surface and thus prevents a further build-up of water from the air on the glasses surface (Shen, et al., 2012).

The hydrophobization is applied as a multistep process and consists first of placing the cleaned glass plates (s. 2.4.1) in an HMDS bath (80 °C) for one hour. After the glasses were cleaned with a cleanroom cloth (Vipers PC 68) with approx. 3 ml ethanol 99.9 % (two repetitions) and placed for one hour under vacuum in a silica gel desiccator and then rinsed in the P2 program described above. At last the glasses were stored in dustproof containers.

2.4.3 Analysis of the printed elements

The printed test chart has lines with widths of 63, 126, 189, 252 and 315 µm printed vertically and horizontally in relation to the squeegee direction (Figure 1a) and a solid tone area of 60 mm × 30 mm printed vertically in relation to the squeegee direction (Figure 1b). The borders of the figures represent the float glass plate.

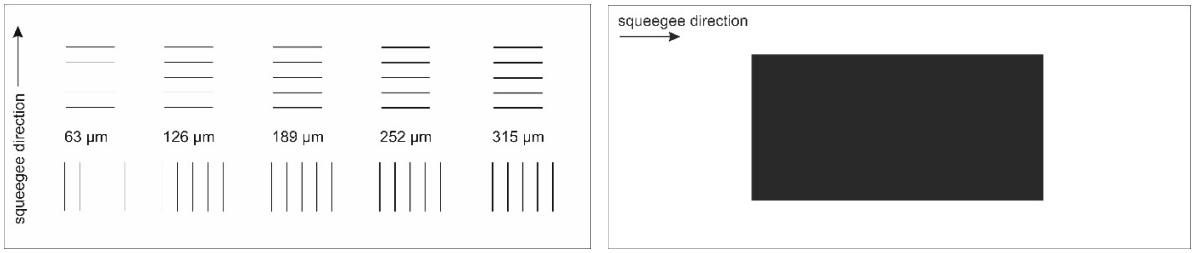

a) *b)*

Figure 1: Printed elements: lines (a) and solid tone printed area (b)

The measurement of line width is a crucial factor in evaluating the accuracy of ink transfer and identifying any variations in ink spread that may arise due to differences in glass sides or surface modifications. The standard ISO/IEC 24790:2017 (International Organization for Standardization, 2017) is typically utilized for measuring line widths in digital printing systems, but it can also be applied to screen printing, as demonstrated in experiments.

The evaluation of the line reproduction based on the ISO/IEC 24790:2017 is calculated using the reflectance ρ. The maximum reflectance (substrate) and minimum reflectance (100 % printed black) are determined to set the reflectance limits $\rho 70$ and $\rho 10$. These data are used in the description of the different reflection zones for the calculation, for example, of line blurriness and line darkness. The line width is the average width of the printed line. The width is calculated along the line from edge to edge (Equation [1]). LETP means "left edge threshold position", RETP "right edge threshold position", both in mm, and k is the dot row within a measuring element (line) to determine a local edge position (Figure 2).

$$\frac{1}{n}\sum_{k=1}^{n}(\text{LETP}) - (\text{RETP}) \qquad [1]$$

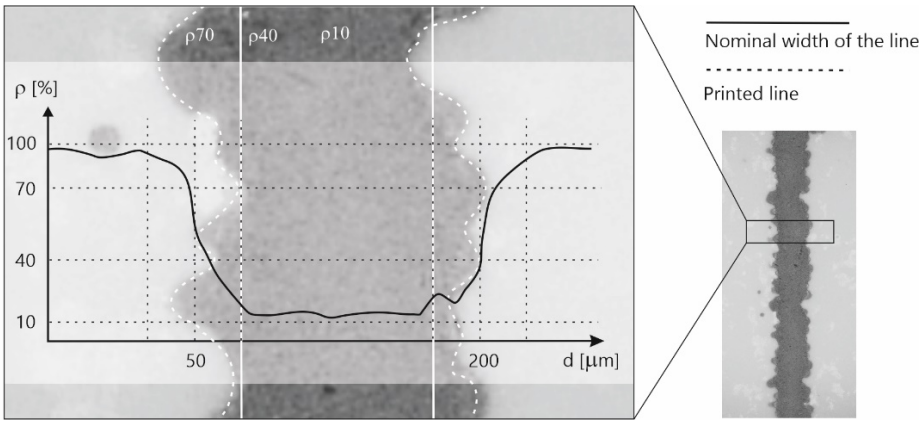

Figure 2: Reflection limits of a printed line according to ISO/IEC 24790:2017 (International Organization for Standardization, 2017) – modified

To determine the thickness and roughness of the ink film, the solid tone printed areas were examined after curing using a 3D laser scanning microscope. For the roughness measurements two parameters, R_z and S_z, were used to quantify roughness, where R_z refers to the 2D with 15 lines spaced 20 pixels apart and S_z measures the 3D areal profile of a 300 µm × 1 046 µm area. Both parameters were calculated by averaging the peak-to-valley height of each sample length. This averaging process ensures that the results are balanced and any isolated high peaks or low valleys along the line or area have minimal impact. The thickness and roughness of the ink film were measured in eight areas, with four located on the edge of the printed rectangle and four in the central section of the printed area (Figure 3).

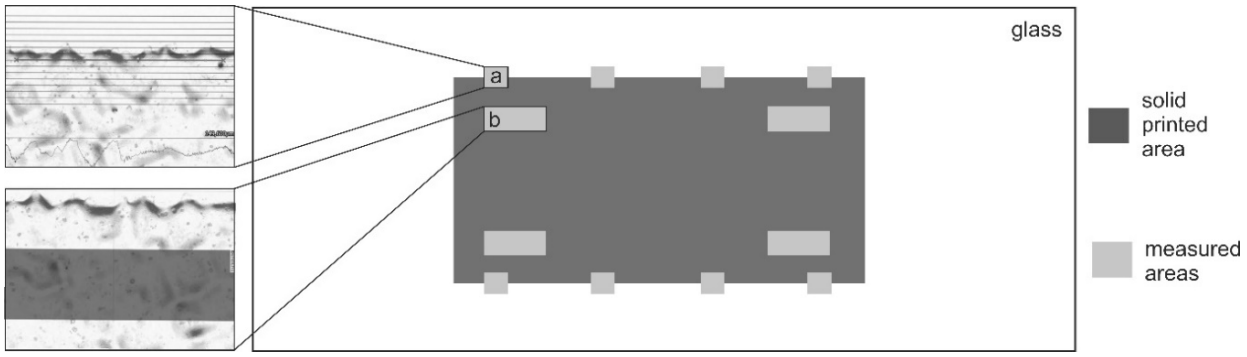

Figure 3: Measured areas and an example of a measurement with lines (a) (R-values) at the edge of the printed area and of an area measurement (b) (S-values) in the internal region of the printed area

Adhesion measurements were conducted in the solid tone printed areas using a peel analyser. The analysis involved applying adhesive tape onto the glass plate with a constant speed and pressure by a special device, and subsequently removing it using the peel analyser. The strength of the adhesion and the degree of delamination of the ink film were both evaluated. These measurements provide key findings into the quality of the ink film and its capacity to adhere to the substrate. In Table 4 are listed the quantity of samples for each analysis, as well as the acronyms used in the following figures and results.

Table 4: Samples quantities and used acronyms (each type indicates both a line width and a printing direction)

Surface modification	Mesh screen	Glass side	Acronyms	Lines (each type / total)	Solid tone areas (edge / central)
Hydrophilization	120-030	air-side	HI-120-AS	25 / 125	120 / 60
		tin-side	HI-120-TS	25 / 125	104 /52
	165-030	air-side	HI-165-AS	25 / 125	120 / 60
		tin-side	HI-165-TS	25 / 125	112 / 56
Hydrophobization	120-030	air-side	HO-120-AS	25 / 125	126 / 68
		tin-side	HO-120-TS	25 / 125	112 / 56
	165-030	air-side	HO-165-AS	25 / 125	112 / 56
		tin-side	HO-165-TS	25 / 125	112 / 56

3. Results and discussion

The results were analyzed by comparing measurements taken from various factors, including the type of mesh screen used (165 and 120), surface modification (HI and HO), glass side (AS and TS) and printing orientation (vertical [V] and horizontal [H] in relation to the print squeegee). The width of printed lines was also analyzed based on the target and actual values. In the following sections, these results will be presented and discussed for the four quality indicators, namely line width, roughness (R_z and S_z), ink film thickness and adhesion forces.

3.1 Line width

Figures 4 and 5 display the relative deviation between the target and actual values for the measured parameter. It is worth noting that the 63 µm lines on mesh screen 165 could not be measured due to the fine mesh. These lines were dotted (not continuous) instead with a continuous shape, which resulted in the fact software is unable to recognize the line borders and returning a measurement error.

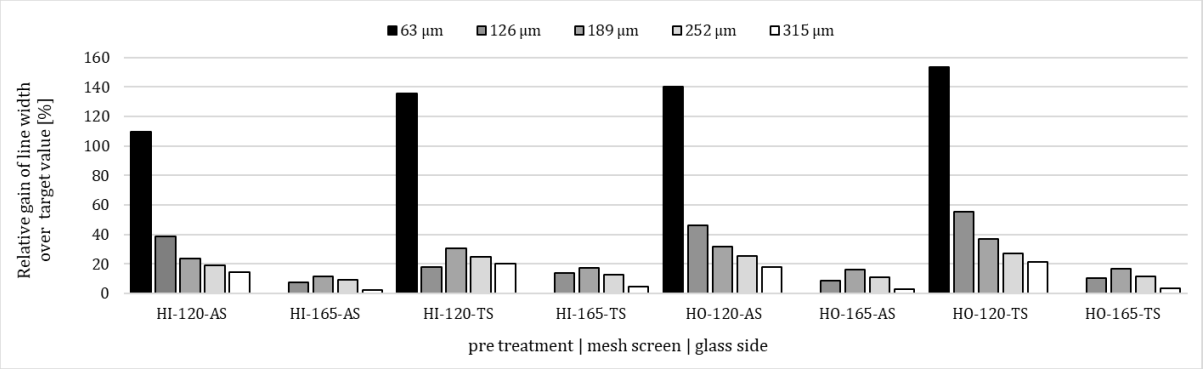

Figure 4: Average relative gain of line width over target value – horizontal direction [%]

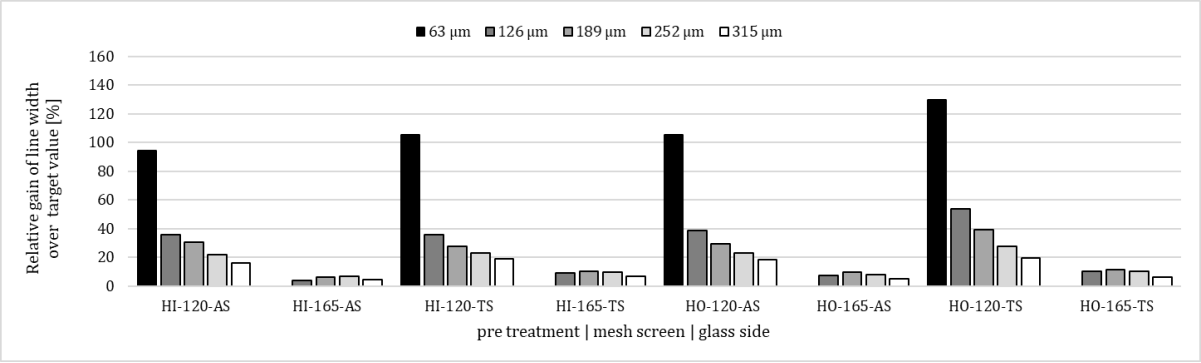

Figure 5: Average relative gain of line width over target value – vertical direction [%]

The deviations from the target value for the lines printed with the 165 mesh are considerably smaller than those of the 120 mesh and this is invariant of the side and treatment of the glass, as well as the printing direction.

In most all cases, measurements show that lines on hydrophilic glass substrates are thinner than their counterparts on hydrophobic glasses. However, this pattern is not observed for the TS 165 samples in the horizontal print direction, where the lines on the hydrophobised glass are actually thinner. This discrepancy could be caused by a distorted preparation process of glass treatment, as this effect is not seen in the vertical orientation. Additionally, the difference in line thickness between hydrophilic and hydrophobic glasses is less pronounced on the 165 mesh than on the 120 mesh. It's worth noting that the UV ink used in the study tends to spread less on hydrophilic surfaces than on hydrophobic ones. See Figures 6 and 7 for detailed results.

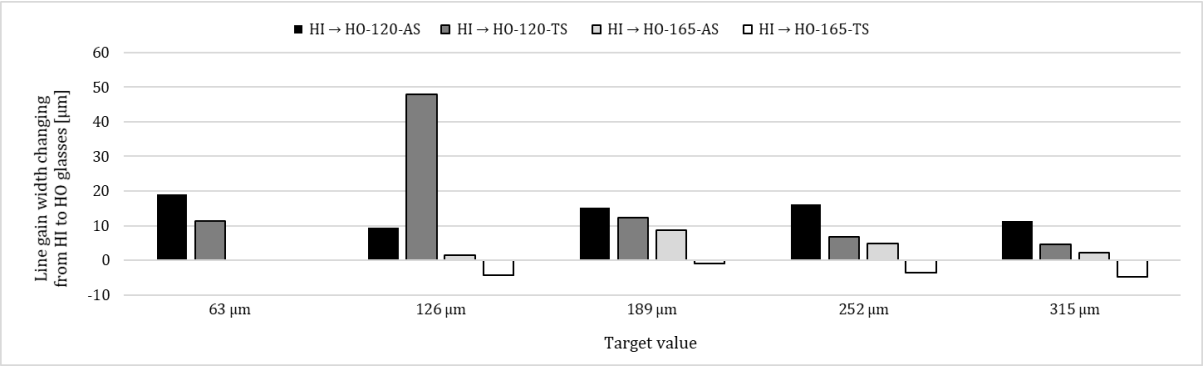

Figure 6: Line gain width changing from HI to HO glasses – horizontal print direction [µm]

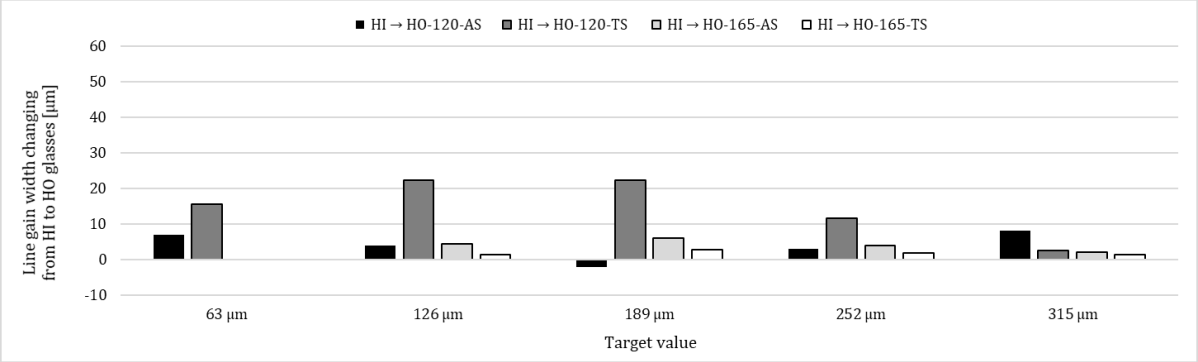

Figure 7: Line gain width changing from HI to HO glasses – vertical print direction [µm]

Lines on the AS are in general thinner than corresponding lines on the glass TS. When comparing the AS and TS side, the horizontal HI-lines exhibit a higher gain in line width than the HO-lines for both 165 mesh and 120 mesh screens. However, the observed line width decrease by the 120 HI-lines when switching from AS to TS (126 µm horizontal and 189 µm vertical, s. Figure 8) is not consistent with the explanations above. It's possible that the glass used in this case contained residues that were not fully removed by the hydrophilization process.

For the vertical lines, a similar trend is seen in the 165 mesh, where the gain is also higher for the HI-lines than the HO-lines. However, the behavior is opposite for the 120 mesh screens. Although lines printed on the TS side are generally thicker, the increase is more significant for the HO-lines. Interestingly, there are two outliers with the HI-120 lines. One outlier is smaller, in the vertical direction at 189 µm nominal line width, where the average TS value is 6.19 µm smaller than the AS value. The other outlier is larger, at 126 µm horizontally, with a difference of 26.31 µm. Figure 7 illustrates these points, where the 126 µm outlier being particularly prominent.

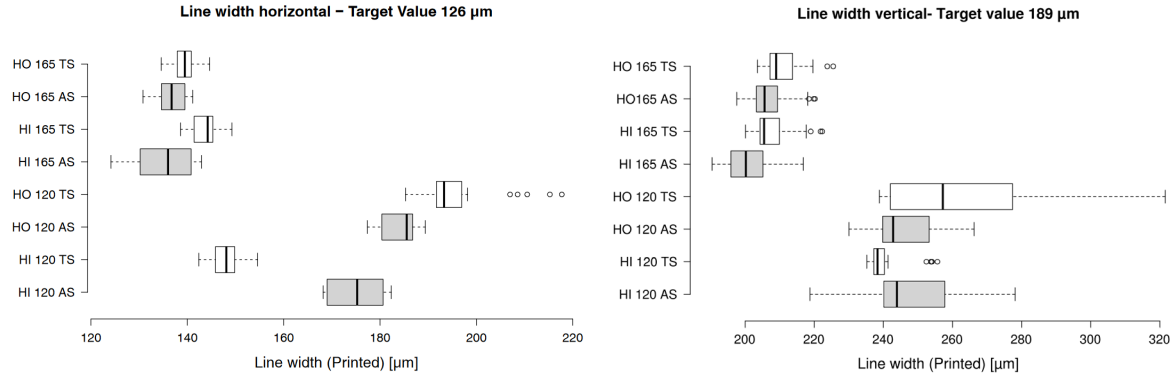

a) *b)*

Figure 8: Line width 126 µm horizontal (a) and 189 µm vertical (b)

Figure 9 shows how large horizontal lines are compared to their vertical counterparts. Positive values mean that the horizontal lines are larger than the vertical ones. Negative values mean that the average line widths in the horizontal orientation are thinner than in the vertical orientation. It can be seen that lines in horizontal printing orientation tend to deviate less from the target value with increasing line thickness than those in vertical orientation. In the line widths of 63 µm to 252 µm, the average values of the vertical line width are predominantly thinner than those of the horizontal. At 315 µm this is the opposite. These deviations could not be explained through the experiments made in this study.

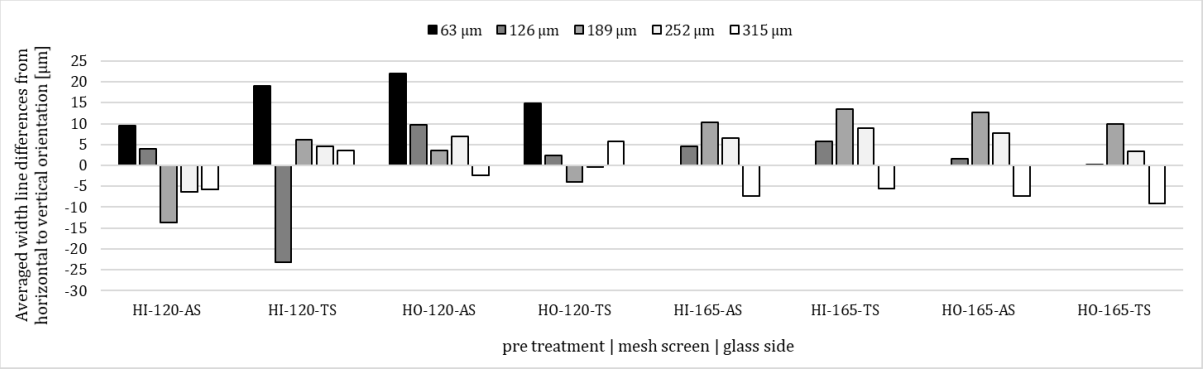

Figure 9: Averaged width line differences from horizontal to vertical orientation [µm]

3.2 Roughness

Line and area roughness of the samples printed with the 165 mesh are significantly lower than those of the 120 mesh across all measurements. An explanation for this result is that the surface roughness of the 165 mesh screen is in itself – due to the higher thread count – lower than that of the 120 mesh screen. Figure 10 shows this as an example using the AS side of the HO-glasses. Both for the measurements of the internal surface and the edges, the largest R_z values of the 165 mesh are smaller than the smallest R_z values of the 120 mesh.

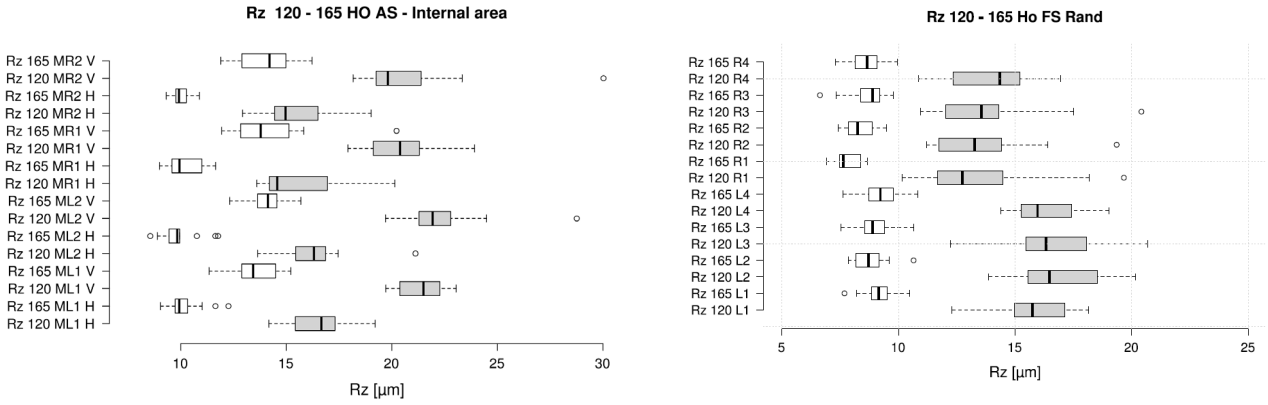

a) *b)*

Figure 10: Comparison of the line roughness R_z between the two mesh screens; (a) in the internal areas of the ink layer surface, and (b) at the edges (printed with the 165 mesh on the AS side of the HO-glasses)

The surface roughness difference on the HI-glasses is between the two mesh screens significantly low. Although the R_z values of the 165 mesh are predominantly smaller as well, there are overlaps in the value ranges between the results of the meshes in the boxplots. The diagrams in Figure 11 shows also that the minimum and maximum values of the 165 mesh are lower than those of the 120 mesh.

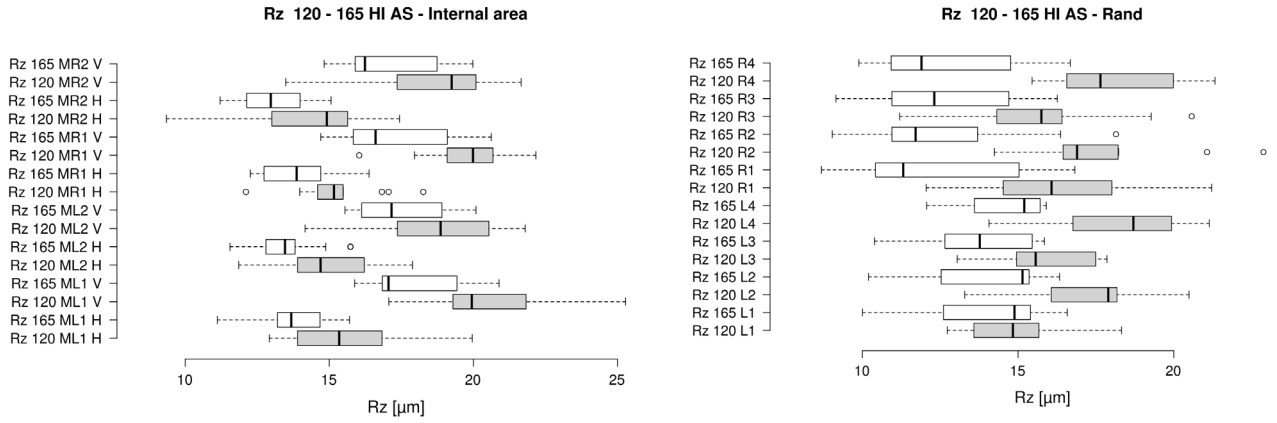

a) *b)*

Figure 11: Comparison of the line roughness R_z between the two mesh screens; (a) the internal areas of the ink layer surface, and (b) at the edges (printed with the 120 mesh on the AS side of the HI-glasses)

The S_z values show a similar performance to the R_z values, with a lower standard deviation, which is expected to measurements in areas in relation to measurements on lines (see Table 6).

Comparing the types of pretreatment, it was observed that both mesh screens show quite different behavior when switching from hydrophilic to hydrophobic glasses. In the case of the 120 mesh, the HO-glasses surface is usually slightly rougher on than its HI counterpart. However, there is usually overlap between the R_z measured values of the respective surfaces. A similar result can be seen by the S_z values. Here, too, the values of the HO-glasses are slightly higher, but overall they are quite close to each other. The behavior of the 165 mesh is different. When comparing HO and HI. The R_z values of the HO-glasses are clearly smaller than those of the HI-glasses. This is not so obvious shown by the S_z values. Although the values of the HO-glasses are also lower than those of the HI-glasses.

There are no major differences between AS or TS or even a tendency in either apparent for either HI or HO-Glasses.

3.3 Ink film thickness

According to the literature (Scheer, 2007), ink thickness is primarily dependent on the mesh screen geometry. Other factors such as ink viscosity, squeegee angle and speed have only a secondary influence. The most important parameter here is the theoretical ink volume (V_{th}). Meshes with a larger ink volume also produce a thicker wet ink film on the substrate (Scheer, 2007). Since UV-curing ink was printed, there should only be a small difference of about 2–3 % between wet and dry ink film thickness (Scheer, 2007; Berufsgenossenschaft Energie Textil Elektro Medienerzeugnisse, 2020). The V_{th} of the 120 and 165 meshes are 18.6 cm^3/m^2 and 8.0 cm^3/m^2 respectively. The ink film thickness measurements are presented in the Figure 12.

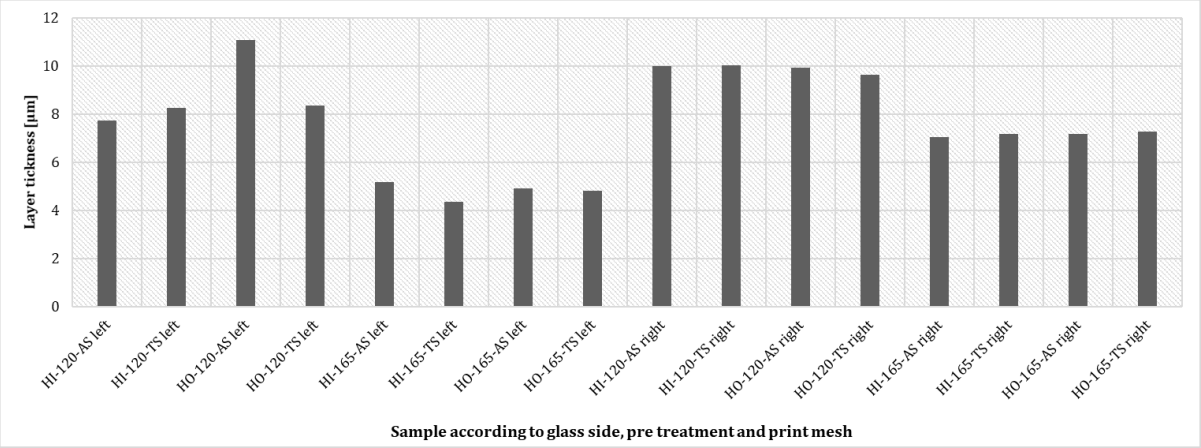

Figure 12: Average ink film thicknesses – right and left side of the solid tone printed area 120 HI AS, 120 HI TS, 120 HO AS, 120 HO TS, 165 HI AS, 165 HI TS, 165 HO AS and 165 HO TS

The results reflect the theoretical assumption. Both on the right and on the left edge side of glass, and widely independent of the type of pre-treatment or the glass side, the results remain constant.

3.4 Adhesion

Figure 13 shows the average peel force required per sample to separate the adhesive tape from the ink layer. Only those specimens were taken into account here in which no delamination (= peeling of the ink layer when the adhesive tape is removed from the glass surface) occurred in the measurement area.

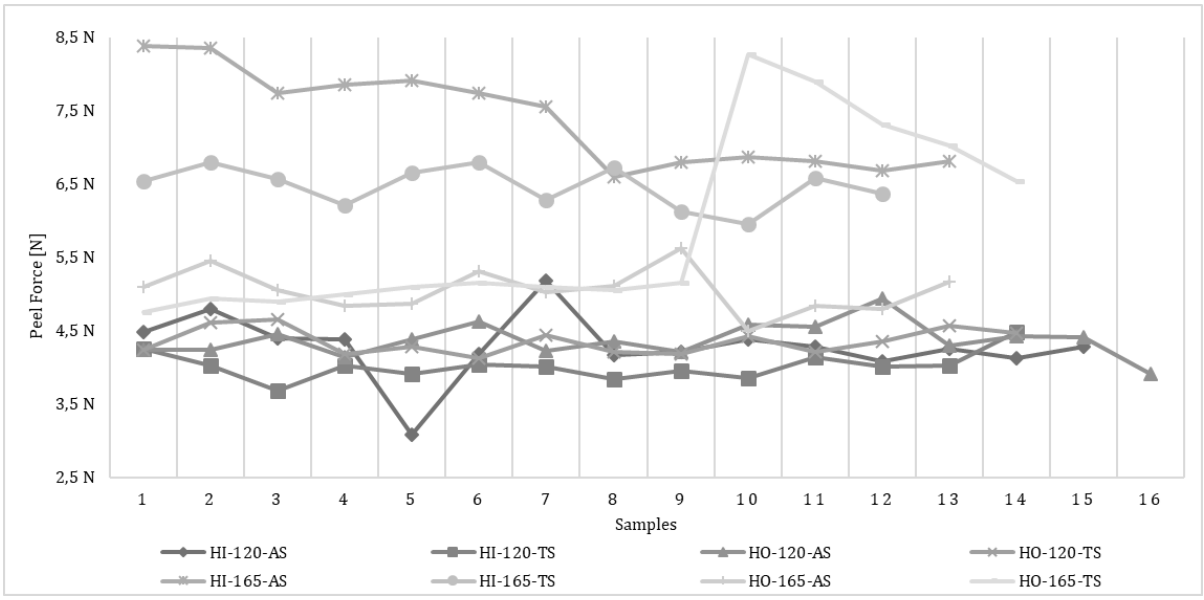

Figure 13: Peeling test – overview of the average peeling force per sample

It can be seen that the specimens printed with the 165 mesh require on average a higher force to trigger the release of the adhesive tape than those printed with the 120 mesh. Table 5 shows the measurements, deviation and delamination (exemplary, Figure 14) of all samples separated by mesh, pre-treatment and glass side.

Table 5: Variation and measurements of the peel test results and delamination (A: number of samples, B: samples with delamination, C: Delamination in % and D: measured points)

Samples	$\bar{x}$ F [N]	Min [N]	Max [N]	Range [N]	σ [N]	A	B	C [%]	D
HI-120-AS	4.38	3.77	5.53	1.76	0.31	14	2	14.29	1573
HI-120-TS	4.02	3.16	4.59	1.43	0.21	14	0	0	1694
HO-120-AS	4.43	3.69	5.25	1.56	0.24	17	2	11.76	1452
HO-120-TS	4.36	4.01	4.78	0.77	0.19	14	0	0	1573
HI-165-AS	7.40	6.41	8.70	2.29	0.65	15	2	13.33	1331
HI-165-TS	6.45	5.80	7.02	1.22	0.28	14	2	14.29	1331
HO-165-AS	5.07	4.19	6.04	1.85	0.33	14	3	21.43	1452
HO-165-TS	5.93	4.46	9.10	4.64	1.26	14	0	0	1573

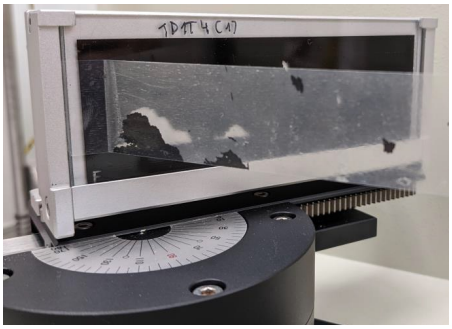

Figure 14: Example of partial delamination

The values of the 120 mesh show only slight variations between the HI and HO-glasses and glass sides (AS/TS). The average peel force ranges from min. 4.02 N to max. 4.43 N. By the 165 mesh varies the average peel force from min. 5.07 N to max. 7.4 N. The average peeling force is also higher for the HI-glasses than for the HO-glasses. In relation to the glass side, there is no clear influence on adhesion.

A possible explanation for the higher peeling forces, and thus also a higher adhesion between the ink surface and the adhesive of the tape, could be found in the different roughnesses of the ink layer produced by the two mesh screens during printing (Figure 15). Depressions appear in the surface which are no longer wetted by the adhesive and thus give rise to air-filled cavities (Habenicht, 2009). The more of these air bubbles are formed per unit area, the more the adhesion effect decreases. Table 6 shows the results. The numerical correlation between roughness and bond strength, in this case was 0.40, this means weak, for both R_z and S_z. The roughness here does not appear to have a preponderant role in the adhesion.

Table 6: Comparison of peel forces to surface roughness

Samples	Average peel force [N]	Average R_z internal area [µm]	Average S_z internal area [µm]
HI-120-AS	4.38	17.24	34.91
HI-165-AS	7.40	15.52	31.83
HI-120-TS	4.02	17.10	33.42
HI-165-TS	6.45	16.67	34.75
HO-120-AS	4.43	18.64	36.37
HO-165-AS	5.07	12.02	29.62
HO-120-TS	4.36	18.42	35.28
HO-165-TS	5.93	12.37	29.74

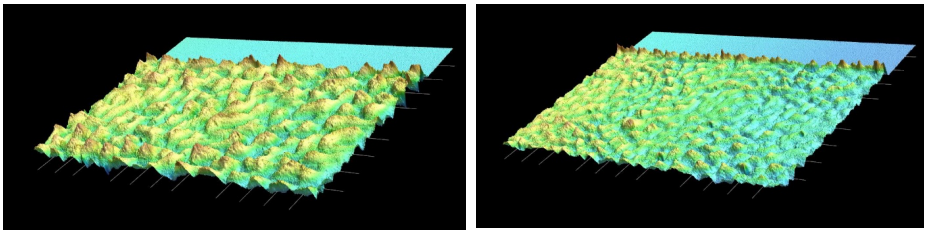

a) *b)*

Figure 15: Screen print 3D-images of 120 mesh (a) and 165 mesh (b) with 700× magnification

Another possible explanation for the phenomena is that the ink films printed by the 120 mesh are thicker than the films printed by the 165 mesh. Thicker films tend to have a higher curing energy. As the same curing time was used for all specimens, it is possible that the ink film on the 120 mesh is not fully cured. Finally, differences in the so called sweating layer should not show significant dependence on the ink film thickness and therefore could not have a major influence on the adhesion in this case.

4. Conclusions

The experiments presented here aim to understand the factors that influence the print quality of UV ink on float glass. According to the literature, the mesh screen is the factor that most influences the final printing result. This could be verified in the experiments. In summary, in relation to the mesh screens (165 and 120) it can be stated, on the basis of the experiments carried out, that the lines printed with the 165 mesh vary less (smaller delta) from the target value, that the printed surface has less roughness, the thickness of the dry ink film is thinner and the adhesion of the ink is higher than when printed with the 120 mesh. In relation to the surface pretreatment (HO and HI) it was possible to note, that the printed lines on the hydrophilic surfaces had less spreading (thinner lines) and showed higher roughness than those printed on the hydrophobic surfaces. The rise in roughness could not be verified for the 120 mesh. Lines printed on the AS are thinner than those printed on the TS. A clear influence of the glass side on the roughness could not be demonstrated.

In order of influence, it was found that the mesh screen geometry has the stronger influence on the aspects tested here (line reproduction, roughness, ink film thickness and adhesion) than the pre-treatment of the glass, and this in turn has a stronger influence than the side of the float glass.

References

Berufsgenossenschaft Energie Textil Elektro Medienerzeugnisse, 2020. *UV-Trocknung*. [online] BG ETEM. Available at: <https://medien.bgetem.de/medienportal/artikel/TUIwMzQ-/> [Accessed 21 March 2023].

Habenicht, G., 2009. *Kleben: Grundlagen, Technologien, Anwendungen*. 6th ed. Berlin: Springer.

International Organization for Standardization, 2017. *ISO/IEC 24790:2017: Information technology – Office equipment – Measurement of image quality attributes for hardcopy output – Monochrome text and graphic images*. Geneva: ISO.

Patejdl, S., Jung, U. and Freieck, K., 2022. Wetting and adhesion phenomena of surface-treated float glass. In: C. Ridgway, ed. *Advances in Print and Media Technology: Proceedings of the 48th International Research Conference of iarigai*. Greenville, USA, 19–21 September 2022. Darmstadt: iarigai.

Scheer, H.G., 2007. *Siebdruck-Handbuch*. Lübeck: Der Siebdruck, pp. 77–78.

Shen, Q., Chen, X., Guo, J., Taeyu, M., Shi, D., Wang, D., Qu, L., Lu, K., Hou, X., Sun, J. and Wu, T., 2012. P-50: Low K acryl resin as planarization layer on TFT LCD. *SID International Symposium Digest of Technical Papers*, 43(1), pp. 1247–1250. https://doi.org/10.1002/j.2168-0159.2012.tb06024.x.

DOI 10.14622/Advances_49_2023_08

Numerical investigation of the lateral movement of doctor blades in gravure printing

Christian Sauder, Tobias Steger, Alina Sersch and Peter Gust

University of Wuppertal, School of Mechanical Engineering and Safety Engineering, Chair of Engineering Design,
Gaußstr. 20, 42119 Wuppertal
E-mails: csauder@uni-wuppertal.de; tobias.steger@uni-wuppertal.de; alina.sersch@uni-wuppertal.de; peter.gust@uni-wuppertal.de

Short abstract

An alternating lateral movement is usually applied to doctor blades to even out wear in gravure printing. This movement leads to an increased load on the doctor blade and can result in damage to the blade edge and thus lead to misprints. The phenomenon is well known to the printing community, but most analytical and numerical models of the doctoring process reduce it to a 2D cross section and are not, therefore, effective in investigating the problem. This study investigates the changes in load during the movement of the doctor blade and the feasibility of using simple shell elements for the given task. One finding is that this simulation approach contributes to the understanding of the doctor blade's lateral movement, especially its displacement. The limitations of the approach are recognised, and future options for improving stress analysis and other physical effects are given.

Keywords: finite element analysis, shell element, doctoring, printing proofer, tip cracking

1. Introduction and background

According to Kipphan (2001) the patterns to be transferred to the substrate in gravure printing are engraved into the surface of a chromed gravure cylinder. The engraved cells are flooded with ink by immersing and rotating the cylinder in a reservoir. The excess ink is then wiped off the unengraved areas by a doctor blade before the substrate is wetted by pushing it into the engraved cells with the help of an impression roller.

The printing quality of the gravure printing process is affected by a large number of parameters (Bohan, Claypole and Gethin, 2000). One important component of a gravure printing press is the doctoring unit with the doctor blade and a backup blade fixed in a blade holder (Swedev AB, Munkfors/S, 2011). The doctoring unit is pneumatically actuated and the doctor blade is pressed against the gravure cylinder. As the doctor blade slides over the chromed surface of the gravure cylinder, it inevitably wears out (Hanumanthu, 1999); in the worst case, high loads can damage the blade's tip (Swedev AB, Munkfors/S, 2011). To even out wear on the doctor blade, the doctoring unit is moved alternately in transverse directions (Ollech, 1993). The literature reports the use of different numerical and analytical models in order to understand the relations of process parameters on the doctoring step in gravure printing. A recent overview is given by Bitsch (2020). Most of these models are reduced to represent a 2D cross section of the doctoring unit, so the effects in the transverse direction are not investigated thoroughly. Scheuter and Bognar (1968) presented an analytical model of a doctor blade utilizing the Kirchhoff-Love theory of thin plates. They investigated the loading and deflection of the blade with respect to shape deviations of the gravure cylinder. Hoang and Ko (2015) conducted a numerical examination of the downward deflection of a doctor blade into an engraved parallel groove. They varied the width of the groove and the doctoring pressure and investigated the effects on cell filling and print quality.

To further understand the doctor blade's behaviour in the transverse direction, we have introduced a new simplified model that also covers the alternating movement of the doctoring unit. This study investigates the global loads and deflections on the doctor blade and support blade, with special interest in the loads at

the ends of the gravure cylinder. In addition, it investigates the feasibility of simple shell elements for the given task and the need for sub-modelling techniques for local effects.

2. Materials and methods

2.1 Materials

A gravure printing proofer (Moser HS 157) was chosen as the subject of this research, since it comprises all components of interest and is equipped with an eccentric drive for the lateral movement of the doctoring unit. The device is shown in Figure 1a; its general specifications are given in Table 1. Figure 1b provides a CAD model of the sub-assembly of the doctoring unit and gravure cylinder.

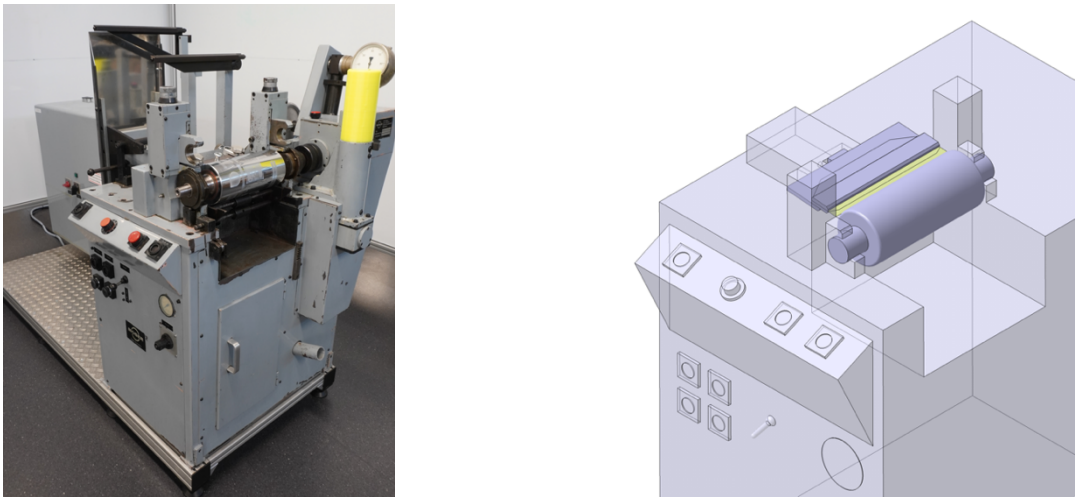

a) *b)*

Figure 1: (a) Gravure printing proofer (Moser HS 157), (b) CAD model of the printing proofer with doctoring unit and gravure cylinder

Table 1: Specifications of the gravure printing proofer (Moser HS 157)

Specification	Value	Unit
Printing speed	10–60	$m \cdot min^{-1}$
Total stroke of doctoring unit	10	mm
Max. doctoring pressure (D50/d22 piston)	2.5	bar
Printing format	297 × 210	mm
Width of doctoring unit	275	mm
Width of gravure cylinder	260	mm

The doctoring unit consists of a rocker, a support plate, and an upper and lower clamping plate, as well as the doctor blade and support blade. Both blades have been modelled as mid-surfaces of the actual blade bodies, neglecting the cut at the tip of the doctor blade. Figure 2 shows the dimensions of the doctoring setup. The doctor blade and support blade protrude 20 mm and 10 mm respectively from the clamping plates and meet the gravure cylinder at a tangent angle of 65°. Their material thicknesses are 0.2 mm and 0.5 mm respectively. The edge of the gravure cylinder is rounded off with a 5 mm radius, and a 1° slope extends 10 mm from the sides. To relieve the doctor blade at the ends of the gravure cylinder, the edges of the support blade are bevelled to effectively extend the gravure cylinder's ends by 10 mm inwards.

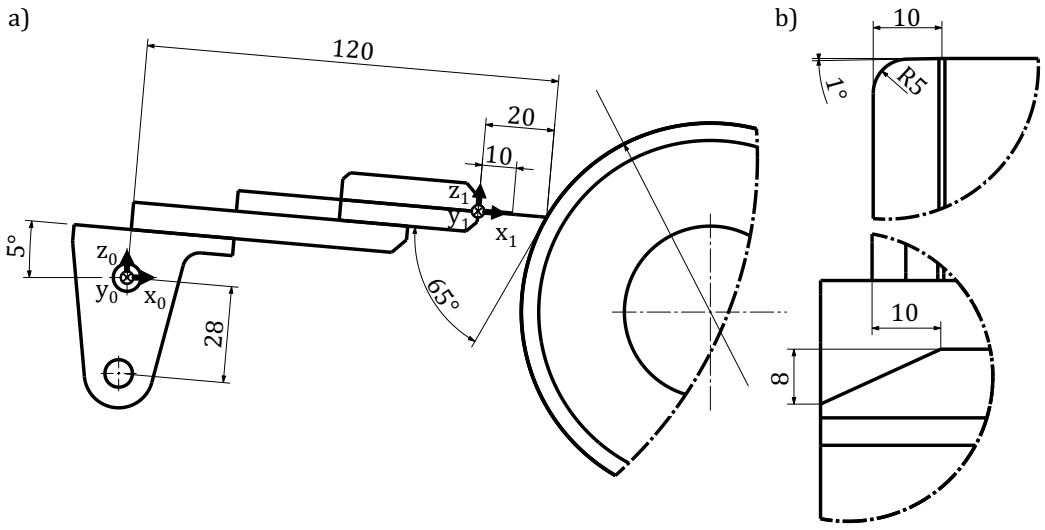

Figure 2: Sketch of the doctoring unit: (a) cross section of the doctor blade unit and the gravure cylinder, (b) detailed view of the end of the gravure cylinder and the edge of the support blade

2.2 Finite element analysis of the doctor blade and support blade

The numerical investigation of the doctoring process is carried out by a static finite element analysis of the doctor blade unit using ANSYS Mechanical 2020 R2.

2.2.1 Material properties and meshing

The doctor blade and support blade are modelled as flexible bodies, while all other bodies are defined as rigid. Steel was assigned as the material of the flexible bodies with a Young's modulus $E = 210 \times 10^3$ MPa and a Poisson's ratio $\nu = 0.3$. Four-node elements are used for meshing both bodies with six degrees of freedom at each node (SHELL 181). This allows the evaluation of membrane and bending stresses. A structured trapezoid-based mesh is used to receive rectangular shaped elements for all sections of the doctor blade and most sections of the support blade. Only in the area of the bevelled edges of the support blade are other trapezoid shapes accepted. The mesh size has been chosen accordingly to give a reasonable resolution and the aspect ratio has been checked to avoid geometric locking effects. Element sizes chosen were 0.2 mm at the sides and 1.0 mm in the middle resulting in 67 257 elements with 92 019 nodes.

2.2.2 Boundary conditions

The rocker, support plate and clamping plates are treated as a single solid. Both blades are connected to the upper clamping plate by rigid multi-point constraints that enable transmission between the three degrees of freedom of the rigid body nodes and the six degrees of freedom of the shell element's flexible body nodes. Contact between the blades is implemented by means of a frictionless contact using the pure penalty method and the thickness effect of the shell elements to minimize unrealistic penetration and allow separation of the blades. A frictional contact with a coefficient of friction of $\mu = 0.01$ was specified for the contact between the doctor blade and the gravure cylinder. This is a first assumption for the lubricated contact in order to investigate changes in the loads in a transverse direction during the doctoring process until measurements are performed. Again, the pure penalty method and thickness effect of the shell elements are used.

Displacement of the components is constrained with respect to the coordinate systems as specified in Figure 2. All six degrees of freedom are restricted for the gravure cylinder at the bearing section. The movement of the doctoring unit is established by limiting all degrees of freedom except rotation around

the y_0-axis and lateral movement in a y_0-direction. That movement is given by a sinusoidal displacement which simulates the eccentric drive of the gravure printing proofer. Displacement in an $x_0$direction is applied to the rocker lever, which increases the reaction force linearly until it reaches a maximum of 250 N. This pivots the doctoring unit. Gravitational loads are neglected at this stage. The load and displacement are applied subsequently in two timesteps. In the first timestep with a duration of one second the displacement is applied to the doctoring unit and both blades bend and press against the gravure cylinder. In the second timestep of one to two seconds a 5 mm lateral movement is performed to each side sinusoidally. The maximum offset positions are reached at 1.25 and 1.75 seconds.

3. Results and discussion

3.1 Results

In Figure 3 the results of the finite element analysis are presented for t = 1 s and t = 1.75 s. The undeformed wireframe of the geometry, as well as the gravure cylinder (top) and blade holder (bottom) are included in the figure for reference purposes. The results are described in further detail below.

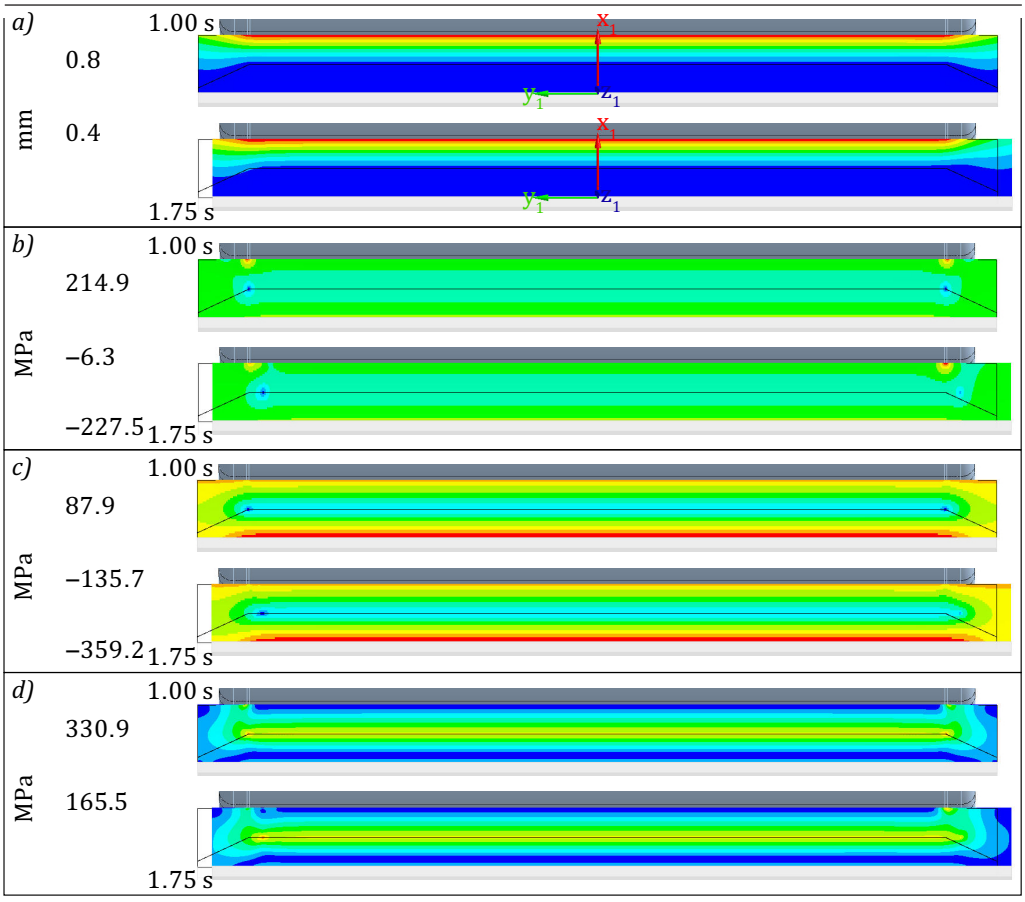

Figure 3: Results after t = 1 s and t = 1.75 s: (a) displacement in z_1-direction, (b) bending stress around the x_1-axis, (c) bending stress around the y_1-axis, (d) von Mises stress

Figure 3a shows the displacement in a $z_1$direction with respect to the local coordinate system defined at the clamped base of the blades, as shown in Figure 2. The deflection is constant over the cylindrical portion of the gravure cylinder. In contrast, less deflection can be observed at the extends of the doctor blade. The maximum deflection of u = 0.809 mm is located at the cylinder's left end at t = 1.75 s when moved inwards,

while the deflection at the right end of the doctor blade decreases. This asymmetric displacement leads to asymmetric stresses while the doctoring unit is off-centred. Figures 3b and 3c present the bending stresses around the x_1-axis and y_1-axis at the top of the doctor blade. In the course of bending around the x_1-axis, high tensile stresses can be observed locally at the ends of the cylinder, where the doctor blade sides are bent downwards. The maximum tensile stress is $\sigma_{\mathrm{bt},x_1} = 214.9$ MPa at $t = 1.75$ s. Additionally, high compressive stresses with a maximum of $\sigma_{\mathrm{bc},x_1} = -227.5$ MPa can be observed for the same timestamp at the edge of the support blade, where it bends upwards. Around the y_1-axis tensile stresses appear at the clamped base of the blade where it deflects downwards, and compressive stresses appear at the contact with the support blade where it is bent upwards. At timestamp $t = 1.75$ s the maximum tensile stress is $\sigma_{\mathrm{bt},y_1} = 87.9$ MPa and the maximum compressive stress is $\sigma_{\mathrm{bc},y_1} = -359.2$ MPa. Figure 3d displays the von Mises stresses for the whole doctor blade. The position of the maximum von Mises stress with $\sigma_{\mathrm{vM}} = 330.9$ MPa is at the left edge of the support blade at $t = 1.75$ s.

3.2 Discussion

With the given simulation model and the results as shown in section 3.1, it can be stated that a quantitative evaluation of doctor blade deflection is achievable accurately. In contrast, evaluation of the stresses should be carried out qualitatively, especially in the contact region. This is because shear stresses are not included in the formulation of the shell elements. Furthermore, high stresses can be anticipated at the doctor blade tip due to the expected Hertzian pressure. The selected shell elements cannot resolve the contact area finely enough to represent the three-dimensional effects, as the height of the doctor blade is only represented by one element. This results in a singularity and a sensitivity of the stresses to the element size in the region of contact.

4. Conclusions and outlook

4.1 Conclusions

By including the lateral movement of the doctor blade unit in the numerical model of the doctoring process in gravure printing, it is shown that, as expected, high stresses appear at the gravure cylinder ends. However, in the given state of the model a quantitative evaluation is not reliable. It is reasonable that the highest stresses appear at the maximum offset positions of lateral movement because of the bevelled support blade and the maximum stiffness in that position. It can be concluded that modelling the doctor blade with shell elements can contribute to an understanding of the lateral movement, but further adaptation of the model is needed to account for all relevant physical effects.

4.2 Outlook

By extending the simulation model, the doctoring process can be analysed even more extensively. In order to simulate the process influence of the doctor blade geometry more precisely, the ground edge should be simulated via variable element thickness or volumetric 3D mesh. This will enable quantitative evaluation of the stresses and contact pressure of the doctor blade against the cylinder in greater detail. Besides this, sub-modelling techniques can be implemented to further improve the simulation model. For this purpose, it may also be useful to include geometric deviations of the cylinder. A promising approach here is the simulation of different process settings, which will facilitate sensitivity analysis with regard to the selected process parameters. These settings can also be reproduced on the laboratory printing machine, and the simulation model can thus be validated by strain gauge or optical measurements during the process. Further investigative approaches can be opened up by combined simulations including wear and flow behaviour.

Acknowledgements

The authors acknowledge TKM Meyer GmbH for bringing the problem to their attention, as well as providing the gravure printing proofer and partially funding the doctoral position of C.S. as part of a cooperative project.

Conflict of interest

The doctoral position of C.S. is partially funded by TKM Meyer GmbH whose parent company TKM GmbH is partly funding the doctoral position of T.S.. All other authors declare no conflict of interest. The funders had no influence on the design of the research, the simulation and interpretation of data, or the writing of the manuscript.

Contributions

Conceptual design, C.S., A.S. and T.S.; Investigation, C.S.; Modelling, C.S. and T.S.; Simulation, C.S.; Discussion of simulation results, C.S., A.S. and T.S.; Writing—original draft preparation, C.S., A.S. and T.S.; Writing—review and editing, C.S., A.S., T.S. and P.G.; Funding acquisition, P.G. and C.S.; Supervision, A.S. and P.G. All authors have read and agreed to the published version of the manuscript.

References

Bitsch, T., 2020. *Experimente zum Strömungs- und Benetzungsverhalten von Fluiden im Hochscherratenbereich am Beispiel des Rakelprozesses*. Ph.D. thesis. Technical University of Darmstadt. https://doi.org/10.26083/tuprints-00017589.

Bohan, M.F.J., Claypole, T.C. and Gethin, D.T., 2000. The effect of process parameters on product quality of rotogravure printing. *Proceedings of the Institution of Mechanical Engineers, Part B: Journal of Engineering Manufacture*. 214(3), pp. 205–219. https://doi.org/10.1243/0954405001517595.

Hanumanthu, R., 1999. Variation of gravure coating thickness during early stages of doctor blade wear. *AIChE Journal*, 45(12), pp. 2487–2494. https://doi.org/0.1002/aic.690451204.

Hoang, H.P. and Ko, S.L., 2015. Effect of doctoring on the performance of direct gravure printing for conductive microfine lines. *Journal of Micromechanics and Microengineering*, 25(11): 115018. https://doi.org/10.1088/0960-1317/25/11/115018.

Kipphan, H., 2001. Fundamentals. In: H. Kipphan, ed. *Handbook of print media: technologies and production methods*. Berlin, Heidelberg: Springer, pp. 1–201. https://doi.org/10.1007/978-3-540-29900-4_1.

Ollech, B., 1993. *Tiefdruck: Grundlagen und Verfahrensschritte der modernen Tiefdrucktechnik*. 2nd ed. Frankfurt am Main: Polygraph.

Scheuter, K.R. and Bognar, D., 1968. Beitrag zum Rakelproblem. *DRUCK-PRINT*, 105(4), pp. 293–299. https://doi.org/10.25534/TUPRINTS-00014126.

Swedev AB, Munkfors/S., 2011. Hart und dennoch flexibel - Wissenswertes über die Auswahl von Rakeln für den Tiefdruck. *Flexo+Tief-Druck*, 22(6), pp. 16–19.

DOI 10.14622/Advances_49_2023_03

A new approach to inkjet printing of high viscosity inks for 3D applications

Stefan Güttler[2], Jan Christoph Janhsen[1], Anna Kolesova[1,2], Antonia Götz[1,2] and Karin Chen[1,3]

[1] Fraunhofer Institute for Manufacturing Engineering and Automation, Department of Additive Manufacturing, 70569 Stuttgart, Germany

[2] Stuttgart Media University, Faculty of Print and Media, 70569 Stuttgart, Germany

[3] Karlsruhe Institute of Technology, Institute for Automation and Applied Computer Science, Hermann-von-Helmholtz-Platz 1, 76344 Eggenstein-Leopoldshafen

Emails: guettler@hdm-stuttgart.de; jan.christoph.janhsen@ipa.fraunhofer.de

Short abstract

By combining recent advancements in high viscosity piezo inkjet and measurement technique for high frequency rheology, we investigate a route to multi-material printing of highly viscous UV polymers that were developed for vat photo polymerization. The application is additive manufacturing of dental prosthesis where a single-material process (vat photo polymerization) should be replaced by a multi-material process (inkjet printing) without compromising the material properties of the prosthesis. We study the printability of UV-polymers from two manufacturers with the recently introduced printhead from Quantica. At temperatures of 60 °C to 80 °C the viscosity and Ohnesorge number lie in a printable range. The integrity of the UV-polymers at elevated temperatures is tested. The (linear) viscoelasticity is studied by oscillatory and vibrational rheology in a frequency range up to 10 kHz and the connection of high frequency rheology to the printability and drop formation in a Quantica printhead is made.

Keywords: high viscosity inkjet, additive manufacturing (3D printing), high frequency rheology

1. Introduction and background: limitations of additive manufacturing and the role of piezo inkjet

Many additive manufacturing (AM) techniques have found their way into manufacturing of customized products in an industrial scale overcoming their former limitation to prototyping. An overview over additive manufacturing can be found in ISO/ASTM 52900 (International Organization for Standardization, 2021). Additive manufacturing processes can be categorized according to their functional principles. In powder-based processes layers of spread powder (metal or thermoplastic polymer) are either selectively sintered or molten (powder bed fusion – PBF) or fixed by a binder that is printed into the powder bed (binder jetting – BJ). The glued powder is subsequently sintered or infiltrated with a resin. A widespread process is melting of a thermoplastic filament that solidifies layer by layer into a 3D shape (material extrusion – MEX). Other AM techniques depend on curing of UV-polymers. A UV polymer in a vat is selectively cured by a laser, digital light projector, or LC screen, layer by layer (vat photo polymerization) or UV inks are layer by layer printed by piezo inkjet and cured. (material jetting – MJ). The properties of the various additive manufacturing techniques widely differ depending on the material and manufacturing method.

What all additive manufacturing technologies have in common is the limitation of the materials that can be processed. All methods but material jetting and material extrusion are limited to a single building material. MEX can only extrude materials strand by strand whereas material jetting with piezo inkjet allows to deposit materials drop by drop (voxel by voxel). This enables tailoring the optical or mechanical properties of a 3D structure by combining a set of process materials (like a color synthesis from the process colors CMY).

An important application of AM is manufacturing of medical prosthesis. Building of customized structures of any desired shape is a clear strength of AM as far as the strict requirements on the material properties can be met. On today dental prosthesis as crowns, dentures, splints, and surgical templates are manufactured by vat photo polymerization. Progress in the development of UV polymers allowed to extend the usage of additive manufactured dental prosthesis from provisory use over temporal to permanent use. Main disadvantage of vat photo polymerization is the restriction to a single building material. For manufacturing of (permanent) dentures or crowns shades of color and transparencies need be precisely reproduced what requires expensive manual retouching. Inkjet printing of UV polymers allows printing of several materials, e.g., colors. But a major limitation of piezo inkjet is the viscosity of printable inks. Polymers designed for vat photo polymerization have a viscosity higher than 1 000 mPa·s at room temperature whereas the viscosity of inks for standard piezo printheads is limited to at most 25 mPa·s at operating temperature. The operating temperature depends on the printhead and can go up to 125–130 °C for hot-melt printheads, according to specifications of hot melt printheads (Canon CrystalPoint, 2018; Dimatix Galaxy 256 HM, 2015; Xerox MDF, 2017). The viscosity of polymers strongly decreases with rising temperature but many functional materials do not withstand such elevated temperatures. Moreover, the diameter of particles (e.g., pigments, ceramics) in inkjet inks need be small ($d_{90} < 1$–3 µm, depending on nozzle size), and the volume fraction of solids in inks cannot be too high. Inkjet inks must be chemically stable (free of sedimentation). In printheads with ink circulation a slow sedimentation of solids is tolerable if particles can be redispersed.

After piezo inkjet found its way into industrial applications as of around 2 000, many attempts were made to extend the viscosity range of inks. When the physics of piezo inkjet was understood it became clear that the functional principle of piezo inkjet limits the viscosity of printable inks. For medium viscous inks (~15–20 mPa·s) the pressure drop caused by viscous dissipation in the nozzle makes up most of the pressure that is generated at the nozzle in a piezo printhead. The maximal pressure at the nozzle is limited because the positive pressure wave that accelerates the ink in the nozzle is accompanied by negative pressure waves due to reflections of the sound waves in the printhead cavity. A too strong positive pressure wave cannot avoid strong negative pressure waves that draw air through the nozzle into the pumping chamber what defeats the pumping mechanism. A comprehensive treatment of the functional principle of piezo printheads is found e.g., in the pioneering works (Wijshoff, 2008; 2010).

Beside the technical limits of piezo printheads also a physical border for the detachment of drops from a fluid surface (capillary, nozzle) exist which cannot be overcome by any dispensing technique. This is because detachment of drops occurs through a Plateau-Rayleigh instability. Two-time scales control the breakup of a cylinder of a Newtonian fluid:

$$t_{\mathrm{R}} = \sqrt{\frac{\rho d^3}{\sigma}} \quad \text{and} \quad t_\eta = \frac{\eta d}{\sigma} \qquad [1]$$

where η, ρ, σ are the viscosity, density and surface tension of the fluid and d is the diameter of the fluid cylinder or nozzle. See e.g., Pekker (2018) for a discussion of the breakup of a cylinder of viscous liquid. With increasing viscosity, the detachment of drops through a Plateau-Rayleigh instability becomes slower what eventually prevents any inkjet process (we do not consider the extrusion of a filament that is cut by a device (valve) as an inkjet process). For Newtonian fluids, the detachment of drops from a fluid surface and the printability of fluids by piezo inkjet is characterized by the Ohnesorge number:

$$Oh = \frac{t_\eta}{t_{\mathrm{R}}} = \frac{\eta}{\sqrt{\rho \cdot d \cdot \sigma}} \qquad [2]$$

According to Derby (2010) (Newtonian) fluids are printable by piezo inkjet in the range $0.1 < Oh < 1$. The lower border corresponds to formation of satellite droplets and the upper border to a fluid viscosity >~25 mPa·s. Many highly viscous fluids are non-Newtonian and their printability cannot be

fully characterized by the Ohnesorge number. More recently Xaar (GB) and Quantica (Germany) developed piezo printheads with an enlarged viscosity range that allow printing of fluids with viscosity up to 60–100 mPa·s, possibly more (Jackson, 2019; Borrell, 2022).

Attempts have also been made to develop digital printing techniques that overcome the technical limitations of piezo inkjet. A successful development is Laser Transfer Printing (LTP), a process based on the Laser Induced Forward Transfer process (LIFT) introduced in 1986 (Serra and Piqué, 2019). LTP is able to print inks with much higher viscosity, larger particle diameter and higher volume fraction of solids than inkjet can. A disadvantage of LTP is the drop generation mechanism that depends on the formation of a vapor bubble. This requires inks that can form vapor bubbles or a sacrificial layer for bubble formation placed beneath the ink film. LFT print engines are large and much more expensive than piezo inkjet engines. This limits the benefit of LTP for multi-material applications.

2. Materials and methods: linking high frequency rheology to printability in a Quantica printhead

The approach followed in this (ongoing) research work is to adapt UV polymers and sols (solid in liquid dispersions) that were developed for vat photo polymerization to the recently introduced printhead from Quantica and possibly to other piezo printheads. The Quantica printhead is not an acoustic printhead, its functional design differs from other piezo printheads (Borrell, 2022; Färber and Hartkopp, 2021). The expected viscosity range is at least up to 100 mPa·s, maybe more. The formation of proper drops from highly viscous fluids is not yet clear. The operating temperature is up to 80 °C. A tradeoff of the design is a large nozzle-to-nozzle distance (1.27 mm) and a rather small maximal printing frequency. The Quantica printheads are in a β-testing stage to date.

In this study, we regard UV-polymers for vat polymerization of dental prosthesis from two manufacturers. The goal is to improve the rheological properties of the dental materials that are important for drop formation without compromising the material properties. This requires to evaluate the relevant rheological properties and to connect them to the chemical composition. This route is not new but advancements in high viscosity printheads and measurement technology cuts out a path for further progress.

Polymers and sols are shear-thinning and viscoelastic fluids. During drop-formation high pressure (up to 1.5 hPa) and high shear rates ($\dot{\gamma} = 10^5$–$10^6\ 1/s$) act on the ink for a few 10 µs. These conditions cannot be reproduced in standard rheometers. During drop formation an equilibrium state of a non-Newtonian fluid is probably not reached (as it is in a rheometer). It is known that some sols can be printed whose viscosity at low shear rates is much too high. Elasticity plays an important role in the behavior of polymers and sols under short acting stresses and therefore has a strong influence on drop formation (Mackley, Vadillo and Tuladhar, 2016). In oscillatory and vibrational rheology, (linear) viscoelasticity is characterized by a storage module G' and a loss module G'' which describe the spring-like behavior (G'), resp. the viscous dissipation (G'') of a complex fluid. The relation between shear stress $\sigma(t)$ and shear strain $\gamma(t)$ of a complex fluid can be written as:

$$\sigma(t) = (G' + iG'')\gamma(t); \quad \sigma(t) = \sigma_0 e^{i\omega t}; \quad \gamma(t) = \gamma_0 e^{i\omega t} \qquad [3]$$

G' and G'' are functions of the oscillatory or vibrational frequency, a shear modulus G (or several shear moduli) and a relaxation time $\tau = \eta/G$ (or several relaxation times) of the polymer or sol. The functions G' and G'' depend on the physical model of the viscoelastic fluid (Barnes, Hutton and Walters, 1989; Larson, 1999; Mackley, Vadillo and Tuladhar 2016). In order to measure the rheological properties that are relevant for drop formation the oscillation period should be in the order of the time scale for drop formation (10 µs to 100 µs).

3. Results and discussion

We measure (Figure 1) the shear-dependent viscosities of two UV-polymers for vat polymerization of dental prosthesis from two manufacturers (material 1 & 2) and a UV-polymer without fillers or pigments for comparison at temperatures of 25 °C to 80 °C (Anton Paar MCR302 rheometer with cone-plate geometry). At 60 °C to 80 °C the viscosities decrease below 100 mPa·s (from above 1 000 mPa·s at 25 °C) and the approximate Ohnesorge numbers lie close to a printable range. Viscosities in Table 1 are measured at a shear rate of 55 000 s^{-1}. The nozzle diameter of the Quantica printhead that enters into the Ohnesorge number is 60 µm.

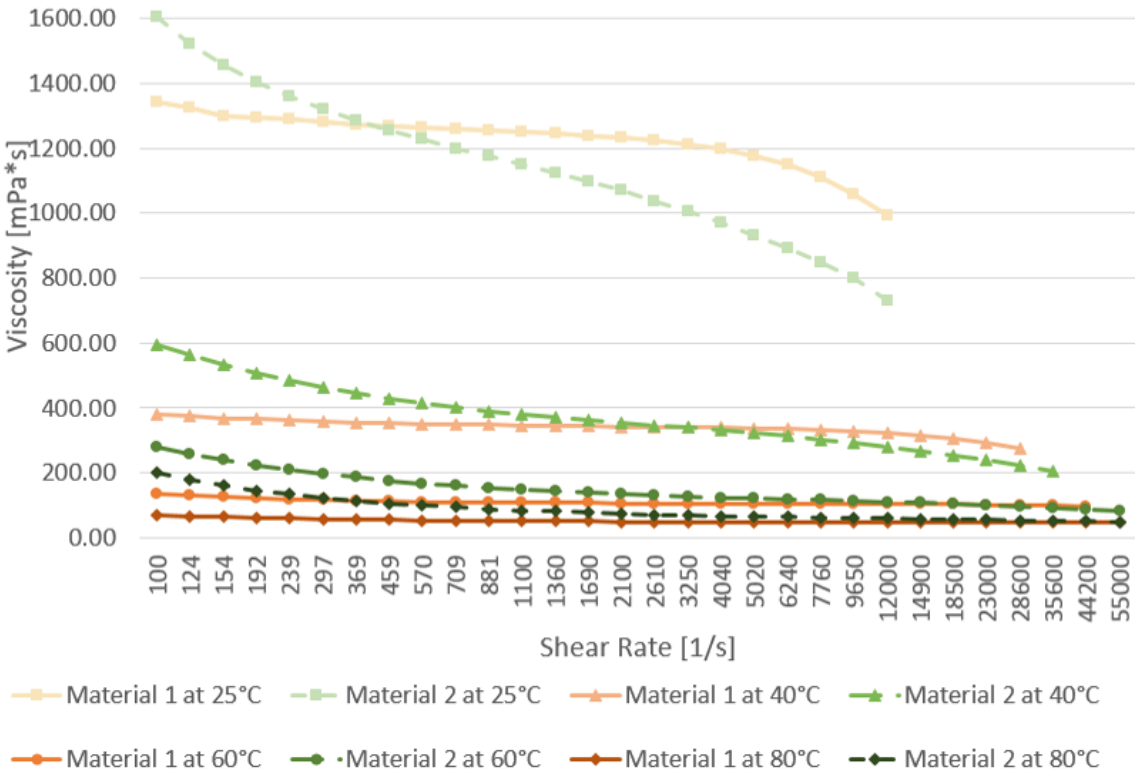

Figure 1: Shear dependent viscosities of the dental materials

Table 1: Basic rheological properties of the dental materials

	Material 1		**Material 2**	
Temperature	60 °C	80 °C	60 °C	80 °C
Viscosity	95 mPa·s	47 mPa·s	83 mPa·s	49 mPa·s
Surface tension	30 mN/m	24 mN/m	38 mN/m	32 mN/m
Density	1.4 g/cm^3	1.4 g/cm^3	1.7 g/cm^3	1.7 g/cm^3
Ohnesorge number	~1.9	~1.0	~1.3	~0.9

Because the dental materials are not designed for processing at elevated temperatures the integrity of the materials was tested. The UV-polymers were stored at 70 °C for 96 h. A UV-LED with 405 nm peak wavelength (M405L3, Thorlabs GmbH) was integrated into the UV module (P-PTD-UV) of the rheometer (Anton Paar MCR302). *G'* and *G''* were measured in oscillatory mode at a frequency of 1 Hz with plate-plate geometry. When the UV-LED was switched on *G'* quickly increased, indicating the onset of the crosslinking reaction (Figure 2). An effect of degradation due to heating was not observed for any material.

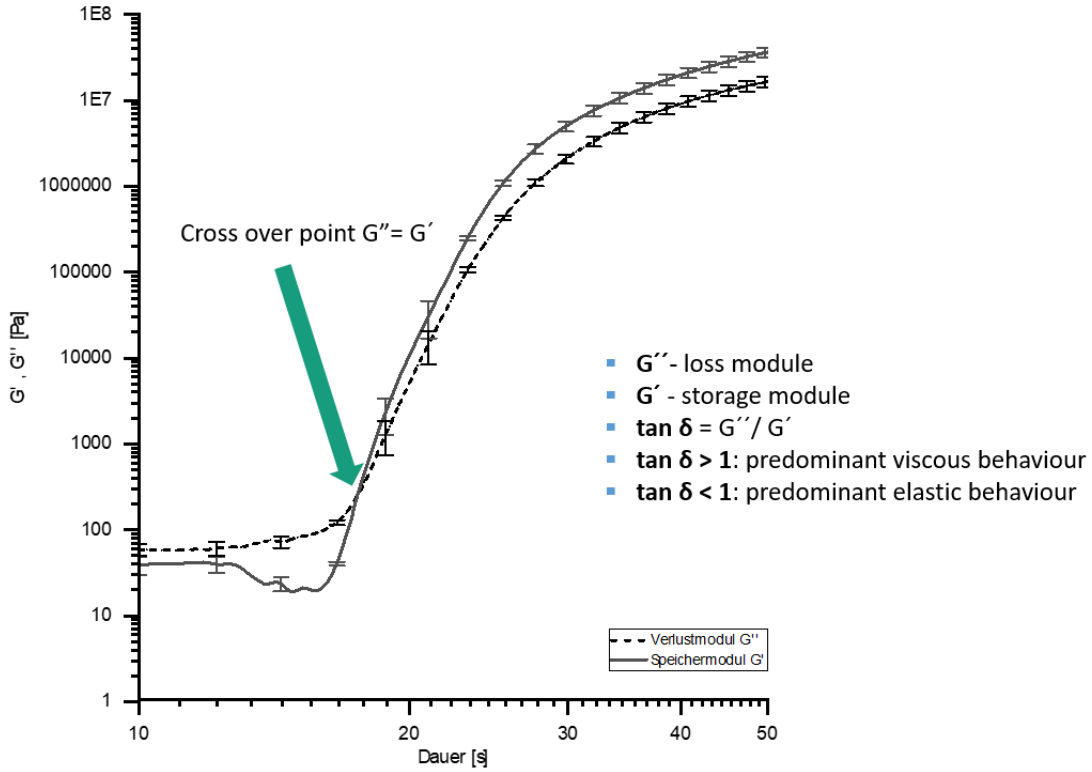

Figure 2: Change of storage module G' and loss module G'' during exposure of the dental materials; the UV-LED is switched on at t = 15 s

We next studied the viscoelastic properties of the UV polymers with a high frequency rheometer (Trijet TriPAV). The functional principle is the vibration of a thin ink film at up to 10 kHz. This allows to evaluate the behavior of polymers and sols under short acting stresses. *G'* of materials 1 & 2 differ at high vibrational frequencies. A preliminary (not yet reliable) result is shown in Figure 3. We found it difficult to calibrate the TriPAV such that measurements are reproducible.

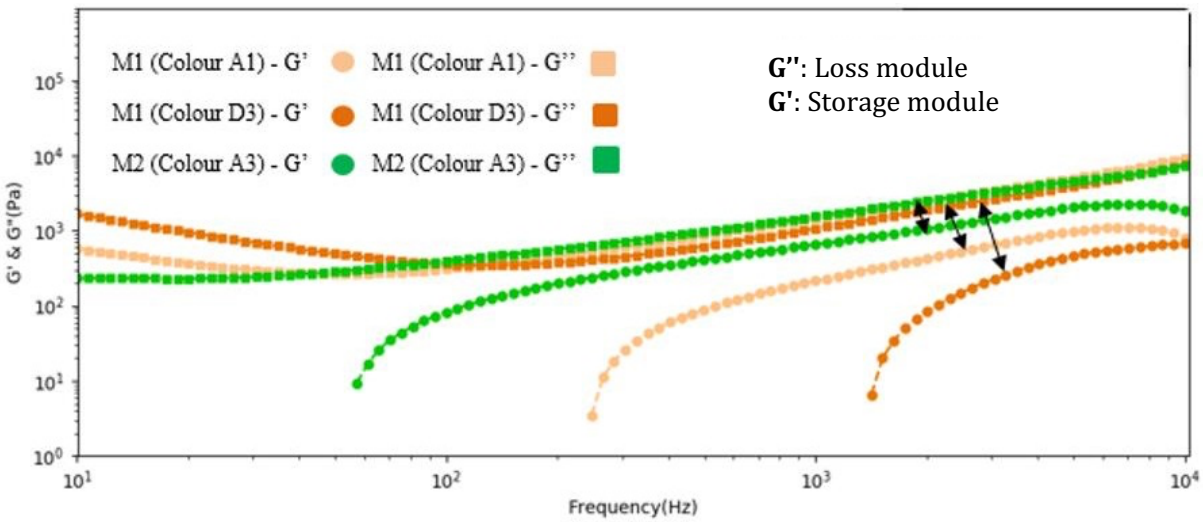

Figure 3: Storage module G' and loss module G'' of materials 1 & 2 measured in the TriPAV (preliminary)

The elasticity of fluids is not only caused by stretching of polymers but also by interaction of suspended particles. These could be insufficiently stabilized pigments. The chemical stability of pigments suffers at elevated temperatures. Therefore, G' and G'' of a UV-polymer without fillers or pigments is studied for comparison.

A first print test with dental material 1 was conducted by Quantica company. It was shown that the UV-polymer can be printed with the Quantica printhead at 60 °C at a printing frequency of 3.8 kHz. The result was not perfect, strong satellite droplets formed. Reliable measurements of the dental materials with the TriPAV and the connection to drop formation in the Quantica printhead are currently under progress.

Acknowledgements

This project is conducted in cooperation with a manufacturer of UV-polymers for additive manufacturing of dental prosthesis. The authors thank Quantica company for their support and the conduction of a first print test. The authors thank Yina Xu for the contributions to the measurements during her internship.

References

Barnes, H.A., Hutton, J.F. and Walters, K., 1989. *An Introduction to Rheology*. Amsterdam: Elsevier.

Borrell, R., 2022. *Revolutionary piezo inkjet technology and printhead capable of jetting extreme viscosity inks* (presentation by Quantica company on the Industrial Print Integration 2022. Düsseldorf, Germany, 18–19 May 2022). [video online] Available at: <https://www.youtube.com/watch?v=qsEd3FNPqlc> [Accessed April 2023].

Canon CrystalPoint, 2018. *Océ Crystal Point® technology*. [online] Available at: <https://csa.canon.com/internet/wcm/connect/us/a3b369d5-60f3-46ff-a594-4048712207b7/oce-crystalpoint-technology.pdf?MOD=AJPERES&CVID=muEpOaD> [Accessed April 2023].

Derby, B., 2010. Inkjet printing of functional and structural materials: fluid property requirements, feature stability, and resolution. *Annual Review of Materials Research,* 40(1), pp. 395–414. https://doi.org/10.1146/annurev-matsci-070909-104502.

Dimatix Galaxy 256 HM, 2015. *Galaxy PH 256/80 HM*. [online] Available at: <https://www.fujifilm.com/us/en/business/inkjet-solutions/industrial-printheads/galaxy-ph-256-80-hm> [Accessed April 2023].

Färber, L., Hartkopp, B., Quantica GmbH. 2021. *Material ejection system, print head, 3d printer, and method for material ejection*. European Patent Application EP 3 825 100 A1.

International Organization for Standardization, 2021. *ISO/ASTM 52900:2021(en) Additive manufacturing – General principles – Fundamentals and vocabulary*. Geneva: ISO.

Jackson, N., 2019. *Expanding the boundaries of piezo inkjet* (presentation by Xaar company on The Inkjet Conference 2019, Düsseldorf). [video online] Available at:<https://www.youtube.com/watch?v=6WSSEX_8098> [Accessed April 2023].

Larson, R.G., 1999. *The structure and rheology of complex fluids*. New York: Oxford University Press.

Mackley, M.R., Vadillo, D.C. and Tuladhar, T.R., 2016. Inkjet fluid characterization. In: S.D. Hoath, ed. *Fundamentals of inkjet printing*. Weinheim: Wiley-VCH.

Pekker, L., 2018. On Plateau-Rayleigh instability of a cylinder of viscous liquid. *Journal of Imaging Science and Technology.* 62(4): 040405. https://doi.org/10.2352/J.ImagingSci.Technol.2018.62.4.040405.

Serra, P. and Piqué, A., 2019. Laser-induced forward transfer: fundamentals and applications. *Advanced. Materials Technologies,* 4(1): 1800099. https://doi.org/10.1002/admt.201800099.

Wijshoff, H., 2008. *Structure and fluid-dynamics in piezo inkjet printheads*. PhD thesis, University of Twente.

Wijshoff, H., 2010. The dynamics of the piezo inkjet printhead operation. *Physics Reports,* 491(2-5), pp. 77–177. 10.1016/j.physrep.2010.03.003.

Xerox MDF, 2017. *Xerox® M Series industrial inkjet printheads*. [online] Available at: <https://oem-printheads.business.xerox.com/products/m-series/> [Accessed April 2023].

Index of authors